NIST CENTER for NEUTRON RESEARCH

accomplishments & opportunities

2011

NIST
National Institute of
Standards and Technology
U.S. Department of Commerce

NIST SP 1127

This page intentionally blank.

ON THE COVER

Doug Ogg pre-aligns new neutron guides for the NCNR guide hall expansion using a laser-tracking system.

2011 NIST Center for Neutron Research

Accomplishments and Opportunities

NIST Special Publication 1127

Robert M. Dimeo, Director

Ronald L. Cappelletti, Editor

December 2011

National Institute of Standards and Technology
Patrick Gallagher, Director

U.S. Department of Commerce
John Bryson, Secretary

DISCLAIMER

Certain commercial entities, equipment, or materials may be identified in this document in order to describe an experimental procedure or concept adequately. Such identification is not intended to imply recommendation or endorsement by the National Institute of Standards and Technology, nor is it intended to imply that the entities, materials, or equipment are necessarily the best available for the purpose.

National Institute of Standards and Technology
Special Publications 1127

Natl. Inst. Stand. Technol. Spec. Publ. 1127, 88 pages
(December 2011)

CODEN: NSPUE2

U.S. GOVERNMENT PRINTING OFFICE-WASHINGTON: 2011

For sale by the Superintendent of Documents,
U.S. Government Printing Office

Internet: bookstore.gpo.gov Phone: 1.866.512.1800
Fax: 202.512.2104 Mail: Stop SSOP, Washington, DC 20402-0001

Table of Contents

Foreword

It is with pleasure that I present this year's annual report for the NIST Center for Neutron Research. When looking back over the last year, the only word that I can use to describe this time period is *dynamic*. User operations were successful and productive, the reactor operating for 142 days out of a scheduled 142 days. The cold source continued to operate reliably and deliver neutrons 99% of the scheduled operating time. This period was marked by considerable scientific productivity and impact as the highlights in this report illustrate. The productivity is due to many factors, but it is worth noting that the number of user experiments on the MACS spectrometer continued to grow as the amount of time available to the user community was increased, industrial research participation on many of the neutron instruments, especially uSANS, was strong, and research opportunities with other laboratories grew, particularly in the area of biology and biosciences. Moreover, significant progress was made towards bringing the isotope labeling laboratory on line which will certainly prove to be a valuable resource for NCNR users.

This year was also marked by a period of many facility enhancements that can best be described as *historic*. On April 3, the reactor shut down, as planned, for a period of 11 months. As I described in last year's annual report this outage was scheduled in order to execute many tasks towards the expansion of our cold neutron measurement capability and enhance the reliability of the reactor. A few of the activities include installation of a new neutron guide system in our expanded guide hall which will hold new and relocated instruments, installation of a new cold source dedicated to the MACS instrument, relocation of MACS, and installation of a new cooling system for the reactor's thermal shield. In addition significant construction in and around the site has taken place during the outage, including the construction of a new secondary cooling system, the addition of a new cooling tower cell, and additional electrical capacity. The commencement and execution of this outage marks the culmination of a significant amount of planning and coordination as well as the hard work and diligent efforts of our staff, especially those from Reactor Operations and Engineering and Research Facility Operations. You can read more about the progress we have made during the outage within this report and on our website: http://www.ncnr.nist.gov/expansion2/ where you will find technical details and photos. I am also pleased to inform you of the release this year of an informal history, "The NIST Center for Neutron Research: Over 40 Years Serving NIST/NBS and the Nation", by Jack Rush and Ron Cappelletti, NIST Special Publication 1120. Contained therein is an account of major events of the NCNR spanning the period from conception of the NIST reactor to the NCNR Expansion Project.

As of this writing we just announced our first call for proposals for experiments to be run upon restart of the reactor. In just a few short months the reactor will restart and users will return to the NCNR. The reason for the outage and expansion is for you, our users. I am looking forward to restoration of user operations and especially offering new measurement capabilities that our expansion project will provide through the coming year. I invite you to take a look at the research highlights from the past year as well as the description of what we have been up to during the outage. As you read through this report, I hope you get the same sense of excitement and opportunity that we are all feeling here.

The NIST Center for Neutron Research

Neutrons provide a uniquely effective probe of the structure and dynamics of materials ranging from water moving near the surface of proteins to magnetic domains in memory storage materials. The properties of neutrons (outlined below) can be exploited using a variety of measurement techniques to provide information not otherwise available. The positions of atomic nuclei in crystals, especially of those of light atoms, can be determined precisely. Atomic motion can be directly measured and monitored as a function of temperature or pressure. Neutrons are especially sensitive to hydrogen, so that hydrogen motion can be followed in H-storage materials and water flow in fuel cells can be imaged. Residual stresses such as those deep within oil pipelines or in highway trusses can be mapped. Neutron-based measurements contribute to a broad spectrum of activities including in engineering, materials development, polymer dynamics, chemical technology, medicine, and physics.

The NCNR's neutron source provides the intense, conditioned beams of neutrons required for these types of measurements. In addition to the thermal neutron beams from the heavy water or graphite moderators, the NCNR has a large area liquid hydrogen moderator, or cold source, that provides long wavelength guided neutron beams for the major cold neutron facility in the U.S.

There are currently 25 experiment stations: four provide high neutron flux positions for irradiation, and 21 are beam facilities most of which are used for neutron scattering research. The subsequent pages provide a schematic description of our instruments. More complete descriptions can be found at www.ncnr.nist.gov/instruments/. Construction of a second guide hall is now complete (see pp. 4-5) and five new instruments are under development.

The Center supports important NIST measurement needs, but is also operated as a major national user facility with merit-based access made available to the entire U.S. technological community. Each year, more than 2000 research participants from government, industry, and academia from all areas of the country are served by the facility (see pp. 56-58). Beam time for research to be published in the open literature is without cost to the user, but full operating costs are recovered for proprietary research. Access is gained mainly through a web-based, peer-reviewed proposal system with user time allotted by a beamtime allocation committee twice a year. For details see www.ncnr.nist.gov/beamtime.html. The National Science Foundation and NIST co-fund the Center for High Resolution Neutron Scattering (CHRNS) that operates six of the world's most advanced instruments (see pp. 59-61). Time on CHRNS instruments is made available through the proposal system. Some access to beam time for collaborative measurements with the NIST science staff can also be arranged on other instruments.

A distorted composite view of the new guide hall, looking through the removed columns towards its center from within the old guide hall (east wing). At the extreme left is the backscattering spectrometer. A portion of the shield assembly for the new guides can be seen in the center of the picture. Far away to the right is all that remains of the wall separating the east and west wings of the guide hall.

Why Neutrons?

Neutrons reveal properties not readily probed by photons or electrons. They are electrically neutral and therefore easily penetrate ordinary matter. They behave like microscopic magnets, propagate as waves, can set particles into motion, losing or gaining energy and momentum in the process, and they can be absorbed with subsequent emission of radiation to uniquely fingerprint chemical elements.

WAVELENGTHS – in practice range from ≈ 0.01 nm (thermal) to ≈ 1.5 nm (cold) (1 nm = 10 Å), allowing the formation of observable interference patterns when scattered from structures as small as atoms to as large as biological cells.

ENERGIES – of millielectronvolts, the same magnitude as atomic motions. Exchanges of energy as small as nanoelectronvolts and as large as tenths of electronvolts can be detected between samples and neutrons, allowing motions in folding proteins, melting glasses and diffusing hydrogen to be measured.

SELECTIVITY – in scattering power varies from nucleus to nucleus somewhat randomly. Specific isotopes can stand out from other isotopes of the same kind of atom. Specific light atoms, difficult to observe with x-rays, are revealed by neutrons. Hydrogen, especially, can be distinguished from chemically equivalent deuterium, allowing a variety of powerful contrast techniques.

MAGNETISM – makes the neutron sensitive to the magnetic moments of both nuclei and electrons, allowing the structure and behavior of ordinary and exotic magnetic materials to be detailed precisely.

NEUTRALITY – of the uncharged neutrons allows them to penetrate deeply without destroying samples, passing through walls that condition a sample's environment, permitting measurements under extreme conditions of temperature and pressure.

CAPTURE – characteristic radiation emanating from specific nuclei capturing incident neutrons can be used to identify and quantify minute amounts of elements in samples as diverse as ancient pottery shards and lake water pollutants.

NIST Center for Neutron Research Instruments (as of Feb. 2012)

[1] BT-5 Perfect Crystal Ultra-Small Angle Neutron Scattering (USANS) Diffractometer for microstructure up to 10^4 nm, part of CHRNS.

[2] BT-4 Filter Analyzer Neutron Spectrometer with cooled Be/Graphite filter analyzer for chemical spectroscopy and thermal triple axis spectrometer.

[3] BT-2 Neutron Imaging Facility for imaging hydrogenous matter in large components such as water in fuel cells and lubricants in engines, in partnership with General Motors and DOE.

[4] BT-1 Powder Diffractometer with 32 detectors; incident wavelengths of 0.208 nm, 0.154 nm, and 0.159 nm, with highest resolution of $\delta d/d \cong 8 \times 10^{-4}$.

[5] VT-5 Thermal Neutron Capture Prompt Gamma-ray Activation Analysis Instrument with a neutron fluence rate of 3×10^8 cm^{-2} s^{-1} used for quantitative elemental analysis of bulk materials. Generally used for the analysis of highly hydrogenous materials ($\cong$ 1 % H) such as foods, oils, and biological materials.

[6] BT-8 Residual Stress Diffractometer optimized for depth profiling of residual stresses in large components.

[7] BT-7 Thermal Triple Axis Spectrometer with large double focusing monochromator, and interchangeable analyzer/detectors systems.

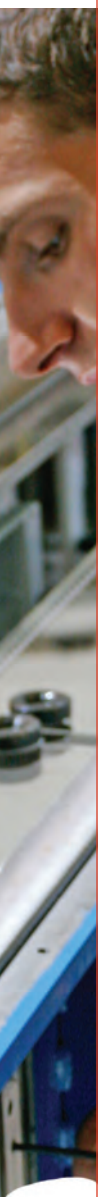

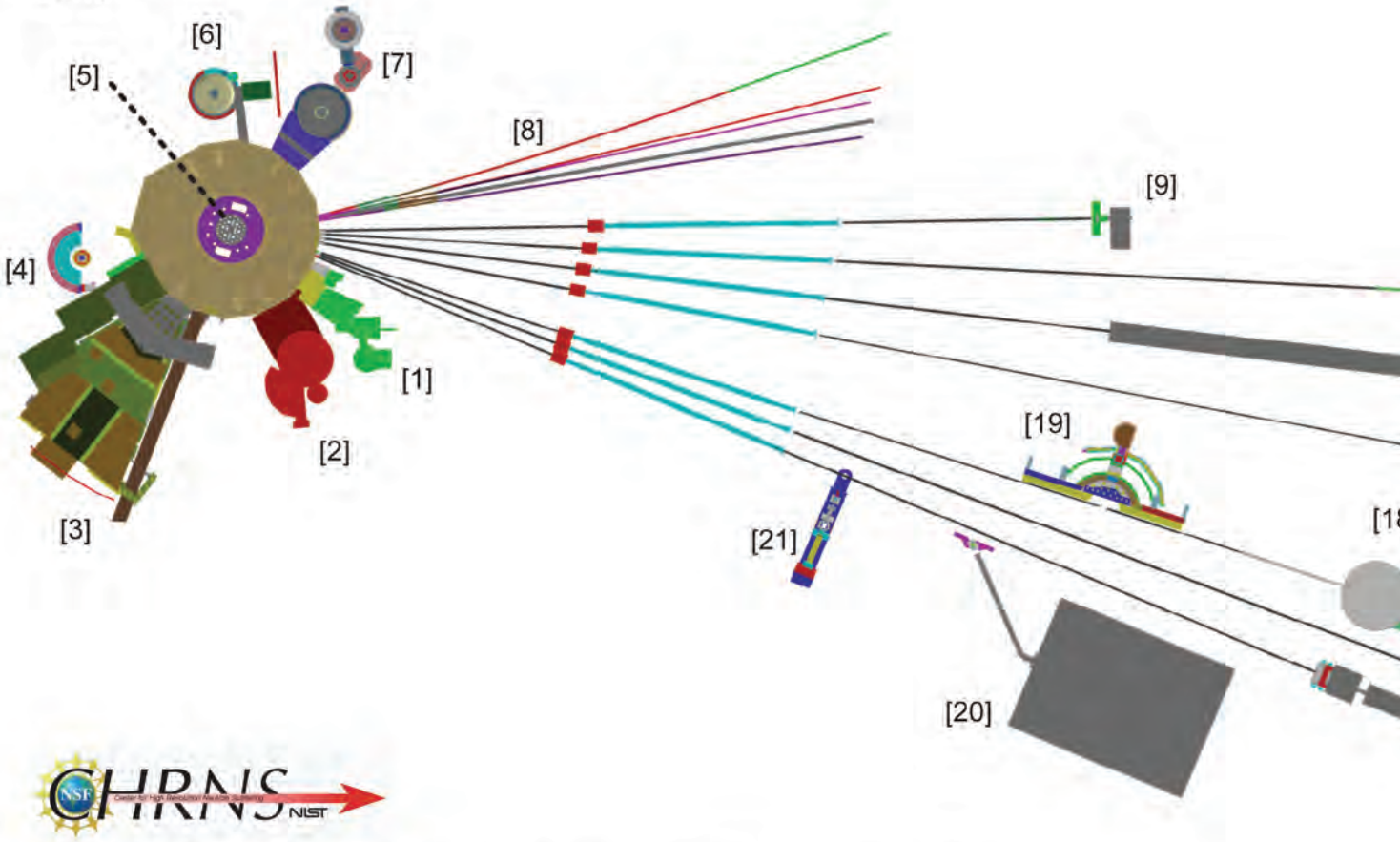

The Center for High Resolution Neutron Scattering (CHRNS) is a partnership between NIST and the National Science Foundation that develops and operates neutron scattering instrumentation for use by the scientific community. The following instruments are part of the Center: 1 (USANS), 10 (HFBS), 11 (NG-3 SANS), 12 (DCS), 18 (NSE), and 19 (SPINS).

[8] NG-A,B,C and D Cold neutron guides being installed into the expansion west wing of the guide hall for new or repositioned instruments.

[9] NG-1 Cold Neutron Depth Profiling instrument for quantitative profiling of subsurface elemental composition.

[10] NG-2 Backscattering Spectrometer (HFBS) high intensity inelastic scattering instrument with energy resolution < 1 μeV, for studies of motion in molecular and biological systems, part of CHRNS.

[11] NG-3 30 m SANS for microstructure measurements, part of CHRNS.

[12] NG-4 Disk Chopper Time-of-Flight Spectrometer for studies of diffusive motions and low energy dynamics of materials. Wavelengths from ≅ 0.18 nm to 2.0 nm give corresponding energy resolutions from ≅ 2 meV to < 10 μeV, part of CHRNS.

[13-15] NG-6 Neutron Physics Station offering three cold neutron beams having wavelengths of 0.5 nm, 0.9 nm, and "white" that are available for fundamental neutron physics experiments.

[16] NG-7 30 m SANS for microstructure measurements, in partnership with ExxonMobil and University of Minnesota's IPrime.

[17] NG-6 Neutron Physics test bed for diffraction-based neutron dipole moment measurement techniques.

[18] NG-5 Neutron Spin-Echo Spectrometer (NSE) for measuring dynamics from 100 ns to 10 ps, part of CHRNS.

[19] NG-5 Spin-Polarized Triple Axis Spectrometer (SPINS) using cold neutrons with position sensitive detector capability for high-resolution studies, part of CHRNS.

[20] NG-7 Neutron Interferometry and Optics Station with perfect crystal silicon interferometer. A vibration isolation system provides exceptional phase stability and fringe visibility.

[21] NG-7 Horizontal Sample Reflectometer allows reflectivity measurements of free surfaces, liquid/vapor interfaces, as well as polymer coatings.

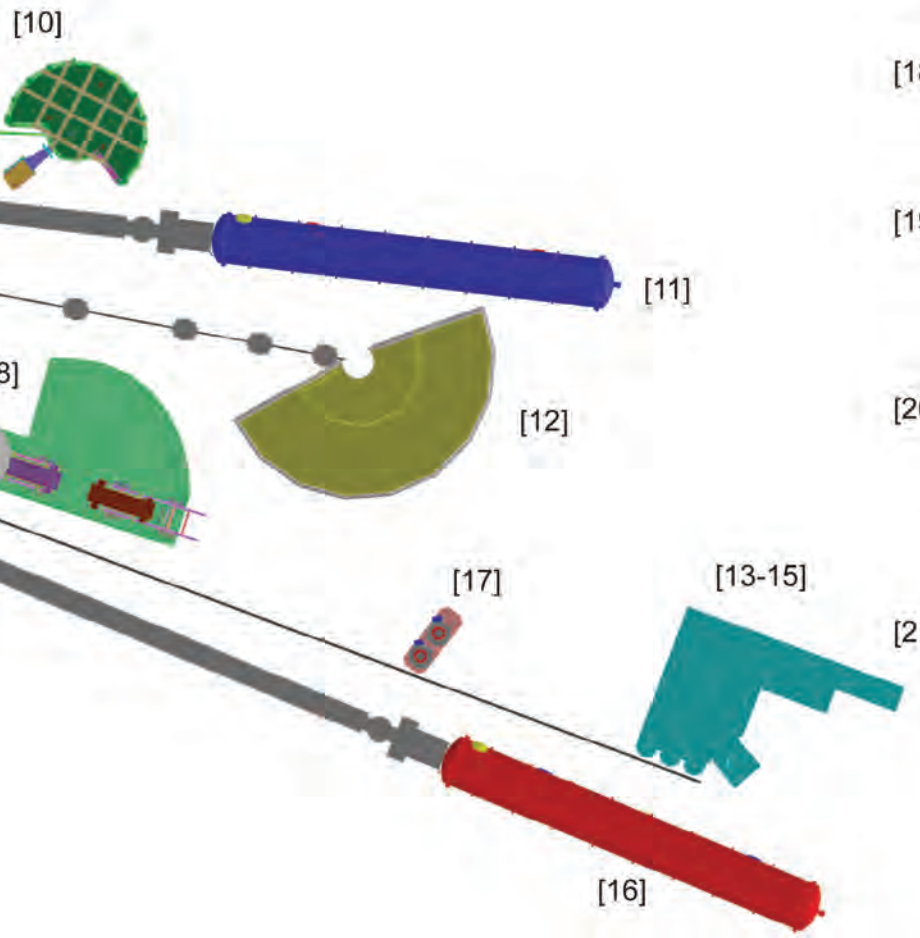

Facility Expansion Activities

Paul Brand and Tony Norbedo (l-r) celebrate the start of commissioning by the ring header of the newly installed thermal shield system.

Mike Rinehart and Doug Ogg (l-r) re-install the NG-1 vacuum jacket in C-100. The first guide elements of existing guides NG-1 thru 7 were replaced as part of the refurbishment program.

Scott Slifer, Dennis Nester, and Pat Connelly (l-r) pause to view remote video feed of inside the BT-9 beam port.....

...during installation of the new cold source.

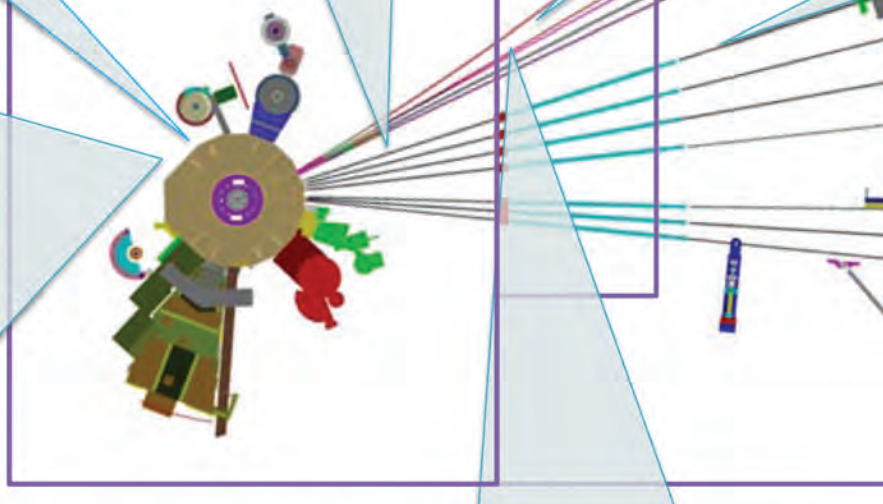

➢The new guides are pre-aligned and assembled In the high bay to expedite installation In C100.

➢(l-r): Mike Murbach, Mike Rinehart, Dan Adler, Doug Ogg, Lukasz Turolski (East Coast Metrology) and George Baltic survey the C100 wall penetrations through which the new guides will run.

Guides, shields, and the MACS analyzer are staged in the new guide hall in readiness for the final installation phase during 2012.

➢ ANDR and the polarized beam reflectometer have been dismantled from NG-1 in the Guide hall making way for the new Guides due for installation in 2012.

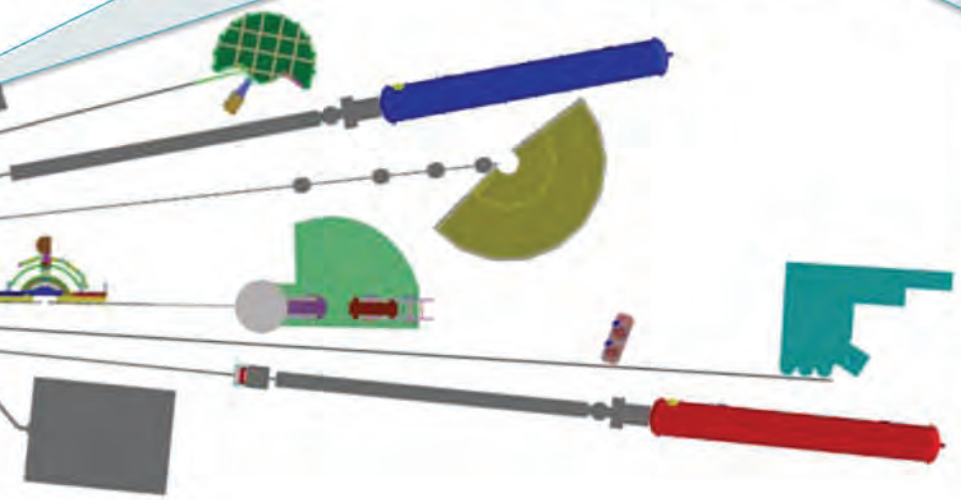

Stanchion removal marked the final phase of demolition of the dividing wall between old (East) and new (West) guide halls.

After years of planning, installation work has begun on the NCNR's Expansion Initiative that will ultimately increase its cold neutron measurement capability by more than 25 percent. The date of 3 April 2011 marked the beginning of an 11-month outage period heralding the start of unprecedented activity toward the installation of five new beam lines, an expanded instrument suite, a new cold source, and numerous refurbishment projects. The changing face of the Facility during the first six months of the outage is highlighted on these pages.

NCNR Images 2011

North American neutron facility representatives meet at the NCNR: L. to R.: Sean O'Kelly, Ian Anderson (SNS), Richard Ibberson, Alan Hurd (LANL), Jim Rhyne (LANL), John Root (Chalk River), Dan Neumann, and Rob Dimeo.

Kathryn Krycka describes contrast matching on a tour of the NG-7 SANS facility.

Cool RFO guys: George Baltic, Bill Clow, Doug Johnson, and Dan Ogg move the MACS analyzer to temporary storage in the new guide hall.

Sammi Jo Cooper, a teacher at Briggs-Chaney MS, checks out crystal growth during the Summer Institute.

Summer Highschool Intern Program (SHIP) students and NCNR personnel take a break from research activity for a group photo on the beautiful grounds in front of the facility.

Pop goes the nucleus! in Juscelino Leão's vivid chain reaction demonstration to a middle school tour.

Jeff Lynn encourages Roberto Clemente Middle School students to do violence! Smash it! Smash that frozen rose into shards!

Yun Liu expounds on the Spin-Echo spectrometer from the "dance floor" (or is he demonstrating the latest dance step?)



And it didn't come tumbling down: removing the final columns between the guide hall east and west wings.


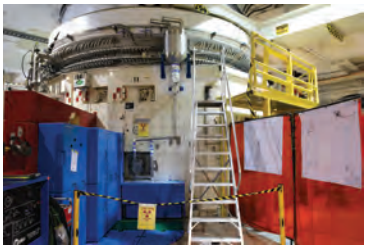


Pee Wee (new cold source for MACS) goes in...it's all connected...and Bob Williams says, Look!...no leaks!

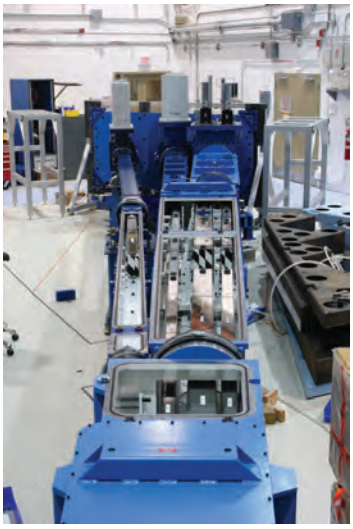


New guides assembled at various stages. Upper right: beam shutters partially installed at the C100 wall. Lower right: John Copley and Jeff Zeigler survey recently arrived guide components.

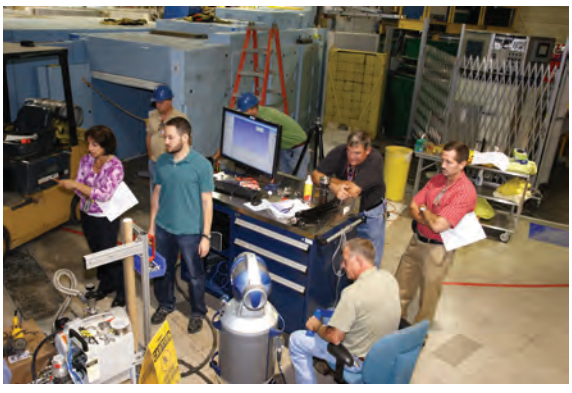

L. to R.: Nancy Hadad, Bill Clow, Dan Adler, Dan Ogg, Mike Rinehart, George Baltic and Don Pierce watch intently as a guide shutter is set into place.

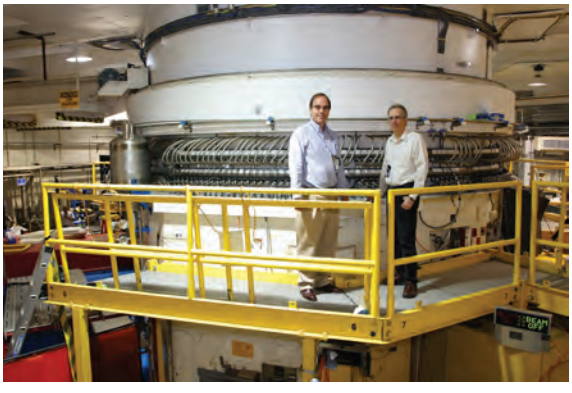

Paul Brand and Tony Norbedo enjoy the success of the thermal shield upgrade, which moves cooling water while maintaining the pressure below atmospheric.

Structural collapse and high-temperature superconductivity in iron-pnictide $CaFe_2As_2$ at ambient pressure

S.R. Saha[1], N.P. Butch[1], T. Drye[1], J. Magill[1], S. Ziemak[1], K. Kirshenbaum[1], P.Y. Zavalij[2], J.W. Lynn[3], and J. Paglione[1]

The discovery of the new family of iron-based high transition temperature (T_c) superconductors has offered a new route to high transition temperatures [1], breaking the copper-oxide based high T_c superconductor monopoly. The highest T_c of ≈ 55 K has been found in the oxypnictide series RFeAs$O_{1-x}F_x$, while the oxygen-free "122" intermetallic series $A_{1-x}K_xFe_2As_2$ (A = Ba, Sr, Ca), crystallizing in the $ThCr_2Si_2$-type tetragonal structure, shows a maximum T_c of 38 K [1] and is the most popular series of the Fe-based superconductors. The 122 parent compounds are tetragonal at room temperature but undergo an orthorhombic structural distortion that is associated with the onset of antiferromagnetic (AFM) order. Tuning the system by elemental substitution or by external pressure suppresses the magnetic and structural ordering temperatures and induces superconductivity. $CaFe_2As_2$ is a unique member of this family; upon pressure application the magnetostructural transition is suppressed, but is abruptly interrupted by a structural collapse of the tetragonal unit cell, which was identified by neutron measurements in a He-gas pressure cell on BT-1 and BT-7 at NIST [4]. Intriguingly, the appearance of superconductivity in $CaFe_2As_2$ under pressure below 12 K only occurs when non-hydrostatic pressure is applied [2], while no trace of superconductivity was found when using a truly hydrostatic He gas pressure environment [3].

This contrast and sensitivity to pressure application encouraged us to use chemical substitution as an effective hydrostatic pressure on the unit cell to induce the structural collapsed tetragonal phase in this compound. Single crystals of $CaFe_2As_2$ were grown with light rare earths (R = La, Ce, Pr, and Nd) substituted into the Ca position to form $Ca_{1-x}R_xFe_2As_2$, in order to investigate the structural and superconducting properties [4]. We find that electron-doping via aliovalent substitution of trivalent R^{3+} ions for divalent Ca^{2+} acts to suppress AFM order and induce superconductivity, with T_c surprisingly as high as 47 K, by far the highest value found in 122 FeAs-based compounds [6]. Moreover, the close match between ionic radii of La, Ce, Pr, and Nd with that of Ca allows us to selectively tune the structural parameters by using the slightly decreasing variation in rare earth size with f-electron count, known as the lanthanide contraction, to tune the unit cell volume in a controllable manner.

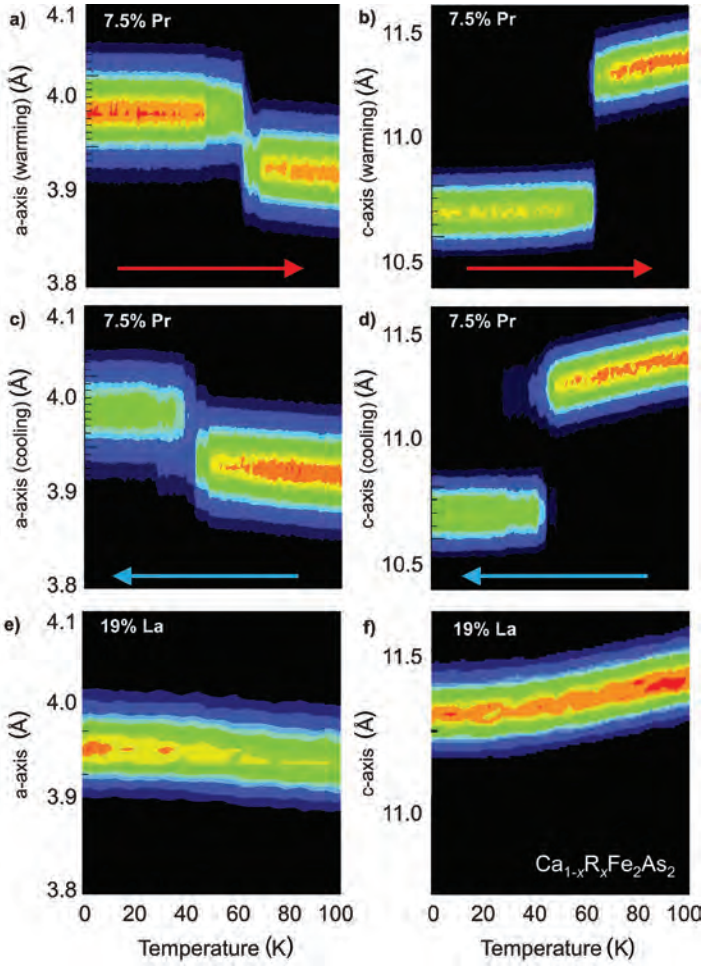

FIGURE 1: Temperature dependence of the *a*- and *c*-axis lattice parameters of $Ca_{1-x}R_xFe_2As_2$. The color-intensity plots highlight the structural collapse of the tetragonal unit cell induced by rare earth substitution upon both warming (red arrows) and cooling (blue arrows) that is present in $Pr_{0.075}Ca_{0.925}Fe_2As_2$ (a-d), but absent in $La_{0.19}Ca_{0.81}Fe_2As_2$ (e-f). The first-order structural transition is strongly hysteretic in nature.

[1]Center for Nanophysics and Advanced Materials, Department of Physics, University of Maryland, College Park, MD 20742
[2]Department of Chemistry and Biochemistry, University of Maryland, College Park, MD 20742
[3]NIST Center for Neutron Research, National Institute of Standards and Technology, Gaithersburg, MD 20899

Single-crystal diffraction studies were carried out to study the $Ca_{1-x}R_xFe_2As_2$ structure, revealing dramatic changes in the structure that include not only an unprecedented thermal expansion, but also a structural collapse of the tetragonal unit cell akin to that previously found under pressure. Figure 1 presents the temperature dependence of lattice parameters determined by single crystal thermal neutron diffraction measurements of the (110) and (002) type nuclear reflections, yielding, respectively, *a*- and *c*-axis parameters. The substitution of only 7.5 % Pr into $CaFe_2As_2$ is enough to drive the collapsed tetragonal transition, with the *a*-axis and *c*-axis lattice parameters undergoing a discontinuous jump. In contrast, the substitution of 19 % La does not drive the system toward any observable transition because the larger ionic radius of La is not amenable to inducing positive chemical pressure.

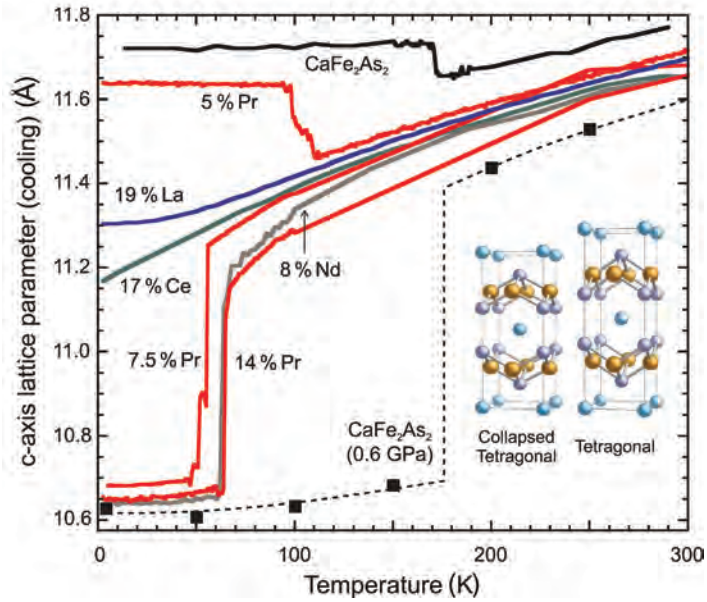

FIGURE 2: Comparison of *c*-axis lattice parameters in the $Ca_{1-x}R_xFe_2As_2$ family for different rare earth substitutions at ambient pressures. The collapse of the *c*-axis in Pr- and Nd-substituted $Ca_{1-x}R_xFe_2As_2$ is directly comparable to that in undoped $CaFe_2As_2$ under applied hydrostatic pressure (black squares; from Ref. 4), while La- and Ce-substituted samples do not undergo a collapse in the substitution range investigated.

Figure 2 presents the temperature dependence of the *c*-axis unit cell dimension upon cooling, determined from neutron diffraction measurements of the (006) nuclear reflection for undoped $CaFe_2As_2$ [4] and several $Ca_{1-x}R_xFe_2As_2$ crystals at ambient pressure. A dramatic collapse in the structure is evident, with Nd substitution acting in a similar manner as Pr to achieve an almost identical collapse transition. Both cases show an absolute change in the *c*-axis through the collapse transition that is nearly identical to that observed in $CaFe_2As_2$ under pressure [4]. In contrast, La- and Ce-substituted crystals fail to undergo a collapse to the lowest measured temperatures, even for the case of Ce where the *c*-axis dimension reaches below the value where the collapse occurs in the lighter rare earth-doped samples. This is understood to be the effect of the interlayer As-As distance, which we believe is the important parameter controlling the collapse of the unit cell [5], which does not reach the critical value of 3 Å in these crystals. However, as is evident by an extremely large *c*-axis thermal expansion of 180 x 10^{-6}/K (the largest known value for any metal), the As-As bonding tendency is extremely strong in these crystals, which is literally on the verge of collapse.

High T_c superconductivity was found to be present in both the collapsed and uncollapsed structures [5], suggesting that the unconventional superconductivity of the iron-based superconductor family appears to occur in this system regardless of the nature of the interlayer bonding. Given the absence of superconductivity in the collapsed phase of undoped $CaFe_2As_2$ under hydrostatic pressure [3], this is quite surprising and may originate from the subtle but important addition of charge doping. The insensitivity of the observed high-T_c superconducting phase to this boundary is unusual, raising important questions regarding which features of the chemical, electronic and magnetic structure are important to Cooper pairing.

References

[1] J. Paglione and R. L. Greene, Nature Phys. **6**, 645 (2010).

[2] M.S. Torikachvili, S.L. Bud'ko, N. Ni, and P.C. Canfield, Phys. Rev. Lett. **101**, 057006 (2008).

[3] W. Yu, A. A. Aczel, T. J. Williams, S. L. Bud'ko, N. Ni, P. C. Canfield, and G. M. Luke, Phys. Rev. B **79**, 020511R (2009).

[4] A. Kreyssig, M. A. Green, Y. Lee, G. D. Samolyuk, P. Zajdel, J. W. Lynn, S. L. Bud'ko, M. S. Torikachvili, N. Ni, S. Nandi, J. B. Leão, S. J. Poulton, D. N. Argyriou, B. N. Harmon, R. J. McQueeney, P. C. Canfield, and A. I. Goldman, Phys. Rev. B **78**, 184517 (2008).

[5] S. R. Saha, N. P. Butch, T. Drye, J. Magill, S. Ziemak, K. Kirshenbaum, P. Y. Zavalij, J. W. Lynn, and J. Paglione, arXiv:1105.4798v1.

Spin liquid state in the $S = 1/2$ triangular lattice $Ba_3CuSb_2O_9$

H.D. Zhou[1], E.S. Choi[1], G. Li[1], L. Balicas[1], C.R. Wiebe[1,2,3], Y. Qiu[4,5], J.R.D. Copley[4], and J.S. Gardner[4,6]

One of the current thrusts of modern condensed matter science has been the realization of an important model compound known as the quantum spin liquid (QSL). The existence of these materials, in which magnetic spins remain disordered by quantum fluctuations in the limit of zero Kelvin, underpins much of modern condensed matter theory. Previous studies have shown that QSL ground states tend to emerge in the geometrically frustrated materials, in which the interactions among the limited magnetic degrees of freedom lead to a strong enhancement of quantum fluctuations. While the study of the QSL state in the organic compounds remains a hot topic, there are very few inorganic materials identified as model systems for QSL ground states. Many efforts to synthesize spin liquids on triangular lattices in inorganic materials have failed. Here, we unveil a new candidate for a spin liquid compound – $Ba_3CuSb_2O_9$ – in which Cu^{2+} species form a geometrically frustrated triangular lattice.

The crystal structure of $Ba_3CuSb_2O_9$, a 6-H perovskite-related material with $a = b = 5.8090$ Å and $c = 14.3210$ Å, can be represented as a framework consisting of corner-sharing SbO_6 octahedra and face-sharing $CuSbO_9$ bi-octahedra, as shown in Fig. 1(a, b). In the bi-octahedra, the Cu and Sb cations are well-ordered. The Cu ions occupy the 2b Wyckoff site of space group $P6_3mc$, and this site forms the triangular lattice in the *ab* plane (Fig. 1(c)). Therefore, the structure can be seen as a two-dimensional triangular magnet, *i.e.*, the Cu magnetic triangular lattices are magnetically separated by the two non-magnetic Sb layers (Fig. 1(b)).

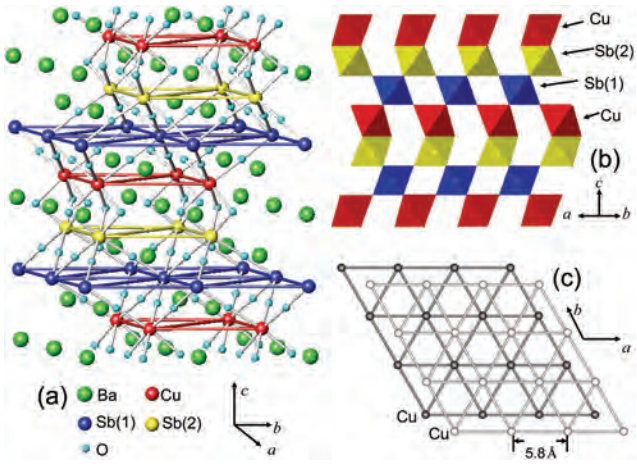

FIGURE 1: (a) Schematic crystal structure for $Ba_3CuSb_2O_9$; (b) The layer structure along the *c*-axis; (c) The triangular lattice of Cu^{2+} in the *ab* plane.

The temperature dependence of the DC magnetic susceptibility measured with $\mu_0 H = 0.5$ T for $Ba_3CuSb_2O_9$ shows no signature for a magnetic transition above 1.8 K, as indicated in Fig. 2(a). The temperature dependence of the AC magnetic susceptibility (Fig. 2(b)) further shows no sign of a magnetic transition down to 0.2 K. The neutron powder diffraction pattern obtained at 0.2 K with $\lambda = 1.8$ Å on the DCS at NIST (Fig. 2(c)) shows no intensity change nor additional peaks from the 4 K data (not shown here), indicating that there is no magnetic transition nor structural distortion down to 0.2 K. The possibility of mixing between the Cu and Sb sites has been tested by refinement of the neutron diffraction data, which show a full occupancy of Sb(1) on the corner-sharing SbO_6 octahedron sites and Cu on one of the ordered bi-octahedra sites. There is a slight amount of site mixing (refined from the neutron data to be 5.1(4) %) of the other ordered bi-octahedra sites - Sb(2) sites are replaced by (orphan) Cu ions. The DC magnetic susceptibility contribution from this 5.1 % Cu^{2+} orphan spins has been calculated by a simple Curie law. The susceptibility, after subtracting this contribution, is shown as open circles in Fig. 2(a). The Curie-Weiss fit of this linear behavior at high temperature gives a $\theta_{CW} =$ -55 K and an effective moment $\mu_{eff} = 1.79\ \mu_B$/Cu, which is consistent with the expected value for Cu^{2+} ($S = 1/2$) ions. The exchange interaction J is estimated to be $J/k_B = 32$ K by fitting the data between 150 K and 300 K to the calculation for the spin 1/2 triangular lattice using a high-temperature-series expansion (HTSE).

[1]National High Magnetic Field Laboratory, Florida State University, Tallahassee, FL 32306-4005
[2]University of Winnipeg, Winnipeg, MB, R3B 2E9 Canada
[3]University of Manitoba, Winnipeg, MB, R3T 2N2 Canada
[4]NIST Center for Neutron Research, National Institute of Standards and Technology, Gaithersburg, MD 20899-6102
[5]University of Maryland, College Park, MD 20742
[6]Indiana University, Bloomington, IN 47408

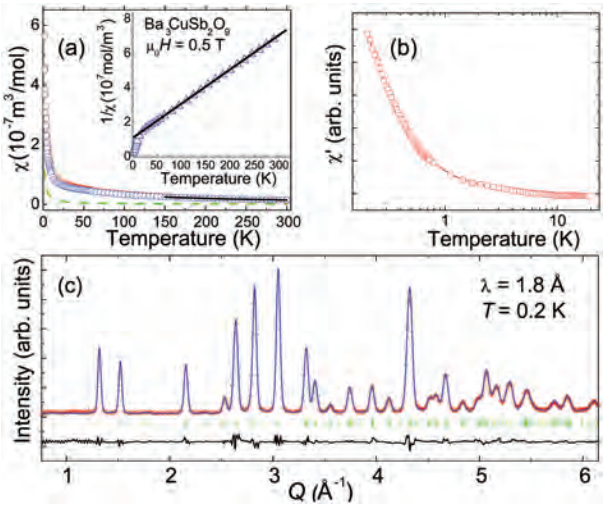

FIGURE 2: (a) The temperature dependences of the DC magnetic susceptibility (χ). The red open squares represent χ as measured, the green dashed line, χ of orphan spins, and the blue open circles, represent χ after deleting orphan spins. The solid curve on χ data above 150 K represents a fit to the high-temperature-series expansion. Inset: $1/\chi$ – after deleting the orphan spin contribution (open triangles). The solid line on the $1/\chi$ data represents a Curie-Weiss fit. (b) The temperature dependence of the real part of the AC magnetic susceptibility (χ'). (c) Neutron diffraction pattern (red crosses) at 0.2 K. The solid blue curve is the best fit from a Rietveld refinement using FullProf. The vertical marks indicate the position of Bragg peaks, and the bottom curve shows the difference between the observed and calculated intensities. The error bars ± σ are too small to be visible on the figures.

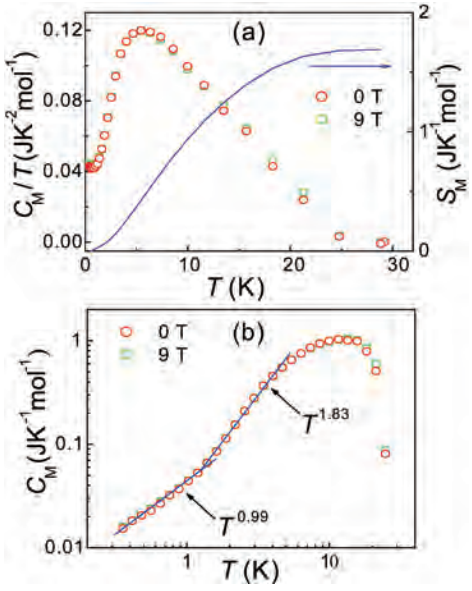

FIGURE 3: (a) The temperature dependences of the reduced heat capacity C_M/T and the magnetic entropy S_M; (b) The temperature dependence of C_M (open symbols). The solid lines are fits as described in the text.

The magnetic specific heat (C_M, Fig. 3) of the Cu^{2+} triangular lattice is obtained by subtracting the lattice contribution (C_P of the non-magnetic $Ba_3ZnSb_2O_9$), and the Schottky anomaly from the Cu^{2+} orphan spins (detail, see Ref. [1]). As shown in Fig. 3(b) with the log-log scale, between 1.4 K and 4 K, C_M can be fitted as $C_M = bT^{\alpha}$ with b = 37.0 mJ $K^{-3}mol^{-1}$ and α = 1.83(2). This α value is near 2.0, showing quadratic temperature dependence. At lower temperatures, between 0.35 K and 1.4 K, C_M can be fit as $C_M = \gamma T^{\alpha}$ with γ = 43.4 mJ $K^{-2}mol^{-1}$ and α = 0.99(2), giving a linear temperature dependence. The integrated magnetic entropy variation below 30 K is 1.7 J $K^{-1}mol^{-1}$, which is around 30 % of Rln(2) = 5.76 J $K^{-1}mol^{-1}$ for a $S = 1/2$ system, where R is the gas constant, as shown in Fig. 3(a). This feature indicates a high degeneracy of low-energy states at low temperatures.

The susceptibility and specific heat both show no magnetic ordering down to 0.2 K for $Ba_3CuSb_2O_9$ despite moderately strong nearest neighbor antiferromagnetic interactions with $J \approx 32$ K, which clearly places this compound in the highly frustrated regime. The field-independent C_M is common in spin liquid candidates, which should be insensitive to moderate applied fields. On the other hand, the linear dependence of C_M is unusual for 2D frustrated lattices, which should have a quadratic dependence for linearly dispersive low energy modes. However, a linear T dependence at low temperatures has been predicted by the resonating-valence-bond model of Anderson, due to the pairing of spins into singlets [2]. One current mode of thought is that a Fermi surface of spinon excitations is formed within the liquid state, which gives rise to a linear term even for Mott insulators [3].

In summary, the synthesis and characterization of $Ba_3CuSb_2O_9$, which has a layered array of Cu^{2+} spins in a triangular lattice, are reported. The magnetic susceptibility and neutron scattering experiments of this material show no magnetic ordering down to 0.2 K with a θ_{CW} = -55 K. The magnetic specific heat reveals a linear dependence on T with γ = 43.4 mJ $K^{-2}mol^{-1}$ below 1.4 K. These observations suggest that $Ba_3CuSb_2O_9$ is a new quantum spin liquid candidate with a $S = 1/2$ triangular lattice.

References

[1] H.D. Zhou, *et al.*, Phys. Rev. Lett. **106**, 147204 (2011).

[2] P. W. Anderson, Science, **235** 1196, (1987).

[3] S. S. Lee, P. A. Lee, and T. Senthil, Phys. Rev. Lett. **98**, 067006 (2007).

Interstitial iron tuning of the spin fluctuations in $Fe_{1+x}Te$

C. Stock[1,2], E.E. Rodriguez[2], M. Green[1,3], P. Zavalij[4], and J. Rodriguez-Rivera[1,3]

Magnetism is directly related to superconductivity in several heavy fermion and *d*-transition metal-ion systems. Most notably, localized magnetism is believed to be directly coupled with high-temperature superconductivity in the cuprates as evidenced through studies as a function of charge concentration. More recently, the discovery of superconductivity in the iron-based compounds has revealed a series of materials were superconductivity and magnetism coexist. Magnetism and superconductivity are strongly intertwined in these systems as illustrated by neutron inelastic-scattering experiments, which have shown a distinct change in the spin fluctuations on cooling through the superconducting transition temperature [1].

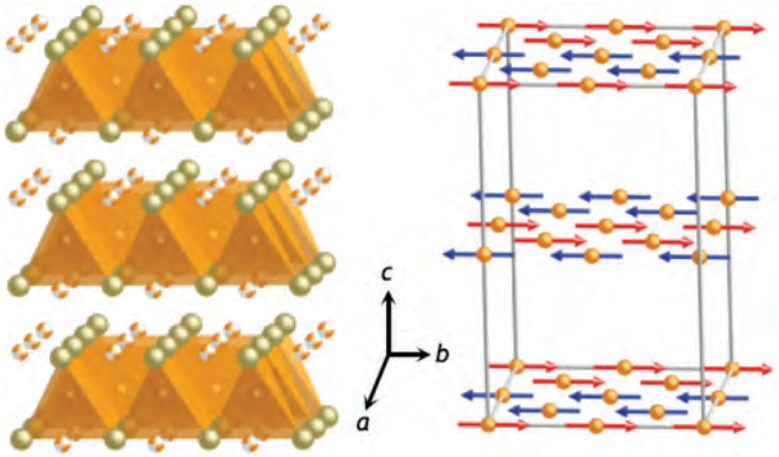

FIGURE 1: Left: crystalline structure of the parent $Fe_{1+x}Te$ compound: the gold/white spheres represent possible interstitial positions of the $+x$ Fe ions, gold spheres represent Fe, and green spheres represent Te. Right: double-stripe magnetic structure on the Fe sublattice at low interstitial Fe concentration.

Using neutron inelastic scattering, we investigate the low-energy spin fluctuations in $Fe_{1+x}Te$ as a function of both temperature and interstitial iron concentration. For $Fe_{1.057(7)}Te$, the magnetic structure is defined by a commensurate wave vector of (1/2, 0, 1/2). The spin fluctuations are gapped with a sharp onset at 7 meV and are three dimensional in momentum transfer, becoming two dimensional at higher-energy transfers. On doping with interstitial iron, we find, in $Fe_{1.141(5)}Te$, the ordering wave vector is located at the incommensurate (0.38, 0, ½) position and the fluctuations are gapless with the intensity peaked at an energy transfer of 4 meV. These results show that the spin fluctuations in the $Fe_{1+x}Te$ system can be tuned not only through selenium doping, but also interstitial iron.

Arguably, the simplest iron-based superconductor is the single layered $Fe_{1+x}Te_{1-y}Se_y$ system where superconductivity has been observed with a maximum transition temperature of 14 K for $y \approx 0.5$. The structure is shown in Fig. 1 illustrating both the cation (iron) and anion (selenium and tellurium) sites. While selenium doping has proven to be the most direct route for inducing superconductivity in this system, recent studies have shown that the selenium concentration is directly tied to the amount of interstitial iron between the FeTe layers. This was demonstrated in a study of $Fe_{1+x}Te_{0.7}Se_{0.3}$ which proved that the superconductivity and the magnetic excitations were directly linked with the level of interstitial iron, independent of the selenium concentration [2]. The magnetic structure of the parent non-superconducting $Fe_{1+x}Te$, in the absence of selenium doping, has been investigated using neutron diffraction illustrating a dramatic change of the magnetic and crystalline structure with changing the interstitial iron concentration [3]. For small amounts of interstitial iron, a commensurate double-stripe spin-density wave phase exists which abruptly changes to a spiral magnet for $x > 0.12$.

The superconducting variants of $Fe_{1+x}Te_{1-y}Se_y$ have been investigated and neutron inelastic scattering has reported the static magnetic order observed in the parent material to be replaced by short-range correlations near the (1/2, 1/2, *L*) position. This position in reciprocal space matches a nesting wave vector proposed from photoemission measurements indicating possible coupling between electronic and magnetic properties. Notably, in the

[1]Indiana University, Bloomington, IN 47404
[2]NIST Center for Neutron Research, National Institute of Standards and Technology, Gaithersburg, MD 20899
[3]Department of Materials Science and Engineering, University of Maryland, College Park, MD 20742
[4]Department of Chemistry, University of Maryland, College Park, MD 20742

superconducting phase, a resonance peak at ≈ 7 meV has been observed in the half-doped ($y \approx 0.5$) systems [4]. The peak appears below the superconducting transition and is sharp in energy. Unlike its counterpart in heavy-fermion superconductors, the momentum dependence is very two dimensional in nature, forming a rod along the c^* direction.

The microscopic nature of the magnetism and its relation to superconductivity in the FeAs-based high temperature superconductors is a matter of current debate and research. While the reduced-ordered moment may indicate itinerant effects are important, there are two key differences with the $Fe_{1+x}Te$ system which may point toward strong localized magnetism in this system. Firstly, the ordered moments are significant. Secondly, the ordering wave vector is not consistent with the nesting wave vector reported from photoemission. Little attention has been placed on the role of excess Fe on the spin fluctuations and transport properties with much activity focused on the role of Se doping.

Using the MACS cold triple-axis spectrometer at NIST, we have measured the magnetic fluctuations as a function of interstitial iron doping in the parent $Fe_{1+x}Te$ compound. In particular, we have focused on two different concentrations of $x = 0.057(7)$ and $x = 0.141(5)$ in the commensurate double-stripe and spiral phase respectively. Single crystal x-ray diffraction on crystals cleaved from the larger crystals was performed to characterize the amount of interstitial iron. Constant energy planes were probed by fixing the final energy to 3.6 meV and scanning momentum transfer with the 20 double-bounce PG(002) analyzing crystals and detectors and varying the incident energy defined by a double-focused PG(002) monochromator.

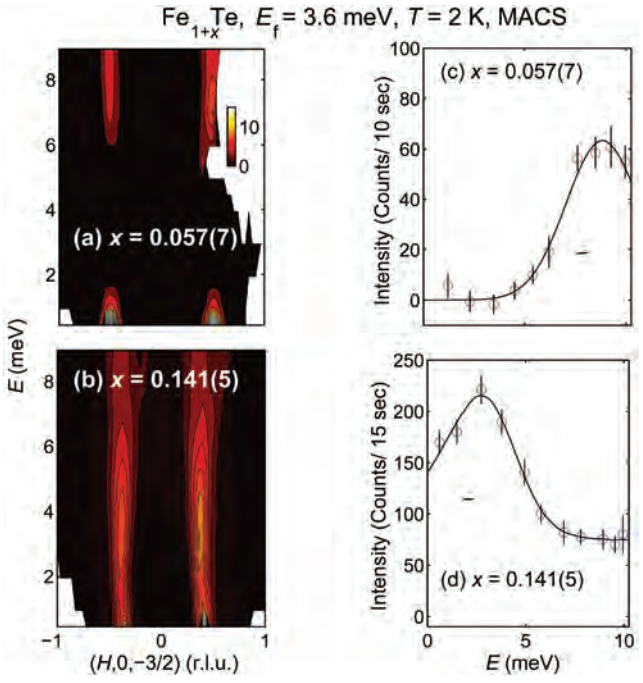

FIGURE 2: Constant-*Q* slices (a,b) and constant –*Q* scans (c,d) obtained using the MACS cold triple-axis spectrometer. Note the gapless spectrum for $x = 0.141$.

The inelastic scattering measured on MACS is summarized at $T = 2$ K in Fig. 2 through a series of constant-*Q* cuts taken by integrating over $L = [-1.55, -1.45]$. Panels (a) and (b) compare the excitations in the ordered state at low temperatures for $Fe_{1+x}Te$ with $x = 0.057(7)$ and 0.141(5), respectively. The excitations in the $x = 0.057(7)$ sample are gapped with a value of 7 meV (panel (c)) while those in the interstitial Fe-rich $x = 0.141(5)$ concentration are gapless, yet with the spectrum peaked at around 4 meV (panel (d)). The excitation spectrum for $x = 0.057(7)$ is broadly consistent with the magnetic structure with a large anisotropy, stabilizing the double stripe commensurate structure shown in Fig. 1. Once this energy scale is tuned to zero with interstitial iron, *e.g.*, $x = 0.141(5)$, the gapless excitation is the required phason for a spiral structure. These results show that the characteristic energy scale of the magnetic fluctuations can be tuned with interstitial iron doping as well as the previously established charge doping through selenium substitution.

One of the most important discoveries of this study is the finding of a well-defined spin-gap in the non-superconducting parent compound with the same energy as the resonance peak found in superconducting concentrations. While the energy is very similar, there are some noteworthy differences between the excitations in the parent and superconducting concentrations. Firstly, the wave vector in the parent compound does not match a Fermi surface nesting wave vector as it does in superconducting concentrations. Secondly, the low-energy fluctuations near the gap value are highly three dimensional in the parent compound investigated here while they are two dimensional in superconducting concentrations of $Fe_{1+x}Te_{1-y}Se_y$. This difference is broadly consistent with theories that suggest that two dimensional magnetic fluctuations are important for unconventional high temperature superconductivity. Our results might also suggest that the resonance peak found in superconducting concentrations may originate from spin fluctuations consistent with several theories proposed for the resonance peak in the cuprate superconductors. This work is further described in Ref. [5].

References

[1] A.D. Christianson *et al.*, Nature **456,** 930 (2008).
[2] E.E. Rodriguez *et al.*, Chem. Sci. **2**, 1782 (2011).
[3] E.E. Rodriguez *et al.*, Phys. Rev. B **84**, 064403 (2011).
[4] Y. Qiu *et al.*, Phys. Rev. Lett. **103**, 067008 (2009).
[5] C. Stock *et al.*, Phys. Rev. B **84**, 045124 (2011).

Delta-doping of ferromagnetism in digitally-synthesized manganite superlattices

T. S. Santos[1], B.J. Kirby[2], S. Kumar[3], S. May[4], J.A. Borchers[2], B.B. Maranville[2], S.G.E. te Velthuis[5], J. Zarestky[6], J. van den Brink[3] and A. Bhattacharya[1,5]

Advances in state-of-the-art thin film deposition techniques have enabled the synthesis of complex oxide heterostructures with single, atomic layer precision (delta-doping). With this high level of control over ordering of atoms in the lattice, we can also tailor the magnetic exchange interactions that operate between nearest neighbors. Starting with antiferromagnetic (AF) $La_{0.5}Sr_{0.5}MnO_3$, which has a composition close to a ferromagnetic (F)/AF phase boundary [1], we used a delta-doping strategy to locally introduce regions of enhanced F double-exchange between spins on the Mn ions, relative to AF superexchange. Altering the charge profile in this manner produced a highly-modulated magnetization. We used polarized neutron reflectometry (PNR) at the NCNR to examine the magnetic depth profile and the length scale over which the delta-doped charges extended in this correlated material, which is a quantity of fundamental interest analogous to the Thomas-Fermi length [2].

The AF host material is a superlattice (SL) comprised of alternating $LaMnO_3$ (LMO) and $SrMnO_3$ (SMO) perovskite unit cell layers (each ≈ 0.4 nm thick), epitaxially grown on a $SrTiO_3$ substrate by ozone-assisted molecular beam epitaxy [3] at Argonne National Laboratory. By periodically inserting an extra LMO unit cell, as shown schematically in the inset of Fig. 1a, we delta-doped the structure with a layer of electrons on the MnO_2 planes, yielding a nominal composition $La_{0.56}Sr_{0.44}MnO_3$. The total SL thickness was ≈ 30nm.

A-type AF order, consisting of F coupling within the MnO_2 planes and AF coupling between adjacent planes, was confirmed by measuring a (0 0 ½) neutron diffraction peak. However, SQUID magnetometry measurements showed that the SL also had a net F moment. This was the first clue that the spins were actually *canted*.

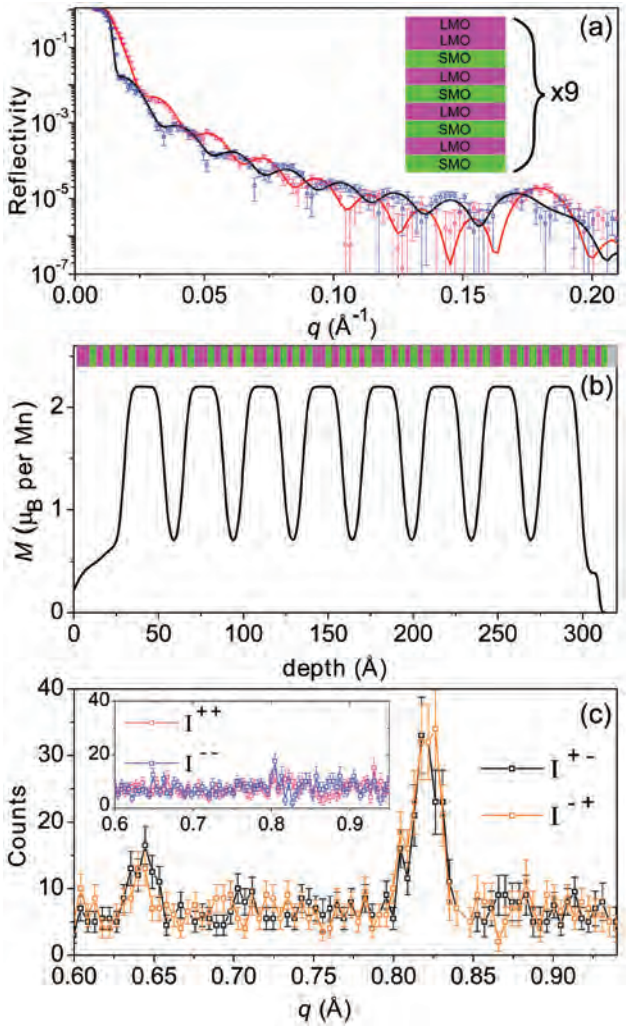

FIGURE 1: (a) Non spin flip PNR measured in 675 mT applied field at 120 K. Inset: schematic of the SL structure. (b) Magnetic depth profile determined by the fit to the PNR spectra. Location of the LMO (pink) and SMO (green) layers are shown. (c) Spin-flip intensity, showing the AF peak and satellite peak. Inset: Non spin flip intensity in the same range.

In order to examine if the net moment varied with the dopant profile of the SL, we performed PNR measurements using the NG1 reflectometer. Because the nuclear scattering

[1]Center for Nanoscale Materials, Argonne National Laboratory, Argonne, IL 60439
[2]NIST Center for Neutron Research, National Institute of Standards and Technology, Gaithersburg, MD 20899
[3]Institute for Theoretical Solid State Physics, IFW Dresden, 01171 Dresden, Germany
[4]Drexel University, Philadelphia, PA 19104
[5]Materials Science Division, Argonne National Laboratory, Argonne, IL 60439
[6]Ames Laboratory and Iowa State University, Ames, IA 50011

length densities of LMO and SMO are nearly identical, only magnetic variations in the layer profile were detectable. Indeed, a Bragg peak was measured in the PNR spectra, shown in Fig. 1b, revealing that the magnetization is modulated, and the period of the magnetic modulation matches the period of the SL structure. In fact, the size of the modulation is quite large, from 0.7 μ_B up to 2.2 μ_B per Mn ion, and the maxima *coincide with the extra* $LaMnO_3$ *layer*, as shown in Fig. 1b. The high moment regions extend across 6 unit cells. This implies that the delta-doped charges spread out to three unit cells from both sides of the delta-doped layer. Spin frustration typical of F/AF interfaces is absent here. Rather, the transitions between highest and lowest moments in the profile occur via a continuous change in canting angle. In comparison, the PNR spectra for an alloy film having a uniform composition profile (no delta-doping) shows a F moment but no Bragg peak.

To investigate this magnetic profile even further, we carried out neutron diffraction measurements with polarized neutrons and polarization analysis (also on NG1 reflectometer) in the q range of the AF peak, as shown in Fig. 1c. The AF peak appears in the spin flip channels of the spectra because the AF spins have a component of magnetization oriented away from the applied field direction, with a periodicity of twice the out-of-plane lattice parameter. Furthermore, because the amount of canting is modulated with a period matching the SL structure, a satellite peak appears to the side of the AF peak. This spin-flip diffraction measurement confirms the *canted, modulated* spin structure of the SL, shown schematically in Fig. 2. In agreement with our experimental determination of this spin structure, a two-orbital tight-binding model showed a strong dependence of canting angle on dopant concentration through the F/AF phase transition.

In his pioneering work in 1960, de Gennes had predicted that the canted AF state results when mobile carriers are added to an AF manganite host [4]. However, experimental observation of the canted AF state had been obscured by tendencies of the material to form a mixed F/AF phase. By using a digital synthesis technique to mitigate the effects of disorder and using polarized neutron reflectometry and diffraction to directly observe the spin canting, we have

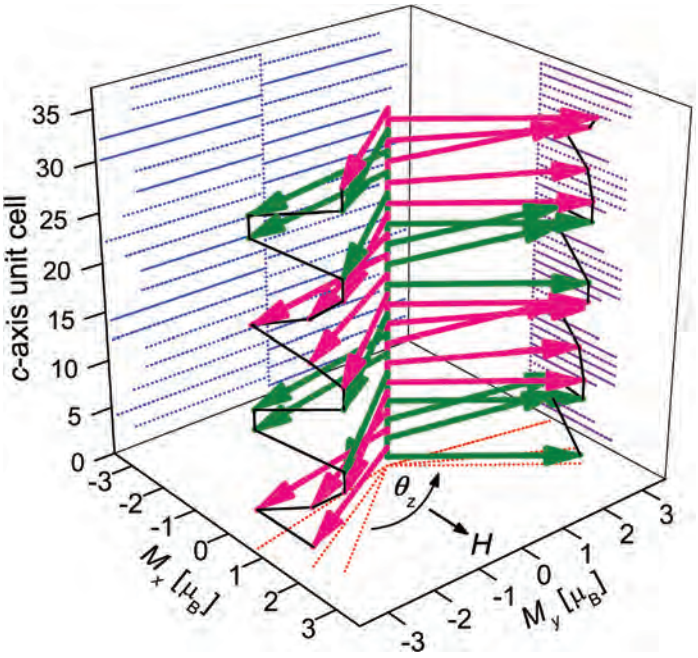

FIGURE 2: Spin structure within 4 supercells (9 unit cells each) of the SL. Pink and green arrows represent the F spin alignment within the MnO_2 planes of the LMO and SMO layers, respectively. The dotted blue lines are the projection of the spins onto the *yz*-plane and signify the magnetic potential measured by neutron diffraction. The dotted purple lines are the projection of the spins onto the *xz*-plane and signify the magnetic potential measured by PNR. The dotted red lines show the canting angle θ_z. The black lines aid the eye in identifying the spin modulation.

indeed realized the canted AF state in the manganites for the first time. Exploiting the competition between F double-exchange and AF superexchange interactions to tailor the magnetic structure as we have shown here, is unique to the correlated manganites and cannot be realized in conventional semiconductors or metals.

References

[1] J. Hemberger *et al.*, Phys. Rev. B **66**, 094410 (2002).

[2] T.S. Santos *et al.*, Phys. Rev. Lett. **107**, 167202 (2011).

[3] T.S. Santos, S.J. May, J.L. Robertson, A. Bhattacharya, Phys. Rev. B **80**, 155114 (2009).

[4] de Gennes, Phys. Rev**. 118**, 141 (1960).

The magnetic structure of multiferroic $BiFeO_3$ epitaxial films

W. Ratcliff II[1], D. Kan[2,3], W.C. Chen[1], S. Watson[1], S. Chi[1], R. Erwin[1], G.J. McIntyre[4], S.C. Capelli[4], and I. Takeuchi[2]

Multiferroics are materials having both ferroelectric and magnetic order. To be ferroelectric, materials must break spatial inversion symmetry. To be magnetic, they must break time reversal symmetry. Materials possessing the requisite symmetries are rare. Materials which break both symmetries at room temperature are rarer still. $BiFeO_3$ (BFO) is the only material thus far to be both multiferroic and to demonstrate strong coupling between magnetism and ferroelectricity at room temperature. $BiFeO_3$ is a cubic perovskite which orders ferroelectrically at 820 °C [1] and antiferromagnetically at 370 °C [2]. It has a rhombohedral distortion along the [111] direction, and in the ferroelectric state can be described by the *R3c* space group. It has been shown that the application of an electric field can change the magnetic domain populations in both films and single crystals [3,4].

The magnetic structure of $BiFeO_3$ was first probed in powders [4]. These studies were able to demonstrate that the magnetic structure was modulated, but were unable to determine the phase of the magnetic ordering. Such a determination would have to await the availability of studies on single crystals which revealed that the magnetic structure was a long wavelength spiral of periodicity of 620 Å, in which spins rotate in an easy-plane containing both the ferroelectric polarization and the propagation vector describing the spiral [4]. However, in very thin films, the spiral collapses to a G-type antiferromagnetic order, evinced by a single peak at the (0.5 0.5 0.5) position [5]. Unfortunately, the direction of the moments in the film is still undetermined.

In our study, we measure neutron diffraction from 1 μm thick epitaxial films of BFO grown by pulsed laser deposition on (110) and (111) oriented $SrTiO_3$ (STO) substrates. A thin $SrRuO_3$ layer was grown between the BFO and STO layers. Measurements were performed on the BT9 and BT7 thermal triple-axis instruments. ^{3}He cells [21] were placed before and after the sample for the polarized beam measurements. The experiments were performed in air at ambient temperatures.

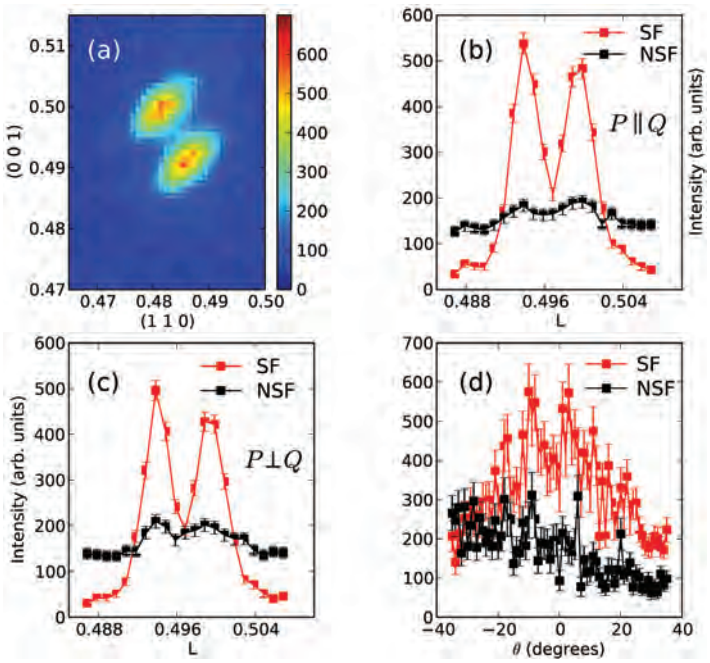

FIGURE 1: Neutron diffraction measurements of the (110) oriented $BiFeO_3$ film. (a) Reciprocal space map taken in the HHL zone using unpolarized neutrons; (b,c) intensity profiles taken in HHL zone with (b) **P**(neutron polarization)$\|$**Q**(scattering vector) and (c) **P**$\perp$**Q**; (d) changes in scattering intensities with the polarization rotated by an angle θ within the scattering plane relative to the scattering wave vector direction (*i.e.*, θ = 0 corresponds to the neutron polarization lying along the scattering vector). The red and black squares represent spin-flip and non-spin-flip scattering, respectively. The data have been corrected for spin transport.

Figure 1a shows a reciprocal space map of the (110) oriented $BiFeO_3$ film in the HHL zone using unpolarized neutrons. We see that for thick films, the modulation is recovered, shown by the presence of two distinct reflections. However, from this measurement alone it is not possible to determine the magnetic structure, so we turn to polarized beam measurements. In Fig. 1b we show measurements of Spin Flip (SF) and Non Spin Flip (NSF) scattering with the neutron polarization parallel to the scattering vector, $\boldsymbol{Q}$ = (0.5 0.5 0.5). We observe that the SF scattering is much stronger than NSF. Thus, a component of the moment is perpendicular to (0.5 0.5 0.5) and is either normal to the scattering plane or along the

[1]NIST Center Neutron Research, National Institute of Standards and Technology, Gaithersburg, MD 20899
[2]University of Maryland, College Park, MD 20742
[3]Kyoto University, Uji, Kyoto, 611-0011, (Japan)
[4]Institut Laue-Langevin BP 156, 38042 Grenoble Cedex 9, France

[1 1 -2] direction. Hence, while from this measurement we learn that magnetic scattering is present, the direction is not determined. Next (Fig. 1c), we place the neutron polarization normal to the scattering plane and again measure SF and NSF scattering. We observe that SF scattering is stronger than NSF scattering. Therefore, the moment has a component along the [1 1 -2] direction, one of the crystallographic hexagonal axes. To further constrain the structure, we measured the intensity of the right peak in Fig. 1b as we rotated the neutron polarization within the scattering plane. In Fig. 1d, we show how the intensity varies with the angle of the polarization as it deviates from the scattering vector, ***Q***. The measurement is also consistent with a magnetic moment having a component along the [1 1 -2] direction. Thus, we conclude that in the (110) oriented film, we have a modulated magnetic structure although we are not able to resolve whether it is a spiral or other modulated structure, due to our lack of sensitivity to a component of the moment along the [111] direction. However, we are able to restrict the moment to the HHL plane.

In Fig. 2, we show measurements of BFO grown on the (111) oriented substrate. In Fig. 2a, we can clearly see that the unpolarized diffraction results are markedly different from those observed in the (110) oriented film. To learn more, we again turn to polarized beam diffraction measurements. Here, we orient the film in the zone defined by the (1 1 1) and (1 -1 0) reflections. From Fig. 2b, we see that SF dominates NSF scattering and observe that only a single peak is present. We note from Fig. 2c that for $P \perp Q$, NSF scattering now dominates SF scattering. We also observe that, unlike the unpolarized neutron measurements, we clearly see two peaks in these scans, which is indicative of a modulated structure. These three measurements are consistent with a picture in which G-type order in the HHL zone coexists with a modulated structure (which is obscured by the [1 1 -2] component of the G-type order in the unpolarized diffraction measurements). In Fig. 2d, we again rotate the neutron polarization within the scattering plane and confirm that the G-type ordering has a strong component along the [1 1 -2] crystallographic hexagonal axis. These measurements do not completely determine the modulated structure. We can say that it is comparable in magnitude to the G-type phase and that it lies within the plane containing [1 -1 0] and [1 1 1].

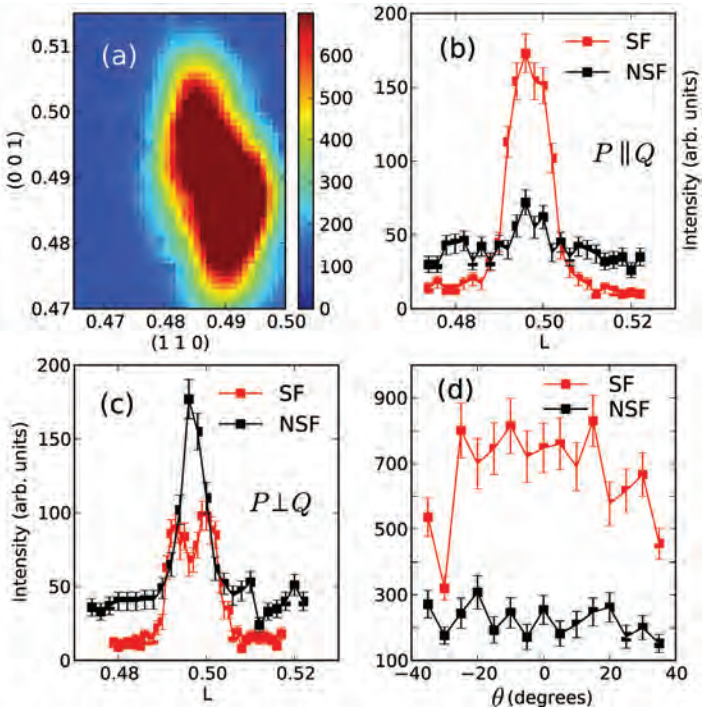

FIGURE 2: Neutron diffraction measurements of the (111) oriented $BiFeO_3$ film. (a) Reciprocal space map taken in the HHL zone using unpolarized neutrons; (b,c) intensity profiles taken with (b) P(neutron polarization)$\|Q$(scattering vector), and (c) $P \perp Q$; (d) changes in scattering intensities with the polarization rotated by an angle θ within the scattering plane relative to the scattering wave vector direction. The red and black squares represent spin-flip and non-spin-flip scattering, respectively. The data have been corrected for spin transport.

Our measurements show that it is possible to recover a modulated structure in BFO thin films. The nature of this magnetic structure can be tailored through the use of strain (for example, by growing the film on different substrate surfaces). Recently it has been found that the magnetic easy axis of permalloy deposited on BFO single crystals can be controlled by an electric field [8]. Thus, re-establishing modulated magnetic structures in thin films opens the doorway to new devices.

References

[1] R.T. Smith, G.D. Achenbac, R. Gerson, W.J. James, J. Appl. Phys. **39**, 70 (1968).

[2] G. Smolenskii and I. Chupis, Sov. Phys. Usp. **25**, 475 (1982); Y. Venevtsev and V. Gagulin, Ferroeletrics **162**, 23 (1994).

[3] T. Zhao, A. Scholl, F. Zavaliche, K. Lee, M. Barry, A. Doran, M.P. Cruz, Y.H. Chu, C. Ederr, N.A. Spaldin, R.R. Das, D.M. Kim, S.H. Baek, C. B. Eom, and R. Ramesh, Nature Materials **5**, 823 (2006).

[4] I. Sonowska, T. Peterlin-Neumaier, E. Steichele, J. Phys. C. **15**, 4835 (1982); R. Przenioslo, M. Regulski, I. Sosnowska, J. Phys. Soc. Jpn **75**, 084718 (2006); S. Lee, T. Choi, W. Ratcliff II, R. Erwin, S-W. Cheong, V. Kiryukhin, Phys. Rev. B **78**, 100101 (2008); D. Lebeugle, D. Colson, A. Forget, M. Viret, A.M. Bataille, A. Gukasov, Phys. Rev. Lett. **100**, 227602 (2008); S. Lee, W. Ratcliff, S-W. Cheong, V. Kiryukhin, Appl. Phys. Lett. **92**, 192906 (2008).

[5] H. Bea, M. Bibes, S. Petit, J. Kreisel, A. Barthelemy, Philos. Mag. Lett, **87**, 165 (2007).

[6] W. Ratcliff II, D. Kan, W.C. Chen, S. Watson, S. Chi, R. Erwin, G. J. McIntyre, S. Capelli, I.Takeuchi, Advanced Functional Materials, **21**, 1567 (2011).

[7] W.C. Chen, R. Erwin, J.W. McIver, S. Watson, C.B. Fu, T.R. Gentile, J.A. Borchers, J.W. Lynn, and G.L. Jones, Physica B **404**, 2663 (2009).

[8] D. Lebeugle, A. Mougin, M. Viret, D. Colson, and L. Ranno, Phys. Rev. Lett. **103**, 257601 (2009).

Quantifying disorder in lipid membranes

M. Mihailescu[1,2], R.G. Vaswani[3], E. Jardón-Valadez[3,4], F. Castro-Román[5], J. Alfredo Freites[6,3,4], D.L. Worcester[6,2,7], A.R. Chamberlin[3,8], D.J. Tobias[3,4], and S.H. White[6,2]

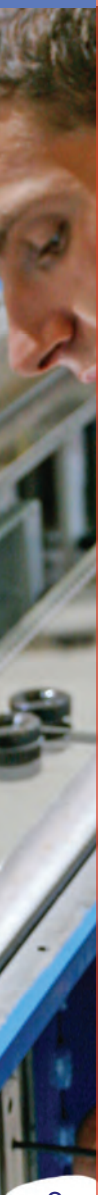

Two opposing layers of lipid molecules packed tightly together with polar sides facing aqueous regions and oily hydrocarbon chains inside, out of contact with water, create a lipid bilayer, the basic element of all cellular membranes. The complex architecture and many essential functions of eukaryotic cells rely on lipid bilayer membranes. About 1/3 of the proteins coded by the human genome are associated with lipid membranes. These proteins are essential to many cellular functions, such as ion, metabolite and water transport, signal transduction, muscle contraction, and cell-cell recognition. Despite the importance of these proteins, little is known about their association with lipid environments. A lipid membrane is normally highly fluid with lipids diffusing rapidly along the bilayer surface and hydrocarbon chains disordered, in constant motion due to rotations about carbon-carbon bonds. But this fluidity can be greatly affected by factors such as composition and temperature.

We use neutron diffraction as a tool for resolving the time-average distribution of atoms in a thermally disordered lipid bilayer by employing specific deuterium labeling. Bragg diffraction from oriented lipid multilayers is converted, via Fourier analysis, into one-dimensional density profiles of the bilayer along the *z*-axis, normal to the bilayer surface. The density profiles reveal the bilayer's molecular architecture. There are peaks for the phosphate-carbonyl groups, and a trough at $z = 0$, corresponding to the terminal methyl groups of the acyl chains (black curve, Fig. 1a). Specific deuteration of the acyl chain terminal methyl groups is used as a direct and quantitative method to determine the extent of chain disorder in the bilayer [1]. Hydration of the lipid in H_2O and D_2O allows for determining the water distribution associated with the polar head-groups. Deuterium difference profiles (lipid deuterated at the terminal methyl groups vs. natural lipid) reveal

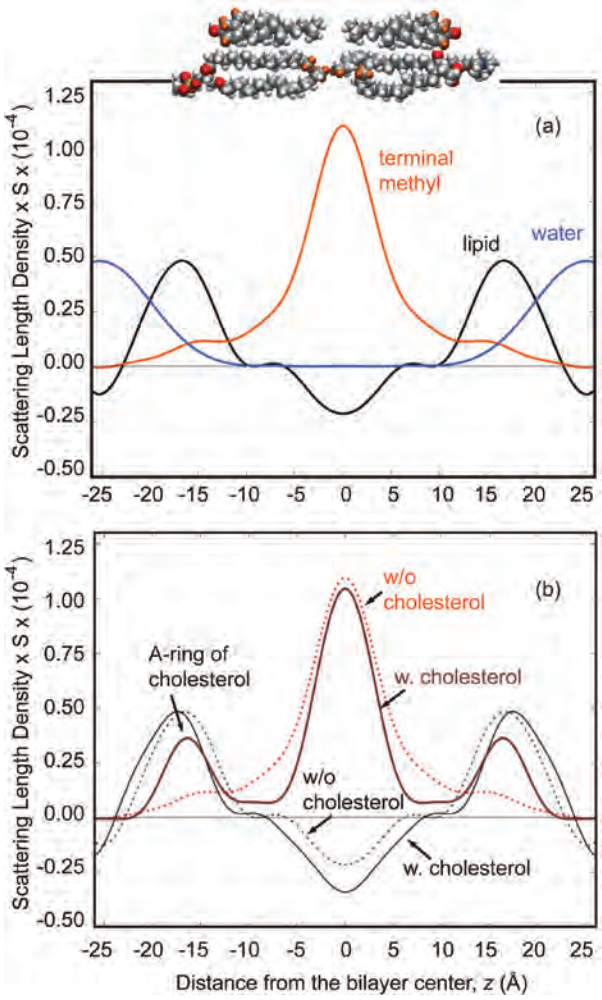

FIGURE 1: (a): Neutron diffraction results on the transbilayer distribution of lipid (black), terminal methyl groups (orange) and water (blue) in a DOPC bilayer. The scattering-length density profiles are on an absolute scale, up to an unknown factor (S), the area per lipid. (b): Transbilayer distribution of the terminal methyl groups in the liquid-ordered phase (2:1 DOPC:cholesterol) (brown, central peak) and the position and distribution of the first steroid ring of cholesterol (brown, side peaks). The brown curve was collected from a single lipid sample that contained cholesterol deuterated near the hydroxyl group and DOPC with deuterated terminal methyl groups. The black curves show the overall lipid profile in a bilayer without cholesterol (dashed) and with cholesterol (solid). Temperature: 21 °C, relative humidity: 86 %. The inset illustrates the disposition of the lipid molecules and cholesterol in the bilayer. Orange spheres indicate the deuterium sites.

[1]Institute of Bioscience and Biotechnology Research, University of Maryland, Rockville, MD 20850
[2]NIST Center for Neutron Research, National Institute of Standards and Technology, Gaithersburg, MD 20899
[3]Department of Chemistry, University of California at Irvine, Irvine, CA 92697
[4]Institute for Surface and Interface Science, University of California at Irvine, Irvine, CA 92697
[5]Centro de Investigación y de Estudios, Avanzados Instituto Politécnico National, México DF, 07360, México
[6]Department of Physiology and Biophysics, Center for Biomembrane Systems, University of California at Irvine, Irvine, CA 92697
[7]University of Missouri, Columbia, MO 65211
[8]Department of Pharmaceutical Sciences, University of California at Irvine, Irvine, CA 92697

a surprising number of acyl-chain methyl groups in the polar head-group region of the membranes. This result provides a direct measure of the disorder of the bilayer hydrocarbon region and shows that some chains exhibit sufficient bending motions to bring the chain methyl groups close to the membrane-water interface.

Natural cellular membranes are complex in composition, having hundreds of lipid species, including cholesterol, plus a variety of proteins. The role of cholesterol in organizing cellular membranes into functional domains or signaling platforms for proteins has been demonstrated in many studies. Direct demonstrations of how cholesterol affects bilayer organization are needed. We determined simultaneously the position of cholesterol and its effects on the hydrocarbon chain organization by using specific deuteration of cholesterol molecules and the terminal methyl groups of the lipids. Cholesterol is largely hydrophobic, made of a rigid steroid ring and a short, branched hydrocarbon tail. It has one polar group, a hydroxyl, making it amphipathic.

Our diffraction data show that cholesterol molecules align with the lipids such that the ring structure faces outwards toward the membrane surface (Fig. 1b). The presence of cholesterol imposes more order on the chains and causes the acyl-chain methyl groups to retreat from the polar region occupied the hydroxyl-containing ring of the cholesterol. The cholesterol-imposed ordering of the chains is consistent with order parameter measurements by NMR as well as molecular dynamics simulations.

In our work, all-atom molecular dynamics simulations of dioleoyl-phosphatidylcholine (DOPC) and DOPC:cholesterol (2:1) bilayers at 7.9 waters/lipid (corresponding to experiments at 86 % relative humidity) were carried out at constant temperature (296 K) and constant pressure (1 bar) for 100 ns. Besides the overall ordering effect on the lipid chains, the molecular dynamics simulations reveal that cholesterol decreases inter-leaflet mixing (Fig 2). These findings are consistent with the idea that the DOPC:cholesterol liquid-ordered phase arises by the straightening of the phospholipid acyl chains.

The membrane properties at both microscopic (molecular interaction) and macroscopic (membrane rigidity, surface tension) levels have been suggested to affect the function of membrane proteins and drive the lateral segregation of certain membrane components. Our results indicate that in the liquid-disordered phase the membrane polar interface can be more hydrophobic than previously thought, due to some mixing of lipid head groups and hydrocarbon methyl groups in the polar region. This may affect molecular binding to the membrane surface (antimicrobial peptides, ligands) but also the interaction of the integral membrane proteins with the bilayer. Cholesterol changes this scenario by ordering the hydrocarbon core and decreasing the degree of overlap between the two leaflets of the bilayer. It also thickens the bilayer by about 2 Å at 2:1 DOPC:cholesterol molar ratio, which partly explains the increased bending rigidity of membranes with cholesterol, observed in other studies.

Taken together, the neutron diffraction and MD simulation results offer a detailed, quantitative picture of the structure and dynamics of the liquid-ordered and liquid-disordered states of lipid membranes. This contributes important basic information to our understanding of membrane protein function in natural cellular membranes.

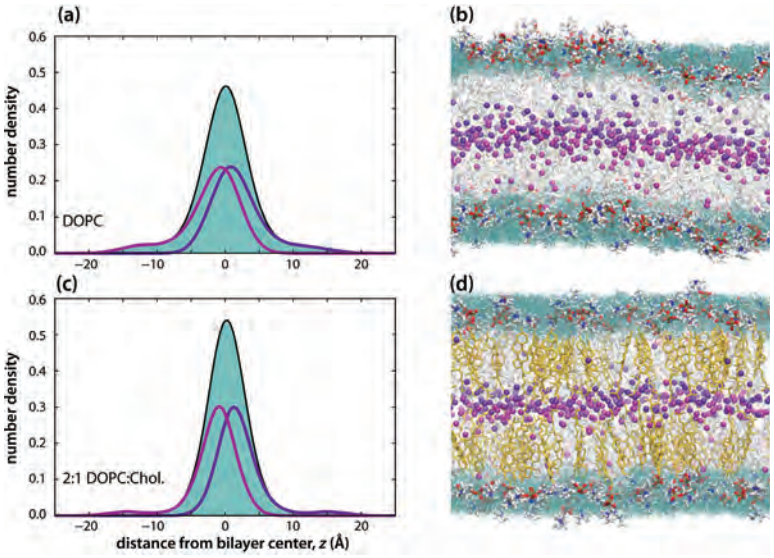

FIGURE 2: Simulated transbilayer distributions of terminal methyl groups in liquid-disordered and liquid-ordered DOPC:cholesterol (2:1) bilayers. (a): Transbilayer distribution of terminal methyls for DOPC observed in the all-atom molecular dynamics (MD) simulations of the results described in Fig. 1. The filled aquamarine curve shows the distribution for all terminal methyl groups. The broad wings observed experimentally are also observed in the simulation. The maroon and purple curves show the distributions of methyl groups associated with the left and right bilayer leaflets, respectively. (b): Snapshot of the all-atom MD simulation of DOPC. The terminal methyl groups are represented as spheres and are colored purple and magenta to distinguish methyls of each leaflet. Acyl chains shown in stick representation are gray. Phosphatidylcholine headgroups are also shown in stick representation colored according to element (red, oxygen; blue, nitrogen; gold, phosphorous; white, hydrogen). Water is shown as aquamarine. (c) and (d): same as in (a) and Fig. 1(b) for 2:1 DOPC:cholesterol. Cholesterol molecules, in gold, are shown in stick representation. As observed experimentally, the bilayer is thicker than for DOPC due to the ordering effect of the cholesterol on the DOPC molecules.

References

[1] M. Mihailescu *et al.*, Biophysical Journal, **100**(6), 1455 (2011).

Neutron reflectometry studies of the Parkinson's disease-related protein, α-synuclein, at the lipid bilayer interface

C. M. Pfefferkorn[1], F. Heinrich[2,3], J. C. Lee[1]

Parkinson's disease (PD) is a prevalent age-related neurodegenerative disease typified by resting tremors, slowness of movement, rigidity, and impaired balance in patients. Intensive research is beginning to shed light on its pathological underpinnings. One clue into the molecular causes of PD is a neuronal protein called α-synuclein (α-syn). Hallmarks of PD include the presence of inclusions (Lewy bodies) in the cells of brain tissues, composed mostly of aggregated or misfolded α-syn, and the loss of neurons that produce dopamine; moreover, genetic findings link mutants and over-expression of α-syn to early-onset PD [1]. Since α-syn is unstructured in solution but converts to a β-sheet enriched, amyloid form in Lewy bodies, these large polypeptide structural rearrangements are associated in the causes of PD. In our work, we investigated the binding of α-syn to a lipid bilayer and its influences on membrane properties using neutron reflectometry (NR) [2].

The role of membranes in mediating α-syn (mis) folding is of particular interest because membranes are ubiquitous *in vivo* and the binding of α-syn to membranes *in vitro* both induces formation of secondary structure (unstructured → α-helix) and modulates the rate of α-syn aggregation. Notably, PD mutations in α-syn can affect membrane binding, and oligomeric α-syn has been shown to disrupt membrane integrity, a process which could initiate cell death [1]. Despite substantial research efforts regarding the interaction of α-syn with model membranes, the molecular mechanism by which they influence α-syn aggregation remains unclear. While our prior work using residue-specific fluorescence spectroscopy examined the interaction of α-syn with small unilamellar vesicles from the perspective of the protein [3], to gain insights into how α-syn protein association affects membrane properties, a simultaneous probe of both α-syn protein and membrane structure is required. Hence, we have employed NR and a surface-stabilized sparsely tethered bilayer lipid membrane (stBLM) [4] towards this objective. Using NR, the depth profile of the different interface layers (*e.g.*, lipid headgroups and α-syn) normal to the bilayer surface can be readily measured. Herein, we describe results in which NR was exploited to elucidate both membrane-bound α-syn and bilayer structure.

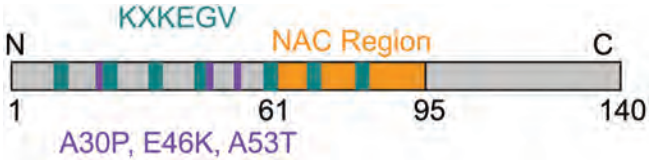

FIGURE 1: Schematic representation of α-syn, with the seven imperfect amino acid repeats in green (KXKEGV) containing both hydrophobic and hydrophilic (amphiphatic) residues, the non-amyloid beta component region in orange, (NAC), and the three disease related α-syn mutations in purple, (A30P, E46K, A53T).

Figure 1 provides a schematic diagram that highlights some of the key features of α-syn primary sequence. There are seven N-terminal imperfect membrane binding amino acid amphiphatic repeats (*i.e.*, containing both hydrophobic and hydrophilic ends). Also, there is the highly hydrophobic and aggregation-prone central region called the non-amyloid β component (NAC).

The stBLM was composed of a 1:1 molar ratio of 1-palmitoyl-2-oleoyl-*sn*-glycero-3-phosphate (POPA): 1-palmitoyl-2-oleoyl-*sn*-glycero-3-phosphocholine (POPC). This POPA:POPC lipid composition was chosen both to facilitate comparison to our prior work [3] and because α-syn has preferential affinity for anionic (POPA) lipid headgroups. Using this stBLM, NR data were collected in the presence and absence of α-syn using the NCNR NG1 reflectometer [5].

The stBLM was first measured in aqueous buffer (10 mmol/L sodium phosphate, 100 mmol/L NaCl, pH 7.4) containing three isotopically different compositions (100 % D_2O, 100 % H_2O, and 2:1 H_2O:D_2O), followed by aqueous buffers containing α-syn (3 μmol/L in 10 mmol/L sodium phosphate, 100 mmol/L NaCl, pH 7.4 in either H_2O or D_2O). Because of the unique flow cell sample chamber design, allowing for in situ solvent exchange, it is possible to perform successive measurements on the same sample (bilayer) area.

[1]National Institutes of Health, Bethesda, MD 20892
[2]Carnegie Mellon University, Pittsburgh, PA 15213
[3]NIST Center for Neutron Research, National Institute of Standards and Technology, Gaithersburg, MD 20899

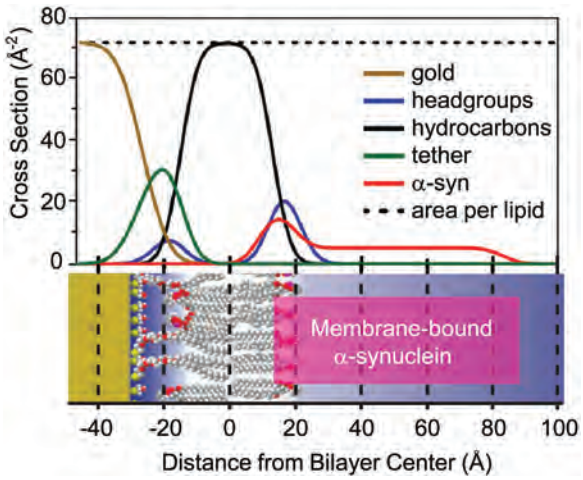

FIGURE 2: Simplified molecular distributions for organic interface layers of the 1:1 POPA:POPC stBLM in the presence of α-syn (3 μmol/L in 10 mmol/L sodium phosphate, 100 mmol/L NaCl, pH 7.4) obtained from the best-fit of reflectivity data to the composition space model. A reference value for the area per lipid is indicated by the dotted line. Data for Si substrate and the SiOx, Cr, and Au layer have been partially omitted. A corresponding schematic of the stBLM is also provided for reference.

Using best fits to NR data based on a composition space model [6], a cross-sectional profile of the different interface layers along with other fit parameters such as scattering length density (nSLD) and α-syn volume occupancy were extracted and are shown in Fig. 2. A schematic view of the stBLM with α-syn superimposed is also provided in Fig. 2 for reference. In the absence of α-syn protein, values for the inner and outer bilayer leaflet thicknesses fall within expected values.

Upon α-syn addition, NR data indicate that it indeed binds to the stBLM at an occupancy level of ≈ 15 % volume fraction in both the outer leaflet headgroups and hydrocarbons. Additionally, α-syn was found to extend into the bulk solvent region, indicating that the protein is partially anchored to the stBLM. This is a new observation, and one plausible explanation for it is that some portion of the α-syn polypeptide inserts into the hydrocarbon region while the remaining segment is exposed to the solvent. A model consistent with published data would be that the high affinity membrane binding site, the N-terminus, serves as the membrane anchor [3]. Interestingly, the thickness of the protein region in the outer leaflet of the stBLM (≈ 13 Å) is consistent with the membrane-bound α-syn adopting an α-helical conformation, which is in accord with solution studies conducted with vesicles. Finally, the binding of α-syn to the stBLM also resulted in sizeable reduction (> 1 Å) in membrane bilayer thickness. While the completeness of the stBLM was maintained during the course of our experiments, we propose that membrane thinning could represent a first step leading to disruption or even permeabilization of the bilayer, which have been linked to PD pathogenesis.

By successfully collecting high resolution NR data simultaneously for both membrane-bound α-syn and the stBLM, we have gained new insights into the orientation and conformation of α-syn at the membrane interface as well as a potential clue into how membrane-bound α-syn initiates membrane perturbation. It is plausible that the observed membrane induced α-syn conformation and subsequent membrane thinning could set the stage for PD progression. In our continued effort to gain a molecular understanding of the role of membranes and α-syn in PD, we aim to elucidate the effects of different solution conditions on α-syn membrane-bound structure and membrane induced perturbations.

References

[1] K. Beyer, Cell Biochem. Biophys. **47**, 285 (2007).

[2] C. M. Pfefferkorn, F. Heinrich, J. C. Lee, (to be submitted).

[3] C. M. Pfefferkorn, J. C. Lee, J. Phys. Chem. B **114**, 4615 (2010).

[4] D. J. McGillivray, G. Valincius, D. J. Vanderah, W. Febo-Ayala, J. T. Woodward, F. Heinrich, J. J. Kasianowicz, M. Lösche, Biointerphases **2**, 21 (2007).

[5] J. A. Dura, D. J. Pierce, C. F. Majkrzak, N. C. Maleszewskyj, D. J. McGillivray, M. Lösche, K. V. O'Donovan, M. Mihailescu, U. Perez-Salas, D. L. Worcester, S. H. White, Rev. Sci. Instrum. **77**, 074301 (2006).

[6] M. Schalke, P. Kruger, M. Weygand, M. Losche, Biochim. Biophys. Acta, Biomembr. **1464**, 113 (2000).

SANS and modeling reveal changes in flexibility of a protein important for DNA replication

S. Krueger[1], J.-H. Shin[2], S. Raghunandan[1], J.E. Curtis[1], Z. Kelman[3]

During reproduction, DNA is separated into two strands to be replicated. How is this done? There are special proteins (helicases) that carry out this task, but the details of the process remain to be worked out. One type of helicase is the minichromosome maintenance (MCM) protein which has many moving parts (domains). In this highlight we describe SANS measurements and computer modeling studies on the N-terminal domain of a MCM protein from the microorganism *Methanothermobacter thermautotrophicus* (N-mtMCM). This work provides structural information that supports the previously reported biochemical observations that large domain motions are required for the activation of the MCM helicase.

A high-resolution x-ray crystal structure [1] of N-mtMCM shows that it is a protein with a 12 subunit (dodecamer) structure, with each monomeric subunit consisting of three domains. Domain A is suggested to play a role in regulating helicase activity, domain B participates in DNA binding, and domain C is involved in the assembly of the protein subunits (multimerization) as well as DNA binding and is necessary for helicase activity [2]. An unstructured loop region consisting of 20 amino acid residues (89 to 108) exists in N-mtMCM between domains A and C. A second unstructured region consisting of 43 amino acid residues (244 to 286) is located at the C-terminus of N-mtMCM. This region would be connected to the catalytic domain in the full mtMCM molecule. Electron microscopy (EM) studies of N-mtMCM revealed a six subunit (hexameric) structure [3], which is different from the dodecamer suggested by the x-ray crystal structure and by biochemical characterization of the protein in solution [4]. Since neither EM nor crystal structure determination reveals the structure of a protein in solution where it is at full hydration under conditions closer to its natural state, the SANS studies were undertaken to provide complementary structural information.

SANS data were obtained from N-mtMCM in the absence of DNA and in the presence of a single-stranded DNA molecule consisting of 50 nucleotides (nt). Fits to the data for N-mtMCM in the absence of DNA resulted in a radius of gyration, R_g, value of 78 Å ± 1 Å. The R_g value for the N-mtMCM/DNA complex was 69 Å ± 1 Å, indicating that there is a significant decrease in the size of the N-mtMCM molecule when the 50 nt DNA is bound. As a starting point for the modeling, an all-atom structure of the N-mtMCM dodecamer molecule was built based on the x-ray crystal structure, with residues 244 to 286 added to the C-terminus of each monomer. The SASSIE software package [5] was used to generate ensembles of structures for comparison to SANS data by randomly varying amino acid residue backbone dihedral angles within chosen regions of the protein. After each randomly chosen angle was rotated by a given value, the final value was checked to determine if it was energetically probable. The new configuration was checked for overlap of basis atoms, usually chosen to be alpha-carbon atoms. If both checks were met, the new structure was accepted.

The measured SANS data were compared to theoretical SANS curves calculated from two different series of accepted structures using the χ^2 test for goodness of fit. An example of each of these structures is shown in Fig. 1. In both cases, domain A is shown in yellow and domains B and C are in blue. The unstructured loop region (residues 89 to 108) between domains A and C in each monomer is shown in green and the unstructured region at the C-terminus of each monomer (244 to 286) is shown in purple. In the first series of structures (Fig. 1a), residues 244 to 286 were treated as unstructured flexible regions in which the dihedral angles were variable as described above. The second series of structures (Fig. 1b) define this same region to be flexible, as well as residues 89 to 108 between domains A and C.

A best-fit family of structures was chosen for each of the samples based on the lowest ≈ 20 % of the χ^2 values for each series. The lowest χ^2 values range between 0.73 and 1.5, except for the MCM sample without DNA compared to

[1]NIST Center for Neutron Research, National Institute of Standards and Technology, Gaithersburg, MD 20899
[2]Kyungpook National University, Daegu 702-701, Republic of Korea
[3]Cell Biology and Molecular Genetics, University of Maryland, College Park, MD 20742 and Institute for Bioscience and Biotechnology Research, University of Maryland, Rockville, MD 20850

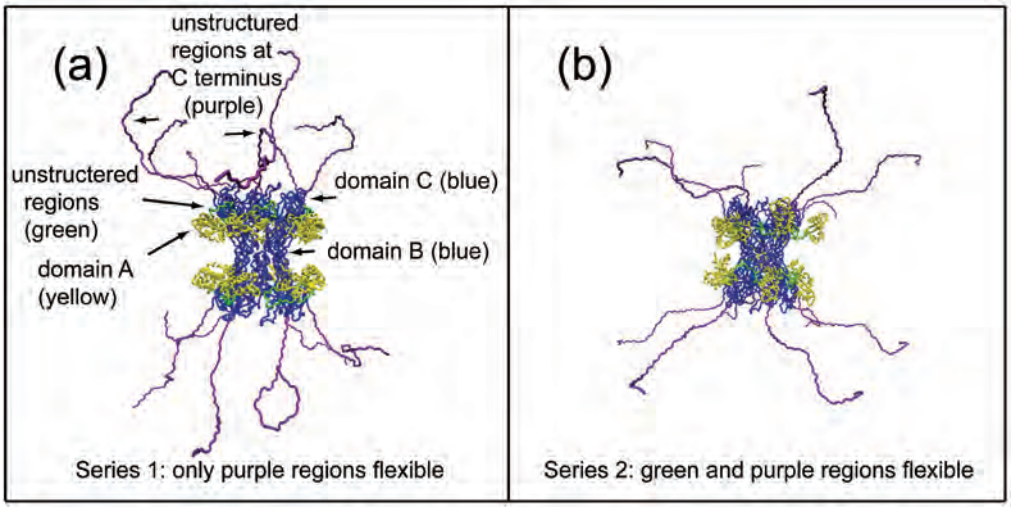

FIGURE 1: Examples of two series of model structures for N-mtMCM. Domain A is shown in yellow and domains B and C are in blue. An unstructured loop region between domains A and C is shown in green and a second unstructured region at the C-terminus is shown in purple. a) Only the C-terminus unstructured region (purple) is allowed to be flexible. b) Both unstructured regions are allowed to be flexible.

the first series of structures, where the values are between 3.6 and 3.9. Figure 2 shows the SANS data from the MCM samples with and without DNA, along with three representative best-fit theoretical curves from the first series of structures. By inspection it can be seen that worst part of the fit to the data from the samples without DNA occurs for $q > 0.07$ Å^{-1}. This leads to the conclusion that structures that do not allow residues 89 to 108 to be flexible are not a good representation of the MCM sample without DNA. On the other hand, the χ^2 analysis shows that equally good fits can be obtained for the DNA-bound sample whether or not this region is modeled as flexible.

From the comparison of the theoretical SANS curves for each of the two series of structures to the SANS data, it is clear that the MCM sample in the absence of DNA must have both flexible C-terminal and N-terminal regions in order to fit the SANS data. This flexibility, while in contrast to the more rigid crystal structure, is consistent with the EM and biochemical studies of the MCM proteins, suggesting that significant movement of domain A is required prior to the initiation of MCM activity and DNA replication. The fact that equally good fits of the DNA-bound sample can be obtained whether the N-terminal residues are flexible or not is significant, as this means that the MCM/DNA complex can have this more rigid structure, while the unbound sample cannot. The data presented here demonstrate that SANS analysis combined with energetically relevant all-atom ensemble structure modeling is a powerful tool that allows the assessment of the degree of flexibility of proteins in solution, even in cases where an ensemble of structures is likely present. The methods developed here for N-mtMCM solution structure modeling can likely be utilized for other large, multimeric protein complexes with unstructured flexible regions.

References

[1] R.J. Fletcher, B.E. Bishop, R.P. Leon, R.A. Sclafani, C.M. Ogata, X.S. Chen, Nature Struct. Biol. **10**, 160 (2003).

[2] N. Sakakibara, L.M. Kelman, Z. Kelman, Mol. Microbiol. **72**, 286 (2009).

[3] Y.-J. Chen, X. Yu, R. Kasiviswanathan, J.-H. Shin, Z. Kelman, E.H. Egelman, J. Mol. Biol. **346**, 389 (2005).

[4] R. Kasiviswanathan, J.-H. Shin, E. Melamud, Z. Kelman, J. Biol. Chem. **279**, 28358 (2004).

[5] J.E. Curtis, S. Raghunandan, H. Nanda, S. Krueger, Computer Physics Comm., accepted (2011); http://www.smallangles.net/sassie/SASSIE/SASSIE_HOME.html

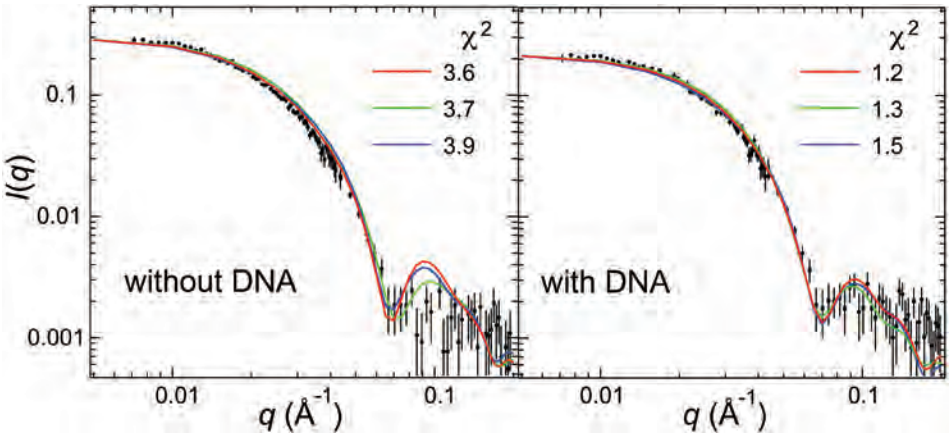

FIGURE 2: log(I) vs log(q) plots of the measured SANS data for the samples without and with DNA bound, along with representative examples of best fit theoretical SANS curves from the ensemble of structures in which only the C-terminus unstructured region is allowed to be flexible (Fig. 1a.)

Residual stresses and mechanical damage in gas pipelines

T. Gnäupel-Herold[1,2], R. Batisse[3], L. Clapham[4]

Pipeline failure comes into the focus of public attention because of loss of human life or from great environmental damage, be it from release of crude oil or from natural gas. These events appear to be rare because large, catastrophic releases > 10^4 m^3 of crude (or gas: $\times 10^3$) of hydrocarbons are rare compared to the much more frequent (> 10^2/ year in Canada alone) small to medium releases [1]. Inherent ruptures tend to be the main cause of large ruptures, but third party damage is the cause of 40 % of pipeline ruptures. Mechanical damage without immediate rupture due to construction or agricultural activity often occurs, and it raises a crucial question: How critical is the damage and what actions need to be taken? In order to address this question damage has to be quantified in some manner, and Magnetic Flux Leakage (MFL) is one of the tools the industry uses for that purpose. In this method a MFL probe records changes in the magnetic field between two magnetic poles that are in close contact with the pipe wall. Dents and gouges create changes in geometry, plastic strains and residual stresses; all of which severely alter the MFL signal in ways that are not completely understood. Geometry changes are more readily quantifiable but the residual stress contribution is difficult to determine due to the lack of experimental data and reliable modeling results. Some progress has been made by annealing the sample, thus eliminating the residual stress contribution [2]. However, this cannot address questions about the role of the multiaxiality of stresses, sign changes of stresses and stress gradients, both laterally and through the thickness [3]. Thus, it is necessary to measure the residual stresses non-destructively, and the only technique capable of handling large pipe sections due to problems of weight, dimensions and wall thickness is neutron diffraction. It is obvious that, in order to put such measurements on a sound footing, one cannot wait for such damage to occur and then remove that pipe section, and perform the necessary measurements. Instead, the various type of gouges and dents that are encountered on real pipelines need to be produced in a controlled and repeatable fashion. By varying the testing speed, the deformation path, and the tool shape it is possible to cover a wide range of real-world damage scenarios (Fig. 1) that combine the two major elements of gouging (which removes material and has some plastic deformation) and denting (which has plastic deformation only).

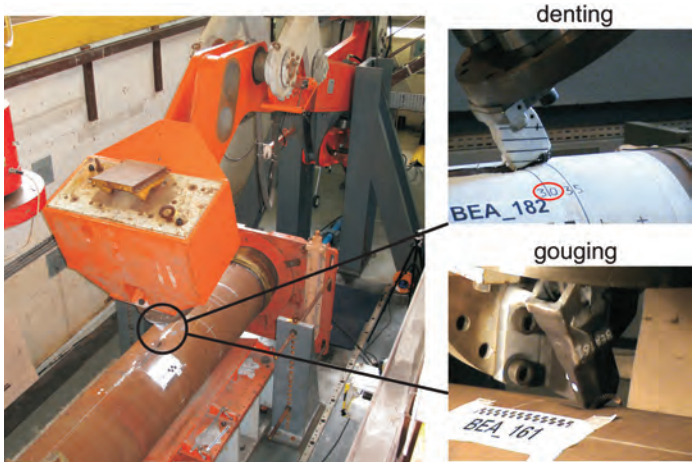

FIGURE 1: Left: testing equipment at GDF SUEZ, France. Right: types of damage. Denting merely deforms but does not remove material as gouging does. BEA161 (gouge) in the lower right corner was investigated here; BEA182 is similar to the dent investigated here.

Figure 1 illustrates the unique challenges to the stress measurement presented by this approach: First, the damaged regions with 300 mm dent length (see circled 30 cm mark in Fig. 1, upper right corner), and 130 mm gouge length, respectively, are unusually large. Second, the pipe should stay intact circumferentially, and retain sufficient length axially as much as possible in order to preserve the stress field. The resulting samples were pipe sections 650 mm in diameter, 500 mm in length, and 8 mm wall thickness. The wall thickness is quite low, and in order to sample the stresses in sufficient detail through the thickness the spatial resolution of the measurement – in other words, the size of the neutron beam – must be chosen appropriately (here: 1 mm). Aside from some basic symmetry considerations – *e.g.*, the stress field is presumed to be laterally symmetric – there is not much one can assume about the stresses, thus creating the necessity for

[1]University of Maryland, College Park, MD 20742
[2]NIST Center for Neutron Research, National Institute of Standards and Technology, Gaithersburg, MD 20899-6102
[3]GDF SUEZ, Saint-Denis la Plaine, France
[4]Queen's University, Kingston, Ontario, K7L 3N6 , Canada

measurements at numerous locations in the defect area and through the thickness.

As shown in Fig. 2, measurements along the line of symmetry show that the stresses created by the two defect types exhibit significant changes in magnitude, particularly near the start and end of the defects. The high tensile hoop stresses near the end of the dent are a red flag because the total stress in a pressurized pipeline– residual stress plus stress from pressure – may reach the tensile strength of the material. The danger of pipe rupture arises if the high stress levels are combined with a weakened cross section at the location of the peak stress due to large strains (dent) or material removal (gouge). However, the stresses must also be considered in the context of MFL measurements, particularly in view of the lateral resolution of MFL probes which can be of the order of 1 mm. The MFL signal is a weighted average through the thickness, which is why it is difficult to assign a depth location to a sub-surface defect. Rather, the interplay of gradients in different directions creates a cumulative effect where different combinations of stresses can produce the similar MFL signals. Thus, the contribution of different through-thickness stress gradients to MFL signals is of particular interest. As shown in Fig. 3 stress gradients near the surface are most severe in the lateral direction away from the defect where over a length of 5 mm stresses change by more than 300 MPa. The stress differential in the radial direction (through the thickness) is of similar magnitude.

Aside from aiding the interpretation of signals from MFL probes these findings also help in addressing safety concerns. Pressure in a pipeline superimposes a stress on the residual stresses, and the total stresses should not exceed certain limits set by the safety factor (between 1.5 and 10). What problems could arise if creating the mechanical damage in the pipes did not cause immediate

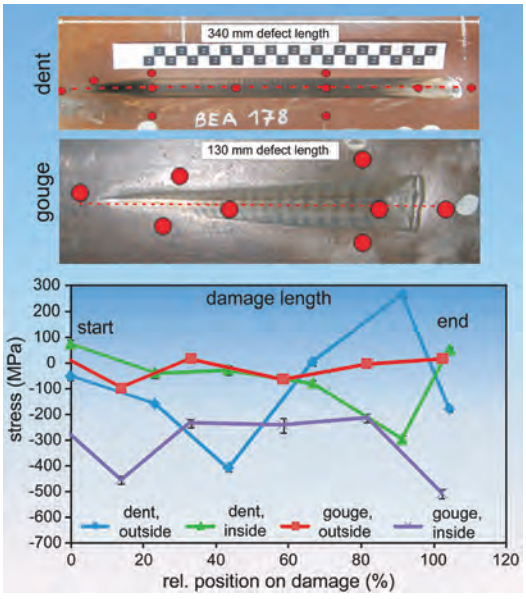

FIGURE 2: Comparison of hoop residual stresses in the gouge and the dent. Dots represent measurements through the thickness. Note the high tensile stresses outside near the end of the dent. Additional tensile stresses are superimposed in pressurized pipelines.

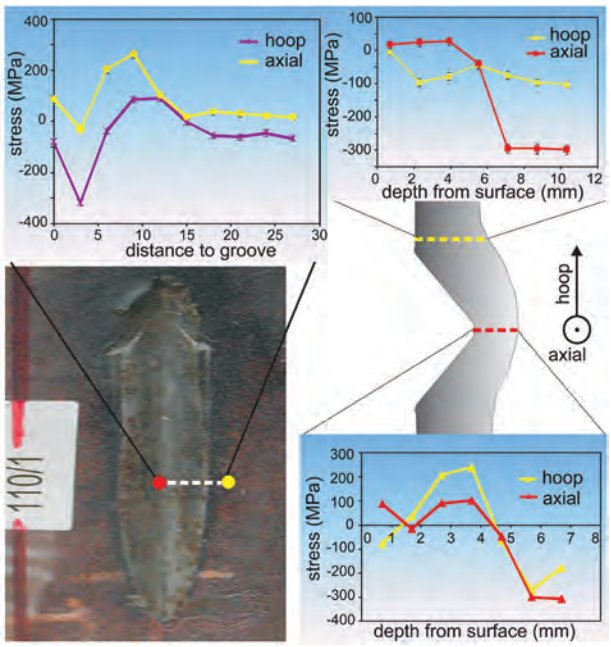

FIGURE 3: Stresses in the center region of a plate sample that was cut from a pipe to allow for measurements in greater number and detail.

pipe rupture? On one hand, these limits are exceeded in pipelines with low safety factors both in regions of peak tensile stresses and where the cross section is reduced the most. On the other hand, the mechanical damage creates work hardening which raises the strength locally. The end result could be viewed as a locally reduced safety factor that in extreme cases may require the reduction of the operating pressure in the pipeline. Another damage-related problem to consider is the increased risk of stress corrosion cracking assisted both by high tensile stresses and coating failure in the dent/gouge region.

These measurements are part of an ongoing international project in which different pipeline defects are produced under realistic conditions, and then characterized with respect to residual stresses and MFL signal distribution. The neutron diffraction measurements are the first of this type and they revealed complex stress patterns both through the thickness and in the lateral directions. It is one of the goals of these efforts to use the neutron data in order to create a functioning magnetic model that allows the separation of the geometry effect and the stress effect on the magnetic flux leakage signal, thus greatly enhancing the scope of MFL probes as an in-line inspection tool.

References

[1] Pipeline Performance in Alberta 1980-1997, Alberta Energy and Utilities Board 1998, available at: http://www.eub.gov.ab.ca

[2] L. Clapham *et al.*, Proc. 2004 Int. Pipeline Conference, Calgary, 983 (2004).

[3] P.A. Ivanov *et al.*, IEEE Transactions on Magnetics, **34**, 3020 (1998).

Nano void volume linked to sensitivity of RDX explosive

C. S. Stoltz[1], B. P. Mason[1], J. P. Hooper[1,2]

The importance of crystalline defects in the initiation of an explosive by a shock wave has been known for many decades, but a detailed relationship between specific structural features and the onset of detonation has proven very challenging. Figure 1 shows optical images of small grains of the explosive RDX, in which the void patterns vary widely based on the synthesis method. The passage of a shock wave through an explosive material results in the formation of regions of locally increased temperature at these voids and defects; often referred to as "hot spots". These are the areas at which chemical reaction begins and propagates. The onset of reaction due to hot spot formation can occur at shock pressures well below that needed to initiate reaction in an ideal, defect-free bulk explosive. Void space thus plays a key role in the safety of explosive materials, but systematic experimental studies of void distributions in explosive grains have been very limited.

In this work we consider a series of crystalline powders of RDX whose density, crystallite size, and impurity levels are very similar but which still have significant variation in their sensitivity to accidental initiation. The sensitivity differences in this case likely arise from mesostructural internal defects within the crystallites themselves. We present the first small and ultra-small angle neutron scattering (SANS/USANS) measurements on RDX to probe the void morphology in these samples on length scales between 1 nm and 20 μm [1]. Samples were mixed with a deuterated solution that effectively masks scattering from the crystallites themselves, allowing the measurements to probe only the internal voids.

Powders of cyclotrimethylene-trinitramine, commonly referred to as RDX, were obtained from four manufacturers as part of a comparative study on insensitive explosives. The impurity content of all samples was tested with high-performance liquid chromatography and ^{1}H NMR to confirm the levels of impurity phases and search for any possible solvent that may have been trapped in interior voids.

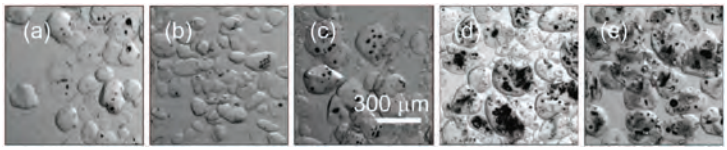

FIGURE 1: Optical microscopy of RDX samples in an index of refraction matching fluid. Dark regions show void spaces that may serve as "hot spots" where reaction begins.

Within the limits of detection (< 1 % volume fraction), no such impurities were observed. Density measurements were taken using a helium gas pycnometer, and within the expected error of the pycnometry measurements the densities of the various RDX samples are nearly identical. The crystalline morphology of these samples was generally similar, and thus we expect that sensitivity differences would likely arise from small variation in submicron voids in the exact range suitable for SANS/USANS studies. Scattering intensity as a function of wave vector Q was measured and was converted to an absolute scattering cross-section per unit volume.

The dominant feature in all neutron studies of our RDX samples is a power-law scattering that extends over a very wide SANS and USANS range (see Fig. 2). The scattering continues to increase even at the lowest Q range (*i.e.*, largest length scale) probed by USANS. A power-law behavior Q^{-m}

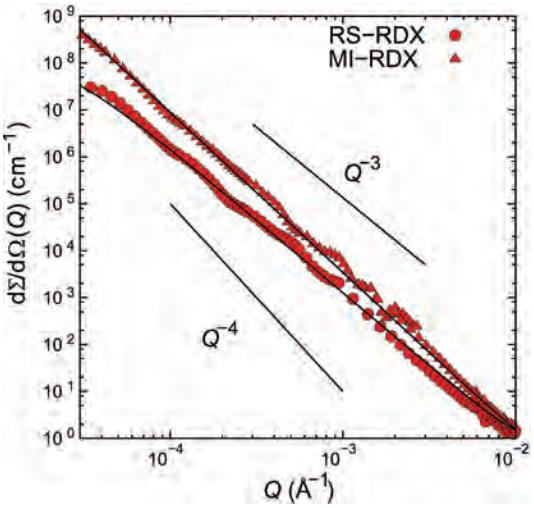

FIGURE 2: SANS and USANS data for two RDX samples. Solid lines are fits to the data using a surface fractal model.

[1]Naval Surface Warfare Center, Indian Head Division, Indian Head, MD 20640
[2]Naval Postgraduate School, Monterey, CA 93943

is observed, where m varies between 3.1 and 3.6. Exponents in this range generally correspond to fractal scattering from surfaces with a dimensionality $D = 6 - m$ between 2 and 3 [2]. The data suggests internal fractal surfaces are present in RDX over a wide range of length scales, from ≈ 50 nm up to ≈ 20 μm. No region of Q^{-4} behavior is observed in any sample; such a power law would indicate scattering from the surface of a smooth 3D object of dimensionality $D = 2$.

A key question in the area of explosive sensitivity is what size a void must be to become a hot spot during initiation. Previous work on powders of the explosive HMX had suggested that polydisperse spherical voids on the order of 3 nm to 60 nm may be present and important for sensitivity [3]; we find no evidence of such features in our RDX samples. Around 10 nm to 30 nm the intensity of the fractal surface scattering becomes comparable to the background, and there is no evidence of any features arising from spherical scatterers.

To compare between the different explosive samples, we have calculated the neutron scattering invariant, which involves an integration of the cross section over Q and is related to the overall volume fraction of void space. In Fig. 3 we plot a correlation between the sensitivity of the explosive measured by the large-scale gap test (LSGT) and the neutron scattering invariant. We find that, though the pycnometry densities of the samples are similar, the invariant tracks with the shock sensitivity values derived from the large-scale gap tests. Thus, with other material properties held constant to the extent possible, the internal void space on length scales from 60 nm to 20 μm appears to be well correlated with macroscopic changes in sensitivity of the explosive RDX. While one would expect this trend based on general theories of hot spot formation in explosives, direct experimental links between specific mesostructural crystal features and accurate shock sensitivity tests have been limited.

What is the origin of the fractal scattering in the explosive samples? One possibility is that these fractal regions arise from a crystal growth process that occurs on the surface of interior voids as solvent diffuses out of the RDX crystals. The commercial samples used were subjected to thermal cycling during the manufacturing and post-production processes that would encourage diffusion of any solvent remaining in the void space. Small amounts of RDX dissolved within the internal solvent would gradually agglomerate on the voids walls, similar to other aggregation processes leading to fractal growth patterns. Recent observations by Melinger and coworkers [4] of a complex dendritic crystal structure formed during drop-cast growth of microgram quantities of RDX on an Au surface may provide support for this hypothesis.

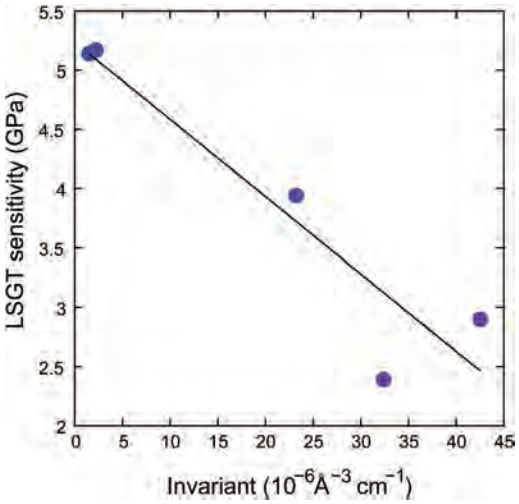

FIGURE 3: The susceptibility to accidental initiation as measured by the large-scale gap test (LSGT) is plotted versus the neutron scattering invariant calculated from the SANS and USANS data. The invariant is a general measure of the volume fraction of void space. As void space in the 60 nm to 20 µm range increases, less shock pressure is needed to induce the explosive to detonate.

In summary, SANS and USANS measurements were performed on RDX powders to characterize the internal void features on length scales between 1 nm and 20 μm. Experiments were performed on five RDX samples with a range of sensitivities to accidental shock initiation. The neutron scattering for all samples exhibits a fractal behavior indicative of surface fractals with a dimensionality between 2.4 and 2.9. The fractal behavior extends up to the maximum length scales measured in our USANS experiments, indicating a fractal correlation length on the order of 30 μm or higher. No evidence of distinct nanometer-scale void distributions is observed. The neutron data are interpreted in terms of surface scattering from internal voids, whose fractal character may arise from crystallite growth on the void walls as solvent diffuses out from the system. The scattering invariant, which serves as a relative comparison of the overall amount of scattering as well as a general measure of the volume fraction of internal voids, differs widely between the different RDX samples and tracks well with the measured shock sensitivities. Despite similarities in density and particle distribution, neutron scattering reveals clear differences between samples that offer a direct link between structural features and sensitivity testing.

References

[1] C. S. Stoltz, B. P. Mason, and J. Hooper. J. Appl. Phys. **107** (10) 103527 (2010).

[2] J. Teixeira, J. Appl. Cryst. **21**, 781 (1988).

[3] J. T. Mang *et al.*, J. Mater. Res. **15,** 1199 (2000).

[4] J. S. Melinger *et al.*, Appl. Phys. Lett. **93**, 011102 (2008).

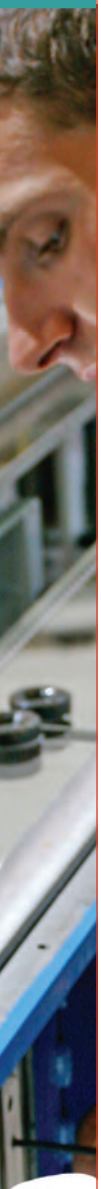

Density hysteresis in nanoconfined water

Y. Zhang[1,2], A. Faraone[3,4], W.A. Kamitakahara[3], K-H. Liu[5], C-Y. Mou[5], J.B. Leão[3], S. Chang[3], S-H. Chen[1]

The properties of water have been explored by many techniques, including neutron scattering. Despite a huge research effort, basic gaps in our understanding persist, especially in the supercooled region where water remains in the liquid state below the melting point. A particularly interesting and controversial hypothesis posits that, across a range of temperatures and pressures, bulk water is composed of a mixture of two structurally distinct liquids: a low-density liquid (LDL) and a high-density liquid (HDL). The latter is water of our everyday experience, whereas the former is characterized by a local intermolecular bonding environment much more like that of solid ice, which leads to a lower density. A central question is whether a first-order liquid-liquid phase transition between LDL and HDL exists, as a thermodynamic extension of the first-order transition established in the amorphous solid waters [1-3]. An experimental determination of water's density in the deeply supercooled region is perhaps the most direct way of investigating the hypothesized liquid-liquid phase transition. By undertaking such measurements, we are seeking evidence of a first-order liquid-liquid phase transition of water that would exist in the macroscopic system if it were possible to avoid crystallization [4].

An experimental challenge arises because the hypothesized transition exists in a region of the phase diagram in which bulk water cannot exist in a liquid state [1]. One method of overcoming this difficulty is to take advantage of confinement. By confining water in a nanoporous silica matrix, MCM-41-S with 15 Å pore diameter, the homogeneous nucleation process (crystallization) can be avoided, allowing us to enter this region. There is still much debate on the differences and similarities between bulk and confined water. However, even if the silica matrix, with its hydrophilic surfaces, might change basic properties of water beyond suppressing crystallization, the properties of the confined water are important in their own right, since they are representative of many environments of interest in biology and geology where similar hydrophilic interfaces are present.

The contrast of the neutron coherent scattering length density (SLD) of heavy water against that of the silica matrix gives rise to a well-defined diffraction peak arising from the (10) plane of a 2-D hexagonal lattice of water cylinders in the grains of MCM-41-S silica matrix. Once the data are corrected for the temperature-independent background arising from the fractal packing of the MCM-41-S crystallites and the incoherent scattering, the only temperature-dependent quantity is the height of the Bragg peak, which is proportional to the square of the difference of SLD between the heavy water and the silica matrix, and therefore a sensitive indicator of the average mass density of the confined water.

Figure 1 shows the hypothesized phase diagrams of low temperature water in the presence of a first-order HDL-LDL transition. When the equilibrium phase boundary is crossed, due to the metastability or the kinetics of the phase transition, the phase separation may take a very long time to happen, especially in confinement [5]. However, a first-order line should still manifest itself with a significant hysteresis when it is crossed from opposite directions of the transition line, shown in Fig. 1(b). Accordingly, we performed a series of warming and cooling scans over a range of pressures.

Figure 2 shows the measured density of confined D_2O with both cooling and warming scans at a series of pressures. The fact that the warming and cooling curves join at both high and low temperature ends implies that the expansion-contraction processes are reversible. Up to 100 MPa, the density difference between the cooling and warming scans is small, which could be attributed to the temperature lag when ramping the temperature continuously. The density difference due to this reason is small and relatively independent of pressure. However, above 100 MPa the density difference (hysteresis) opens up progressively

[1]Massachusetts Institute of Technology, Cambridge, MA 02139
[2]Oak Ridge National Laboratory, Oak Ridge, TN 37831
[3]NIST Center for Neutron Research, National Institute of Standards and Technology, Gaithersburg, MD 20899
[4]University of Maryland, College Park, MD 20742
[5]National Taiwan University, Taipei 106, Taiwan

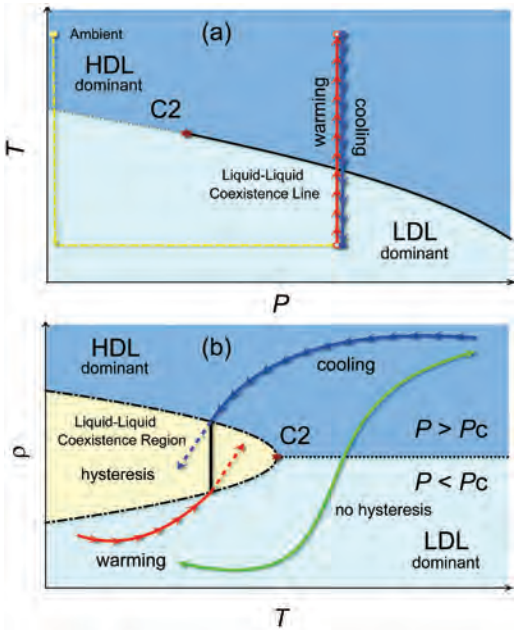

FIGURE 1: The hypothesized (a) *T*-*P* and (b) *ρ*-*T* phase diagrams of water in the presence of a first-order liquid-liquid phase transition. If a first-order HDL-LDL transition exists at high pressures, a hysteresis phenomenon should be observed, as shown by the difference between the red and blue curves in panel (b). At low pressures, when no first-order line is crossed, there should be no hysteresis (green curve).

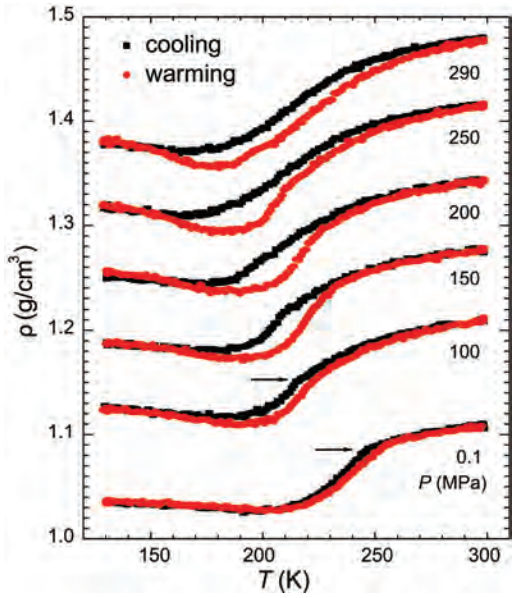

FIGURE 2: The density profiles of confined D_2O in a hydrophilic substrate MCM-41-S are measured in both warming and cooling scans. The data are shifted by 0.05 g/cm^3 between adjacent pressures for clarity. A hysteresis phenomenon becomes prominent above 100 MPa. The two horizontal arrows indicate the locations of the sudden change of slope in the density profiles ("kink") at 0.1 MPa and 100 MPa.

as the pressure is increased. We expect the magnitude of the density difference might depend on the temperature ramping rate. Considering the feasibility of neutron scattering experiments, we chose a ramping rate of 0.2 K/min. With such a slow rate, a rather uniform temperature distribution over the sample is assured, but the system may require much longer times to reach physical equilibrium after crossing a phase boundary.

Note that the accuracy of the absolute density we determined depends on the background subtraction and the scaling. However, the relative shape of the density profiles is independent of the analysis. The observed density hysteresis, although it is not a definitive proof, is consistent with the hypothesis of the coexistence of two liquid phases of confined heavy water with different densities, at pressures larger than 100 MPa. We also observed an unexpected sudden change of slope in the density profiles (a "kink") at the temperatures of the maximum slope at and below 100 MPa. The kink might be related to the previously observed fragile-to-strong dynamic crossover of confined H_2O [6].

Using the SPINS triple-axis instrument, we were able to obtain sensitive measurements of the density of D_2O confined in MCM-41-S. We observed a prominent hysteresis phenomenon in the measured density profiles between warming and cooling scans above 100 MPa. We interpret this observation as support, although not proof, of the proposed presence of a first-order liquid-liquid phase transition of water that would exist in the macroscopic system if crystallization could be avoided in the relevant phase region.

References

[1] O. Mishima and H. Eugene Stanley, Nature **396**, 329 (1998).

[2] P.G. Debenedetti, J. Phys. Condens. Mat. **15**, R1669 (2003).

[3] C. A. Angell, Science **319**, 582 (2008).

[4] Y. Zhang, A. Faraone, W. A. Kamitakahara, K-H. Liu, C-Y. Mou, J.B. Leão, S. Chang, and S-H. Chen, PNAS **108**, 12206 (2011).

[5] L. D. Gelb, K. E. Gubbins, R. Radhakrishnan, and M. Sliwinska-Bartkowiak, Rep. Prog. Phys. **62**, 1573 (1999).

[6] A. Faraone, L. Liu, C-Y. Mou, C-W. Yen, and S-H. Chen, J. Chem. Phys. **121**, 10843 (2004).

Cholesterol transport rates in model membranes

S. Garg[1], A.C. Woodka[2], P.D. Butler[2], U. Perez-Salas[1,3], L. Porcar[4,5]

Cholesterol is an essential structural component of most cell membranes which are composed of phospholipids, sterols, and proteins. Phospholipids are the main component of the membrane, acting as the scaffold in which the other components embed. Cholesterol contributes to the organization, dynamics, and bending modulus of the lipid membrane; helps regulate the membrane interactions with the cytoskeleton; and in some cases controls the functions of membrane proteins crucial for several trans-membrane signaling processes. Healthy cells maintain a large cholesterol gradient with only 0.05 % to 1 % of the cellular cholesterol residing where it is generated in the interior of the cell, while 60 % to 70 % resides in the plasma membrane or cell wall. Thus, proper cholesterol movement within the cell, and indeed throughout the body, is critical. Not only does cholesterol movement play a key role in atherosclerosis and heart disease, the leading causes of death in the US, it has been implicated in dementias (such as Alzheimer's), diabetes, cancer, and several rare but fatal diseases.

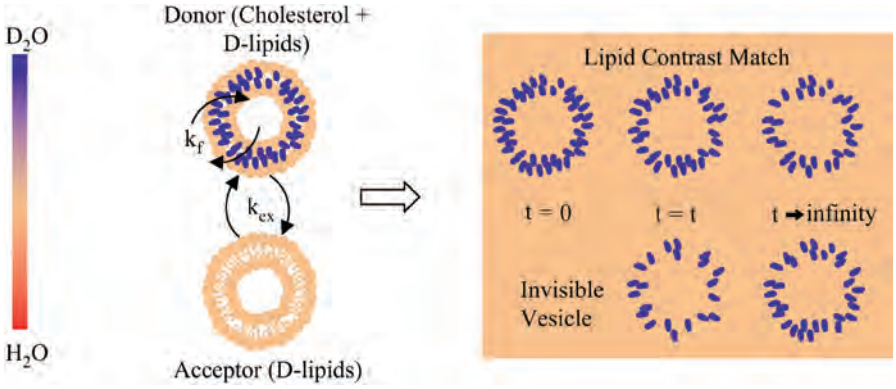

FIGURE 1: Cholesterol-rich (donor) and cholesterol-free (acceptor) vesicles made of dPOPC in a contrast matched solvent.

Despite the essential role of cholesterol transport within the cell, progress has been hampered by confusion associated with the wide variation in transfer rates reported in the literature. In particular, the transfer of cholesterol from one side of the lipid bilayer to the other, known as *flipping*, has reported half-lives that range from several hours to a few milliseconds. A potential source for these discrepancies is that most techniques used to measure these rates require labeling the cholesterol with a fluorescent dye. The assumption is that such chemical labels will not affect the rates being measured. Similarly, additives such as cyclodextrin and cholesterol oxidase are often introduced to measure cholesterol flipping rates assuming that, while they will accelerate the ejection of cholesterol from the outer layer of the bilayer, they will not affect the flipping process from the inner layer to the outer layer. Finally, most of the studies of cholesterol exchange kinetics involve mixing cholesterol donor and acceptor vesicles requiring a periodic isolation step to assay the amount of cholesterol exchanged, introducing additional uncertainties.

In this study [1] we circumvent these potential limitations by using Time-Resolved Small Angle Neutron Scattering (TR-SANS) as an *in situ* probe of the transfer rate of the particular component of interest in the absence of chemical tags or extraneous compounds. In this method, cholesterol enriched donor vesicles and cholesterol free acceptor vesicles are added together and the total scattered neutron intensity of the solution is measured as a function of time to quantitatively track the redistribution of cholesterol between vesicles. Lipid contrast matched solvent is used to render the lipid component invisible to neutrons and to ensure that all the observed scattering originates from the cholesterol alone, as shown schematically in Fig. 1. Under these experimental conditions the overall intensity decreases as cholesterol moves from donor to acceptor vesicles, reaching half the original intensity once fully equilibrated.

The success of this quantitative approach relies on two critical assumptions: that the pure lipid vesicles are invisible and that the integrity of the vesicles is maintained throughout the entire cholesterol transfer process. The data in Fig. 2a demonstrate the validity of these assumptions. Our contrast matched, cholesterol-free vesicles, which are made of deuterated1-palmitoyl-2-oleoyl-sn-glycero-3-phosphocholine (dPOPC) show no scattering above background. From time t = 0 min to t = 600 min the shape of the curves does not change while the intensity decreases by a factor of two, indicating that the vesicles are intact and full equilibrium has been achieved. Figure 2b shows that normalized decay rates increase with temperature.

While the normalized intensity decay data of Fig. 2b and Fig. 3 can be modeled as a single decay process, the fit is not very satisfactory and a two-process model provides a much better description. Two locations of cholesterol are considered: one in the inner layer and the other in the outer layer. Cholesterol in the outer layer is directly available for exchange, while cholesterol in the inner layer can only exchange after flipping to the outer layer, thereby limiting the exchange rate. Modeling the data as the result of two kinetic processes leads to a set of differential equations which can be solved to yield two

[1]Argonne National Laboratory, Argonne, IL 60439
[2]NIST Center for Neutron Research, National Institute of Standards and Technology, Gaithersburg, MD 20899-6102
[3]University of Illinois at Chicago, Chicago, IL 60607
[4]Institut Laue Langevin, Grenoble Cedex 9, France
[5]University of Delaware, Newark, DE 19716

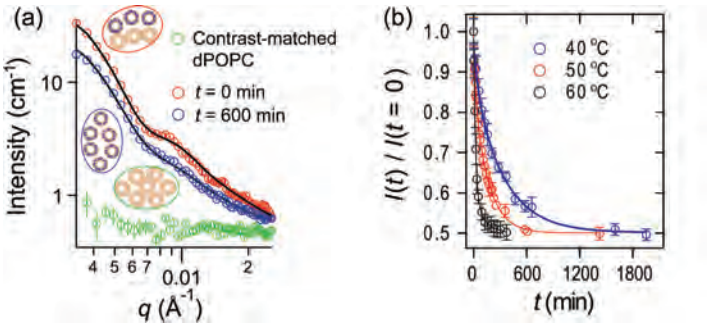

FIGURE 2: (a) Scattering curves for the dPOPC contrast matched sample (green), and a sample with donor (cholesterol + dPOPC) and acceptor (dPOPC) vesicles mixed together at t = 0 (red) and t = 600 min (blue). (b) Decay rates increase with temperature.

effective rate constants, k_f and k_{ex}, for flipping and exchange, respectively.

Applying the above analysis leads to excellent fits of the 50 °C decay curves of Fig. 3 whose fitting parameters are given in Table 1. We estimate the flipping half-life of cholesterol to be 3 h and 20 min (± 13 min) and the exchange half-life to be 1 h and 28 min (± 2 min). Our inter-vesicle exchange half-life is on the slower end of previously reported exchange half-lives which vary from several hours down to tens of minutes. Our half-life for intra-membrane cholesterol flipping is orders of magnitude longer than most recently reported half-lives which range from seconds to milliseconds (though several older studies do report flipping half-lives of a few hours), raising questions regarding the validity of our model.

	k_f (min^{-1})	$T_{1/2\_f}$ (min)	k_{ex} (min^{-1})	$T_{1/2\_ex}$ (min)
cholesterol	0.0035 ± 0.0002	200 ± 13	0.0079 ± 0.0002	88 ± 2
cholesterol-sulfate	0.0038 ± 0.0005	182±25	0.15 ± 0.03	4.6 ± 0.8
DHE	0.03 ± 0.01	22 ± 7	0.033 ± 0.003	21 ± 2
cholesterol with β-cyclodextrin	0.021 ± 0.002	33 ± 3	0.055 ± 0.003	12.5 ± 0.6

Table 1: Intra- and inter-membrane diffusion rates and half-lives for cholesterol transport from the decay curves in Fig. 3.

In order to better test this two-process model, we set out to more clearly decouple flipping and exchange by replacing cholesterol with cholesterol sulfate. The cholesterol-sulfate molecule is structurally very similar to cholesterol but the sulfate group makes the head group far more hydrophilic. Thus the flipping rate, requiring the hydrophilic headgroup to transition through the hydrophobic interior of the membrane, should be inhibited, while the exchange rate, requiring the molecule to transit through the aqueous phase, should be enhanced. The decay curve for pure cholesterol-sulfate (Fig. 3a) clearly shows two distinct decays, validating the use of a two-process model. The break point in the decay curve occurs after 11 min, while it takes nearly 17 h to achieve full equilibrium. From the normalized intensity at the breakpoint we know that exactly 25 % of the cholesterol is transferred from the donor to the acceptor vesicles in the first process. This provides strong support for our model in which the cholesterol in the outer layer of the donor vesicles (50 %) fully equilibrates between vesicle populations long before the 50 % in the inner layer can flip to the outer layer and thus become available to participate in the exchange.

A potential source for the fast flipping rates reported in the literature is the use of fluorescent cholesterol substitutes and additives to extract transport properties. To test this concept we probed two systems commonly used to measure cholesterol transfer rates: cholesterol with cyclodextrin added, and pure DHE. Cyclodextrin increases cholesterol's aqueous solubility and is known to accelerate inter-membrane exchange, while DHE is a self-fluorescent cholesterol analogue with similarities to cholesterol in structure, organization, and dynamics. The assumptions are that cyclodextrin does not affect the inner layer and thus has no effect on cholesterol flipping rates, and that DHE is sufficiently similar to true cholesterol that it has no effect on either inter or intra-membrane transfer rates. Using our existing protocol, we measured cholesterol transfer rates in the presence of cyclodextrin at a concentration of 0.002 mol/L typically used in such studies. We also measured the transfer rates of DHE by substituting it for the cholesterol. The data for pure DHE and for cholesterol with cylcodextrin are compared to pure cholesterol in Fig. 3a.

As expected, the cyclodextrin causes an increase in inter-membrane exchange rates. However, the flipping rates also increase 6 fold. In the DHE system both flipping and exchange rates are much faster than for normal cholesterol by factors of 10 and 4 times, respectively. These results clearly challenge the assumptions underlying the use of cyclodextrin and DHE for accurate measurements of cholesterol transfer kinetics.

The cell membrane is a rich and complex environment and it is easy to see, given this exquisite sensitivity of cholesterol transport to the details of that environment, how organisms might be able to very finely tune the cholesterol balance within their cellular structures. Our results, using non-invasive in situ measurements clearly challenge many of the assumptions made in previous studies and more generally highlight the difficulty in utilizing chemical tags or additives to understand the transport properties and energetics of self-assembled systems. They suggest that cholesterol flipping rates may be much slower than currently believed and shed light on the wide variability in reported values. These results should significantly impact our understanding of cholesterol transport and regulation.

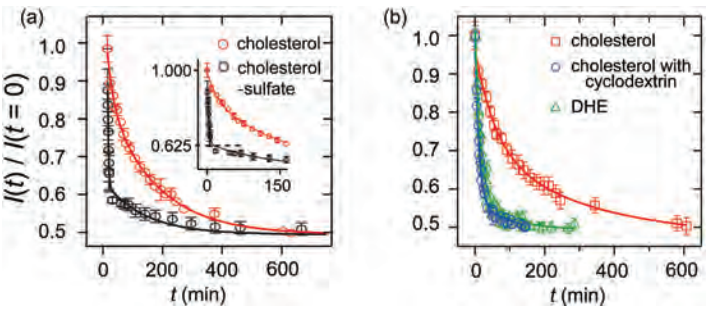

FIGURE 3: Normalized intensity decay curves for cholesterol exchange between dPOPC vesicles at 50 °C; pure cholesterol (red) is shown for reference. (a) pure cholesterol-sulfate (black) (inset expands the view at the breakpoint), and (b) cholesterol with 0.002 mol/L cyclodextrin (blue) and pure DHE (green). Kinetic constants for the fits are compared in Table 1.

References

[1] S. Garg, L. Porcar, A.C. Woodka, P.D. Butler, and U. Perez-Salas, Biophys. J. **101**, 370 (2011).

The first mixed-metal amidoborane: sodium magnesium amidoborane, a good hydrogen storage candidate

H. Wu[1,2], W. Zhou[1,2], Q. Yao[4], S. Gadipelli[1,3], T. J. Udovic[1], T. Yildirim[1], J. J. Rush[1], F. E. Pinkerton[5] and M. S. Meyer[5]

Suitable hydrogen storage materials with high hydrogen contents and superior properties are essential for the development of a hydrogen-based energy economy. Metal amidoboranes $M(NH_2BH_3)_x$ (or MAB) with the rarely seen $NH_2BH_3^-$ anion group [1,2,3] show properties superior to ammonia borane (NH_3BH_3, AB) in terms of reduced dehydrogenation temperatures, accelerated H_2 release kinetics, and minimized borazine ($(BH)_3(NH)_3$) release. However, the purity of hydrogen released has been found to suffer from the simultaneous formation of ammonia for almost all MAB compounds. Moreover, due to the limited number of metal amidoboranes reported to date, the optimization of this class of compounds is far from complete, and information on the nature of $NH_2BH_3^-$ and related ligands is thus far inadequate. Therefore, it is of great interest to discover and develop new $MM'(NH_2BH_3)_x$ containing cheap, abundant, light-weight metals. Introducing multiple metal species with various sizes, charges, electronegativities, and coordination preferences could increase the array of possible bonding interactions with the $NH_2BH_3^-$ group, ultimately allowing one to tailor more favorable materials properties compared to monometallic amidoboranes.

In our recent study [4], we report the synthesis, crystal structure, and dehydrogenation properties of the first example of a mixed-metal amidoborane, $Na_2Mg(NH_2BH_3)_4$. Unlike the monometallic amidoboranes, where the cation interacts with both N^- and BH_3 units, in $Na_2Mg(NH_2BH_3)_4$, each cation coordinates solely with one type of the end unit in the $NH_2BH_3^-$ group. Such a structure with distinct cation-anion bonding environment ordering is found to have a great impact on the dehydrogenation properties. As a result, $Na_2Mg(NH_2BH_3)_4$ can release 8.4 % mass fraction pure hydrogen starting at 65 °C with little contamination from toxic gases such as borazine, ammonia, or diborane.

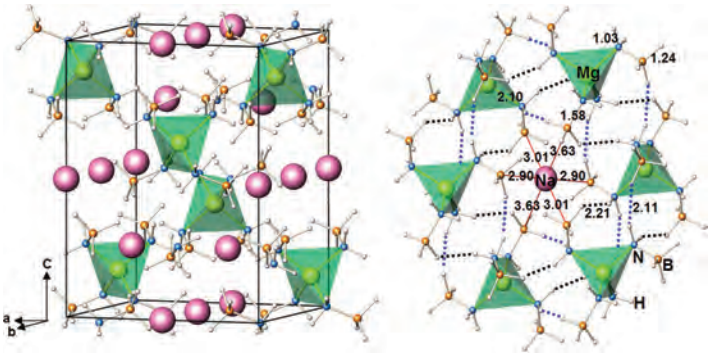

FIGURE 1: Crystal structure and bonding environments of $Na_2Mg(NH_2BH_3)_4$. Each Mg^{2+} is tetrahedrally bonded to N^- of four $NH_2BH_3^-$ groups, forming a $Mg(NH_2BH_3)_4$ tetrahedron, and each Na^+ is octahedrally coordinated to BH_3 unit of six $NH_2BH_3^-$ groups. Na, pink; Mg, yellow; N, blue; B, orange; H, white. $BH^{\delta-\cdots\delta+}HN$ interactions are indicated in dotted lines. Distances are measured in angstroms.

Figure 1 illustrates the structure of $Na_2Mg(NH_2BH_3)_4$. The divalent Mg^{2+} connects exclusively with four $NH_2BH_3^-$ units, forming a $Mg[NH_2BH_3]_4$ tetrahedron. The monovalent Na^+ octahedrally coordinates only with six BH_3 units with the Na-B separations in the range of 2.900 Å to 3.634 Å, resulting in a distorted octahedral environment. As a result, Na^+ and Mg^{2+} are linked through interactions with two different end units of the bridging $NH_2BH_3^-$ groups. Another manifest distinction compared to the monometallic amidoboranes is that the shortest $BH^{\delta-\cdots\delta+}HN$ distance between the neighboring $NH_2BH_3^-$'s in $Na_2Mg(NH_2BH_3)_4$ is 2.107 Å, slightly longer than that in AB (2.02 Å), but much shorter than those observed in the monometallic amidoboranes. Therefore, the $NH_2BH_3^-$ units establish a strong intermolecular dihydrogen bonding network, which together with the cation-anion interactions, is responsible for the stabilization of the structure of $Na_2Mg(NH_2BH_3)_4$.

The structure and the bonding environments of $Na_2Mg(NH_2BH_3)_4$ are further investigated by neutron vibrational (NV) spectroscopy (Fig. 2). The first-principles calculated spectrum is also shown to facilitate the interpretation of the observed spectrum. Most of the observed phonon bands can be assigned to the modes of

[1]NIST Center for Neutron Research, National Institute of Standards and Technology, Gaithersburg, MD 20899-6102
[2]University of Maryland, College Park, MD 20742-2115
[3]University of Pennsylvania, Philadelphia, PA 19104-6272
[4]Guilin Electronic University, Guilin, China
[5]General Motors Research and Development Center, Warren, MI 48090-9055

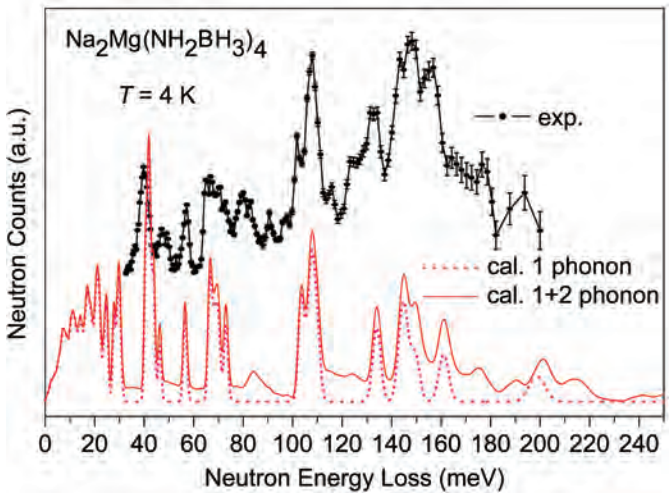

FIGURE 2: Observed and calculated neutron vibrational spectra of $Na_2Mg(NH_2BH_3)_4$.

B-H, N-H, and B-N in the $NH_2BH_3^-$ groups. In particular, two vibrational modes are observed at 49 meV and 59 meV, which correspond to the Mg-N stretching modes and the deformation modes of the $Mg[NH_2BH_3]_4$ tetrahedra, indicating strong and directional Mg-N ionic bonding. In general, the calculated spectra agree well with the observed NV spectra, and thus further support the validity of our determined structure.

Figures 3 show the thermal decomposition of $Na_2Mg(NH_2BH_3)_4$ obtained using volumetric temperature programmed desorption (TPD) analysis and independent thermogravimetry with mass spectroscopy (TGA-MS). $Na_2Mg(NH_2BH_3)_4$ started to release hydrogen as low as 65 ºC for a total of 8.4 % mass fraction hydrogen released below 200 ºC with a residual product of $Na_2Mg(NBH)_4$. The observed ammonia amounts to < 1 % mole fraction of

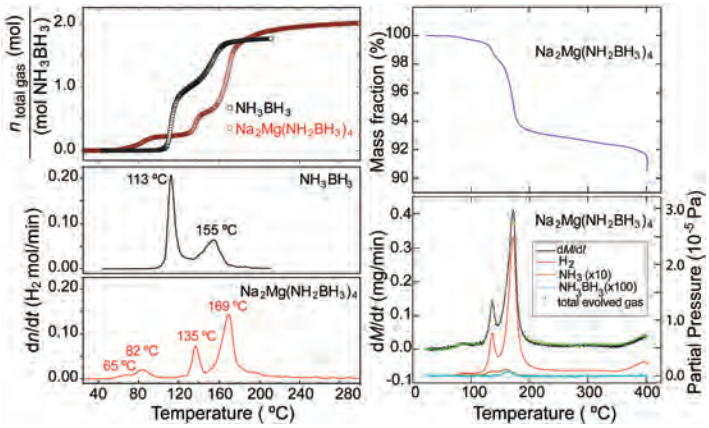

FIGURE 3: (Left) TPD results of hydrogen release from $Na_2Mg(NH_2BH_3)_4$ with 2 °C/min heating rate to 300 °C. The amount of H_2 gas released (top panel) has been normalized as *n* (H_2 gas)/ mol NH_3BH_3. The hydrogen release rates are shown in the lower panels. (Right) TGA weight loss (upper panel) and the accompanying MS partial pressures (lower panel) measured at 1.7 °C/min to 400 °C. The rate of mass loss d*M*/d*t* (black curve) is also shown. Note that the NH_3 signal has been multiplied by a factor of 10 and the $(NH)_3(BH)_3$ signal has been multiplied by 100 to be visible on the same scale as H_2. The green crosses are the total mass contribution H_2+ NH_3 + borazine to the evolved gas, scaled to compare with d*M*/d*t*.

the evolved gas, and the trace of borazine in the leading edge of the third peak totals ≈ 200 µg/g. The ammonia is significantly suppressed compared to the monometallic amidoboranes, *e.g.*, ≈ 15.4 % mole fraction NH_3 was observed in $NaNH_2BH_3$. The ammonia detected (as well as the trace borazine) may also be from a small amount of unreacted AB left during the synthesis, as suggested recently.

Compared to almost all monometallic amidoboranes, $Na_2Mg(NH_2BH_3)_4$ shows significantly reduced ammonia release. The minimization of NH_3 in $Na_2Mg(NH_2BH_3)_4$ is likely related to its unique structural motif and the ionic character of the cations, which favors the release of H_2. According to the previous proposed dehydrogenation mechanism of MAB, an intermediate M-H cluster would form involving the M-N bond and B-H bond breaking [5]. Such an intermediate M-H cluster is believed to play a catalytic role in the hydrogen release process. In $Na_2Mg(NH_2BH_3)_4$, Na^+ cations do not bond to N^- but only to BH_3 units. Therefore, the intermediate catalytic NaH can form without any M-N bond breaking. In addition, the calculation predicted that of all alkali and alkaline earth metal amidoboranes, $NaNH_2BH_3$ shows the most accelerated hydrogen release rate [5]. It also suggested that magnesium amidoborane would release hydrogen via a "direct" pathway instead of by an N-B chain oligomerization pathway. The latter was found in the MAB systems with significant NH_3 detected. Therefore, the co-existing Na^+ and Mg^{2+} cations accentuate the H_2 release, which will surpass the formation and release rate of NH_3. As a result, the gas released from $Na_2Mg(NH_2BH_3)_4$ is predominantly H_2.

In summary, the first example of mixed metal amidoborane, $Na_2Mg(NH_2BH_3)_4$, was successfully synthesized and crystal structure determined. $Na_2Mg(NH_2BH_3)_4$ releases a 8.4 % mass fraction pure hydrogen with minimal toxic gases contamination. Our study demonstrates that hydrogen release properties of amidoboranes can be rationally and significantly improved by tuning the atomic interactions through the formation of mixed-metal amidoboranes.

References

[1] Z. Xiong, C.K. Yong, G. Wu, P. Chen, W. Shaw, A. Karkamkar, T. Autrey, M.O. Jones, S.R. Johnson, P.P. Edwards, W.I.F. David, Nature Mater. **7**, 138 (2008).

[2] H. Wu, W. Zhou, T. Yildirim, J. Am. Chem. Soc. **130**, 14834 (2008).

[3] H.V.K. Diyabalanage, T. Nakagawa, R.P. Shrestha, B.L. Davis, A.K. Burrell, W.I.F. David, M.O. Jones, P.P. Edwards, J. Am. Chem. Soc. **132**, 11836 (2010).

[4] H. Wu, W. Zhou, F.E. Pinkerton, M.S. Meyer, Q. Yao, S. Gadipelli, T.J. Udovic, T. Yildirim, J.J. Rush, Chem. Comm. **47**, 4102 (2011).

[5] D.Y. Kim, H.M. Lee, J. Seo, S.K. Shin, K.S. Kim, Phys. Chem. Chem. Phys. **12**, 5446 (2010).

Nature of CO_2 adsorption in Mg-MOF 74: A combined neutron diffraction and first-principles study

W.L. Queen[1], C.M. Brown[1], M.R. Hudson[1,2], D.K. Britt[3], W. Zhou[1,2], T. Yildirim[1,4] and O.M. Yaghi[3]

One of the most pressing issues facing the energy sector is the mitigation of CO_2, a greenhouse gas implicated in global warming, through post-combustion capture applications. While methods exist to separate CO_2 from the other components of a post-combustion stream, primarily scrubbing with liquid amine solutions, their implementation on an industrial scale has not been possible due to the massive energy requirements of such processes [1]. Efficient methods for effecting such a separation are urgently sought. Here we highlight our work on Mg-MOF 74, a candidate CO_2 separation compound.

Metal-organic frameworks (MOFs) are a versatile class of compounds with a very large number of building block combinations. Their high internal surface areas coupled with chemical tunability make them particularly attractive for the selective capture of CO_2. Recent work has shown that the incorporation of coordinatively unsaturated metal centers (UMCs) into the frameworks provide enhanced binding energy and an increase in surface packing density of adsorbates, due to the highly reactive, electron deficient nature of the sites [2]. While adsorption capacity is important, high selectivity and facile regeneration are pertinent properties for post-combustion capture. MOFs containing UMCs provide interactions that are strong enough to achieve CO_2 adsorption close to room temperature and slightly above; however, these interactions are weak relative to the formation of chemical bonds, also allowing facile CO_2 release during regeneration processes. Furthermore, MOFs can be tuned to alter selectivity, a property which has been attributed to a number of phenomena including exclusion due to the size/shape of the pores, adsorbent/adsorbate surface interactions, and varying diffusion rates between different components in a gas mixture.

Mg-MOF 74, a candidate for selective adsorption of CO_2, has unsaturated 5-coordinate Mg-ions (upon solvent removal) decorating the inside of 1-dimensional hexagonal channels, as shown schematically in Fig. 1. This material was recently found to exhibit an exceptionally high CO_2 uptake at low pressure (< 0.1 bar) and room temperature, and easy, reversible adsorption/desorption of CO_2 [3-4]. In order to obtain a better understanding of how structure dictates function during adsorption/desorption processes we have performed detailed neutron powder diffraction (NPD) experiments using the high resolution diffractometer, BT1, while systematically increasing temperature and amount of adsorbed gas. In addition, first principle calculations based on density functional theory (DFT) were performed to provide more insight into site specific binding properties of the adsorbate [5-6].

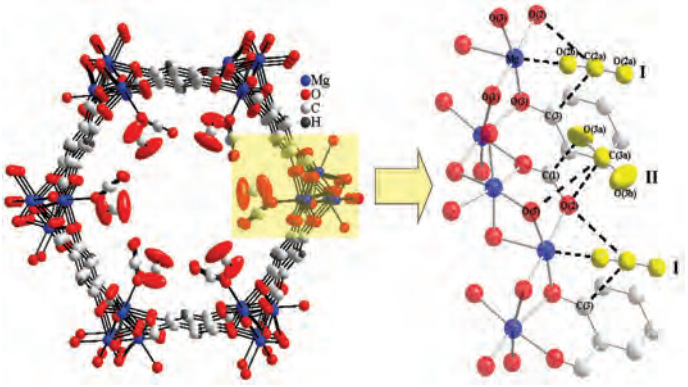

FIGURE 1: Ball and stick model derived from neutron diffraction of Mg-MOF-74 loaded with 1.75 CO_2 per Mg viewed along the crystallographic c axis. The highlighted region reveals nearest neighbor interactions (drawn as dashed black lines) found between the CO_2 sites I and II (shown in yellow) and the framework. Oxygen atoms of the second CO_2 site were refined anisotropically to illustrate the disorder found in the nuclear scattering density. The ellipsoids are drawn at 50% probability.

NPD data (20 K) obtained from loading, ≈ 0.25 CO_2 per Mg, reveals that CO_2 only populates a single site, I, located at the UMC. The Mg-CO_2 interaction exhibits "end on" coordination, Fig. 1, with a highly angular Mg-O(2b)-C(2a) orientation, 125(7)°, which can be rationalized based on two short (≈ 3.1 Å) lateral interactions between the electron deficient C(2a) of the CO_2 molecule, and the framework atoms, O(2) and C(3). The relatively short Mg-O(2b) distance, 2.39(6) Å, is consistent with the reported high initial isosteric heat of adsorption, ≈ −39 kJ/mol. The next closest CO_2/framework distance, approximately 2.9 Å, is found between O(2b) and the O(2) atom, which is equatorially coordinated to the Mg-ion. This distance, only slightly shorter than the sum of the van der Waals radii for two O atoms (3.04 Å) is likely to be a limiting factor in the approach of the CO_2 molecule to the framework surface as electrostatic repulsion would begin to destabilize the CO_2 adsorption.

[1]NIST Center for Neutron Research, National Institute of Standards and Technology, Gaithersburg, MD 20899
[2]University of Maryland, College Park, MD 20742
[3]University of California, Los Angeles, Los Angeles, CA 90095
[4]University of Pennsylvania, Philadelphia, PA 19104

As the loading level is increased, the fitting refinements of the diffraction data progress in a systematic fashion, until 1.0 CO_2:Mg where the first sign of population of the second site, II, occurs. Increasing the loading to 1.75 CO_2 per Mg leads to an even greater increase in site II occupancy, 0.86(2), and large displacement parameters for the oxygen associated with this additional molecule that are likely indicative of slight differences in molecular orientation within the channel rather than thermal motion in the molecules at 20 K. Furthermore, weak van der Waals interaction between the site II CO_2 and framework, as determined by long CO_2/framework distances, could lead to a lack in orientation preference upon adsorption. The CO_2 orientation in site II is not parallel to that in site I, and instead is found canted. Although the exact intermolecular distances are susceptible to some uncertainties in site II O(3a,b), there appear to be strong interactions along the pore-channel direction, leading to an average intermolecular distance of approximately 3 Å. This distance, similar to those observed between site II and the framework walls, indicates similarities in interaction strength.

Several studies indicate that CO_2 coordination at the UMC in MOF-74 derivatives leads to a significant deviation of the CO_2 bond angle from its normally linear geometry, an unusual event for reversible physisorption. There are several phenomena that could contribute to such a behavior including: (1) an actual bending due to direct charge transfer between the UMC and site I CO_2, (2) static disorder in the positions of C(2a) and O(2a), a direct result of weak interactions between these atoms and framework walls, and (3) phonon induced dynamic disorder resulting from an asymmetric wagging motion. Bond angles derived from DFT calculations indicate bond bending of 175.0° and 178.6° for LDA (local density approximation) and GGA (generalized gradient approximation) respectively. The lack of agreement between the calculated angles and those determined by NPD experiments, ≈ 150° to 170° for loadings ranging from 0.25 to 1.75 CO_2 per Mg, may imply that the structural model is biased by the presence of either static or dynamic disorder. Furthermore, calculations of the vibrational/rotational mode energies show that the lowest energy modes occurring at ≈ 4.3 meV for Mg-MOF-74 would likely not be easily populated at the measurement temperature of 20 K. The calculated potential energy curves for free CO_2 and CO_2 adsorbed on open Mg, are shown in Fig. 2. In order to account for the large bond bending (≈ 150 °) observed in the fitting of the diffraction data, there would be a significant energy penalty or much larger charge transfer than expected. Therefore, the observed bond bending is likely to be a contribution of both slight polarization of the CO_2 resulting from strong Mg-CO_2 interaction as well as static disorder of the adsorbed gas molecule.

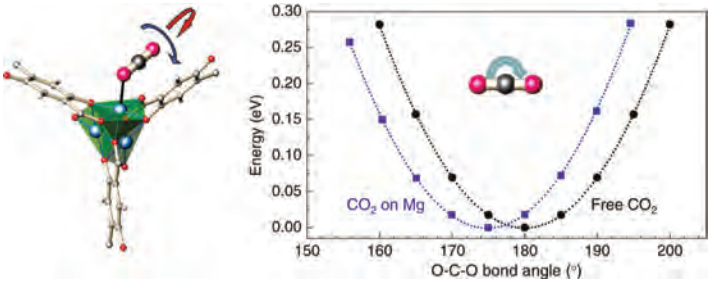

FIGURE 2: Left: two lowest energy vibrational/rotational modes at energies 4.3 meV and 8.5 meV for the red and blue arrows respectively, of CO_2 in Mg-MOF-74, indicating that one oxygen strongly bonds to the metal center while the rest of the CO_2 molecule has more rotational freedom, albeit somewhat limited by the association with the Mg bound O atom. Right: the calculated DFT-LDA Potential energy curve of the O-C-O Bond-bending for a free CO_2 molecule and the CO_2 adsorbed on an open Mg site, indicating very small bond bending.

After collecting 20 K NPD data on the sample loaded with 0.5 and 1.75 CO_2 per Mg, the temperature was increased to 300 K and data were collected again. The 0.5 loading showed no significant change in the site I CO_2 occupancy upon heating, while for the 1.75 loading, site II was completely desorbed and site I maintained a relatively high CO_2 occupancy of 0.94(3). These results confirm that the high initial isosteric heat of adsorption for Mg-MOF 74 is directly related to the UMC. A significant lengthening of the Mg-O(2b) bond occurs at 300 K (2.48(5) Å and 2.58(5) Å for 0.5 and 1.75 loadings, respectively). Unit cell parameters of the bare and loaded phases reveal a slight contraction in the *a*/*b* axes and simultaneous expansion of *c* axis with higher CO_2 loading. These shifts lead to no significant change in the unit cell volume for room temperature CO_2 adsorption (bare, 0.5, and 1.5 loadings at 300 K are 3993.5(5) $Å^3$, 3992.3(5) $Å^3$, and 3992.0(5) $Å^3$ respectively). In fact the volume is constant from the bare to loaded phase within ≈ 0.06 % error (± 1.5 $Å^3$), a property that might be of particular interest for the future implementation of adsorbent materials in separation/storage applications.

Neutron diffraction data support the view that the UMC is responsible for high initial isosteric heat of adsorption in Mg-MOF-74. We have observed the first evidence of a second CO_2 adsorption site that is populated only at low temperatures, and only after the first absorption site is fully occupied. First principles calculations reveal that the bond bending observed in the Mg bound CO_2 is largely due to static disorder, a direct result of rotational freedom in the two CO_2 molecules that have a weak association with the framework surface. Calculations show that the actual deviation of the CO_2 bond angle from its normal linear geometry is likely very small, indicating that the CO_2 interaction at the UMC is still largely physisorptive in nature. Systematic studies of this kind will inform the design of future materials for CO_2 capture.

References

[1] A.L. Kohl, R.B. Nielsen, *Gas Purification*; 5th ed.; Gulf Publishing Company: Houston, 1997.

[2] Y. Liu, H. Kabbour, C.M. Brown, D.A. Neumann, C.C. Ahn,. Langmuir, **24**, 4772 (2008).

[3] S.R. Caskey, A.G.Wong-Foy, A.J. Matzger, J. Am. Chem. Soc. **130**, 10870 (2008).

[4] Z.R. Herm, J.A. Swisher, B. Smit, R. Krishna, J.R. Long, J. Am. Chem. Soc., **133**, 5664 (2011).

[5] W.L. Queen, C.M. Brown, D.K. Britt, P. Zajdel, M.R. Hudson, O.M. Yaghi, Submitted, 2011.

[6] H. Wu, J.M. Simmons, S. Gadipelli, W. Zhou, T. Yildirim, Phys. Chem. Lett., **1**, 1946 (2010).

Neutron scattering techniques shed new light on gel formation

A.P.R. Eberle[1,2], N.J. Wagner[2] and R. Castañeda-Priego[2,3]

Colloidal dispersions are used in many household products ranging from paints to shaving cream to gelatin and even to foods such as salad dressings or mayonnaise. The stability and processing of these and similar products highly depend on the state of the material. Of particular interest is the phase transition from fluid to a solid, called a gel at low particle volume fractions, $\phi < \approx 0.40$, and a glass at higher volume fractions. While the phase behavior for such systems has been studied for decades, the boundary separating a fluid from a gel is still debated.

In this work we study gelation using a model nanoparticle system with thermoreversible interactions. The system consists of nanometer spheres of silica dioxide (≈ 30 nm) coated with a short carbon chain (C_{14}), and suspended in tetradecane. At high temperatures $T > \approx 32$ °C the particles are stable and the system behaves like a simple hard sphere fluid. Upon quenching the system, particles aggregate in connection with a phase transition of the molecular brush [1]. This in-turn causes a short-range attraction between particles, and if the particle volume fraction is sufficient, $\phi \geq 0.05$, the system will form a stress-supporting gel. We define gelation and determine the gel temperature (T_{gel}) to within ± 0.1 °C using a combination of rheological experiments and an experimental study of the dynamics using fiber-optic quasi-elastic light scattering (FOQELS). Finally, we study the structure of the dispersion at and around the gel transition using small-angle neutron scattering (SANS).

Small-amplitude oscillatory shear (SAOS) rheological measurements are used to identify the transition from the fluid state to the gel state employing a well-defined criterion established for cross linking polymer resins [2]. The SAOS results for a temperature ramp experiment for one dispersion, $\phi = 0.12$, can be seen in Fig. 1. At high temperatures ($T > \approx 31$ °C), in the fluid state, the suspension exhibits a negligible storage modulus G', which defines the amount of elastic energy the fluid can store.

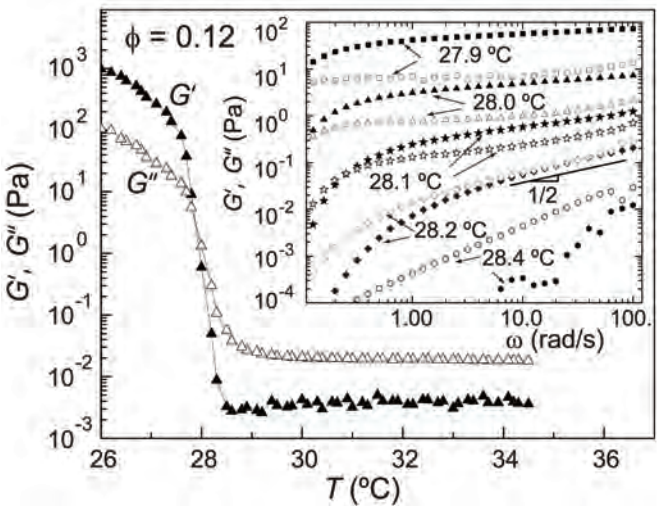

FIGURE 1: Storage, G′ (closed symbols), and loss, G″ (open symbols), moduli vs. temperature in a small-amplitude oscillatory (stress amplitude, σ_0 = 17.68 mPa, frequency, $\omega = 2\pi$ rad/s) temperature ramp experiment (ramp rate 0.2 °C/min). Inset: G′ and G″ from frequency sweep measurements at temperatures around the gel-point. Data are offset vertically for clarity by factors 0.03, 0.05, 0.08, and 0.2 for temperatures (28.4, 28.2, 28.1, and 28) °C, respectively.

As the system is quenched to lower temperatures from the fluid state, the elastic modulus increases over five orders of magnitude in the narrow temperature range of 29 °C to 27 °C. This shows the suspension undergoes a transition to a strong viscoelastic solid similar to cooled Jello. Frequency sweep measurements provide a determination of the strength of the gel. Frequency sweep experiments on the same sample can be seen in the inset to Fig. 1 as a function of temperature near the gel point. At the highest temperature shown, 28.4 °C, G″ (the loss modulus) is larger than G′ over the whole frequency range tested. As the temperature is decreased to 28.2 °C, G′ and G″ become comparable at high frequencies. At lower temperatures the sample has a greater elastic modulus, characteristic of solid-like behavior. At 28.2 °C, G′ and G″ are nearly equal with power law slopes of ½, over more than a decade of frequency, which is a characteristic feature of gelation [2]. The gel temperature is confirmed using FOQELS (not shown) which provides a measure of the particles' dynamics. From FOQELS measurements it can be shown that the dynamics decrease and exhibit an entire relaxation spectrum at the gel temperature determined from rheology.

[1]NIST Center for Neutron Research, National Institute of Standards and Technology, Gaithersburg, MD 20899
[2]University of Delaware, Newark, DE 19716, USA
[3]Universidad de Guanajuato, 37150 León, Mexico

SANS measurements were performed over a range of temperatures spanning the transition from the fluid-state through gelation. The low-Q scattering intensity systematically evolves for decreasing temperature in the range where aggregation occurs until T_{gel}, where structure on the length scales accessible by SANS becomes arrested. Figure 2 shows the SANS spectra at T_{gel}, as identified from rheology, for the entire concentration range.

The spectra at the gel point evolve from fractal-like scattering at low ϕ to a glass-like spectra at high ϕ. The scattering intensity is fitted (solid lines), using well established theories assuming a square-well interaction potential for the particles. From the fits we extract the strength of attraction defined by a reduced temperature, $\tau = (\varepsilon/12)\exp(-U/k_BT)$, called the Baxter temperature, where U is the square-well depth, ε is a perturbation parameter $\varepsilon = \Delta/(a+\Delta)$, where Δ is the square-well width and a is the particle diameter, and k_BT is the thermal energy. As τ decreases, the strength of attraction increases.

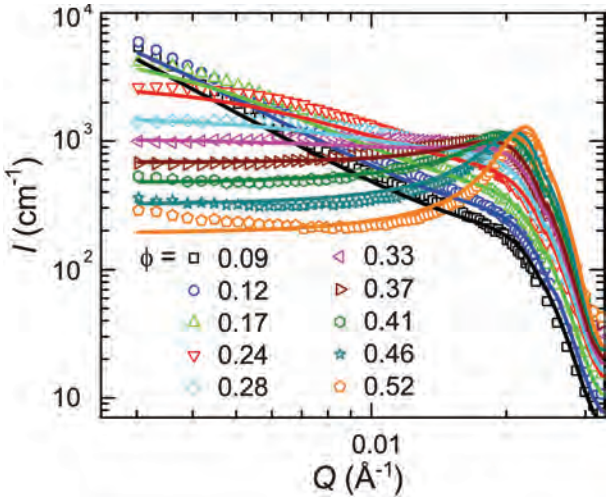

FIGURE 2: SANS measurements at the gel point for various volume fractions ϕ and the corresponding model fits.

The state diagram with our experimentally determined gel transition for the AHS system is presented in Fig. 3. At intermediate to low ϕ and high attractive strength there is a liquid/vapor coexistence region. Conversely, at high ϕ and low attractive strength there is a liquid/crystal coexistence region.

This is in addition to a repulsive driven glass (RDG) line which intersects the attractive driven glass (ADG) line with mode coupling theory (MCT) singularity, A_3. As is typically done, the location of the RDG and ADG lines calculated from MCT are shifted to higher particle densities using known experimental data, since MCT under-predicts the RDG line [6,7]. The percolation line for the AHS fluid can be seen extending from the liquid/vapor coexistence region at low ϕ to the liquid/crystal coexistence region at high ϕ. The experimentally determined points defining the gel transition (triangles) agree well with percolation

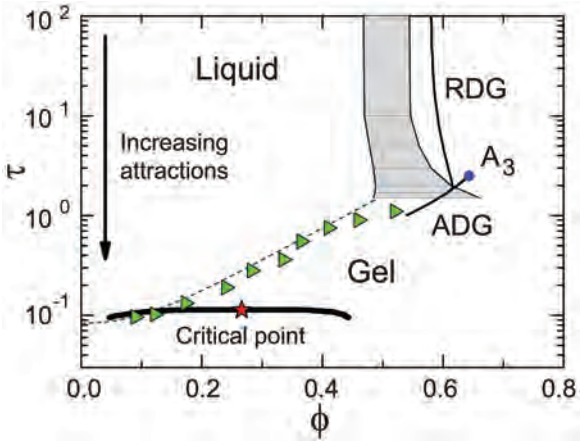

FIGURE 3: State diagram for the model adhesive hard sphere system (AHS). (—) Is the liquid/vapor coexistence region with critical point (star, τ = 0.1133 and ϕ = 0.266) as determined by Monte Carlo (MC) simulations [3]; broken line is the analytical solution to the percolation line [4]; grey shaded region is the liquid/crystal coexistence region from the modified weighted-density approximation (MWDA) theory [5]; (—) repulsive and attractive driven glass (RDG and ADG) lines from model coupling theory (MCT) with point singularity, A_3 (circle) [6]. The triangles are the experimentally determined dynamical arrest transition.

theory up to $\phi \approx 0.41$. For concentrations $\phi > \approx 0.41$ the boundary for dynamical arrest tends toward and joins the ADG line. Thus, the major conclusions of this work show that for this AHS nanoparticle system: *The dynamical arrest transition extends from the dilute particle concentration side of the liquid/vapor coexistence above the critical point following predictions of percolation theory until at sufficiently high particle concentrations it subtends the predictions and joins the MCT ADG line.*

We experimentally determine the fluid-to-gel transition of a model nanoparticle dispersion with short-ranged attractions. Our experiments demonstrate a continuous boundary that extends from the gas-liquid phase separation region at low concentrations to the attractive driven glass line at high concentrations. The conclusions presented herein have implications in a wide range of colloidal systems that interact via a short range interaction. The anticipation is that this work will direct the development of advanced theory and simulation efforts. These will in turn help us to further understand the underlying mechanisms that drive gelation and ultimately allow for the optimization of products through predictive tools rather than guess and check formulation.

References

[1] A.P.R. Eberle *et al.*, Langmuir **26**, 3003 (2010).

[2] H.H. Winter, and F. Chambon, J. Rheol. **30**, 367 (1986).

[3] M.A. Miller, and D. Frenkel, Phys. Rev. Lett. **90**, 135702 (2003).

[4] Y.C. Chiew, and E.D. Glandt, J. Phys. A-Math Gen. **16**, 2599 (1983).

[5] D.W. Marr, and A.P. Gast, J. Chem. Phys. **99**, 2024 (1993).

[6] J. Bergenholtz, and M. Fuchs, Phys. Rev. E **59**, 5706 (1999).

[7] P.N. Pusey, and W. van Megen, Phys. Rev. Lett. **59**, 2083 (1987).

Interlayer distance dependence of thickness fluctuations in a swollen lamellar phase

M. Nagao[1,2], S. Chawang[3], T. Hawa[3]

Surfactants are one of the basic building blocks of nanoscale self-assembling structures, such as micelles, microemulsions, and biological membranes. In particular, surfactant membranes play important roles from household (*e.g.*, detergents) and pharmaceutical (*e.g.*, drugs) products to biological (*e.g.*, drug delivery and virus infections) and industrial (*e.g.*, oil recovery plants) applications. Understanding the behaviors of surfactant membranes and their properties is thus of both fundamental and industrial relevance. One of the unique features of the membranes is collective dynamics of surfactant molecules near room temperature. Membrane bending motion has been established both theoretically and experimentally, while membrane thickness fluctuations remain the subject of research. The thickness scale of surfactant membranes in solution is on the order of nanometers, and thus the neutron spin echo (NSE) technique is well suited to probe the dynamics [1,2]. A previous investigation of the dynamics [2] showed that the thickness fluctuations were clearly seen by NSE in the nonionic surfactant pentaethylene glycol dodecyl ether ($C_{12}E_5$) mixed with deuterated water (D_2O) and deuterated octane (C_8D_{18}). In the study highlighted here, we examined the same system while changing the effective membrane thickness, d_m, as controlled by the ratio of the volume fractions of oil, ϕ_o, to surfactant, ϕ_s, defined as $R = \phi_o/\phi_s$. In addition to the NSE measurement, we have employed molecular dynamics (MD) simulations to calculate the dynamics since the time scale covered by NSE matches that covered by MD. The combined use of these techniques provides further insight into the dynamics of membranes.

Figure 1(a) shows the small-angle neutron scattering (SANS) profiles at $T = (59.6 \pm 0.2)$ °C for $R = 0.0$ and at $T = (31.6 \pm 0.1)$ °C for $0.3 \le R \le 2.0$. In the low-q region, a broad scattering peak originating from the Bragg reflection of the membrane stacking is observed at the same q (≈ 0.08 nm^{-1}) for R =1.5 and $R = 2.0$ as shown by a vertical straight line in the figure. Although the peak position of the lamellae is not clear for samples for $R \le 1.2$, it is considered

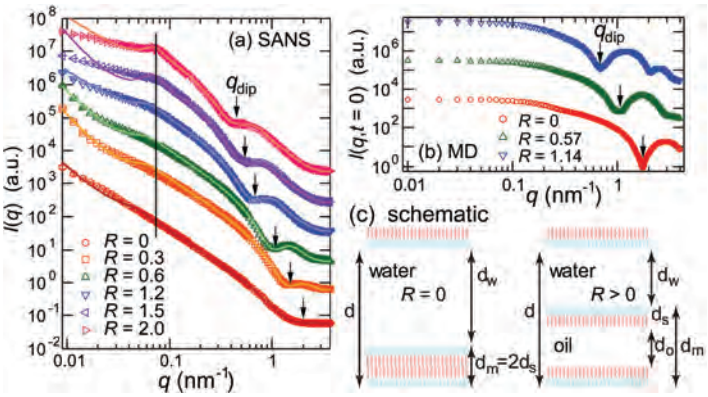

FIGURE 1: (a) SANS profiles show that the interlamellar mean repeat distance d is constant (vertical line) while the dip position q_{dip}, which relates to the membrane thicknesses d_m, is changing with R. (b) MD calculation of the SANS equivalent $I(q,t = 0)$, shows a similar dependence of q_{dip} on R. (c) Schematic illustrating constant d while d_m increases with R, as confirmed by SANS and MD.

to be almost independent of R. On the other hand, in the high-q region, another peak profile originating from the form factor of the membranes is observed. With increasing R, the characteristic q value, q_{dip}, shifts toward lower q. Utilizing a model scattering function for isotropic lamellar structures, membrane thickness, d_m, which follows the ideal swelling law, is estimated from $d_m = 3.1$ nm at $R = 0.0$ to $d_m = 9.2$ nm at $R = 2.0$. A constant inter-lamellar distance d with changing d_m is confirmed from the SANS profiles, schematically shown in Fig. 1(c) [3].

The structure was also confirmed using course-grained (CG) MD simulations [3] by calculating the intermediate scattering function, $I(q,t)=\frac{1}{N}\sum_{i=1}^{N}\sum_{j=1}^{N}\left\langle \exp\left[i\vec{q}\cdot\left\{\vec{r}_i(t)-\vec{r}_j(0)\right\}\right]\right\rangle$, where $\vec{r}_i$ is a position vector for particle i, t is a time, N is the number of surfactant molecules, and $\langle\ \rangle$ represents an ensemble average. The simulations were performed with an integration time step of 25 fs and were run for 200 ns at 30 °C (1 bar) to equilibrate the system, and for 50 ns to calculate $I(q,t)$. Figure 1(b) shows $I(q,t = 0)$ calculated after the MD simulation, corresponding to the respective SANS profile. The behavior of q_{dip} with R, similar to the SANS result, confirms that the MD calculation reconstructs a similar structure in the computational space.

Figure 2(a) shows $I(q,t)$ normalized by $I(q,0)$ observed by NSE at R = 0.3 and $T = 30$ °C [3]. $I(q,t)/I(q,0)$ follows a

[1]NIST Center for Neutron Research, National Institute of Standards and Technology, Gaithersburg, MD 20899
[2]Indiana University, Bloomington, IN 47408
[3]The University of Oklahoma. Norman, OK 73019

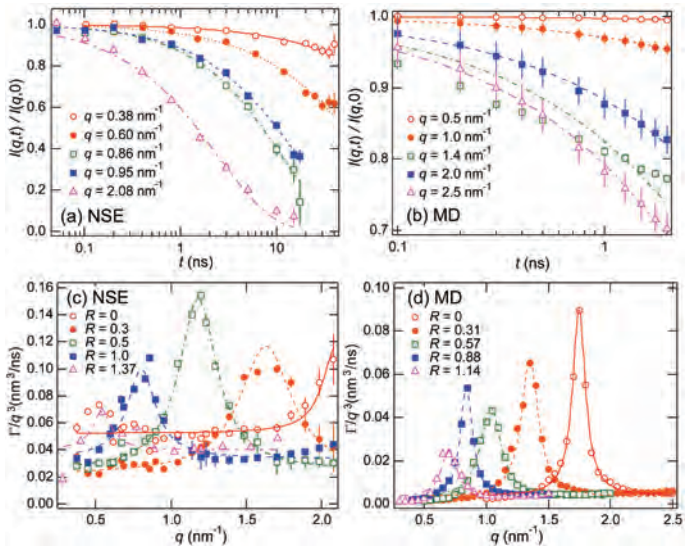

FIGURE 2: $I(q,t)/I(q,0)$ measured by (a) NSE and (b) calculated by MD show good agreement in membrane dynamics. Both results by (c) NSE and (d) MD show that the decay rate Γ is no longer growing with q^3, which indicates that the current theory is not adequate to explain the membrane dynamics. The widths of the peaks are related to the thickness fluctuation amplitudes.

stretched exponential function $\frac{I(q,t)}{I(q,0)} = \exp[-(\Gamma t)^{2/3}]$ with the decay rate Γ. The lines obtained from the MD simulations also decay with time as shown in Fig. 2(b). The decay function is well explained with the above equation except for the intermediate q range, *e.g.*, $q = 1.4$ nm^{-1} in Fig. 2(b). This result suggests that a better analysis in the intermediate q-range may require multiple exponential functions to account for multiple modes.

Figures 2(c) and 2(d) show the q-dependence of Γ/q^3 at various values of R for NSE and MD, respectively [3]. To characterize the dynamics, a Lorentz function $\frac{\Gamma}{q^3} = \frac{\Gamma_{TF}}{q_0^3}\frac{1}{1+(q-q_0)2\,\xi^{-2}} + \frac{\Gamma_{BEND}}{q^3}$ is utilized. The lines in Fig. 2(c) and 2(d) are the results of fitting to this equation. In this procedure, two terms of membrane dynamics, the bending and thickness fluctuations, are considered. The contributions from these motions are characterized by decay rates Γ_{BEND} and Γ_{TF}, respectively. Each parameter relates to the thickness fluctuations: Γ_{TF}/q_0^3 and ξ^{-1} are proportional to the damping frequency of the mode and the mode amplitude, respectively, and q_0 is the center of the motion, which relates to the membrane thickness. It is noted that the thickness fluctuations are observed even for the $R = 0.0$ sample, corresponding to the bilayers. On the other hand, the $R = 1.37$ (NSE data) and $R = 1.14$ (MD data) samples show a small enhancement of the dynamics. This suggests that a large amount of oil, which swells the bilayers, suppresses the thickness fluctuations.

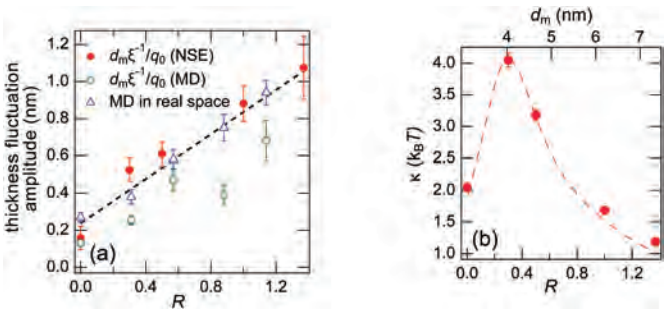

FIGURE 3: (a) NSE and MD data show excellent agreement in predictions of thickness fluctuation amplitude. (b) An unexpected enhancement of the bending modulus κ is observed near $R = 0.3$.

The thickness fluctuation amplitudes are given by $d_m\xi^{-1}/q_0$ where the parameters, both from NSE and MD, are obtained from reciprocal space information and the Lorentz function fit. The values obtained from this expression are compared to the distribution of local fluctuations of surfactants in real space by MD simulation, as shown in Fig. 3(a). Excellent agreement was obtained, especially between NSE (reciprocal) and MD (real) data. This result confirms that the motion observed by NSE is the thickness fluctuations of surfactant membranes and that the thickness fluctuation amplitude increases linearly with R.

The membrane bending motion is well predicted by the Zilman-Granek (ZG) single membrane fluctuation model [4]. Utilizing the ZG theory, the bending modulus of the membrane κ is estimated from the values of Γ_{BEND}, as shown in Fig. 3(b). The κ at $R = 0.3$ is larger than that at $R = 0.0$ (bilayer), indicating more rigid membranes around $R = 0.3$ than the bilayers. Two possible scenarios are the increase of κ due to the change of the bilayer thickness and that the increase of κ originates from the enhanced thickness fluctuations. When oil thickness is small enough, the fluctuations of the two monolayers are synchronized and they behave as a single thick membrane (pseudo bilayers). With increasing R at $R > 0.3$ the value of κ becomes smaller, and finally $\kappa \approx 1\ k_BT$ at $R = 1.37$. In this regime the synchronization between two monolayers becomes smaller and each monolayer fluctuation dominates the system dynamics when d_m is large enough.

The present study shows that combined use of NSE and MD gives an excellent agreement of the thickness fluctuations of surfactant membranes. The importance of intra-membrane dynamics to the elastic properties of the overall membrane is also confirmed. The rigidity of membranes is controlled by the interactions among molecules as well as by the energy dissipation mechanisms within the membranes. The present results and the methods described here are very useful in understanding the dynamics of surfactant membranes, in particular, bilayer lipid membranes, interaction of drugs with biological membranes, and molecular transport across membranes.

Reference

[1] B. Farago, M. Monkenbusch, K. D. Goecking, D. Richter, J. S. Huang, Physica B **213&214**, 712 (1995).; B. Farago, Physica B **226**, 51 (1996).

[2] M. Nagao, Phys. Rev. E **80**, 031606 (2009).

[3] M. Nagao, S. Chawang, and T. Hawa, Soft Matter **7**, 6598 (2011).

[4] A. G. Zilman, R. Granek, Phys. Rev. Lett. **77**, 4788 (1996).

Morphological characterization of polymer-based solar cells

H. Lu[1], B. Akgun[2,3], T.P. Russell[1]

Solar energy might be more widely used if the cost of the solar cells could be reduced. Polymer-based bulk heterojunction (BHJ) organic photovoltaic (OPV) systems offer cost reduction and potential for scale-up using solution processing. However, achieving efficiencies in excess of 10 % is an important milestone in making OPV devices economically viable. While there have been advances in the synthesis of novel low bandgap polymers and block copolymers with tailored morphologies, translating these advances to large scale production requires understanding the morphology of the active layer developed during processing, the relationship of the morphology to device performance, and routes to tailor the morphology to optimize efficiency [1]. The spatial distribution of the components normal to the film surface and the segregation of the components at the electrode interfaces in BHJ blend films are crucial to the charge generation and transport, thereby affecting the efficiency of the device.

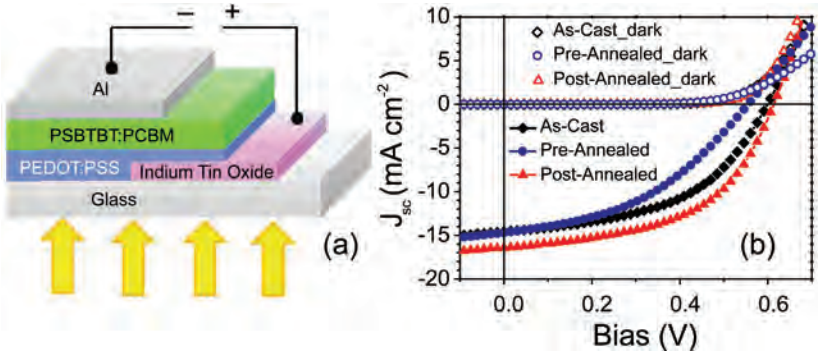

FIGURE 1: (a) Schematic of the PSBTBT:PCBM-based solar cell devices. Abbreviations are indicated in the text. (b) The current density–voltage curves of the As-Cast, Pre-Annealed, and Post-Annealed solar cells at dark (open symbols) and under solar-simulated irradiation (filled symbols). Pre-Annealed and Post-Annealed samples are annealed at 150 °C for 1 min.

In the work highlighted here [2], we systematically investigated the morphology of blends of [6,6] phenyl-C61-butyric acid methyl ester (PCBM) with a silole-containing low-bandgap polymer, poly[(4,4′-bis(2-ethylhexyl)dithieno[3,2-b:2′,3′-*d*]silole)-2,6-diyl-alt-(4,7-bis(2-thienyl)-2,1,3-benzothiadiazole)-5,5′-diyl] (PSBTBT). PSBTBT is a highly crystalline polymer with improved charge transport properties, reduced bimolecular recombination, and reduced formation of charge transfer complexes when blended with a fullerene derivative [3]. Due to significant natural neutron contrast between PCBM and PSBTBT, neutron reflectivity (NR), which has a resolution of the order of a nanometer in the direction normal to the surface, was used to resolve the vertical distribution of components in the active layer. Scattering length density (SLD) profiles obtained from NR are compared with the depth profiles measured by dynamic secondary ion mass spectroscopy (DSIMS). To elucidate the performance of the blends in actual devices, measurements were performed on thin films on substrates coated with a layer of poly(ethylenedioxythiophene):polystyrene sulfonate (PEDOT:PSS). Thermal annealing was done prior to (Pre-Annealing) or after (Post-Annealing) the deposition of Al cathodes, mimicking actual solar cell structures. The schematic of a PSBTBT/PCBM based solar cell device is shown in Fig. 1a.

Current density-voltage (J-V) curves for the As-Cast, Post-Annealed and Pre-Annealed devices were measured under dark and solar-simulated (AM1.5G) illumination and representative curves are shown in Fig. 1b. Pre-Annealing at 150 °C decreased the power conversion efficiency by 18 % relative to the As-Cast device. A brief Post-Annealing at 150 °C improved the device performance, while longer time annealing degraded the device performance.

Pure PSBTBT film is hydrophobic and has a static water contact angle of 104°, while pure PCBM film is hydrophilic with a contact angle of 51°. The contact angle of the As-Cast blend film was slightly lower, but very close to that of the pure PSBTBT film, indicating that the surface was richer in PSBTBT, due to the lower surface energy of PSBTBT. Pre-Annealing at 150 °C increased the contact angle of the blend film further, which could be either due to an increase in the concentration of PSBTBT at the surface or a roughening of the surface. After removing the Al layer, Post-Annealed films showed a large drop in contact angle (78°), due to the diffusion of PCBM to the interface and further annealing increased the contact angle to 88°. Segregation of PCBM to the cathode/active layer interface is beneficial for device performance, since this increases the charge transport to the Al electrode. This correlates well with the device performance results where short Post-

[1]University of Massachusetts, Amherst, MA 01003
[2]NIST Center for Neutron Research, National Institute of Standards and Technology, Gaithersburg, MD 20899
[3]University of Maryland, College Park, MD 20742

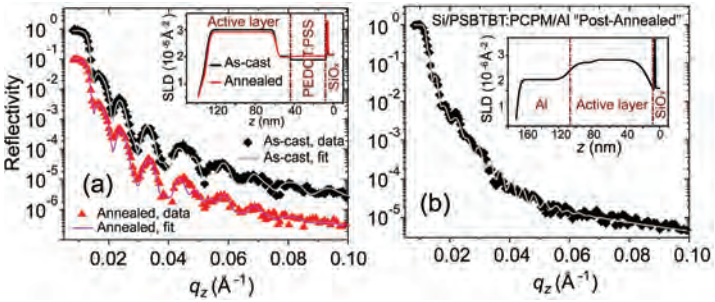

FIGURE 2: Neutron reflectivity profiles of (a) Si/SiO_X/PEDOT:PSS/PSBTBT:PCBM films and (b) Si/SiO_X/PSBTBT:PCBM/Al films. The solid lines indicate the best fits for the reflectivity profiles. The insets are the corresponding profiles of SLD as a function of z, where z = 0 is the Si substrate.

Annealing times improved the device performance but longer Post-Annealing times degraded the performance.

NR data of the As-Cast, Pre-Annealed, and Post-Annealed films and their corresponding SLD profiles are shown in Fig. 2. The As-Cast and Pre-Annealed films have very similar SLD profiles, showing an enrichment of PSBTBT and depletion of PCBM at the air surface, and Pre-Annealing causes this depletion layer to be slightly thicker (Fig. 2a). In the As-Cast film, a thin layer closest to the PEDOT:PSS layer corresponds to the active layer in which the volume fraction of PCBM (ϕ_{PCBM}) is 0.28. In the bulk of the As-Cast active layer, ϕ_{PCBM} is 0.57 which is close to the volume fraction of the two components in the blend solution (ϕ_{PCBM} = 0.53 and ϕ_{PSBTBT} = 0.47). While Pre-Annealing did not change the distribution in the bulk, it did increase the SLD of the PEDOT:PSS layer, indicating the diffusion of PCBM into the PEDOT:PSS layer.

The Post-Annealed sample, on the other hand, showed markedly different NR and SLD profiles (Fig. 2b). To simplify the fitting procedure, the active layer was spin-cast directly onto a UV-ozone-treated Si substrate, followed by evaporation of an Al electrode on top. PCBM and PSBTBT are distributed more uniformly than in the As-Cast and Pre-Annealed samples. The drop in the SLD at the substrate suggests a depletion of PCBM (≈ 4 nm thick) at the substrate. The layer located at z ≈ 110 nm to 160 nm was ascribed to aluminum oxide. The rough interface between the active layer and the cathode (rms roughness ≈ 7.7 nm) indicated a diffusion of Al into the active layer during thermal annealing or thermal evaporation of Al, which is also confirmed by high-resolution transmission electron microscopy.

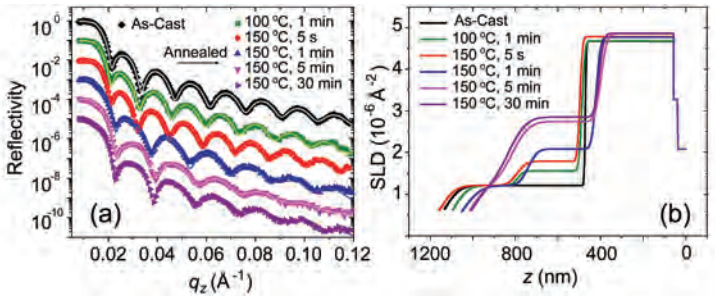

FIGURE 3: (a) Neutron reflectivity profiles for the PCBM/PSBTBT bilayer films (PSBTBT film was Pre-Annealed at 150 °C for 5 min) before and after annealing. The solid lines indicated the best fits for the reflectivity profiles. (b) The corresponding SLD profiles as a function of z (where z = 0 is the Si wafer). SLD profiles do not overlap along the horizontal axis due to the varying thickness of each sample.

The depth distribution obtained by NR is in good agreement with that measured by DSIMS, showing the depletion of PCBM and enrichment of PSBTBT at the air interface for As-Cast and Pre-Annealed films and an increase of PCBM concentration at the cathode interface after Post-Annealing. Segregation of the donor at the anode and acceptor at the cathode interfaces in OPV devices is beneficial for charge transport and collection, and, as such, Post-Annealing leads to better device performance.

Diffusion of PCBM into PSBTBT was measured using NR in a bilayer system. Shown in Fig. 3 are NR curves and the corresponding SLD profiles for PCBM/PSBTBT bilayer films under different annealing conditions (PSBTBT films were pre-annealed at 150 °C for 5 min before they were floated onto PCBM layers.) The sharp interface between the two layers for As-Cast film indicates that there was no interdiffusion between PCBM and PSBTBT at room temperature. Even a mild annealing at 100 °C for 1 min was enough to initiate diffusion of PCBM into the PSBTBT layer. At the beginning PCBM did not completely diffuse into the entire polymer layer but after annealing at 150 °C for 5 min PCBM was uniformly distributed in the polymer layer except a very thin layer at the air surface. The SLD of the polymer layer did not show obvious changes after 5 min, suggesting a saturation of PCBM (ϕ_{PCBM} = 0.19) in the PSBTBT layer. The slight increase in the SLD of the PCBM film upon annealing at 150 °C can be attributed to a densification of the PCBM. The diffusion behavior of PCBM within the PCBM/PSBTBT bilayers is quite similar to that seen in the PCBM/P3HT system where PCBM was seen to rapidly diffuse into the amorphous regions of P3HT without perturbing the ordering of P3HT [4].

In summary, a systematic investigation on the morphology of the active layer and the structure at the interfaces under different treatments was accomplished *in situ* using neutron reflectivity employing the natural neutron contrast between the components in the active layer. This study indicates how Post-Annealing improves device performance by enhancing segregation of the donor at the anode and acceptor at the cathode interfaces. Such studies are important for improving the performance of the polymer-based solar cells.

References

[1] J. Peet, A.J. Heeger, G.C. Bazan, Acc. Chem. Res. **42**, 1700 (2009).

[2] H. Lu, B. Akgun, T.P. Russell, Adv. Energy Mater. *ASAP* (DOI: 10.1002/aenm.201100128).

[3] H.Y. Chen, J.H. Hou, A.E. Hayden, H. Yang, K.N. Houk, Y. Yang, Adv. Mater. **22**, 371 (2010).

[4] D. Chen, F. Liu, C. Wang, A. Nakahara, T.P. Russell, Nano Lett. **11**, 2071 (2011).

Nanoscale mixing of soft solids

S-H. Choi,[1] S. Lee,[1] H.E. Soto,[3] T.P. Lodge,[1,2] and F.S. Bates[1]

Mixing of materials on the molecular scale represents a fundamental and demanding facet of modern chemical technology. Blending thermodynamically compatible liquids such as water and methanol is trivial, whereas combining inorganic solids at low temperatures is virtually impossible. Soft solids such as colloids, biological materials, and polymer melts show complicated and delicate thermodynamic and dynamic properties within both limits of behavior, necessitating innovative mixing processes. While the properties of blends and alloys are highly dependent on the precise arrangement of the constituents, assessing the state of mixing at the molecular scale is extremely challenging. In this highlight, we demonstrate that statistically perfect nanoscale mixing of ordered block copolymer micellar solutions can be achieved using a simple laboratory-scale mixer, as characterized by SANS measurements (see Fig. 1)

Poly(styrene-*b*-ethylene-*alt*-propylene) (PS-PEP) diblock copolymers were dispersed in a mixture of normal and deuterated squalane ($C_{30}H_{62}$ and $C_{30}D_{62}$), resulting in spherical micelles containing glassy PS cores and swollen PEP coronas. These micelles form liquid-like solutions at low concentrations (< 7 % mass fraction), but soft solid body-centered cubic (bcc) ordered arrangements at higher concentrations. Nearly chemically identical normal (PS(H)-PEP) and

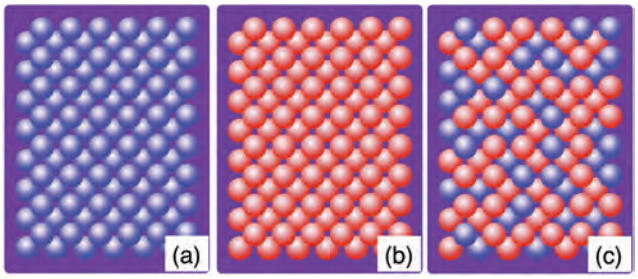

FIGURE 1: Illustration of PS(H) (blue) and PS(D) (red) spheres ordered on a body-centered cubic lattice and immersed in a contrast-matched matrix of squalane ($C_{30}H_{62}$ + $C_{30}D_{62}$) (purple). SANS from both (a) and (b) results in Bragg diffraction, while random placement of blue and red spheres (c) extinguishes interparticle interference, thus exposing single-sphere scattering.

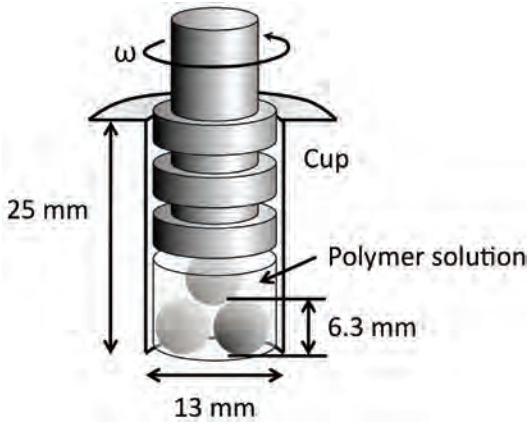

FIGURE 2: Schematic illustration of the MiniMax mixer (CSI Co.) employed to blend ordered block copolymer micelles at room temperature. The specimen is held in a cup, along with three balls that facilitate mixing, confined by a rotor that applies a macroscopic shear stress.

selectively perdeuterated (PS(D)-PEP) block copolymers were synthesized for this study, then blended with the solvent in two ways. Premixed solutions contain micelle cores with 50 % PS(D) and 50 % PS(H) molar fractions, designed to perfectly contrast match the isotopically labelled squalane solvent. Postmixed solutions were formed by mechanically mixing ordered blends of PS(D)-PEP and PS(H)-PEP micelles.

Complete mixing of liquid micelle solutions (*e.g.*, 1 % volume fraction) can be achieved by simple stirring at room temperature [1]. However, mixing ordered micellar solutions is considerably more challenging because these are soft yet solid-like materials. Here we employed a simple MiniMax mixer (CSI Co., see Fig. 2) to postmix 15 % volume fraction of PS(H)-PEP and PS(D)-PEP copolymer solutions at room temperature. Since the PS cores are glassy ($T_g \approx 70$ °C) at room temperature, copolymer chains are not able to exchange between micelles during mechanical blending.

SANS measurements were performed with the NG-7 30 m instrument at NIST, with a neutron wavelength of 7 Å. SAXS measurements were conducted with the equipment maintained by the DuPont-Northwestern-Dow Collaborative Access Team at Argonne National

[1]Department of Chemical Engineering and Materials Science, University of Minnesota, Minneapolis, MN 55455
[2]Department of Chemistry, University of Minnesota, Minneapolis, MN 55455
[3]University of Texas-Pan America, Edinburg, TX 78541

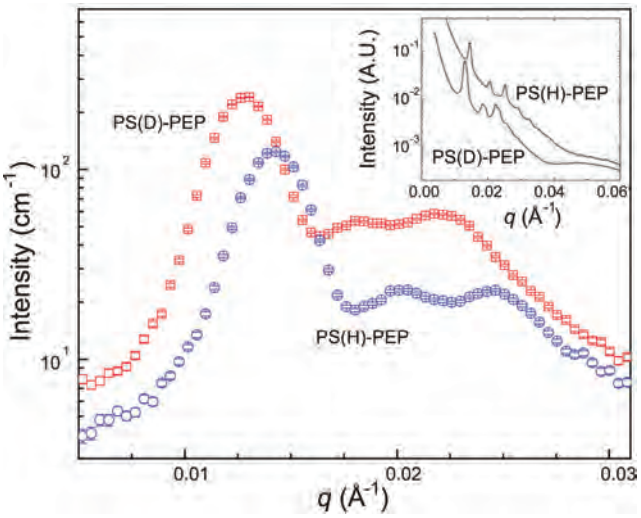

FIGURE 3: SANS profiles obtained from 15 % volume fraction PS(D)-PEP (red) and PS(H)-PEP (blue) in an isotopic squalane mixture (42 % $C_{30}H_{62}$ and 58 % $C_{30}D_{62}$ volume fractions) at 30 ºC. Inset shows the corresponding SAXS patterns.

Laboratory, with an x-ray wavelength of 0.729 Å. Figure 3 displays SANS and SAXS (inset) data obtained from the 15 % volume fraction PS(H)-PEP and PS(D)-PEP solutions prior to blending at room temperature. Bragg peaks are evident, consistent with a bcc lattice with unit cell parameters a_{bcc} = 62 nm and a_{bcc} = 68 nm for PS(H)-PEP and PS(D)-PEP micelles, respectively. We attribute the small difference in lattice parameter to the minor variations in the molecular characteristics of the block copolymers.

For a blend containing equal numbers ($N_H = N_D = N/2$) of perfectly randomly mixed and identically sized normal and perdeuterated spheres, the neutron scattering intensity can be described by the sum of intraparticle, P(q) and interparticle Q(q) contributions:

$$\frac{I(q)}{A} = \left[\frac{(\Delta\rho_H)^2+(\Delta\rho_D)^2}{2}\right]P(q)+\left[\frac{\Delta\rho_H+\Delta\rho_D}{2}\right]^2 NQ(q), \qquad (1)$$

where A is the system-specific constant. Here $\Delta\rho_H$ and $\Delta\rho_D$ are the excess scattering length density of PS(H) and PS(D), respectively, determined with the isotopic squalane solvent. In this case we ignore scattering from the solvated PEP blocks, which can be shown to be insignificant relative to the micelle core scattering. Critically, Eq. (1) is satisfied only if the normal and deuterated spheres are randomly distributed within the specimen, either on a disordered or ordered basis. When the scattering length density of the isotopic solvent is designed to be $(\rho_H + \rho_D)/2$, the interparicle contribution to Eq (1) is exactly eliminated leaving only the interparticle contribution. An isotopic mixture containing 42 % volume fraction of normal squalane and 58 % volume fraction of deuterated squalane meets this criterion.

Figure 4 shows SANS data obtained from postmixed and premixed solutions. Clearly, the Bragg peaks are completely suppressed for the scattering pattern obtained from the postmixed solution (blended at room temperature using the MiniMax mixer) and the resulting data are quantitatively accounted for using a hard-sphere form factor (solid curve) with a core radius of 11.0 nm. An independent SAXS measurement verifies that this blend retains a well-defined bcc structure (see inset to figure). This result confirms that the blend contains uniformly distributed PS(D)- and PS(H)-PEP micelles on a bcc lattice, as illustrated in Fig. 1. As anticipated by Eq. 1, the SANS profile obtained from the premixed solution shows almost no coherent scattering intensity.

In conclusion, we have demonstrated complete mixing of bcc ordered block copolymer micelles using a simple commercial mixer. Realization of nanoscale mixing was confirmed by SANS and SAXS measurements. This work also highlights the application of small-angle neutron scattering using the contrast matching technique to investigate particle form factors under circumstances where ordering (*i.e.*, interparticle interference) generally dominates the overall scattering intensity.

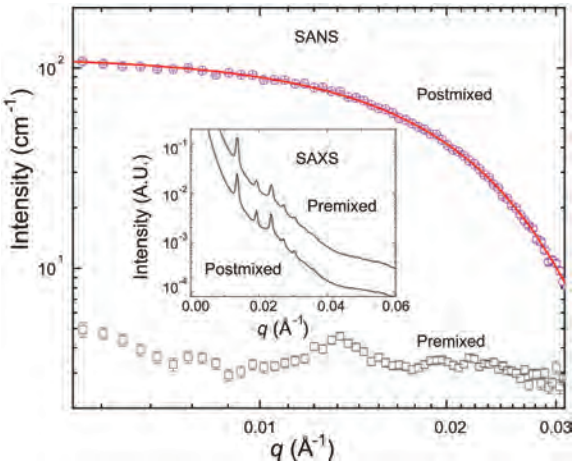

FIGURE 4: SANS pattern obtained from postmixed (purple) and premixed (black) solutions. The postmixed solutions were prepared by blending PS(H)-PEP and PS(D)-PEP micelle solutions (each 15 % volume fraction in contrast-matched squalane) at 30 ºC. The solid curve represents a best fit to the hard-sphere form factor. A synchrotron SAXS pattern (inset) obtained from the same mixtures confirms a bcc crystal structure.

References

[1] S. Choi, T. P. Lodge, F. S. Bates, Phys. Rev. Lett. **104**, 047802 (2010).

[2] S. Choi, F. S. Bates, T. P. Lodge, Macromolecules **44**, 3594 (2011).

[3] S. Choi, T. P. Lodge, F. S. Bates, Phys. Rev. Lett. **104**, 047802 (2010).

[4] S. Choi, F. S. Bates, T. P. Lodge, Macromolecules **44**, 3594 (2011).

Zone refinement effect to remove impurities in organic semiconductor polymer blends for printable electronics

V. M. Prabhu[1], D. M. DeLongchamp[1], R. J. Kline[1], D.Y. Yoon[2], S.K. Satija[3], J. E. Anthony[4]

A problem in making thin-film printable organic semiconductor devices is the appearance of impurities within the charge-transport region, limiting device performance. Here we highlight our work on a processing strategy for manufacture that improves the uniformity of the films and that significantly reduces the effect of trap impurities.

Organic semiconductors are the most critical element of a new generation of optoelectronic devices that includes printable flexible electronics and photovoltaic devices. The vertical distribution and orientation of crystalline semiconductors in an organic thin film field-effect transistor (OTFT) must be controlled by processing to achieve optimal switching speed and current flow, often for a specific OTFT architecture. Common OTFT architecture variations involve different placements of the contacts and gate dielectric. For large-area flexible displays, many technology developers prefer a bottom-gated OTFT to a top-gated one. Gate placement is critical to device optimization because charge carriers are formed within the semiconductor layer only at its interface with the gate dielectric. Charge transport occurs within the 2 nm region adjacent to the gate dielectric, and the composition and orientation of the semiconductor layer at this interface is critical to device performance.

Formulation and processing are key contributors to the structure of the organic semiconductor layer at the dielectric gate interface. Since organic semiconductors can be processed from solution, they offer advantages over inorganic semiconductors such as amorphous silicon that requires processing under vacuum. While synthetic advances in recent years have produced organic semiconductors with performance characteristics that match amorphous silicon, there remain challenges in manufacturing process development for methods such as ink jet drop-on-demand printing, roll-casting, and spin coating. A processing challenge affecting some of the highest-performing organic semiconductors is that the neat solution viscosity is too low for common coating methods, preventing the formation of high-quality films.

An attractive approach to organic semiconductor formulation was proposed by Brown *et al.*, who blended a high-performance organic semiconductor in solution with an insulating polymer binder [1]. Due to the polymer binder, the blend solution forms high-quality conformal films, and the films had charge carrier mobility greater than 0.3 cm^2/Vs in top-gated OTFTs. Because the top-gated mobility was quite high, Brown *et al.* postulated that the semiconducting small molecules were vertically segregated to the top surface of the thin blend film. Although this approach represented a significant advance in formulation, the top-gated architecture is not preferred for manufacturing electronic devices, such as displays because the active layer can be damaged by subsequent fabrication steps such as gate electrode patterning and wiring. Instead, the bottom-gate architecture is favored.

Building upon the pioneering work of Brown et al., the NIST-SNU team developed a blend formulation approach to ensure that the semiconducting molecules can also segregate to a bottom gate interface [2]. Neutron reflectivity experiments performed on the NG7 horizontal reflectometer provided the critical data proving that blends of deuterium-labeled 6,13-bis(triisopropylsilylethynyl)pentacene (TIPS-pentacene) with high molecular weight poly(α-methylstyrene)(PaMS) form a non-uniform vertical composition profile in films spin-coated onto silicon wafers from the homogeneous mixture solutions. These experiments showed conclusively that the organic semiconductor was preferentially segregated to the gate-dielectric interface with segregation characteristics controlled by the number-average relative molecular mass of the PaMS.

In follow-up work, the NIST-SNU team investigated the surprising relationship between vertical segregation in these blend films and the presence of impurities in the semiconductor. It is generally known that organic semiconductors can contain or develop impurities that act as charge carrier traps; they can be formed on exposure to ultraviolet (UV) light, for example. The NIST-SNU

[1]Polymers Division, Material Measurement Laboratory, National Institute of Standards and Technology, Gaithersburg, MD 20899
[2]Seoul National University, Seoul, Korea
[3]NIST Center for Neutron Research, National Institute of Standards and Technology, Gaithersburg, MD 20899
[4]University of Kentucky, Lexington, KY 40506

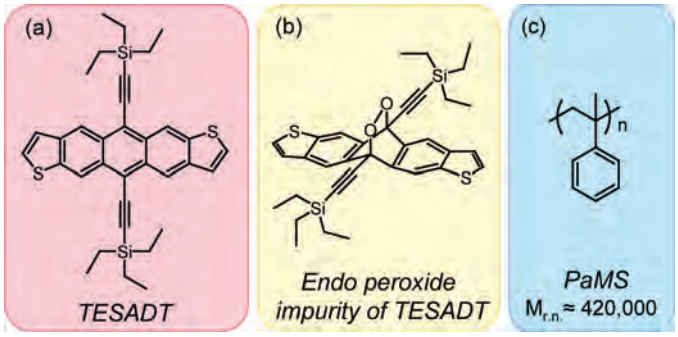

FIGURE 1: Chemical structures of (a) TESADT, (b) the impurity in light-exposed TESADT, (c) poly(α-methylstyrene) (PαMS).

team investigated impurities [3] in the semiconductor triethylsilylethynyl anthradithiophene (TESADT) (Fig. 1a) that forms an endo peroxide impurity (Fig. 1c) upon prolonged exposure to UV light.

Impure TESADT had drastically reduced field-effect mobility (< 10^{-5} cm^2/Vs) and lost its high-temperature crystal phase. When mixed with PaMS binder polymer, however, the impure TESADT recovered completely, to exhibit performance like that of highly purified TESADT (0.040 cm^2/Vs). The expected phase transition characteristics also returned in part of the film. It is clear that the impurities must be removed by the binder polymer, at least within the 2 nm at the gate dielectric interface. Neutron reflectivity provided a route to measure the vertical composition profile of deuterium-labeled TESADT blend films. Figure 2 shows the specular neutron reflectivity data for the blend films (30/70 by mass) of d-TESADT with PaMS of number-average relative molecular mass ($M_{r,n}$) ≈ 420 000 g·mol^{-1}, spin-cast on a thick silicon substrate. In general, reflectivity arises from the interference of the reflected neutrons from the air and

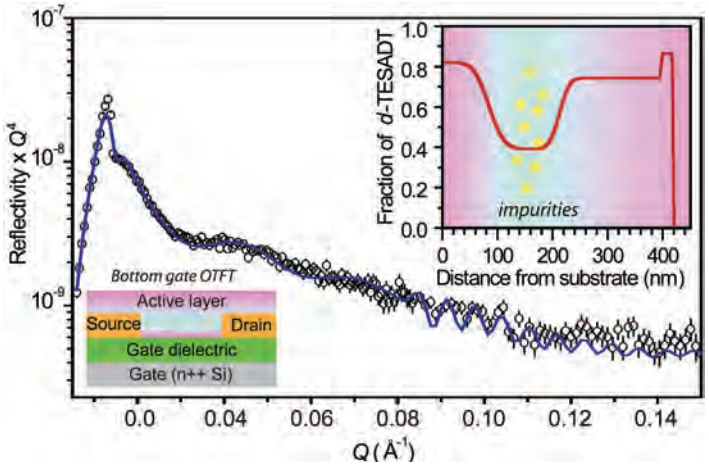

FIGURE 2: Neutron reflectivity profile and fitted concentration profile (in the top inset) of d-TESADT in 7:3 (by mass) blend films of d-TESADT and high molecular-mass PαMS. The experimental and fitted reflectivity curves are shown by circles and line, respectively. The lower inset shows the geometry of a bottom-gated OTFT. Colored regions in the active layer correspond to the top inset.

the substrate interfaces. Fits to the data provide scattering-length density (SLD) profiles that were interpreted as d-TESADT volume fraction depth profiles using known pure component SLD values. For this blend, the phase-segregated structure forms a d-TESADT-rich layer not only at the air surface, but also at the blend/silicon substrate interface (Fig. 2 inset). The central polymer-rich layer surprisingly appears to collect and isolate the impure TESADT. The "purified" TESADT-rich segregated surface layer was characterized by near-edge x-ray absorption fine structure (NEXAFS) spectroscopy, which showed the absence of endo peroxide type impurity at the critical bottom-gate interface. Bottom-gated OTFTs show charge carrier mobility that is completely recovered. The blend formulation strategy is therefore valuable for at least two reasons: it aids coating by enhancing viscosity, and it also increases shelf stability by purifying the semiconductor at the charge-transporting interface.

The self-purification of TESADT impurities during the film forming and semiconductor crystallization process is reminiscent of an inorganic semiconductor process called zone refinement. This methodology is used in the manufacturing of defect-free inorganic semiconductors and plays an analogous role during the phase segregation and crystallization process to remove impurity species that are detrimental to devices from the critical charge-transporting interface region.

Our approach of using specular neutron reflectivity to measure the vertical composition profile in semiconducting blend formulations provides a general paradigm for formulation and process development in organic electronics. Direct measurement of the composition profile identifies processing strategies that permit advantageous segregation to the desired device interface. NR, when combined with other methods, provides a route to correctly assign the impacts of process and formulation variables to differences in segregation, crystallinity, or nanoscale morphology. Application of this measurement strategy can accelerate formulation and manufacturing process development and hasten the introduction of new products from printed, flexible electronics.

References

[1] B.A. Brown, J. Veres, R.M. Anemian, R.T. Williams, S.D. Ogier, S.W. Leeming, In International Application Published Under the Patent Cooperation Treaty, WO 2005/055248 A2, 2005.

[2] J. Kang, N. Shin, D.Y. Jang, V.M. Prabhu and D.Y. Yoon. J. Am. Chem. Soc. **130**, 12273 (2008).

[3] Y.S. Chung, N. Shin, J. Kang, Y. Jo, V.M. Prabhu, S.K. Satija, R.J. Kline, D.M. DeLongchamp, M.F. Toney, M.A. Loth, B. Purushothaman, J.E. Anthony, D.Y. Yoon, J. Am. Chem. Soc. **133**, 412 (2011).

Limit on parity-violating neutron spin rotation in ^{4}He

J.S. Nico[1], C.D. Bass[1], T.D. Bass[1], B.E. Crawford[2], K. Gan[3], B.R. Heckel[4], D. Luo[5], D.M. Markoff[6], A.M. Micherdzinska[3], H.P. Mumm[1], A.K. Opper[3], M. Sarsour[7], E.I. Sharapov[8], W.M. Snow[5], H.E. Swanson[4], S.B. Walbridge[5], and V. Zhumabekova[9]

The weak interaction between nucleons (protons and neutrons) remains one of the most poorly-understood areas of the Standard Model. It has proven difficult both experimentally and theoretically to test the fundamental nucleon-nucleon (NN) weak interaction. Measurements using low-energy neutrons, however, have lead to significant experimental progress and have the potential to illuminate previously unknown features of the theory of quantum chromodynamics. A collaboration involving several institutions recently completed an experiment on the NG6 beamline at the NIST Center for Neutron Research (NCNR) to study the strong interaction using weak interaction properties of the neutron. The neutron spin-rotation experiment operated by measuring the extremely small rotation angle of polarized neutrons traversing a target of liquid helium [1].

In the 19th century Louis Pasteur discovered that the plane of polarization of light often corkscrews as it moves through a material even if there is no obvious axis defined by the material structure. Later, it was discovered that many substances (biological molecules, in particular) have an internal structure which possesses a handedness-violating mirror symmetry, and the electromagnetic interaction of the light with the electronic structure of a material with handed structures causes the rotation of the plane of polarization. The present collaboration searched for a neutron analogue of this phenomenon (neutron spin rotation) in liquid helium. In this case, the violation of mirror symmetry that causes the neutron plane of polarization to rotate comes not from any mirror-asymmetric internal structure but rather from the parity-violating (PV) weak interaction between the neutron beam and the neutrons and protons in the helium nucleus. Although the degree of violation of mirror symmetry in interactions between the quarks inside the nucleons is known, the strong interactions which confines the quarks in nucleons and binds the nucleons in the helium nucleus modifies the size of the effect. The purpose of this work is to measure the neutron optical activity (*i.e.*, spin rotation angle per unit length of the medium) in helium and use it to learn about quark dynamics in the nucleon.

The weak interaction between the neutrons and the medium causes the amplitudes of the positive and negative neutron helicity states of polarized neutrons to accumulate different phases. The difference ϕ_{PV} between the phase shifts of the helicity states leads to a rotation of the neutron polarization vector about its momentum, which manifestly violates parity [2]. The rotation angle per unit length of a neutron of wave vector $\boldsymbol{k}$ in a medium of density ρ is $d\phi_{PV}/dz = 4\pi\rho f_{PV}/|\boldsymbol{k}|$, where f_{PV} is the forward limit of the parity-odd p-wave scattering amplitude. Because f_{PV} is proportional to the parity-odd correlation $\sigma_n \cdot \boldsymbol{k}$, with σ_n the neutron spin vector and $\boldsymbol{k}$ the neutron momentum, $d\phi/dz$ is constant as $k \to 0$ in the absence of resonances [3].

Theoretically, the NN interaction can be described in terms of the Desplanques, Donoghue, and Holstein (DDH) nucleon-meson weak coupling amplitudes [4] and, more recently, effective field theory coupling parameters [5]. Within the DDH parameterization, the calculation for spin rotation in the n-^{4}He system in terms of the weak couplings f and h yields where $\frac{d\phi}{dz} = -0.97 f_\pi - 0.22 h_\omega^o + 0.22 h_\omega^1 - 0.32 h_\rho^o + 0.11 h_\rho^1$, subscripts π, ρ, and ω are the meson couplings at the NN vertex and the superscripts indicate the isospin change. The possible numerical values span a broad range of $\pm 1.5 \times 10^{-6}$ rad/m and are dominated by the uncertainties in the weak couplings. Because the values of these couplings are not well-constrained by theory or experiment, a precision measurement of the spin rotation in liquid helium can provide significant constraints on the range of values.

The neutron spin rotation apparatus is fundamentally a neutron polarimeter consisting of a crossed polarizer and analyzer pair. It measured the count rate asymmetry of neutrons that passed through two liquid helium target chambers immediately upstream and downstream of a centrally-located solenoid (π-coil), as shown in Fig. 1. To measure such a small rotation angle, one must shield magnetic fields and their fluctuations, because

[1]National Institute of Standards and Technology, Gaithersburg, MD 20899
[2]Gettysburg College, Gettysburg, PA 17325
[3]The George Washington University, Washington, DC 20052
[4]University of Washington/CENPA, Seattle, WA 98195
[5]Indiana University/CEEM, Bloomington, IN 47408
[6]North Carolina Central University/TUNL, Durham, NC 27707
[7]Georgia State University, Atlanta, GA 30303
[8]Joint Institute for Nuclear Research, 141980 Dubna, Russia
[9]Al-Farabi Kazakh National University, 050038 Almaty, Kazakhstan

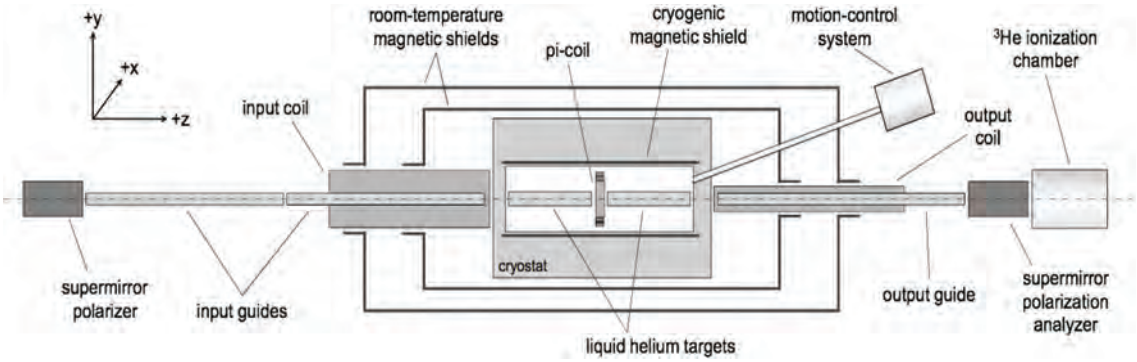

FIGURE 1: Overview of the apparatus to search for parity-violating spin rotation in liquid helium.

stray magnetic fields can give rise to very large parity-conserving rotations that are orders of magnitude larger than the PV signal. Thus, the apparatus is buried in three layers of mumetal. What may not be so obvious is that for a measurement of this type in which (due to the high rate in the direct beam) we can only measure the current of the neutrons as opposed to counting individual neutrons, we are susceptible to reactor intensity fluctuations (which end up following the near-universal 1/f noise spectrum). We therefore split the entire experiment down the middle and simultaneously performed two measurements in parallel to eliminate this common-mode source of noise.

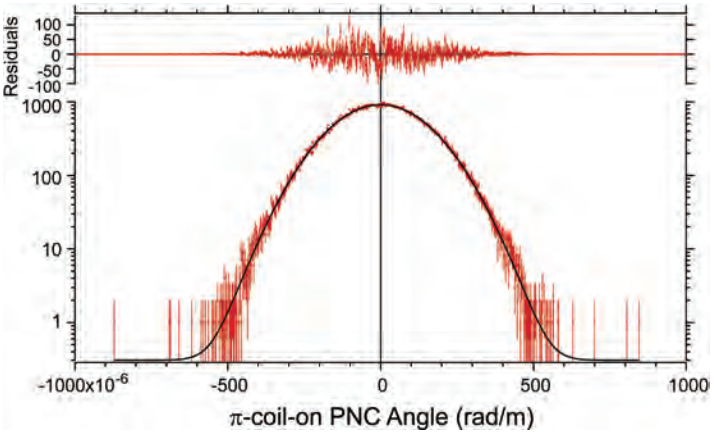

FIGURE 2: Distribution of measured parity non-conserving (PNC) rotation angles per meter. The solid line is a fit to a Gaussian distribution with a constant background.

While passing through the filled target, the neutrons experience a parity-violating spin rotation transverse to their momentum direction ($\hat{z}$), which is proportional to their path length in the liquid helium target. They also experience a parity-conserving rotation proportional to both their path length and the strength of the residual magnetic fields throughout the entire target region (Fig. 1). These rotations were reduced significantly by passive magnetic shielding and the implementation of the π-coil. The field of the π-coil was aligned in the direction of the initial neutron polarization and constructed so that when neutrons pass through it, their spin vector precessed 180°. One of the target positions was filled with liquid helium and the other was empty; the contents of each target could be remotely filled or emptied, so that two target states were possible [6]. An output coil adiabatically rotated the x-component of the neutron polarization by $\pi/2$ in the x-y plane. This rotated spin component produced an asymmetry in the flux transmitted through the polarization analyzer given by $\frac{N^+ - N^-}{N^+ + N^-} = \langle PA \sin\phi \rangle$ where PA is the product of the neutron polarization P and the analyzing power A, N^+ and N^- are the count rates in the two states of the output coil, and ϕ is the measured rotation angle.

Data were acquired in five months of running in 2008. Possible false effects from slow drifts in the polarimetry were suppressed by analyzing the time sequence of asymmetries with an algorithm that canceled linear and quadratic time-dependent effects. Systematic effects associated with beam parameters and neutron polarimetry that could cause a false asymmetry were studied in detail [7]. Additional measurements amplified potential systematic effects, such as the magnetic field amplitude and magnetic field gradient, that allowed one to place upper bounds on their magnitude. Figure 2 shows the distribution of spin rotation angles with the π-coil on for the complete data set. The result for neutron spin rotation in

$$\frac{d\phi_{PV}}{dz} = [1.7 \pm 9.1(stat) \pm 1.4(sys)] \times 10^{-7} \text{ rad/m},$$

liquid helium is where the overall uncertainty is dominated by statistics [8]. This experiment represents the most sensitive search for neutron weak optical activity ever performed and yields a significant advance in precision in comparison to past measurements in heavy nuclei. Regardless, it is necessary to improve the overall precision to further constrain the NN weak amplitudes. A second phase of the experiment is planned at a more intense beam line under construction at the NCNR, where it is expected that an upgraded apparatus would achieve a precision of $\leq 2 \times 10^{-7}$ rad/m on the n-^{4}He rotation angle.

References

[1] B. Heckel, NBS SP **711**, 90 (1986).

[2] F.C. Michel, Phys. Rev. **133**, B329 (1964).

[3] L. Stodolsky, Nucl. Phys. B **197**, 213 (1982).

[4] B. Desplanques, J.F. Donoghue, and B.R. Holstein, Ann. Phys. **124**, 449 (1980).

[5] M.J. Ramsey-Musolf and S.A. Page, Ann. Rev. Nucl. Part. Sci. **56**, 1 (2006).

[6] C.D. Bass *et al.*, Nucl. Instrum. Meth. A **612**, 69 (2009).

[7] A. Micherdzinska *et al.*, Nucl. Instrum. Meth. A **631**, 80 (2011).

[8] W.M. Snow *et al.*, Phys. Rev. C **83**, 022501(R) (2011).

Improving the measurement of trace selenium by neutron activation analysis

I.J. Kim[1], R.P. Watson[2], and R.M. Lindstrom[2]

Selenium is an essential element in humans, but it is also a potential toxin, making the reliable determination of trace selenium in the environment a critical need. The Analytical Chemistry Division at NIST therefore provides Standard Reference Material (SRM) 3149, a standard selenium solution, as a primary calibration standard to industrial and academic institutions around the world who wish to validate their own methods for elemental analyses of selenium. The goal of any elemental analysis is to return a value as close as possible to the actual amount of the element in the sample, *i.e.*, provide high accuracy, while minimizing the uncertainty in the measurement itself, thus also providing high precision. In order to certify with high accuracy and precision the level of selenium in SRM 3149, we measured its selenium content by instrumental neutron activation analysis (INAA). In INAA, a sample is irradiated with neutrons to produce radionuclides whose characteristic decay radiation, typically γ-rays, may be used to identify the elements present and, more importantly, quantify the amounts of these elements.

The use of INAA in determining selenium content presents several advantages: There is minimal sample preparation; pure elemental selenium may be conveniently used as an exceptionally accurate standard; the target isotope of naturally occurring selenium, ^{74}Se, has an adequate natural abundance and thermal neutron capture cross section for the measurement; the activated radioisotope, ^{75}Se, emits several γ-rays, each of which may provide independent corroboration of the measurement; and ^{75}Se is long-lived (half-life of *ca.* 120 days), allowing for careful γ-ray counting.

While the use of elemental selenium in our analysis improved the accuracy of the measurement, it also introduced a potential obstacle to high precision in that the uncertainty in the measurement could be increased by the neutron self-shielding of the selenium fragments used as standards. We employed a semi-empirical solution to this problem by measuring the specific activities of several selenium fragments of differing masses and applying a model that followed the decrease in specific activity as a function of mass caused by the self-shielding phenomenon. As shown in Fig. 1, the dependence of specific activity on mass is nonlinear and is modeled by the curve described in Eq. (1), where $f_n(x)$

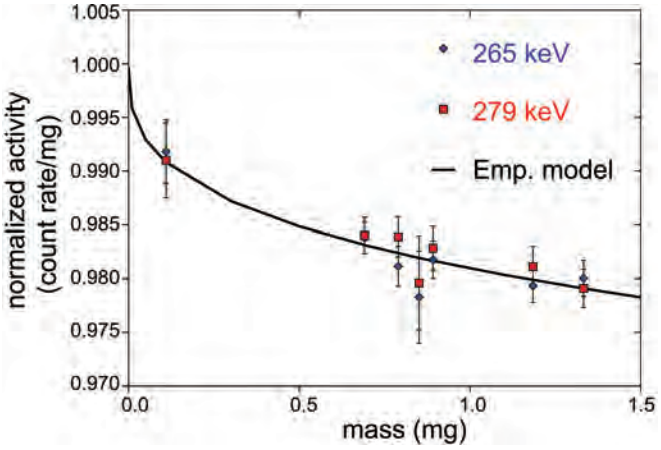

FIGURE 1: INAA data and curve of normalized specific activity fitted by the empirical model of Eq. (1). Uncertainties propagated from 1 s counting statistics are indicated by error bars.

and $f_\gamma(x)$ are idealized predictions of the neutron and gamma-ray self-shielding behaviors in a fragment with mass x, p is the empirical correction factor reconciling the idealized behavior with the observed trend, and $N(x)$ is the observed activity. The extrapolated N_0, being the theoretical activity of a selenium standard exhibiting no self-shielding, is the value used in calculating the selenium content in the SRM samples. The use of Eq. (1) allowed us to treat the uncertainty in the self-shielding correction with conventional statistical analyses that lowered the overall uncertainty and improved the precision of the measurement.

$$\frac{N(x)}{N_0} = 1 - p[1 - f_n(x) f_\gamma(x)] \qquad (1)$$

In addition to the neutron self-shielding factor, several other aspects of the measurement were carefully monitored to minimize the measurement uncertainty. The most important of these were the counting statistical uncertainty, the repeatability of the measurement, the neutron fluence gradient present during irradiation, the uncertainty due to differences in counting geometry, and the pile-up correction of the counting system. The INAA-determined selenium content in each sample of SRM 3149 was found to be 10.09 mg/g ± 0.06 mg/g. The uncertainty of 0.06 mg/g represents 0.5 % of the measured value and demonstrates the role INAA can have in providing excellent accuracy and precision in elemental analyses.

Reference

I. J. Kim, R. P. Watson, R. M. Lindstrom, Anal. Chem. **83** (9), 3493 (2011).

[1]Korea Research Institute of Standards and Science, Daejeon, Republic of Korea
[2]Analytical Chemistry Division, Material Measurement Laboratory, National Institute of Standards and Technology, Gaithersburg, MD, USA 20899

Directly probing anisotropy gradients using polarized neutron reflectometry

B. J. Kirby[1], J. E. Davies[2,3], Peter Greene[4], Kai Liu[4], S. M. Watson[1], G. T. Zimanyi[4], R. D. Shull[2], P. A. Kienzle[1], and J. A. Borchers[1]

For magnetic recording media, it is desirable to reduce energy consumption by writing magnetic bits into the intended up or down state using the smallest possible magnetic field. However, ease of writing must be balanced with thermal stability – if the bits are too loose, unintentional flips can occur, degrading or erasing stored data. Recent work [1] predicts that an optimal balance between ease of switching and thermal stability can be achieved by gradually varying the magnetic anisotropy throughout a stack of magnetic multilayers. In principle, high anisotropy "hard" layers anchor the stack against thermal fluctuations, while low anisotropy "soft" layers assist the hard layers during switching.

However, definitive experimental evidence of an anisotropy gradient is difficult to obtain with standard magnetometry techniques which measure the collective magnetic response of the entire multilayer structure. Even if layers in the stack are known to be harder or softer when separated, such individual characteristics are subject to change in a multilayer structure due to interlayer coupling. Therefore, a spatially sensitive magnetic probe is ideal for characterizing an anisotropy gradient. Polarized neutron reflectometry (PNR) is just such a technique, sensitive to the nuclear composition and magnetization depth profiles, and we have used PNR to unambiguously identify anisotropy gradients in magnetic nanostructures [2].

For a Co/Pd multilayer, magnetic anisotropy should decrease with increased Co layer thickness. Thus to achieve an anisotropy gradient, we deposited 15 Co/Pd bilayers where the Co thickness progressively increased with each bilayer (from 0.3 nm to 1.1 nm) while the Pd layer thickness (0.9 nm) remained fixed. This graded multilayer structure was deposited on top of a constant structure of 15 repeats of 0.3 nm Co/0.9 nm Pd. We used the NG-1 Reflectometer at the NCNR to perform PNR measurements and determine the nuclear and field-dependent magnetic profiles of this sample. Figure 1 shows an example of fitted non spin-flip, scattering vector (Q) dependent reflectivities, taken at 660 mT. Clear, spin-dependent oscillations are observed, indicating sensitivity to the magnetic depth profile.

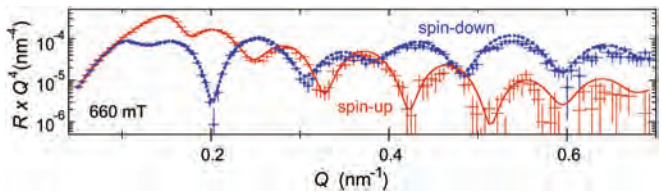

FIGURE 1: Fitted spin-down (blue) and spin-up (red) non spin-flip reflectivities, measured at 660 mT. Data and fits are multiplied by Q^4 for clarity.

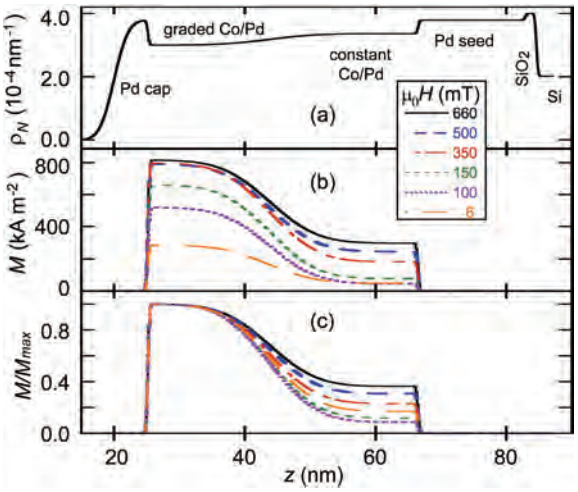

FIGURE 2: Nuclear (a), magnetization (b), and normalized magnetization (c) depth profiles, determined from fits to the PNR data. That the normalized profiles are different demonstrates graded anisotropy.

The profiles determined from fits to the data are shown in Fig. 2 with respect to z, the depth into the sample. The nuclear profile (panel a) gives a structural reference for the magnetization profiles shown below it (panels b-c). While pronounced magnetization gradients are observed at all fields (panel b), this alone does not prove an anisotropy gradient, as the variation in magnetization is partially due to an increase in Co moments near the free surface (*i.e.*, the individual Co layers get thicker). Thus, to illuminate anisotropy variations, Fig. 2c shows each of the magnetization profiles in Fig. 2b normalized by the respective maximum values. If the sample were to exhibit uniform anisotropy, the magnetization at all depths of the sample should respond to field at the same rate, meaning all the profiles in Fig. 2c would be identical. Instead, the normalized profiles show that the low Co thickness portion of the sample (high z) becomes progressively more similar to the higher Co thickness portion (low z) as magnetic field is increased. This shows that the top of the sample is magnetically softer than the bottom, a definitive demonstration of graded anisotropy.

With an anisotropy gradient firmly established, magnetometry was used to correlate the gradient with a real reduction in write field, demonstrating the advantage of graded anisotropy media.

References

[1] D. Suess, Appl. Phys. Lett. **89**, 189901 (2006).
[2] B. J. Kirby, *et al.*, Phys. Rev. B **81**, 100405(R) (2010).

[1]NIST Center for Neutron Research, National Institute of Standards and Technology, Gaithersburg, MD 20899
[2]Metallurgy Division, National Institute of Standards and Technology, Gaithersburg, MD 20899
[3]Advanced Technology Group, NVE Corporation, Eden Prairie, MN 5534
[4]University of California at Davis, Davis, CA 95616

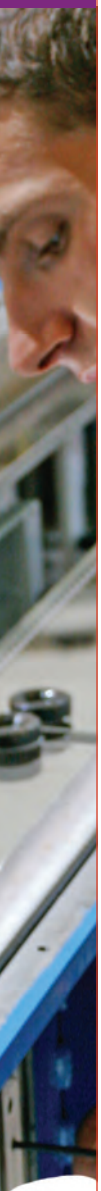

Detection of dynamical transitions in hydrogenous materials by transmission of very cold neutrons

N. Verdal[1], T. J. Udovic[1], J.R.D. Copley[1] and J.J. Rush[1,2]

For over half a century, neutron scattering, aided by the large scattering cross section for hydrogen, has been an invaluable tool to study vibrational, rotational, and diffusive motions in hydrogenous materials. Many of these studies involve measurements to probe transitions in dynamical behavior which occur as a function of temperature, pressure, or molecular adsorption. The extensive use of neutron spectrometers around the world in such research often relies on previous thermal scans, NMR, or diffraction experiments to decide at what temperature or pressure to carry out scattering measurements to probe dynamical details. Here, we demonstrate that simple and rapid measurements of the transmission of very cold neutrons are a highly sensitive *in situ* probe of such dynamical changes, and can be a useful guide for complex scattering experiments which ultimately determine the details of the motional changes.

It was demonstrated decades ago that cross section measurements at long neutron wavelength (λ) are very sensitive to total inelastic scattering from energy-gain scattering processes involving large amplitude vibrational or rotational modes in hydrogenous materials [1,2]. If the velocity of the incident neutron is much less than that of the scattered neutrons, the total inelastic scattering, and thus the scattering cross section, increases linearly with $1/v_i$ (or with λ_i). A key point is that the cross section continues to increase with λ_i, so that the sensitivity to the dynamics of the hydrogenous species is greatly enhanced at very long λ_i.

To test the method, representative neutron transmission measurements were performed on the Disk Chopper Spectrometer. Samples with ≈ 50 % transmission at 30 Å were prepared of several materials, including ammonium iodide (NH_4I), hexamethylbenzene (HMB), and dicesium dodecahydro-*closo*-dodecaborate ($Cs_2{}^{11}B_{12}H_{12}$), all of which undergo transitions involving dynamical changes. Samples were placed in a cryostat capable of controlled temperature ramps and centered in a 30 Å neutron beam emerging from the neutron guide after the monochromating chopper array. A "black" ^{3}He detector array was placed 40 cm beyond the sample. The resulting neutron transmission intensities vs. temperature primarily reflect changes in energy-gain scattering.

Figure 1 shows the change in transmitted intensity vs. temperature for each material. NH_4I exhibits a phase transition from a bcc to an fcc structure at 280 K [3], at which the NH_4^+ motion changes from torsional vibration to quasi-free rotation. A major drop in neutron intensity is observed near 280 K, which reflects the removal of 30 Å incident neutrons by a sharp increase in rotational inelastic scattering. Moreover, the transmission technique shows hysteresis effects, *i.e.*, the intensities obtained on cooling show an enormous shift of the transition down to ≈ 200 K.

HMB undergoes a less dramatic transition at 118 K [3] that has been shown to involve the methyl torsional mode, due to a change in intermolecular interactions between methyl groups. The vibrational spectra for HMB in the inset, as measured with FANS, show a smearing of the torsional band above the transition due to dynamical changes. These changes are easily observed as a decrease in transmitted intensity, due primarily to an increase in energy-gain scattering from the increased population of CH_3 torsional levels.

The transmission for $Cs_2{}^{11}B_{12}H_{12}$ clearly changes at the subtle second-order phase transition near 529 K to a more disordered orientational state for the large $B_{12}H_{12}{}^{2-}$ ions. This confirms the sensitivity of the method to even relatively small dynamical changes of larger molecular species. Thus the method could be appropriate for dynamical transformations of larger molecules or polymers.

Finally, we would point out that the thickness of $Cs_2B_{12}H_{12}$ provides a ≈ 90 % transmission at (5 to 6) Å, which minimizes multiple scattering effects. Therefore, the same sample in a cryostat, furnace, pressure device, *etc.* can be used first for a quick transmission scan (over several hours) for searching for a dynamical transition and then, without removal, for scattering measurements.

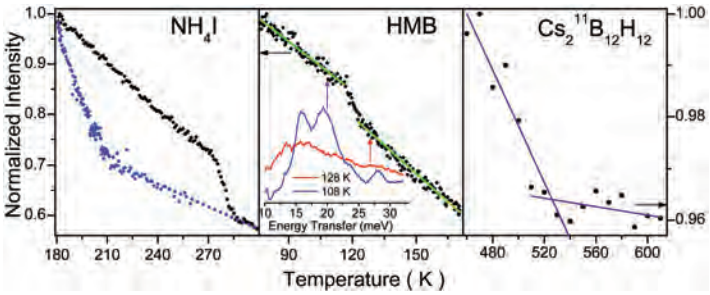

FIGURE 1: The transmitted, reduced neutron intensities (I/I_{max}) through HMB, NH_4I, and $Cs_2{}^{11}B_{12}H_{12}$ as functions of temperature. The blue data points for NH_4I were measured upon cooling from room temperature, demonstrating a hysteresis in its structural phase transition. The HMB inset shows the vibrational density of states below and above its transition. Uncertainties are commensurate with the scatter in the data.

References

[1] J. J. Rush, T. I. Taylor, W. W. Havens, Phys. Rev. Lett. **5**, 507 (1960).

[2] P. S. Leung, J. J. Rush, T. I. Taylor, J. Chem. Phys. **57**, 175 (1972).

[3] N. Verdal, T. J. Udovic, J. R.D. Copley, J. J. Rush, J. Solid State Chem. (2011), doi:10.1016/j.jssc.2011.07.046

[1]NIST Center for Neutron Research, National Institute of Standards and Technology, Gaithersburg, MD 20899-6102
[2]University of Maryland, College Park, MD 20742-2115

Uniformity of a large cross section neutron spin analyzer for SANS polarization analysis

W.C. Chen[1,2], S.M. Watson[1], K.L. Krycka[1], and J.A. Borchers[1]

A ^{3}He neutron spin filter (NSF) is based on the strong spin dependence of the neutron absorption cross section for ^{3}He and has the following advantages over the supermirror analyzer: 1) it can polarize a large area and widely divergent neutron beam; and 2) it can efficiently flip the neutron polarization by reversing the ^{3}He nuclear polarization. Polarization analysis with ^{3}He NSFs [1,2] has recently been employed for studies of magnetic nanoparticles by small-angle neutron scattering [3,4]. These experiments required careful attention to polarization corrections, which result from the imperfection of the ^{3}He spin filter, supermirror polarizer, precession coil spin flipper, and spin transport. For reasons of practicality, a uniform neutron polarization over the scattered beam for the ^{3}He spin analyzer was assumed [3,4]. Spin transport is often the most difficult issue in polarized neutron scattering because the neutron spin must be adiabatically rotated within a couple of centimeters from the strong, transverse, sample field to the relatively weak longitudinal field of the shielded solenoid used to maintain the ^{3}He polarization. The spin transport efficiency can thus vary across the neutron beam. There is also an intrinsic inhomogeneity of the analyzing efficiency due to small variation of the gas thickness of the ^{3}He analyzer. The homogeneity in polarization efficiency will be problematic in performing polarization analysis, especially in probing a weak magnetic signal from the sample, as shown in reference [4] where uncertainties of polarization efficiencies greater than 1 % could mask the expected weak magnetic features. Hence, accurate knowledge of any spatial variation of the overall instrumental polarization efficiency is essential.

We have developed and characterized a large cross section ^{3}He NSF with uniform analyzing efficiency for polarization analysis on the NG-3 SANS. The ^{3}He cells have a diameter approaching 12 cm, large enough to extend the area detector data to a reasonably high Q (the maximum Q is 1.1 nm^{-1} at a wavelength of 0.5 nm without the detector offset). We have mapped the spatial variation of the overall instrumental polarization efficiency $P = \frac{N^+ - N^-}{N^+ + N^-}$ over the 2-D position-sensitive-detector (PSD) by measuring scattering with the incident neutron spin flipper OFF (N^+) and ON (N^-) from a strong coherent scatterer (Glassy Carbon). These measurements have been performed in fields ranging from 5 mT to 1.6 T. Fig. 1 shows the spatial variation of the overall instrumental polarization efficiency over the 2-D PSD and the instrumental polarization efficiency as a function of the wave vector transfer at 0.7 T. The spatial variation of the overall instrumental neutron polarization in the usable area of the cell window (the large circle in the center, defined by the end-cap holes through which scattered neutrons must pass) is about 1 %, including any possible spin transport and spatial variation of ^{3}He gas thickness. As expected, polarization efficiency begins to fall-off rapidly at the edge of the end-cap hole of the solenoid due to use of neutron shielding materials outside the hole. We have modeled the spatial variation of ^{3}He gas thickness of the cell for the scattered neutron beams based on the spherical cell windows and the relative location of the cell from both the sample and the detector. As shown in Fig. 1(b), the polarization efficiency has been calculated as a function of Q, and is consistent with the measurements. After taking account of the intrinsic inhomogeneity of the analyzing efficiency, the spin transport loss over all scattered beams passing through the cell should be no more than 1 %, indicating that the scattered neutron spin is adiabatically rotated by $\pi/2$ from the transverse horizontal to longitudinal direction for the large solid angle divergent scattered beams. To our knowledge, this is the first direct measurement for such a level of large area spatial homogeneity in polarization efficiency. Our next step is to incorporate the spatial variations of the efficiencies in the SANS polarization correction software to allow for the detection of even smaller magnetic signals.

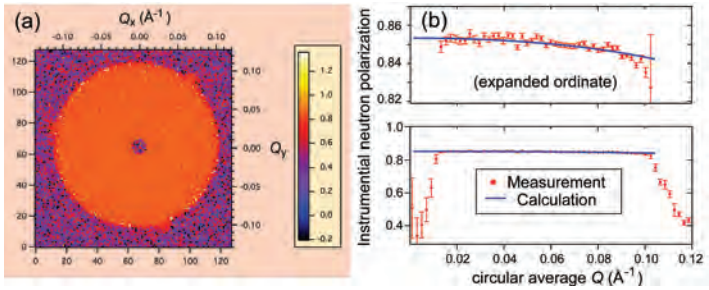

FIGURE 1: (a) Spatial variation of the measured instrumental polarization efficiency over the 2-D PSD at 0.7 T. (b) The polarization efficiency (circularly averaged) as a function of the wave vector transfer. The red circles are the measured values. The solid line is calculated by modeling the cell path length variation for different scattering angles. The expanded section (above) shows a gentle decrease in polarization efficiency due to the cell path length variation.

References

[1] T.R. Gentile *et al.,* J. Appl. Crystallog. **33,** 771 (2000).
[2] W.C. Chen *et al.,* Physica B **404**, 2663 (2009).
[3] K. Krycka *et al.,* Physica B **404**, 2561 (2009).
[4] K. Krycka *et al.,* Phys. Rev. Lett. **104,** 207203 (2010).

[1]NIST Center for Neutron Research, National Institute of Standards and Technology, Gaithersburg, MD 20899
[2]University of Maryland, College Park, MD 20742

Neutron Source Operations

The NCNR Source (NBSR) operated for 142 days this past year providing 99 % availability before shutting down, as scheduled, for the Outage. The Expansion Outage that began on April 3 has provided many opportunities for minor and major upgrades to the reactor systems for enhanced reliability of operations.

To minimize interference with the new neutron guides that will be installed during the current Outage it was necessary to move the majority of the NCNR secondary cooling system. The new system will replace the six, single speed Main Secondary Pumps with four energy-efficient, variable speed pumps and will provide equivalent cooling and flow rates. In addition, a new cooling tower cell will be installed to supplement the 22 MW cooling capacity of the existing towers during the summer when heat and humidity levels reduce the tower cooling efficiency. The majority of the installation of the upgrade to the secondary cooling system has been performed under an American Recovery and Reinvestment Act (ARRA) project but the Reactor Operations/Engineering (ROE) group prepared the full system for long-term dry layup of the piping and will be responsible for interfacing the new system to the reactor control room and bringing the system back into full service.

The Thermal Shield cooling system's function is to cool a radiation shield that protects the concrete surrounding the NCNR source by circulating water through cooling tubes. Over the lifetime of the facility, the tubes have developed small water leaks that had become operationally inconvenient. Patching the leaks was only a temporary repair so the NCNR developed a system that utilized low vacuum

Paul Liposky and Jim Moody work on the RT-4 pneumatic transfer system.

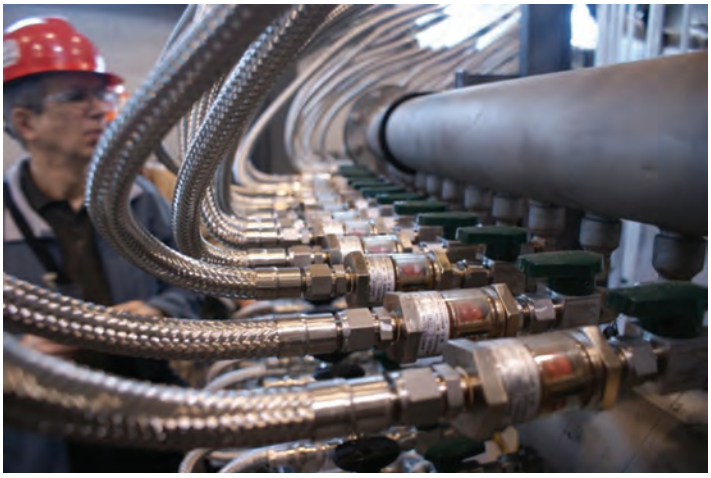

Tony Norbedo examines the new stainless-steel lines on the upgraded Thermal Shield cooling system.

rather than pressure, to move cooling water around the Thermal Shield. The strategy has been successfully tested in prototypes and full-scale mockups. During the current Outage, a complete upgrade of the Thermal Shield cooling system has been installed that will move water by using aspirators to maintain the highest pressure in the system just below one atmosphere, thus preventing outleaks.

ROE is performing a phased-upgrade to the reactor control console. Phase I involves building an information acquisition system that will store data routinely available to the reactor operators. This data will be acquired in real-time during and used to develop a new display and control system for the control room that will use contemporary human-machine interface (HMI) best-practice for Phase II. Phase I has progressed throughout the Outage and many of the older displays, alarm indicators, and controllers have been replaced with modern systems that will output directly to the Console data-acquisition system. Initially, the system will provide only an internal display of data in the NCNR control room and an auxiliary HMI development laboratory but the data could be eventually provided to experimenters or other areas of the NCNR that might need to monitor the system remotely.

The installation of the second NCNR liquid hydrogen cold-source in BT-9 is the culmination of years of design and development work. The successful source installation was delayed because both BT-9 and the fabricated cold source required machining to compensate for distortions in the experimental tube and the small tolerance differences between the cold source and the tube dimensions. The source was fully installed in the first week of September but there is still a great deal of work before the system will be filled with hydrogen. Complete installation and testing is expected to occur in early 2012.

Facility Development

Facility support staff have taken advantage of the scheduled outage period of the Expansion Initiative program to progress design and construction of new instruments—scheduled for installation in the post-outage period—while developing and refurbishing existing instrumentation, software, and sample environment equipment.

Instrument Development

The past year has seen the preassembly and staging of the 10 m SANS instrument to be installed on the new NG-B guide. The diffractometer has been outfitted with motion controls and other ancillary electronics, and adaptation of the 30 m SANS instrument control software is underway. The pre-staged 10 m SANS instrument will also provide a test bed for the new Instrument Control Environment (NICE) software system; the alpha release of this major refactoring and development project is scheduled early in 2012.

The Facility supports a growing program to develop and commission new detector systems to address the needs of new instruments in the Expansion Initiative and beyond. The detector project for the CANDOR white-beam reflectometer has recently been awarded NIST intramural funding and these additional funds will expedite development of the detector and speed the process of bringing the final design into production. The current design is based on 6LiF/ZnS(Ag) impregnated plastic scintillator technologies coupled via wavelength shifting fibers to silicon photomultiplier devices (SiPMs). The promising early results from a prototype detector have led to refinements of the neutron converter portion of the detector that will be tested in the near term.

The design of the Very Small Angle Neutron Scattering (vSANS) diffractometer calls for two types of detectors: a high-resolution area detector typical of most instruments of this type and arrays of linear position sensitive tubes. In discussions with GE Reuter Stokes, a design has been finalized for eight panels consisting of

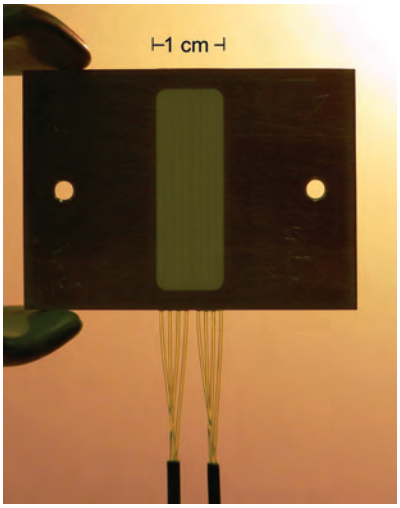

FIGURE 1: A backlit picture of an assembly in which are embedded wavelength shifting fibers in a neutron detecting ^{6}LiF-ZnS(Ag) scintillator matrix. The scintillation pulses travel via the fibers to silicon photomultiplier devices.

"8-pack" linear position sensitive proportional counters for incorporation into the vSANS spectrometer. These panel arrays will also feature readout electronics based on the SNS data acquisition standard. Fabrication of the panel assemblies is underway and delivery is projected for December 2011.

The primary detector for the MAGIK spectrometer, soon to be installed on the new NG-D guide, has been procured and integrated into data acquisition for the instrument. This detector, a DENEX 200TN, is a 20 cm × 20 cm ^{3}He gas-filled area detector with 1 mm × 2 mm spatial resolution.

Data Analysis Software Development

The Data Analysis and Visualization Environment (DAVE) project provides software solutions for data reduction, viewing, and interpretation covering a wide range of inelastic neutron scattering instruments at the NCNR and elsewhere. DAVE is based on the IDL iTool paradigm and has been under development for close to a decade. It is now in its second major developmental phase realizing improvements in many aspects of the application suite especially with regards to usability and visualization functionality.

Coincident with the extended outage period, work has progressed to address some long-standing issues and add new features covering all aspects of DAVE functionality from planning tools, reduction and visualization to basic data analysis. A new reduction component designed for the multi-channel detector system on BT-7 is being developed using an identical interface to the recently completed FANS reduction module. When complete, it will readily enable loading of multiple raw datasets, apply normalization and other raw data corrections, and calculate the wavevector and energy transfer taking into account the variation in angle and energy across the multichannel detector. Diffraction data from powder samples and diffraction or inelastic data from single crystal samples are also supported. In many cases, the reduced data are volumetric (multi-dimensional) and can thus be analyzed (sliced and cut) further using the DAVE Mslice tool.

Support for MACS data reduction was introduced last year and since then users have had the opportunity to provide much feedback that has resulted in a significant revision of the interface along with the addition of new functionality. The data reduction package for Neutron Spin Echo has been upgraded to allow treatment of multiple sample and background datasets, which is especially useful when employing partial deuteration techniques.

A new reflectometry fitting package, Refl1D, has been released. Developed as part of the NSF funded DANSE project for neutron scattering software, this package provides state of the art global optimization and uncertainty analysis software to the reflectometry community. The modeling engine allows users to combine freeform and slab layers into profiles and simultaneously refine profiles for multiple datasets. Magnetism is fully supported, including polarized and unpolarized measurements from time of flight and steady state sources. Users are free to extend their models in arbitrary ways, including support for different measurement techniques; results can be combined for a robust uncertainty assessment incorporating information from all measurements on the sample. DANSE has also released DIRefl for direct inversion analysis on surround variation reflectometry data, yielding profiles without fitting, and OsRefl for analysis on in-plane scattering data from patterned magnetic and non-magnetic samples. Numerous publications within the NCNR and from the broader community include results from DANSE reflectometry software packages. (http://reflectometry.org/danse/software.html)

Sample Environment

The NCNR provides a wide range of state-of-the-art sample environment equipment and technical expertise to support user research programs. The outage period has afforded time for a number of development and refurbishment projects, in particular to support operational capacity and reliability of low-temperature high magnetic field operations. The 10 T cryogen-free magnet has been outfitted with a cryogen-free variable-temperature insert and is now under test. The 7 T vertical field magnet is now redeployed with its ^{3}He low-temperature insert and the 11.5 T vertical field magnet with dilution refrigerator has undergone repairs and is being re-commissioned. Maintenance and repairs to the entire fleet of cryostats and of bottom-loading closed-cycle refrigerators will be completed in time for the re-start of Facility operations.

Neutron Spin Filters

NCNR supports a world-class user-driven program of polarized beam experiments and demand for ^{3}He neutron spin filters (NSFs) continues to be strong and increasing. The Facility program to support and develop NSFs is run in collaboration with the Physical Measurement Laboratory at NIST and during the past year has serviced 37 user experiments totaling over 130 days of beam time. Experiments are routinely carried out on the thermal neutron triple-axis spectrometer BT-7 and the suite of small-angle neutron scattering instruments and reflectometers. The program was expanded this year with proof-of-principle experiments performed on MACS for wide-angle polarization analysis.

^{3}He gas is polarized by spin-exchange optical pumping (SEOP), in which alkali-metal atoms are polarized by optical pumping and this electronic polarization is transferred to ^{3}He nuclei in spin-exchange collisions. Efforts continue to develop the SEOP systems and ^{3}He cells yielding improve to the overall ^{3}He polarization performance. The NSF team has built two state-of-the-art SEOP systems dedicated for the NCNR user program in polarized neutron scattering. Each SEOP system is equipped with two 100 W spectrally narrowed lasers to illuminate the gas cell from opposite sides, and this year saw implementation of a chirp volume Bragg grating for each laser, which has delivered higher power and improved suppression of broadband background. The lasers now routinely operate continuously for days with only occasional need for minor re-tuning of the wavelength. The best performance for large volume cells is achieved by the use of potassium-rubidium mixtures, but this requires careful control of the mix ratio in sealed cells and a standard protocol to optimize this ratio has now been developed. This enhanced SEOP capability, combined with an advanced cell fabrication facility, allows the polarization of 1 L cells to 80 % ^{3}He polarization within a day or two. Moreover, this year saw record breaking levels of ^{3}He polarizations from 82 % to 85 % obtained for user experiments on both ANDR and BT-7.

There has been a continued focus on developing user-friendly hardware and software to control ^{3}He NSFs that is readily incorporated into the instrument software. Software is now implemented to predict and monitor the polarized neutronic performance and flip the ^{3}He polarization when taking data on each instrument. The software provides a user-friendly interface and allows the instrument computer to perform NMR measurements, flip the ^{3}He polarization and control the neutron spin. An alternative method for ^{3}He, the polarization-flipping scheme has been implemented that uses an amplitude-modulated radio-frequency field when performing a frequency-sweep based adiabatic fast passage NMR. The new scheme promises to reduce the ^{3}He polarization loss per flip by a factor of at least 4 and will be tested on the beam lines when following the source re-start in 2012. User-friendly polarization efficiency correction software, which includes the ^{3}He polarization decay, is being implemented on the triple-axis spectrometer and SANS.

Progress has been made to advance polarized neutron instrumentation for each specific instrument class. On BT-7, one of the most important advances was to develop polarized inelastic neutron instrumentation. A polarized beam setup with a conventional precession coil spin flipper was not effective for elastic experiments at large scattering angles and inelastic experiments due to the impact of space constraints. However, the successful development of automated ^{3}He spin flipping capability on the beam line now enables efficient flipping and transport the neutron spin without the conventional flipper. This enhanced measurement capability has made the first successful polarized-beam inelastic experiment on BT-7 with an energy transfer up to 35 meV. The successful development of a high-field magic box has led to improvements—by a factor x3—in the ^{3}He polarization relaxation enabling reliable operation with a relaxation time of up to 100 h.

Development activity for SANS experiments has included work to increase the maximum sample field available from 1.2 T up to 1.6 T. This was achieved by the modification of an existing high field electromagnet to minimize its stray field using soft-iron plates and enable the passage of a polarized beam. Polarized neutron tests have shown the neutron spin transport with this magnet is not an issue and tests of the effect on the relaxation of the ^{3}He polarization are on-going.

Serving the Science and Technology Community

The mission of the NIST Center for Neutron Research is to assure the availability of neutron measurement capabilities to meet the needs of U.S. researchers from industry, academia and from other U.S. government agencies. To carry out this mission, the NCNR uses several different mechanisms to work with participants from outside NIST, including a competitive proposal process, instrument partnerships, and collaborative research with NIST.

Proposal System

Most of the time on NCNR instruments is made available through a competitive, peer-review proposal process. The NCNR issues calls for proposals approximately twice a year. Proposals are reviewed at several different levels. First, expert external referees evaluate each proposal on merit and provide us with written comments and ratings. This is a very thorough process where several different referees review each proposal. Second, the proposals are evaluated on technical feasibility and safety by NCNR staff. Third, we convene our Beam Time Allocation Committee (BTAC) to assess the reviews and to allocate the available instrument time. Using the results of the external peer review and their own judgment, the BTAC makes recommendations to the NCNR Director on the amount of beam time to allocate to each approved experiment. Approved experiments are scheduled by NCNR staff members in consultation with the experimenters.

The current BTAC members are:

- Andrew Allen (NIST Ceramics Division)
- Jeffrey Allen (Michigan Technological University)
- Collin Broholm (Johns Hopkins University)
- Leslie Butler (Louisiana State University)
- Kalina Hristova (Johns Hopkins University)
- Ramanan Krishnamoorti (University of Houston)
- Valery Kiryukhin (Rutgers University)
- Raul Lobo (University of Delaware)
- Lee Magid (University of Tennessee, Knoxville)
- Janna Maranas (The Pennsylvania State University)
- Alan Nakatani (The Dow Chemical Company)
- Stephan Rosenkranz (Argonne National Laboratory)
- Lynn Walker (Carnegie-Mellon University)

Partnerships

The NCNR may form partnerships with other institutions to fund the development and operation of selected instruments. These partnerships, or "Participating Research Teams", may have access to as much as 75 % of the available beam time on the instrument depending on the share of total costs borne by the team. A minimum of 25 % of the available beam time is always made available through the NCNR proposal program to all users. Partnerships are negotiated for a fixed period (usually three years) and may be renewed if there is mutual interest and a continued need. These partnerships have proven to be an important and effective way to expand the research community's access to NCNR capabilities and have been very successful in developing new instruments.

Collaboration with NIST

Some time on all instruments is available to NIST staff in support of our mission. This time is used to work on NIST research needs, instrument development, and promoting the widespread use of neutron measurements in important research areas, particularly by new users. As a result of these objectives, a significant fraction of the time available to NIST staff is used collaboratively by external users, who often take the lead in the research. Access through such collaborations is managed through written beam time requests. In contrast to proposals, beam time requests are reviewed and approved internally by NCNR staff. We encourage users interested in exploring collaborative

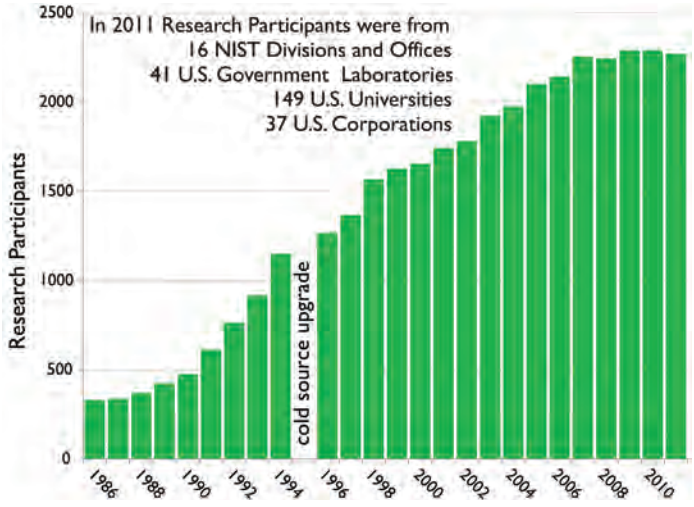

FIGURE 1: Research participants and publications at the NCNR 1986-2011.

research opportunities to contact an appropriate NCNR staff member.

Research Participation and Productivity

The NCNR continued its strong record of serving the U.S. research community this year. Over the 2011 reporting year, 2265 research participants benefited from use of the NCNR. (Research participants include users who come to the NCNR to use the facility as well as active collaborators, including co-proposers of approved experiments, and co-authors of publications resulting from work performed at the NCNR.) As the number of participants has grown, the number of publications per year has increased in proportion. The quality of the publications has been maintained at a very high level. The trend of the past few years, however, suggests that the number of participants and publications is beginning to saturate, as one might expect as the capacity of the facility is reached. The Expansion Initiative, currently in progress, promises increasing activity and productivity.

2011 NCNR Proposal Program

Only one call for proposals, rather than the usual two, was issued in the past year, because of the outage that began in April 2011 for the NCNR Expansion Initiative. We received 357 proposals, of which 170 were approved and received beam time. The oversubscription, *i.e.*, the ratio of days requested on all proposals to the days available, was 2.9 on the average, but as high as 6 for specific instruments. Proposal demand has grown constantly since the NCNR first began accepting proposals in 1991, and has doubled in the past eight years. The following table shows the data for several instrument classes.

Instrument class	Proposals	Days requested	Days allocated
SANS and USANS	119	458	175
Reflectometers	56	417	156
Spectrometers	163	1081	341
Diffraction	7	27	12
Imaging	12	60	26
Total	357	2043	710

User Group Conducts Survey

The NCNR Users Group (NUG) provides an independent forum for all facility users to raise issues to NCNR management, working through its executive officers to carry out this function. The current officers are Mark Dadmun (University of Tennessee, chair), John Katsaras (Oak Ridge National Laboratory), Michel Kenzelmann (Paul Scherrer Institute, Switzerland), Despina Louca (University of Virginia), Dale Schaefer (University of Cincinnati), Lynn Walker (Carnegie-Mellon University), and Erik Watkins (University of California, Davis). In

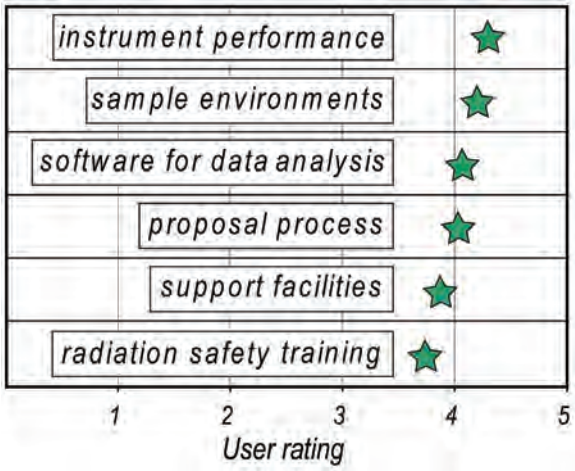

FIGURE 2: User ratings from the survey; the top rating is 5.

December 2011, the NUG conducted a comprehensive survey of user satisfaction and concerns, addressing areas such as support from NCNR staff, proposal review, sample environments, instrument hardware and software, data analysis, and user laboratories. Many useful comments were received in the 327 responses. As a result, several policy changes are planned, beginning with a revamping of our radiation safety training process for incoming users.

Panel of Assessment

The major organizational components of NIST are evaluated annually for quality and effectiveness by the National Research Council (NRC), the principal operating agency of both the National Academy of Sciences and the National Academy of Engineering. A panel appointed by the NRC reported on the NIST Center of Neutron Research in January 2011. Their findings for the previous year are summarized in a document that may be viewed online at http://www.nist.gov/director/nrc/upload/NR-Panel-2010-Report-Final-9-23-10.pdf The 2011 panel members included Tonya Kuhl of the University of California, Davis (chair), Meigan Aronson , Stony Brook University, Frank Bates, University of Minnesota, Donald Engelmann, Yale University, Paul Fleury, Yale University, Christopher Gould, North Carolina State University, Alan Hurd, Los Alamos National Laboratory, James Lee, Sandia National Laboratory, John Parise, Stony Brook University, and Sunil Sinha, University of California, San Diego.

The Center for High Resolution Neutron Scattering (CHRNS)

CHRNS is a national user facility that is jointly funded by the National Science Foundation and the NCNR. Its primary goal is to maximize access to state-of-the-art neutron scattering instrumentation for the research community. It operates seven neutron scattering

instruments at the NCNR, enabling users from around the nation to observe dynamical phenomena involving energies from ≈ 30 neV to ≈ 100 meV, and to obtain structural information on length scales from 1 nm to ≈ 10 μm. A more detailed account of CHRNS activities may be found on pp 59-61 of this report.

Partnerships for Specific Instruments
NG-7 SANS Consortium

A consortium that includes NIST, the Industrial Partnership for Research in Interfacial and Materials Engineering (IPRIME) led by the University of Minnesota, and the ExxonMobil Research and Engineering Company, operates, maintains, and conducts research at the NG-7 30 m SANS instrument. The consortium uses 57 % of the beam time on this instrument, with the remaining 43 % allocated to the general scientific community through the NCNR's proposal system. Consortium members conduct independent research programs primarily in the area of large-scale structure in soft matter. For example, ExxonMobil has used this instrument to deepen their understanding of the underlying nature of ExxonMobil's products and processes, especially in the fields of polymers, complex fluids, and petroleum mixtures.

NIST/General Motors – Neutron Imaging

An ongoing partnership and collaboration between General Motors and NIST continues to yield exciting results using neutron imaging. Neutron imaging has been employed to visualize the operation of fuel cells and lithium-ion batteries for automotive vehicle applications. Neutron imaging is an ideal method for visualizing both hydrogen and lithium, the fuel of electric vehicles engines. These unique, fundamental measurements, provide valuable material characterizations that will help improve the performance, increase the reliability, and reduce the time to market introduction of the next generation electric car engines. The GM/NIST partnership is entitled to 25% of the time on the BT-2 Neutron Imaging Facility.

Interagency Collaborations

The Smithsonian Institution's Nuclear Laboratory for Archeological Research is part of the Anthropology Department at the National Museum of Natural History. It has had a productive 33 year partnership with the NCNR, during which time it has chemically analyzed over 42,500 archaeological artifacts by Instrumental Neutron Activation Analysis (INAA), drawing extensively on the collections of the Smithsonian, as well as on those of many other institutions in this country and abroad. Such chemical analyses provide a means of linking these diverse collections together in order to study continuity and change involved in the production of ceramic and other artifacts.

The Center for Food Safety and Applied Nutrition, U.S. Food and Drug Administration (FDA), directs and maintains a multi-laboratory facility at the NCNR that provides agency-wide analytical support for food safety and food defense programs. Neutron activation (instrumental, neutron-capture prompt-gamma, and radiochemical), x-ray fluorescence spectrometry, and low-level gamma-ray detection techniques provide diverse multi-element and radiological information about foods and related materials. Current studies include preparation of swordfish in-house reference material, revalidation of cocoa powder in-house reference material, measuring cesium levels in soil to study cesium uptake behavior into food products, screening food products for dangerous levels of cadmium, lead, and mercury in beverages and residual bromine in baked goods, and evaluation of procedural losses of mercury, arsenic, selenium, and bromine from foods.

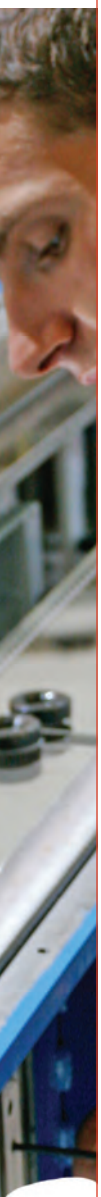

The Center for High Resolution Neutron Scattering (CHRNS)

The Center for High Resolution Neutron Scattering (CHRNS) is a national user facility that is jointly funded by the National Science Foundation through its Division of Materials Research (grant number DMR-0944772), and by the NCNR. The primary purpose of this partnership is to maximize access to state-of-the-art neutron scattering instrumentation for the research community using the NCNR's proposal system. Proposals to use the CHRNS instruments are critically reviewed on the basis of scientific merit and/or technological importance.

The core mission of CHRNS is fourfold: (i) to develop and operate neutron scattering instrumentation, with broad application in materials research, for use by the general scientific community; (ii) to promote the effective use of the CHRNS instruments by having an identifiable staff whose primary function is to assist users; (iii) to conduct research that advances the capabilities and utilization of CHRNS facilities; and (iv) to contribute to the development of human resources through educational and outreach efforts.

Scattering Instruments and Research

CHRNS supports operation of the following instruments:

- the NG-3 30 m Small Angle Neutron Scattering (SANS) instrument,
- the Ultra-Small Angle Neutron Scattering (USANS) instrument,
- the Spin-Polarized Inelastic Neutron Scattering (SPINS) spectrometer,
- the Multi-Angle Crystal Spectrometer (MACS),
- the Disk Chopper Spectrometer (DCS),
- the High Flux Backscattering Spectrometer (HFBS), and
- the Neutron Spin-Echo (NSE) spectrometer.

The small angle scattering instruments provide structural information over length scales from ≈ 1 nm to ≈ 10 μm. The spectrometers collectively yield dynamical information over time scales from ≈ 3×10^{-14} s to ≈ 10^{-7} s (energy scales from ≈ 100 meV to ≈ 30 neV). These wide ranges of accessible distances and times support a very diverse scientific program, allowing researchers in materials science, chemistry, biology, and condensed matter physics to investigate materials such as polymers, metals, ceramics, magnetic materials, porous media, fluids and gels, and biological molecules.

In the most recent Call for Proposals (call 27), 258 proposals requested CHRNS instruments, of which 106 received beam time. Of the 1359 days requested for the CHRNS instruments, 453 were awarded. The corresponding numbers for all instruments were 357 proposals received, 171 proposals approved, 2043 days requested, and 712 days awarded. Roughly half of the users of neutron scattering techniques at the NCNR use CHRNS-funded instruments, and more than one third of NCNR publications (see the "Publications" section on p. 65), over the current one-year period, are based on research performed using these instruments. In 2010 more than 25 Ph.D. dissertations were completed using results from CHRNS-sponsored instruments.

Scientific Support Services

An important ingredient of the CHRNS operation is its support of staff whose principal responsibility is to provide services that are essential to the success of neutron scattering investigations. One such service is the provision and operation of an expanding range of sample

FIGURE 1: Participants in the NCNR 2011 Summer School "Methods and Applications of High Resolution Neutron Spectroscopy and Small Angle Neutron Scattering."

FIGURE 2: The 2011 SURF students, NCNR director Rob Dimeo (left), and CHRNS director Dan Neumann (second from right).

environment equipment, covering low and high temperatures, elevated pressures, gas handling, magnetic fields, motion and temperature control and electronics. This past year sample environment team members concentrated their efforts on providing service to users so that they could successfully run their experiments before the scheduled long outage. During the outage they worked on a variety of projects designed to ensure that the equipment works properly and meets the users' needs.

These projects have included

- installation and testing of a new variable temperature insert for the 10 T magnet,
- deployment of a ^{3}He refrigerator for the 7 T magnet,
- re-commissioning of the 11.5 T magnet with dilution refrigerator,
- maintenance and refurbishment of the entire helium cryostat fleet,
- maintenance of the bottom-loading closed-cycle refrigerators, including testing and deployment of swivel fittings to aid in hose management.

Other CHRNS-supported services include the maintenance of several well-equipped user laboratories, and the development, documentation and maintenance of data reduction, visualization, and analysis software through the DAVE project.

The DAVE software continues to be maintained and developed to keep abreast with feature requests and with improvements in instrumentation. DAVE is distributed as a desktop application and is available free of charge from the web site http://www.ncnr.nist.gov/dave/, either as a binary executable with an embedded runtime license or as the complete source code. Our development efforts over the past year have been focused on improving and extending the planning, reduction and analysis of data collected on supported instruments, especially the triple axis instruments MACS and BT-7. Both instruments require sophisticated data treatment to handle the large datasets accumulated using multi-detector systems.

Education and Outreach

One of the principal missions of the CHRNS program is to contribute to the development of human resources through education and outreach, thereby fostering future generations of scientists and neutron scatterers.

The CHRNS summer schools are very effective in educating potential new users of neutron scattering since typically more than 70 % of the participants return to the NCNR for their own research. The reactor shutdown in 2011 provided a unique opportunity to enhance and expand the summer school offerings. A school entitled "Methods and Applications of High Resolution Neutron Spectroscopy and Small Angle Neutron Scattering" was held on June 12-16, and a school on "Methods and Applications of Cold and Thermal Neutron Spectroscopy" was held the following week, from June 19-23. Together the schools served 62 students, almost double the number served in a typical year. Lectures, research seminars, and hands-on instruction in data reduction and analysis techniques were highlighted for a wide variety of neutron measurement techniques from spin echo to triple-axis

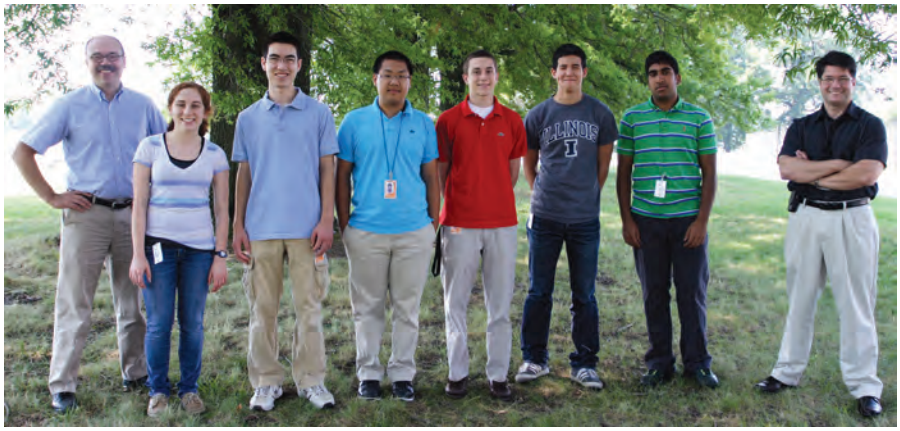

FIGURE 3: Participants in the NIST Summer High School Internship Program, flanked by Dan Neumann (left) and Rob Dimeo (right).

spectroscopy. The student to staff ratio was low, as in previous years, and the students had many opportunities to consult with the guest lecturers. A new feature of this year's schools was an oral session in which the students introduced themselves and gave two minute presentations describing their current research. NCNR staff members agreed that the introductory session enabled them to better tailor their instruction to the specific backgrounds of the students.

Another school, entitled "Modeling Neutron Data of Biological Systems", was held at the NCNR on July 11-15, 2011. The 21 student attendees were taught modern atomistic approaches to modeling SANS, reflectivity, and backscattering data. The modeling methods included molecular dynamics and molecular Monte Carlo simulations of proteins and protein-nucleic acid systems. The school also featured an introductory tutorial prepared by Prasad Gerard from Poolesville High School, who worked with the school organizers during the summer as part of the RET (Research Experience for Teachers) program at the NCNR.

The "Second School on Representational Analysis and Magnetic Structures" was held at Georgetown University on July 31 – August 5. The school highlighted guest lectures on representational analysis of inherent symmetries in complex magnetic structures. There were 21 participants, many of whom were treated to a tour of the NCNR facilities earlier in the week.

In 2011 CHRNS once again participated in NIST's Summer Undergraduate Research Fellowship (SURF) program, this time hosting ten students who worked with staff members studying topics such as thin-film deposition, x-ray characterization, biological sample deuteration, web-based data reduction, and reactor control systems development. Two of the students were stationed at the Institute for Bioscience and Biotechnology Research. The students' accomplishments were highlighted in oral presentations that they gave during the SURF colloquium in early August.

The NCNR also took part in the NIST Summer High School Internship Program, known as SHIP. Six students from four local high schools performed research with NCNR staff members. Three of them worked as a team to develop web-based data analysis capabilities for SANS, reflectometry, and triple axis measurements. The others had projects that involved fabrication of magnetic refrigerants, the analysis of magnetic reflections in crystal diffraction data, and the extension of NIST-authored FiPy software to the analysis of thin films of photomagnetic materials. The students presented their results in an oral session at the NCNR and at a NIST-wide poster session.

The NCNR once again participated in the annual "Summer Institute for Middle School Science Teachers." This two week program, sponsored by NIST, provides middle school teachers with an enhanced understanding of the scientific process. This year the program hosted twenty-one teachers from Maryland, Virginia, Washington DC, Illinois, North Carolina, and South Carolina. On July 25 the group toured the NCNR and attended lectures and demonstrations that described how neutrons are used to probe matter. They were also provided the opportunity to interact with SURF students, SHIP students, and the scientific staff. The highlight of the presentation as always was the mousetrap and ping pong ball demonstration of a chain reaction. In their evaluations, the teachers indicated that they had gained a greater appreciation of what can be accomplished using neutron scattering.

Other education and outreach activities during the year included "Take Your Daughters and Sons to Work Day" in April. Every year NIST hosts more than 250 elementary and middle school students. As part of this site-wide yearly program, the NCNR provides tours of the facility, lectures, and specially designed demonstrations that show middle school age children how neutrons are used to probe matter. In addition, the NCNR provided tours to elementary, middle and high school students from private and public schools. The students from the magnet programs at Roberto Clemente and Takoma Park middle schools were particularly impressed with the interactive demonstration of liquid nitrogen and its applications in sample environment.

FIGURE 4: Middle school science teachers and NCNR/CHRNS staff members.

Awards 2011

NCNR's **Hui Wu** is the 2010 recipient of the (Professor Surhain) Sidhu Award of the Pittsburgh Diffraction Society "for her exceptional contribution to the structural investigation of new materials for energy storage applications." The award goes to an outstanding scientist who is within 6 years of having earned the Ph.D. or its equivalent. The prize, bestowed biannually, carries a cash prize of $2000. Dr. Wu received the award at the Society conference where she also presented the Sidhu Award Lecture.

Daniel Hussey, an instrument scientist for the Neutron Imaging Facility of the NCNR, received a 2010 Presidential Early Career Awards for Scientists and Engineers (PECASE) for showing scientific excellence at an early stage of his career. In the recent past, he has played a key role in the development of neutron imaging methods for hydrogen fuel cell research for automotive applications. He is also involved in a project aimed at the improvement of Li-ion batteries, as well as in several other projects relevant to the structure of materials and the fundamental properties of the neutron. Dr. Hussey is currently designing an advanced cold-neutron phase imaging instrument for neutron radiography.

NCNR's **Craig Brown** received a Department of Commerce Silver Medal. He is being recognized "For critical advances in our understanding of new materials for hydrogen energy storage in next-generation clean automobiles."

Reactor Health Physicist **Jim Clark** received a Department of Commerce Silver Medal.The citation reads as follows: "For leadership in managing the recovery and restoration of the NIST Boulder laboratories that were contaminated as a result of the Plutonium Spill Incident of June 9, 2008."

NCNR's **Daniel Dender** and **Julia K. Scherschligt** have won the 2010 NIST Safety Award. The purpose of this award is "to recognize NIST employees and organizations for substantial contributions to improving safety at NIST." Julia and Dan are being recognized for their "innovative design, used nationwide, of a robust safety system to prevent accidental build-up of dangerous over-pressure conditions in cryostats."

NCNR's **Matt Hudson** was the co-winner of Sigma Xi's annual NIST Post-doc Poster Presentation in the area of Materials for his poster entitled "CO_2 Separation and Hydrogen Storage Properties of Zeolites for Clean Energy Applications."

NCNR's **Efrain Rodriguez** was named a runner-up of Sigma Xi's annual NIST Post-doc Poster Presentation in the area of Materials, for his poster entitled "Neutron Scattering of New Iron-Based Superconductors."

NCNR's **Alan Munter** has received a Special Act Award from the NIST Safety Office for his "significant role in the chemical inventory migration of all NIST Organizational Units."

Matt Helgeson has been awarded the 2011 Victor K. LaMer award from the Division of Colloid & Surface Chemistry of the American Chemical Society. Helgeson received his Ph.D. in chemical engineering from the University of Delaware in 2009 making many of his dissertation measurements at the NCNR. He is currently a postdoctoral associate in the Novartis-MIT Center for Continuous Manufacturing.

In March 2011, **Robert J. Cava** of Princeton University received the ACS Award in Inorganic Chemistry from the American Chemical Society. He has also received the Gutenberg Lecture Award worth □10,000 from the MAINZ Graduate School for his research on superconductivity. Cava, who was a NIST post-doc in the late 1970's, has 500 publications which have been cited 30,000 times. 100 of these papers are in collaboration with NCNR scientists.

The Canadian Association of Physicists and the Division of Condensed Matter and Materials Physics has awarded the 2011 CAP/DCMMP Brockhouse Medal to **Bruce D. Gaulin**, McMaster University, for his internationally recognized contributions to the field of collective phenomena in magnetic, superconducting and structural systems using x-ray and neutron scattering techniques. Gaulin is a frequent facility user at the NCNR.

In the student paper competition at the 2010 Canadian Association of Physicists congress, McMaster University graduate students Bruce Gaulin, **Patrick Clancy** and **Kate Ross**, won 1st and 3rd place, respectively, in the division of Condensed Matter and Materials Physics. Ross and Clancy carried out many of their neutron measurements at the NCNR. **Patrick Clancy** went on to be awarded one of 70 inaugural $140,000 (Canadian $) two-year Banting postdoctoral fellowships.

Ioanna Bakaimi of the Institute of Electronic Structure & Laser (IESL), Foundation for Research & Technology - Hellas (FORTH) won an award at the XXVI Panhellenic Conference on Solid State Physics and Materials Science for the best oral presentation: "Frustration and Induced Magnetodielectric Coupling in $NaMgO_2$ Polymorphs." The work was largely carried out while Bakaimi was guest scientist at the NCNR.

Publications: August 1, 2010 to July 31, 2011

Aaron, D.S., Borole, A.P., Hussey, D.S., Jacobson, D.L., Yiacoumi, S., Tsouris, C., "Quantifying the Water Content in the Cathode of Enzyme Fuel Cells via Neutron Imaging," J. Power Sources **196**(4), 1769 (2011).

Akcora, P., Kumar, S.K., Garcia Sakai, V., Li, Y., Benicewicz, B.C., Schadler, L.S., "Segmental Dynamics in PMMA-Grafted Nanoparticle Composites," Macromol. **43**(19), 8275 (2010). **[CHRNS]**

Angelova, L.V., Terech, P., Natali, I., Dei, L., Carretti, E., Weiss, R.G., "Cosolvent Gel-like Materials from Partially Hydrolyzed Poly(vinyl acetate)s and Borax," Langmuir, in press.

Armstrong, C.L., Kaye, M.D., Zamponi, M., Mamontov, E., Tyagi, M., Jenkins, T., Rheinstädter, M.C., "Diffusion in Single Supported Lipid Bilayers Studied by Quasi-Elastic Neutron Scattering," Soft Matter **6**, 5864 (2010). **[CHRNS]**

Aronson, M., Kim, M., Bennett, M., Janssen, Y., Sokolov, D.A., Wu, L., "Field Tuning and Quantum Criticality in Ytterbium Based Heavy Electron Compounds," J. Low Temp. Phys. **161**, 98 (2010). **[CHRNS]**

Asada, M., Gin, P., Endoh, M.K., Satija, S.K., Taniguchi, T., Koga, T., "Directed Self-Assembly of Nanoparticles at the Polymer Surface by Highly Compressible Supercritical Carbon Dioxide," Soft Matter, in press.

Babcock, E., Boag, S., Beecham, C., Chupp, T.E., Gentile, T.R., Jones, G.L., Petukhov, A.K., Walker, T.G., "Effects of High Intensity Neutron Flux on In-situ Spin-exchange Optical Pumping of ^{3}He," J. Phys.: Conf. Series **294**, 012011 (2011).

Bai, Z., Xie, Y., Chen, C., Cosgrove, T., Qiu, D., "A Small-Angle Neutron Scattering Study of Poly(ethylene oxide) Microstructure in Aqueous Poly(styrenesulfonate Sodium) Solutions," J. Colloid Interface Sci. **358**, 226 (2011).

Balzar, D., "Coherency Strain and Dislocations in Copper-Rich-Precipitate Embrittled A710 Ferritic Steels," Metall. Mater. Trans. A, in press.

Bao, W., Huang, Q., Chen, G.F., Green, M.A., Wang, D.M., He, J.B., Wang, X.Q., Qiu, Y., "A Novel Large Moment Antiferromagnetic Order in $K_{0.8}Fe_{1.6}Se_2$ Superconductor," Chinese Phys. Lett. **28**(8), 086104-1 (2011).

Bianoco, C.L., Schneider, C.S., Santonicola, M., Lenhoff, A.M., Kaler, E.W., "Effects of Urea on the Microstructure and Phase Behavior of Aqueous Solutions of Poly(oxyethylene) Surfactants," Ind. Eng. Chem. Res. **50**, 85 (2011). **[CHRNS]**

Bloch, E.D., Murray, L.J., Queen, W., Chavan, S., Maximoff, S.N., Bigi, J.P., Krishna, R., Peterson, V.K., Grandjean, F., Long, G.J., Smit, B., Bordiga, S., Brown, C.M., Long, J.R., "Selective Binding of O_2 over N_2 in a Redox-Active Metal-Organic Framework with Open Iron(II) Coordination Sites," J. Am. Chem. Soc., in press.Borreguero, J.M., He, J., Meilleur, F., Weiss, K., Brown, C.M., Myles, D.A., Herwig, K.W., Agarwal, P.K., "Redox-Promoting Protein Motions in Rubredoxin," J. Am. Chem. Soc. **115**, 8925 (2011).

Borreguero, J.M., He, J., Meilleur, F., Weiss, K., Brown, C.M., Myles, D.A., Herwig, K.W., Agarwal, P.K., "Redox-Promoting Protein Motions in Rubredoxin," J. Am. Chem. Soc. **115**, 8925 (2011). **[CHRNS]**

Braisted, J., Schneider, E., O'Kelly, S., Van der Hoeven, C., "Design of an Irradiation Facility with a Real-Time Radiation Effects Monitoring Capability," Nucl. Instrum. Meth. A, in press.

Braunagel, J., Junghans, A., Koper, I., "Membrane-Based Sensing Approaches," Australian J. Chem. **64**(1), 54 (2011).

Burgess, I.J., "Applications of Neutron Reflectivity in Biochemistry," in "Advances in Electrochemical Science and Engineering, Volume 13 – Bioelectrochemistry," edited by Alkire, R.C., Kolb, D.M., Lipkowski, J. (Wiley-VCH, Weinheim, Germany), Chap. 3, 143 (2011).

Burress, J., Srinivas, G., Ford, J., Simmons, J.M., Zhou, W., Yildirim, T., "Graphene Oxide Framework Materials: Theoretical Predictions and Experimental Results," Angew. Chem. Int. Edit. **49**, 8902 (2010).

Butch, N.P., Jeffries, J.R., Chi, S.X., Leão, J.B., Lynn, J.W., Maple, M. Brian, "Antiferromagnetic Critical Pressure in URu_2Si_2 Under Hydrostatic Conditions," Phys. Rev. B **82**(6), 060408-1 (2010).

Butch, N.P., Jeffries, J.R., Evans, W.J., Chi, S.X., Leão, J.B., Lynn, J.W., Sinogeikin, S.V., Hamlin, J., Zocco, D.A., Maple, M.B., "The Pressure-Temperature Phase Diagram of URu_2Si_2 Under Hydrostatic Conditions" in "Basic Actinide Science and Materials for Nuclear Applications," edited by Gibson, J.K., McCall, S.K., Bauer, E.D., Soderholm, L., Fanghaenel, T., Devanathan, R., Misra, A., Trautmann, C., Wirth, B.D., (Mater. Res. Soc. Symp. Proc., Cambridge Univ. Press, April 2010, San Francisco, CA) **1264**, Z10-03 (2010).

Cappelletti, R.L., editor, "2010 NIST Center for Neutron Research Accomplishments and Opportunities," NIST SP 1110 (2010).

Chan, A.S.W., Groves, M.N., Li, X., Malardier-Jugroot, C., "Conformation of pH Responsive Alternating Copolymers and Self-assembly in Nanoarchitectures" in "TechConnect World 2010 Proceedings: Nanotechnology 2010 Volume 1 - Advanced Materials, CNTs, Particles, Films and Composites," (NSTI, June 2010, Anaheim, CA) Chap. 1, 41 (2010).

Chang, L.J., Schweika, W., Kao, Y.-J., Chou, Y.Z., PerBon, J., Bruckel, T., Yang, H.C., Chen, Y.Y., Gardner, J.S., "Magnetic Correlations in $Ho_xTb_{2-x}Ti_2O_7$," Phys. Rev. B **83**(14), 14413-1 (2011).

Chen, L., Hu, F.X., Wang, J., Shen, J., Sun, J.R., Shen, B.G., Yin, J.H., Pan, L.Q., Huang, Q., "Effect of Post-Annealing on Martensitic Transformation and Magnetocaloric Effect in $Ni_{45}Co_5Mn_{36.7}In_{13.3}$ Alloys," J. Appl. Phys. **109**(7), 07A939-1 (2011).

Chen, S., Zhang, Y.N., "Dynamic Crossover Phenomenon in Confined Water and Its Relation to the Liquid-Liquid Critical Point: Experiments and MD Simulations" in "Proceedings of the International School of Physics 'Enrico Fermi', Course CLXXVI," edited by Mallamace, F., Stanley, E., (SIF and IOS Press, June 2010, Varenna, Italy), in press. **[CHRNS]**

Chen, W., Gentile, T.R., Fu, C.B., Watson, S., Jones, G.L., McIver, J.W., Rich, D.R., "Polarized ^{3}He Cell Development and Application at NIST," J. Phys.: Conf. Series **294**, 012003 (2011).

Chen, W., Wang, J., Wei, X., Balazs, A.C., Matyjaszewski, K., Russell, T.P., "UV-Enhanced Ordering in Azobenzene-Containing Polystyrene-block-Poly(n-Butyl Methacrylate) Copolymer Blends," Macromol. **44**, 278 (2011).

Chen, W., Wei, X., Balazs, A.C., Matyjaszewski, K., Russell, T.P., "Phase Behavior and Photoresponse of Azobenzene-Containing Polystyrene-block-poly(n-butyl methacrylate) Block Copolymers," Macromol. **44**(5), 1125 (2011).

Cheng, G., Liu, Z., Murton, J.K., Jablin, M., Dubey, M., Majewski, J., Halbert, C., Browning, J., Ankner, J.F., Akgun, B., Wang, C., Esker, A.R., Sale, K.L., Simmons, B., Kent, M.S., "Neutron Reflectometry and QCM-D Study of the Interaction of Cellulases with Films of Amorphous Cellulose," Biomacromol. **12**, 2216 (2011).

Chi, S.X., Lynn, J.W., Chen, Y., Ratcliff, II, W., Ueland, B., Butch, N.P., Saha, S.R., Kirshenbaum, K., Paglione, J., "Nitrogen Contamination in Elastic Neutron Scattering," Meas. Sci. Tech. **22**, 047001-1 (2011).

Choi, S., Bates, F.S., Lodge, T.P., "Molecular Exchange in Ordered Diblock Copolymer Micelles," Macromol. **44**, 3594 (2011).

Choi, S., Lee, S., Soto, H.E., Lodge, T.P., Bates, F.S., "Nanoscale Mixing of Soft Solids," J. Am. Chem. Soc. **133**, 1722 (2011).

Chu, X., Liu, K., Tyagi, M., Mou, C., Chen, S., "Low-Temperature Dynamics of Water Confined in a Hydrophogic Mesoporous Material," Phys. Rev. E **82**(2), 020501-1 (2010). **[CHRNS]**

Chuang, A.C., Liu, Y., Udovic, T.J., Liaw, P.K., Yu, G., Huang, J., "Inelastic Neutron Scattering Study of Hydrogenated $(Zr_{55}Cu_{30}Ni_5Al_{10})_{99}Y_1$ Bulk Metallic Glass," Phys. Rev. B **83**(17), 174206-1 (2011).

Chung, J.-H., Song, Y., Yoo, T., Chung, S., Lee, S., Kirby, B.J., Liu, X., Furdyna, J.K., "Investigation of Weak Interlayer Exchange Coupling in the GaMnAs/GaAs Superlattice with Insulating Nonmagnetic Spacers," J. Appl. Phys. **110**(1), 013912 (2011).

Chung, S., Lee, S., Chung, J., Yoo, T., Lee, H., Kirby, B.J., Liu, X., Furdyna, J.K., "Giant Magnetoresistance and Long-Range Antiferromagnetic Interlayer Exchange Coupling in (Ga,Mn)As/GaAs:Be Multilayers," Phys. Rev. B **82**(5), 054420-1 (2010).

Chung, Y.S., Shin, N., Kang, J., Jo, Y., Prabhu, V.M., Satija, S.K., Kline, R.J., DeLongchamp, D.M., Toney, M.F., Loth, M.A., Purushothaman, B., Anthony, J.E., Yoon, D.Y., "Zone-Refinement Effect in Small-Molecule-Polymer Blend Semiconductors for Organic Thin-Film Transistors," J. Am. Chem. Soc. **133**, 412 (2011).

Cicerone, M.T., Zhong, Q.N., Johnson, J., Aamer, K.A., Tyagi, M., "Surrogate for Debye-Waller Factors from Dynamic Stokes Shifts," J. Phys. Chem. Lett. **2**, 1464 (2011). **[CHRNS]**

Climent-Pascual, E., Ni, N., Jia, S., Huang, Q., Cava, R.J., "Polymorphism in $BaPb_{1-x}Bi_xO_3$ at the Superconducting Composition," Phys. Rev. B **83**(17), 174152-1 (2011).

Couet, A., Motta, A.T., Comstock, R.J., Paul, R.L., "Cold Neutron Prompt Gamma Activation Analysis, a Non-destructive Technique for Hydrogen Level Assessment in Zirconium Alloys," J. Nucl. Mater., in press.

Curtis, J., Bates, F.S., Fultz, B., Harmon, B.N., Herwig, K.W., Myles, D.A.A., Rez, P., Trouw, F., Fultz, B., "Nanostructures: Structure and Dynamics," in "Workshop on Computational Scattering Science," edited by Fultz, B., Herwig, K.W., Long, G.G. (Workshop Rep., July 2010, Argonne National Laboratory, Argonne, IL), 24 (2010).

Da Luz, M.S., Neumeier, J.J., dos Santos, C.A.M., White, B.D., Izario Filho, H.J., Leão, J.B., Huang, Q., "Neutron Diffraction Study of Quasi-one-dimensional Lithium Purple Bronze: Possible Mechanism for Dimensional Crossover," Phys. Rev. B **84**(1), 014108-1 (2011).

Das, N.C., Sokol, P.E., "Hybrid Photovoltaic Devices from Regioregular Polythiophene and ZnO Nanoparticles Composites," Renewable Energy **35**, 2683 (2010).

Datta, S., Heinrich, F., Raghunandan, S., Krueger, S., Curtis, J., Rein, A., Nanda, H., "HIV-1 Gag Extension: Conformational Changes Require Simultaneous Interaction with Membrane and Nucleic Acid," J. Mol. Biol. **406**, 205 (2011). **[CHRNS]**

DeCaluwe, S.C., Grass, M.E., Zhang, C., El Gabaly, F., Bluhm, H., Liu, Z., Jackson, G.S., McDaniel, A.H., McCarty, K.F., Farrow, R.L., Linne, M.A., Hussain, Z., Eichhorn, B.W., "In Situ Characterization of Ceria Oxidation States in High-Temperature Electrochemical Cells with Ambient Pressure XPS," J. Phys. Chem. C **114**, 19853 (2010).

Diallo, S.O., Azuah, R.T., Glyde, H.R., "The Quest for Bose-Einstein Condensation in Solid ^{4}He," J. Low Temp. Phys. **162**, 449 (2010).

Dufour, C., Fitzsimmons, M.R., Borchers, J.A., Krycka, K.L., Dumesnil, K., Watson, S.M., Chen, W., Won, J., Singh, S., "Nanometer-size Magnetic Domains and Coherent Magnetization Reversal in a Giant Exchange-bias System," Phys. Rev. B **84**(6), 064420-1 (2011).

Dumas, R.K., Fang, Y., Kirby, B.J., Zha, C., Bonanni, V., Nogues, J., Akerman, J., "Probing Vertically Graded Anisotropy in FePtCu Films," Phys. Rev. B **84**(5), 054434-1 (2011).

Dura, J.A., Kelly, S.T., Kienzle, P.A., Her, J.-H., Udovic, T.J., Majkrzak, C.F., Chung, C., Clemens, B.M., "Porous Mg Formation Upon Dehydrogenation of MgH_2 Thin Films," J. Appl. Phys. **109**(9), 093501-1 (2011).

Dutton, S.E., Huang, Q., Tchernyshyov, O., Broholm, C.L., Cava, R.J., "Sensitivity of the Magnetic Properties of the $ZnCr_2O_4$ and $MgCr_2O_4$ Spinels to Nonstoichiometry," Phys. Rev. B **83**(6), 064407-1 (2011).

Eberle, A.P.R., Wagner, N.J., Castañeda-Priego, R., "Dynamical Arrest Transition in Nanoparticle Dispersions with Short-Range Interactions," Phys. Rev. Lett. **106**(10), 105704-1 (2011). **[CHRNS]**

Eckert, J., Trouw, F.R., Mojet, B., Forster, P., Lobo, R., "Interaction of Hydrogen with Extraframework Cations in Zeolite Hosts Probed by Inelastic Neutron Scattering Spectroscopy," J. Nanosci. Nanotech. **10**, 49 (2010).

El-Khatib, S., Bose, S., He, C., Kuplic, J., Laver, M., Borchers, J.A., Huang, Q., Lynn, J.W., Mitchell, J.F., "Spontaneous Formation of an Exchange Spring Composite via Magnetic Phase Separation in $Pr_{1-x}Ca_xCoO_3$," Phys. Rev. B **82**(10), 100411-1 (2010). **[CHRNS]**

Fagan, J.A., Bauer, B.J., Becker, M.L., Hight Walker, A.R., Simpson, J., Chun, J., Obrzut, J., Phelan, F.R., Simien, D., Huh, J.Y., Migler, K., "Carbon Nanotubes: Measuring Dispersion and Length," Adv. Mater. **23**, 338 (2011).

Fagan, J.A., Lin, N.J., Zeisler, R, Hight, W.A.R., "Effects of Gamma Irradiation for Sterilization on Aqueous Dispersions of Length Sorted Carbon Nanotubes," Nano Res. **4**(4), 393 (2011).

Fahey, A.J., Zeissler, C.J., Newbury, D.E., Lindstrom, R.M., "Postdetonation Nuclear Debris for Attribution," Proc. Natl. Acad. Sci. USA **107**(47), 20207 (2010).

Faraone, A., Hagaman, E.W., Han, K.S., Fratini, E., "A Low-Temperature Crossover in Water Dynamics in an Aqueous LiCl Solution: Diffusion Probed by Neutron Spin-Echo and Nuclear Magnetic Resonance," J. Phys. Chem. B **114**(50), 16737 (2010).

Ferguson, P.P., Todd, A.D.W., Dahn, J.R., "Importance of Nanostructure for High Capacity Negative Electrode Materials for Li-ion Batteries," Electrochem. Commun. **12**, 1041 (2010).

Feygenson, M., Teng, X., Inderhees, S.E., Yiu, Y., Du, W., Han, W., Wen, J., Xu, Z., Podlesnyak, A.A., Niedziela, J.L., Hagen, M., Qiu, Y., Brown, C.M., Zhang, L., Aronson, M.C., "Low-Energy Magnetic Excitations in Co/CoO Core/Shell Nanoparticles," Phys. Rev. B **83**(17), 174414-1 (2011). **[CHRNS]**

Finnerty, P., MacMullin, S., Back, H.O., Henning, R., Long, A., Macon, K.T., Strain, J., Lindstrom, R.M., Vogelaar, R.B., "Low-Background Gamma Counting at the Kimballton Underground Research Facility," Nucl. Instrum. Meth. A **642**, 65 (2011).

Fisher, B.M., Abdurashitov, J.N., Coakley, K.J., Gavrin, V.N., Gilliam, D.M., Nico, J.S., Shikhin, A.A., Thompson, A.K., Vecchia, D.F., Yants, V.E., "Fast Neutron Detection with ^{6}Li-Loaded Liquid Scintillator," Nucl. Instrum. Meth. A **646**, 126 (2011).

Fratini, E., Faraone, A., Todea, A.M., Baglioni, P., "Hydrated $Mo_{72}Fe_{30}$ Clusters: Low-Frequency Hydrogen Modes and Self-Aggregation," Inorg. Chim. Acta **363**, 4234 (2010). **[CHRNS]**

Freedman, D.E., Han, T.H., Prodi, A., Muller, P., Huang, Q., Chen, Y., Webb, S.M., Lee, Y.S., McQueen, T.M., Nocera, D.G., "Site Specific X-ray Anomalous Dispersion of the Geometrically Frustrated Kagomé Magnet, Herbertsmithite, $ZnCu_3(OH)_6Cl_2$," J. Am. Chem. Soc. **132**, 16185 (2010).

Freitas, R.S., Gardner, J.S., "The Magnetic Phase Diagram of $Gd_2Sn_2O_7$," J. Phys.: Condens. Matter **23**, 164215-1 (2011).

Frick, B., Neumann, D.A., "Neutron Backscattering," in "Neutrons in Soft Matter," edited by Imae, T., Kanaya,T., Furusaka, M., and Torikai, N. (John Wiley & Sons, Inc., May 2011, Hoboken, NJ), Chap. II.3.2, 183 (2011).

Fu, C.B., Gentile, T.R., Jones, G.L., Chen, W., Erwin, R.W., Watson, S., Broholm, C.L., Rodriguez, J.A., Scherschligt, J.K., "A Wide Angle Neutron Spin Filter System Using Polarized ^{3}He," Physica B **406**, 2419 (2011). **[CHRNS]**

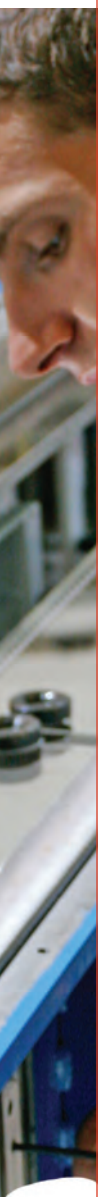

Fu, C.B., Gentile, T.R., Snow, W.M., "Limits on Possible New Nucleon Monopole-Dipole Interactions from the Spin Relaxation Rate of Polarized ^{3}He Gas," Phys. Rev. D **83**(3), 031504-1 (2011).

Fu, R.S., Preston, J.S., Pasaogullari, U., Shiomi, T., Miyazaki, S., Tabuchi, Y., Hussey, D.S., Jacobson, D.L., "Water Transport Across a Polymer Electrolyte Membrane Under Thermal Gradients," J. Electrochem. Soc. **158**(3), B303 (2011).

Gao, Y., Van Nguyen, T., Hussey, D.S., Jacobson, D.L., "In-situ Imaging of Water Distribution in a Gas Diffusion Layer by Neutron Radiography," ECS Trans. **33**(1), 1435 (2010).

Gardner, J.S., "Geometrically Frustrated Magnetism," J. Phys.: Condens. Matter **23**, 160301 (2011).

Gardner, J.S., Ehlers, G., Fouquet, P., Farago, B., Stewart, J.R., "Slow and Static Spin Correlations in $Dy_{2+\chi}$ $Ti_{2-\chi}$ $O_{7-\delta}$," J. Phys.: Condens. Matter **23**(16), 164220 (2011).

Gardner, J.S., Rule, K.C., Ruff, J.P.C., Clancy, J.P., Gaulin, B.D., "Cold Neutron Scattering Studies of Frustrated Pyrochlore Antiferromagnets," Nucl. Eng. Tech. **43**(1), 7 (2011).

Garg, S., Porcar, L., Woodka, A.C.,Butler, P., Perez-Salas, U., "Noninvasive Neutron Scattering Measurements Reveal Slower Cholesterol Transport in Model Lipid Membranes," Biophys. J. **101**, 370 (2011). **[CHRNS]**

Geissler, E., Hecht, A.-M., Horkay, F., "Scaling Behavior of Hyaluronic Acid in Solution with Mono- and Divalent Ions," Macromol. Symp. **291-292**, 362 (2010). **[CHRNS]**

Gentile, T.R., Bass, C.D., Nico, J.S., Breuer, H., Farrell, R., "Magnetic Field Effects on Large Area Avalanche Photodiodes at Cryogenic Temperatures," Nucl. Instrum. Meth. A, in press.

Gentile, T.R., Crawford, C.B., "Neutron Charge Radius and the Neutron Electric Form Factor," Phys. Rev. C **83**(5), 055203-1 (2011).

Gericke, M.T., Alarcon, R., Balascuta, S., Barron-Palos, L., Blessinger, C., Bowman, J.D., Carlini, R.D., Chen, W., Chupp, T.E., Crawford, C., Covrig, S., Dabaghyan, M., Fomin, N., Freedman, S.J., Gentile, T.R., Gillis, R.C., Greene, G.L., Hersman, F.W., Ino, T., Jones, G.L., Lauss, B., Leuschner, M., Lozowski, W.R., Mahurin, R., Masuda, Y., Mei, J., Mitchell, G.S., Muto, S., Nann, H., Page, S.A., Penttila, S.I., Ramsay, W.D., Salas-Bacci, A., Santra, S., Sharma, M., Seo, P., Sharapov, E.I., Smith, T.B., Snow, W.M., Wilburn, W.S., Yuan, V., "Measurement of Parity-Violating γ-ray Asymmetry in the Capture of Polarized Cold Neutrons on Protons," Phys. Rev. C **83**(1), 015505-1 (2011).

Ghosh, S., Zhou, H.D., Balicas, L., Hill, S., Gardner, J.S., Qiu, Y., Wiebe, C.R., "Short Range Ordering in the Modified Honeycomb Lattice Compound $SrHo_2O_4$," J. Phys.: Condens. Matter **23**, 164203 (2011). **[CHRNS]**

Ginley, T.P., Borchers, J.A., Kirby, B.J., Dennis, C.L., Carey, M.J., Childress, J.R., "Magnetization Reversal Mechanisms in Heusler Alloy Spin Valves," J. Appl. Phys. **109**(7), 07B110 (2011).

Glinka, C.J., "Incoherent Neutron Scattering from Multi-Element Materials," J. Appl. Crystallogr. **44**, 618 (2011).

Glyde, H.R., Diallo, S.O., Azuah, R., Kirichek, O., Taylor, J.W., "Bose-Einstein Condensation in Liquid ^{4}He Under Pressure," Phys. Rev. B **83**(10), 100507-1 (2011).

Gnäupel-Herold, T.H., Creuziger, A.A., "Diffraction Study of the Retained Austenite Content in TRIP Steels," Mater. Sci. Eng. A **528**, 3594 (2011).

Gomez del Rio, J., Hayes, D.G., Urban, V.S., "Partitioning Behavior of an Acid-Cleavable, 1,3-Dioxolane Alkyl Ethoxylate, Surfactant in Single and Binary Surfactant Mixtures for 2- and 3- Phase Microemulsion Systems According to Ethoxylate Head Group Size," J. Colloid Interface Sci. **352**, 424 (2010).

Greenberg, R.R., Bode, P., De Nadai Fernandes, E.A., "Neutron Activation Analysis: A Primary Method of Measurement," Spectrochim. Acta B: Atom. Spectr. **66**, 193 (2011).

Grieshaber, S.E., Nie, T., Yan, C., Zhong, S., Teller, S.S., Clifton, R.J., Pochan, D.J., Kiick, K.L., Jia, X., "Assembly Properties of an Alanine-Rich, Lysine-Containing Peptide and the Formation of Peptide/Polymer Hybrid Hydrogels," Macromol. Chem. Phys. **212**, 229 (2011).

Guidi, T., "Neutron Spectroscopy of Molecular Nanomagnets," in "Molecular Cluster Magnets," edited by Winpenny, R. (World Scientific Series in Nanoscience and Nanotechnology), in press. **[CHRNS]**

Guo, Y., Wu, H., Zhou, W., Yu, X., "Dehydrogenation Tuning of Ammine Borohydrides using Double-Metal Cations," J. Am. Chem. Soc. **113**, 4690 (2011).

Guo, Z., Wu, H., Srinivas, G., Zhou, Y., Xiang, S., Chen, Z., Yang, Y., Zhou, W., O'Keeffe, M., Chen, B., "A Metal-Organic Framework with Optimized Open Metal Sites and Pore Spaces for High Methane Storage at Room Temperature," Angew. Chem. Int. Edit. **50**(14), 3178 (2011).

Ham, M., Choi, J.H., Boghossian, A.A., Jeng, E.S., Graff, R.A., Heller, D.A., Chang, A.C., Mattis, A., Bayburt, T.H., Grinkova, Y.V., Zeiger, A.S., Van Vliet, K., Hobbie, E.K., Sligar, S., Wraight, C., Strano, M.S., "Photoelectrochemical Complexes for Solar Energy Conversion That Chemically and Autonomously Regenerate," Nat. Chem. **2**, 929 (2010).

Hammouda, B., "A New Guinier-Porod Model," J. Appl. Crystallogr. **43**, 716 (2010). **[CHRNS]**

Hammouda, B., "Analysis of the Beaucage Model," J. Appl. Crystallogr. **43**, 1474 (2010).

Hammouda, B., "Clustering in Polar Media," J. Chem. Phys. **133**(8), 084901-1 (2010). [CHRNS]

Hammouda, B., "SANS from Pluronic P85 in d-water," Eur. Polym. J. **46**, 2275 (2010). [CHRNS]

Han, T.H., Helton, J.S., Chu, S., Prodi, A., Singh, D.K., Mazzoli, C., Muller, P., Nocera, D.G., Lee, Y.S., "Synthesis and Characterization of Single Crystals of the Spin-½ Kagome-Lattice Antiferromagnets $Zn_xCu_{4-x}(OH)_6Cl_2$," Phys. Rev. B **83**(10), 100402-1 (2011). [CHRNS]

Hanson, H.A., Wang, X., Dimitrov, I.K., Shi, J., Ling, X.S., Maranville, B.B., Majkrzak, C.F., Laver, M., Keiderling, U., Russina, M., "Structural Evidence for an Edge-Contaminated Vortex Phase in a Nb Crystal Using Neutron Diffraction," Phys. Rev. B **84**(1), 014506-1 (2011).

Harrower, C., Poirier, E., Fritzsche, H., Kalisvaart, P., Satija, S.K., Akgun, B., Mitlin, D., "Early Deuteration Steps of Pd-and Ta/Pd-Catalyzed $Mg_{70}Al_{30}$ Thin Films Observed at Room Temperature," Int. J. Hydrogen Energy **35**, 10343 (2010).

Hatzell, M.C., Turhan, A., Kim, S., Hussey, D.S., Jacobson, D.L., Mench, M.M., "Quantification of Temperature Driven Flow in a Polymer Electrolyte Fuel Cell Using High-Resolution Neutron Radiograpy," J. Electrochem. Soc. **158**(6), B717 (2011).

He, F., Wang, W., Chen, W., Xu, T., Darling, S.B., Strzalka, J., Liu, Y., Yu, L., "Tetrathienoanthracene-Based Copolymers for Efficient Solar Cells," J. Am. Chem. Soc. **133**, 3284 (2011).

Helgeson, M.E., Porcar, L., Lopez-Barron, C., Wagner, N.J., "Direct Observation of Flow-Concentration Coupling in a Shear-Banding Fluid," Phys. Rev. Lett. **105**(8), 084501-1 (2010). [CHRNS]

Helgeson, M.E., Wagner, N.J., "Colloidal Interactions Mediated by End-adsorbing Polymer-Like Micelles," J. Chem. Phys., in press.

Helton, J., Singh, D., Nair, H.S., Elizabeth, S., "Magnetic Order of the Hexagonal Rare Earth Manganite $Dy_{0.5}Y_{0.5}MnO_3$," Phys. Rev. B, in press. [CHRNS]

Hong, T., Kim, Y.H., Hotta, C., Takano, Y., Tremelling, G., Turnbull, M.M., Landee, C.P., Kang, H., Christensen, N., Lefmann, K., Schmidt, K.P., Uhrig, G.S., Broholm, C., "Field-Induced Tomonaga-Luttinger Liquid Phase of a Two-Leg Spin-1/2 Ladder with Strong Leg Interactions," Phys. Rev. Lett. **105**, 137207-1 (2010). [CHRNS]

Hong, T., Poulton, S.J., Stock, C., Cabrera, I., Broholm, C.L., Qiu, Y., Leão, J.B, Copley, J.R.D., "Neutron Scattering Study of a Quasi-two-Dimensional Spin-1/2 Dimer System: Piperazinium Hexachlorodicuprate Under Hydrostatic Pressure," Phys. Rev. B **82**(18), 184424-1 (2010).

Hopkins, A.R., Tomczak, S.J., Vij, V., Jackson, A.J., "Small Angle Neutron Scattering (SANS) Characterization of Electrically Conducting Polyaniline Nanofiber/Polyimide Nanocomposties," Thin Solid Films, in press. [CHRNS]

Horkay, F., "Ionic Effects and Self-Assembly in the Solution of the Biopolymer Aggrecan," Polym. Prepr. **51**, 301 (2010).

Horkay, F., Magda, J., Alcoutlabi, M., Atzet, S., Zarembinski, T., "Structural, Mechanical and Osmotic Properties of Injectable Hyaluronan-Based Composite Hydrogels," Polymer **51**, 4424 (2010). [CHRNS]

Hould, N.D., Lobo, R.F., Wagner, N.J., "Indirect Fourier Transform and Model Fitting of Small Angle Neutron Scattering from Silica Nanoparticles," Part. Part. Sys. Charact., in press. [CHRNS]

Hu, N., Borkar, N., Kohls, D., Schaefer, D.W., "Characterization of Porous Materials Using Combined Small-Angle X-ray and Neutron Scattering Techniques," J. Membr. Sci. **379**, 138 (2011). [CHRNS]

Hu, Y., Liu, X.P., Ma, X., Rawal, A., Prozorov, T., Akinc, M., Mallapragada, S.K., Schmidt-Rohr, K., "Biomimetic Self-Assembling Copolymer-Hydroxyapatite Nanocomposities with the Nanocrystal Size Controlled by Citrate," Chem. Mater. **23**, 2481 (2011).

Huang, E., Liu, Y., Ren, Y., Porcar, L., Kai, J., Liaw, P.K., Smith, G.S., Chen, W., "Evolution of Microstructure in a Nickel-based Superalloy as a Function of Ageing Time," Phil. Mag. Lett. **91**(7), 483 (2011).

Hucker, M., Zimmermann, M.v., Gu, G.D., Xu, Z.J., Wen, J.S., Xu, G., Kang, H.J., Zheludev, A., Tranquada, J.M., "Stripe Order in Superconducting $La_{2-x}Ba_xCuO_4$ ($0.095 \leq x \leq 0.155$)," Phys. Rev. B **83**(10), 104506-1 (2011).

Hughes, P.P., Coplan, M.A., Thompson, A.K., Vest, R.E., Clark, C.W., "Far-Ultraviolet Signatures of the ^{3}He(n, tp) Reaction in Noble Gas Mixtures," Appl. Phys. Lett. **97**(23), 234105-1 (2010).

Hussey, D.S., Baltic, E., Jacobson, D.L., "Water Content Measurement of Gas Diffusion Media and Membranes by Neutron Radiography," ECS Trans. **33**(1), 1385 (2010).

Hussey, D.S., Jacobson, D.L., Baltic, E.M., "Changing Optical Axis due to Reactor Operation," Nucl. Instrum. Meth. A, in press.

Hyland, L.L., Taraban, M.B., Hammouda, B., Yu, Y.B., "Mutually Reinforced Multi-Component Polysaccharide Networks," Macromol., in press. [CHRNS]

Iida, K., Qiu, Y., Sato, T.J., "Dzyaloshinsky-Moriya Interaction and Long Lifetime of the Spin State in the Cu_3 Triangular Spin Cluster by Inelastic Neutron Scattering Measurements," Phys. Rev. B, in press. **[CHRNS]**

Iqbal, U., Albaghadadi, H., Nieh, M., Tuor, U.I., Mester, Z., Stanimirovic, D., Katsaras, J., Abulrob, A., "Small Unilamellar Vesicles: A Platform Technology for Molecular Imaging of Brain Tumors," Nanotech. **22**, 195102-1 (2011).

Ishii, R., Tanaka, S., Onuma, K., Nambu, Y., Tokunaga, M., Sakakibara, T., Kawashima, N., Maeno, Y., Broholm, C.L., Gautreaux, D.P., Chan, J.Y., Nakatsuji, S., "Successive Phase Transitions and Phase Diagrams for the Quasi-two-dimensional Easy-Axis Triangular Antiferromagnet $Rb_4Mn(MoO_4)_3$," Europhys. Lett. **94**(1), 17001-p1 (2011).

Jackson, A.J., McGillivray, D.J., "Protein Aggregate Structure Under High Pressure," Chem. Comm. **47**, 487 (2011). **[CHRNS]**

Jacobson, D.L., Hussey, D.S., Baltic, E.M., Udovic, T.J., Rush, J.J., Bowman, J.R.C., "Neutron Imaging Studies of Metal-Hydride Storage Beds," Int. J. Hydrogen Energy **35**, 12837 (2010).

Jacques, D.A., Langley, D.B., Hynson, R.M.G., Whitten, A.E., Kwan, A., Guss, J.M., Trewhella, J., "A Novel Structure of an Antikinase and its Inhibitor," J. Mol. Biol. **405**, 214 (2011). **[CHRNS]**

Jacquin, M., Muller, P., Cottet, H., Theodoly, O., "Self-Assembly of Charged Amphiphilic Diblock Copolymers with Insoluble Blocks of Decreasing Hydrophobicity: From Kinetically Frozen Colloids to Macrosurfactants," Langmuir **24**(24), 18681 (2010). **[CHRNS]**

Jeong, Y., Chung, T.C. Mike, "The Synthesis and Characterization of a Super-Activated Carbon Containing Substitutional Boron (BC_x) and its Applications in Hydrogen Storage," Carbon **48**, 2526 (2010).

Jiang, P., Li, J., Sleight, A.W., Subramanian, M.A., "New Oxides Showing an Intense Orange Color Based on Fe^{3+} in Trigonal-Bipyramidal Coordination," Inorg. Chem. **50**, 5858 (2011).

Jiang, Y., Huq, A., Booth, C.H., Ehlers, G., Greedan, J.E., Gardner, J.S., "Order and Disorder in the Local and Long-Range Structure of the Spin-Glass Pyrochlore, $Tb_2Mo_2O_7$," J. Phys.: Condens. Matter **23**, 164214 (2011).

Jin, L., Rother, G., Cole, D.R., Mildner, D.F.R., Duffy, C.J., Brantley, S.L., "Characterization of Deep Weathering and Nanoporosity Development in Shale - a Neutron Study," Am. Mineral. **96**(4), 498 (2011). **[CHRNS]**

Johansen, D., Jeffries, C.M., Hammouda, B., Trewhella, J., Goldenberg, D.P., "Macromolecular Crowding of an Intrinsically Disordered Protein Characterized by Small Angle Neutron Scattering," Biophys. J. **100**, 1120 (2011). **[CHRNS]**

Ju, H., Heuser, B.J., Abernathy, D., Udovic, T.J., "Comparison of FANS and ARCS Incoherent Inelastic Neutron Scattering Measurements of Hydrogen Trapped at Dislocations in Deformed Pd," Nucl. Instrum. Meth. A, in press.

Junghans, A., Champagne, C., Cayot, P., Loupiac, C., Koper, I., "Probing Protein-Membrane Interactions Using Solid Supported Membranes," Langmuir **27**, 2709 (2011).

Kalinichev, A., Iskrenova-Tchoukova, E., Faraone, A., Kirkpatrick, R., "Molecular Mechanisms of the Librational Motions of Water in the Interlayers of Hydrocalumite," Geochim. Cosmochim. Acta **74**(12), A489 (2010). **[CHRNS]**

Kamazawa, K., Nozkai, H., Harada, M., Mukai, K., Ikedo, Y., Iida, K., Sato, T.J., Qiu, Y., Tyagi, M., Sugiyama, J., "Interrelationship Among Li^+ Diffusion, Charge, and Magnetism for $^7LiMn_2O_4$ and $^7Li_{1.1}Mn_{1.9}O_4$: Elastic, Inelastic, and Quasielastic Neutron Scattering," Phys. Rev. B **83**(9), 094401-1 (2011).

Kang, H.J., Lee, Y.S., Lynn, J.W., Shiryaev, S.V., Barilo, S.N., "Soft Phonons and Structural Phase Transition in Superconducting $Ba_{0.59}K_{0.41}BiO_3$," Physica C **471**, 303 (2011).

Karhu, E.A., Kahwaji, S., Robertson, M.D., Fritzche, H., Kirby, B.J., Majkrzak, C.F., Monchesky, T.L., "Helical Magnetic Order in MnSi Thin Films," Phys. Rev. B, in press.

Kassi, E., Loizou, E., Porcar, L., Patrickios, C.S., "Di(*n*-butyl) Itaconate End-functionalized Polymers: Synthesis by Group Transfer Polymerization and Solution Characterization," Eur. Polymer J. **47**, 816 (2011).

Katayama, N., Ji, S., Louca, D., Lee, S.L., Fujita, M., Sato, T.J., Wen, J., Xu, Z., Gu, G., Xu, G., Lin, Z., Enoki, M., Chang, S., Yamada, K., Tranquada, J.M., "Investigation of the Spin-Glass Regime Between the Antiferromagnetic and Superconducting Phases in $Fe_{1+y}Se_xTe_{1-x}$," J. Phys. Soc. Jpn. **79**(11), 113702 (2010). **[CHRNS]**

Kelley, E.G., Smart, T.P., Jackson, A., Sullivan, M.O., Epps, III, T.H., "Structural Changes in Block Copolymer Micelles Induced by Cosolvent Mixtures," Soft Matter, in press.

Kent, M.S., Cheng, G., Murton, J.K., Carles, E.L., Dibble, D.C., Zendejas, F., Rodriquez, M.A., Tran, H., Holmes, B., Simmons, B.A., Knierim, B., Auer, M., Banuelos, J.L., Urquidi, J., Hjelm, R.P., "Study of Enzymatic Digestion of Cellulose by Small Angle Neutron Scattering," Biomacromol. **11**(2), 357 (2010). **[CHRNS]**

Kent, M.S., Murton, J.K., Sasaki, D.Y., Satija, S.K., Akgun, B., Nanda, H., Curtis, J., Majewski, J., Morgan, C.R., Engen, J.R., "Neutron Reflectometry Study of the Conformation of HIV Nef Bound to Lipid Membranes," Biophys. J. **99**, 1940 (2010).

Khan, A.S., Pandey, A., Gnäupel-Herold, T.H., Mishra, R.K., "Mechanical Response and Texture Evolution of AZ31 Alloy at Large Strains for Different Strain Rates and Temperatures," Int. J. Plast. **27**, 688 (2011).

Khodadadi, S., Curtis, J., Sokolov, A.P., "Nanosecond Relaxation Dynamics of Hydrated Proteins: Water Versus Protein Contributions," J. Phys. Chem. B **115**, 6222 (2011). [CHRNS]

Kiel, J.W., Eberle, A.P.R., Mackey, M.E., "Nanoparticle Agglomeration in Polymer-Based Solar Cells," Phys. Rev. Lett. **105**, 168701 (2010). [CHRNS]

Kiel, J.W., Mackay, M.E., Kirby, B.J., Maranville, B.B., Majkrzak, C.F., "Phase-Sensitive Neutron Reflectometry Measurements Applied in the Study of Photovoltaic Films," J. Chem. Phys. **133**(7), 074902-1 (2010).

Kim, F.S., Penumadu, D., Hussey, D.S., "Water Distribution Variation in Partially Saturated Granular Materials Using Neutron Imaging," J. Geotech. Geoenviron. Eng., in press.

Kim, I.J., Watson, R.P., Lindstrom, R.M., "Accurate and Precise Measurement of Selenium by Instrumental Neutron Activation Analysis," Anal. Chem. **83**, 3493 (2011).

Kim, J., van der Vegte, M.A., Scaramucci, A., Artyukhin, S., Chung, J., Park, S., Cheong, S.-W., Mostovoy, M., Lee, S.-H., "Magnetic Excitations in the Low-Temperature Ferroelectric Phase of Multiferroic YMn_2O_5 Using Inelastic Neutron Scattering," Phys. Rev. Lett. **107**(9), 097401-1 (2011).

Kim, J.M., Castañeda-Priego, R., Liu, Y., Wagner, N.J., "On the Importance of Thermodynamic Self-Consistency for Calculating Stable Clusters in Hard-Core Double Yukawa Fluids," J. Chem. Phys. **134**, 064904-1 (2011).

Kim, S.-H., Halasyamani, P.S., Melot, B.C., Seshadri, R., Green, M.A., Sefat, A.S., Mandrus, D., "Experimental and Computational Investigation of the Polar Ferrimagnet $VOSe_2O_5$," Chem. Mater. **22**, 5074 (2010).

Kim, S.Y., Park, M.J., Balsara, N.P., Jackson, A., "Confinement Effects on Watery Domains in Hydrated Block Copolymer Electrolyte Membranes," Macromol. **43**, 8128 (2010). [CHRNS]

Kim, S.Y., Zukoski, C.F., "Role of Polymer Segment-Particle Surface Interactions in Controlling Nanoparticle Dispersions in Concentrated Polymer Solutions," Langmuir, in press.

Kirby, B.J., Lau, J.W., Williams, D.V., Bauer, C.A., Miller, C.W., "Impact of Interfacial Magnetism on Magnetocaloric Properties of Thin Film Heterostructures," Appl. Phys. Lett. **109**(6), 063905-1 (2011).

Kjallman, T.H., Nelson, A.J., James, M., Dura, J.A., Travas-Sejdic, J., McGillivray, D., "A Neutron Reflectivity Study of the Interfacial and Thermal Behaviour of Surface-Attached Hairpin DNA," Soft Matter **7**, 5020 (2011).

Klimczuk, T., Wang, C.H., Lawrence, J.M., Xu, Q., Durakiewicz, T., Ronning, F., Llobet, A., Trouw, F., Kurita, N., Tokiwa, Y., Lee, H., Booth, C.H., Gardner, J.S., Bauer, E.D., Joyce, J.J., Zandbergen, H.W., Movshovich, R., Cava, R.J., Thompson, J.D., "Crystal Fields, Disorder, and Antiferromagnetic Short-Range Order in $Yb_{0.24}Sn_{0.76}Ru$," Phys. Rev. B **84**(7), 075152-1 (2011).

Koga, T., Gin, P., Yamaguchi, H., Endoh, M.K., Asada, M., Sendogdular, L., Kobayashi, M., Takahara, A., Akgun, B., Satija, S.K., Sumi, T., "Generality of Anomalous Expansion of Polymer Chains in Supercritical Fluids," Polymer **52**, 4331 (2011).

Kohlmann, H., Skripov, A.V., Soloninin, A.V., Udovic, T.J., "The Anti-Perovskite Type Hydride $InPd_3H_{0.89}$," J. Solid State Chem. **183**, 2461 (2010).

Kopetka, P., Middleton, M., Williams, R.E., Rowe, J.M., "A Second Liquid Hydrogen Cold Source for the NIST Reactor," in "Proceedings of the 12th Meeting of the International Group on Research Reactors," (IGORR-12, October 2009, Beijing, China), Session 3, Paper 6 (2009).

Kravtsov, E.A., Haskel, D., te Velthuis, S.G.E., Jiang, J.S., Kirby, B.J., "Application of Polarized Neutron Reflectometry and X-Ray Resonant Magnetic Reflectometry for Determining the Inhomogeneous Magnetic Structure in Fe/Gd Multilayers," Bull. Russian Acad. Sci.: Phys. **74**(10), 1471 (2010).

Kruk, I., Zajdel, P., Van Beek, W., Bakaimi, I., Lappas, A., Stock, C., Green, M., "Coupled Commensurate Cation and Charge Modulation in the Tunneled Structure, $Na_{0.40(2)}MnO_2$," J. Am. Chem. Soc. **133**, 13950 (2011).

Krycka, K., Jackson, A.J., Borchers, J.A., Shih, J., Briber, R.M., Ivkov, R., Gruttner, C., Dennis, C.L., "Internal Magnetic Structure of Dextran Coated Magnetite Nanoparticles in Solution using Small Angle Neutron Scattering with Polarization Analysis," J. Appl. Phys. **109**(7), 07B513-1 (2011). [CHRNS]

Kucerka, N., Nieh, M., Katsaras, J., "Fluid Phase Lipid Areas and Bilayer Thickness of Commonly used Phosphatidylcholines as a Function of Temperature," Biochim. Biophys. Acta, in press. [CHRNS]

LaFollette, T.A., Walker, L.M., "Structural and Mechanical Hysteresis at the Order-Order Transition of Block Copolymer Micellar Crystals," Polymers **3**, 281 (2011).

Lavery, K.A., Prabhu, V., Satija, S.K., Wu, W., "Lateral Uniformity in Chemical Composition along a Buried Reaction Front in Polymers using Off-Specular Reflectivity," J. Phys.: Condens. Matter **22**, 474001-1 (2010).

LeBrun, A.P., Holt, S.A., Shah, D.S., Majkrzak, C.F., Lakey, J.H., "The Structural Orientation of Antibody Layers Bound to Engineered Biosensor Surfaces," Biomaterials **32**, 3303 (2011).

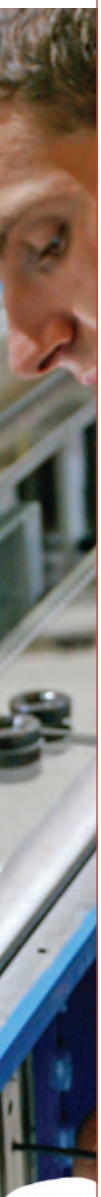

Lee, D., Gutowski, I.A., Bailey, A.E., Rubatat, L., de Bruyn, J.R., Frisken, B.J., "Investigating the Microstructure of a Yield-Stress Fluid by Light Scattering," Phys. Rev. E **83**(3), 031401-1 (2011).

Lee, H., Diehn, K.K., Ko, S.W., Tung, S.-H., Raghavan, S.R., "Can Simple Salts Influence Self-Assembly in Oil? Multivalent Cations as Efficient Gelators of Lecithin Organosols," Langmuir **26**(17), 13831 (2010). **[CHRNS]**

Lee, N., Choi, Y.J., Ramazanoglu, M., Ratcliff, II, W., Kiryukhin, V., Cheong, S.W., "Mechanism of Exchange Striction of Ferroelectricity in Multiferroic Orthorhombic $HoMnO_3$ Single Crystals," Phys. Rev. B **84**(2), 020101-1 (2011).

Lee, S., Schomer, M., Peng, H.N., Page, K.A., Wilms, D., Frey, H., Soles, C.L., Yoon, D.Y., "Correlations Between Ion Conductivity and Polymer Dynamics in Hyperbranched Poly(ethylene oxide) Electrolytes for Lithium-Ion Batteries," Chem. Mater. **23**, 2685 (2011). **[CHRNS]**

Lee, W.-T., Tong, X., Fleenor, M., Ismaili, A., Robertson, J.L., Chen, W., Gentile, T.R., Hailemariam, A., Goyette, R., Parizzi, A., Lauter, V., Klose, F., Kaiser, H., Lavelle, C.M., Baxter, D.V., Jones, G.L., Wexler, J., McCollum, L., Pierce, J., "In-Situ Polarized ^{3}He-Based Neutron Polarization Analyzer for SNS Magnetism Reflectometer," J. Phys.: Conf. Series **251**, 012086 (2010).

Leiner, J., Lee, H., Yoo, T., Lee, S., Kirby, B.J., Tivakornsasithorn, K., Liu, X., Furdyna, J.K., Dobrowolska, M., "Observations of Antiferromagnetic Interlayer Exchange Coupling in a $Ga_{1-x}Mn_xAs$/GaAs:Be/$Ga_{1-x}Mn_xAs$ Trilayer Structure," Phys. Rev. B **82**(19), 195205-1 (2010).

Leiner, J., Tivakornsasithorn, K., Liu, X., Furdyna, J.K., Dobrowolska, M., Kirby, B.J., Lee, H., Yoo, T., Lee, S., "Antiferromagnetic Exchange Coupling Between GaMnAs Layers Separated by a Nonmagnetic GaAsBe spacer," J. Appl. Phys. **109**(7), 07C307-1 (2011).

Lerbret, A., Lelong, G., Mason, P.E., Saboungi, M., Brady, J.W., "Molecular Dynamics and Neutron Scattering Study of Glucose Solutions Confined in MCM-41," J. Phys. Chem. B **115**, 910 (2011). **[CHRNS]**

Leventis, N., Sotiriou-Leventis, C., Chandrasekaran, N., Mulik, S., Larimore, Z.J., Lu, H., Churu, G., Mang, J.T., "Multifunctional Polyurea Aerogels From Isocyanates and Water. A Structure-Property Case Study," Chem. Mater. **22**, 6692 (2010).

Levin, I., Tucker, M.G., Wu, H., Provenzano, V., Dennis, C.L., Karimi, S., Comyn, T.P., Stevenson, T.J., Smith, R.I., Reaney, I.M., "Displacive Phase Transitions and Magnetic Structures in Nd-Substituted $BiFeO_3$," Chem. Mater. **23**(8), 2166 (2011).

Li, H., Broholm, C., Vaknin, D., Fernandes, R.M., Abernathy, D.L., Stone, M.B., Pratt, D.K., Tian, W., Qiu, Y., Ni, N., Diallo, S.O., Zarestky, J.L., Bud'ko, S.L., Canfield, P.C., McQueeney, R., "Anisotropic and Quasipropagating Spin Excitations in Superconducting $Ba(Fe_{0.926}Co_{0.074})_2As_2$," Phys. Rev. B **82**(14), 140503-1 (2010).

Li, H., Chiang, W., Fratini, E., Ridi, F., Bausi, F., Baglioni, P., Tyagi, M., Chen, S., "Dynamic Crossover in Hydration Water of Curing Cement Paste: The Effect of Superplasticizer," J. Phys.: Condens. Matter, in press. **[CHRNS]**

Li, J., Siritanon, T., Stalick, J.K., Sleight, A.W., Subramanian, M.A., "Electronic Conduction Mechanism in Mixed-Valent Tellurate Pyrochlores," Inorg. Chem. **50**, 5747 (2011).

Li, J., Siritanon, T., Stalick, J.K., Sleight, A.W., Subramanian, M.A., "Structural Studies and Electrical Properties of Cs/Al/Te/O Phases with the Pyrochlore Structure," Inorg. Chem. **50**, 5747 (2011).

Li, S., Lu, X., Wang, M., Luo, H., Wang, M., Zhang, C., Faulhaber, E., Regnault, L., Singh, D., Dai, P., "Effect of the In-plane Magnetic Field on the Neutron Spin Resonance in Optimally Doped $FeSe_{0.4}Te_{0.6}$ and $BaFe_{1.9}Ni_{0.1}As_2$ Superconductors," Phys. Rev. B **84**(2), 024518-1 (2011). **[CHRNS]**

Li, X., Buttrey, D.J., Blom, D.A., Vogt, T., "Improvement of the Structural Model for the M1 Phase Mo-V-Nb-Te-O Propane (Amm)oxidation Catalyst," Top. Catal. **54**, 614 (2011).

Li, X., Hong, K., Liu, Y., Shew, C., Liu, E., Herwig, K.W., Smith, G.S., Chen, W., "Water Distributions in Polystyrene-block-poly[styrene-g-poly(ethylene oxide)] Block Grafted Copolymer System in Aqueous Solutions Revealed by Contrast Variation Small Angle Neutron Scattering Study," J. Chem. Phys. **133**, 144912 (2010).

Li, X., Shew, C.-Y., Liu, Y., Pynn, R., Liu, E., Herwig, K.W., Smith, G.S., Robertson, J.L., Chen, W., "Prospect for Characterizing Interacting Soft Colloidal Structures Using Spin-Echo Small Angle Neutron Scattering," J. Chem. Phys. **134**(9), 094504-1 (2011).

Li, X., Zamponi, M., Hong, K., Porcar, L., Shew, C.-Y., Jenkins, T., Liu, E., Smith, G.S., Herwig, K.W., Liu, Y., Chen, W., "pH Responsiveness of Polyelectrolyte Dendrimers: A Dynamical Perspective," Soft Matter **7**(2), 618 (2011). **[CHRNS]**

Li, Z., Cheng, H., Li, J., Hao, J., Zhang, L., Hammouda, B., Han, C.C., "Large-Scale Structures in Tetrahydrofuran-Water Mixture with a Trace Amount of Antioxidant Butylhydroxytoluene (BHT)," J. Phys. Chem. B **115**, 7887 (2011). **[CHRNS]**

Lin, L.Y., Lee, N.S., Zhu, J., Nystrom, A.M., Pochan, D.J., Dorshow, R.B., Wooley, K.L., "Tuning Core vs. Shell Dimensions to Adjust the Performance of Nanoscopic Containers for the Loading and Release of Doxorubicin," J. Controlled Release **152**, 37 (2011). **[CHRNS]**

Lindstrom, R.M., "Hydrogen Measurement in Steel: A Query," J. Radioanal. Nucl. Chem., in press.

Lindstrom, R.M., Fischbach, E., Buncher, J.B., Greene, G.L., Jenkins, J.H., Krause, D.E., Mattes, J.J., Yue, A., "Study of the Dependence of ^{198}Au Half-life on Source Geometry," Nucl. Instrum. Meth. A **622**, 93 (2010).

Linton, P., Rennie, A.R., Alfredsson, V., "Evolution of Structure and Composition During the Synthesis of Mesoporous Silica SBA-15 Studied by Small-Angle Neutron Scattering," Solid State Sci. **13**, 793 (2011).

Liu, L.J., Liu, D.M., Huang, Q., Zhang, T.L., Zhang, L., Yue, M., Lynn, J.W., Zhang, J.X., "Neutron Diffraction Study of the Magnetic Refrigerant $Mn_{1.1}Fe_{0.9}P_{0.76}Ge_{0.24}$," Powder Diffr. **25**(S1), S25 (2010).

Liu, T.J., Hu, J., Qian, B., Fobes, D., Mao, Z.Q., Bao, W., Reehuis, M., Kimber, S.A.J., Prokes, K., Matas, S., Argyriou, D.N., Hiess, A., Rotaru, A., Pham, H., Spinu, L., Qiu, Y., Thampy, V., Savici, A.T., Rodriguez, J.A., Broholm, C.L., "From (π,0) Magnetic Order to Superconductivity with (π,π) Magnetic Resonance in $Fe_{1.02}Te_{1-x}Se_x$," Nat. Mater. **9**(9), 718 (2010). **[CHRNS]**

Liu, Y., Porcar, L., Chen, J., Chen, W.-R., Falus, P., Faraone, A., Fratini, E., Hong, K., Baglioni, P., "Lysozyme Protein Solution with an Intermediate Range Order Structure," J. Phys. Chem. B **115**, 7238 (2010). **[CHRNS]**

Lu, H., Akgun, B., Russell, T.P., "Morphological Characterization of a Low-Bandgap Crystalline Polymer:PCBM Bulk Heterojunction Solar Cells," Adv. Energy Mater., in press.

Lucas, G.E., "An Evolution of Understanding of Reactor Pressure Vessel Steel Embrittlement," J. Nucl. Mater. **407**, 59 (2010). **[CHRNS]**

Luzin, V., Spencer, K., Zhang, M.-X., "Residual Stress and Thermo-Mechanical Properties of Cold Spray Metal Coatings," Acta Mater. **59**, 1259 (2011).

Lynn, J.W., "Magnetic Neutron Scattering," in "Methods in Materials Research," edited by Kaufmann, E.N. (John Wiley & Sons), in press.

Maitland, C.F., Buckley, C.E., O'Connor, B.H., Butler, P.D., Hart, R.D., "Characterization of the Pore Structure of Metakaolin-derived Geopolymers by Neutron Scattering and Electron Microscopy," J. Appl. Crystallogr. **44**(4), 697 (2011). **[CHRNS]**

Majkrzak, C.F., Carpenter, E., Heinrich, F., Berk, N.F., "When Beauty is Only Skin Deep; Optimizing the Sensitivity of Specular Neutron Reflectivity for Probing Structure Beneath the Surface of Thin Films," J. Appl. Phys., in press.

Mallia, V.A., Butler, P.B., Sarkar, B., Holman, K.T., Weiss, R.G., "Reversible Phase Transitions Within Self-Assembled Fibrillar Networks of (R)-18-(n-alkylamino)octadecan-7-ols in their Carbon Tetrachloride Gels," J. Am. Chem. Soc. **133**(38), 15045 (2011). **[CHRNS]**

Manahan, M.P., Hatzell, M.C., Kumbur, E.C., Mench, M.M., "Laser Perforated Fuel Cell Diffusion Media. Part I: Related Changes in Performance and Water Content," J. Power Sources **196**, 5573 (2011).

Marques, C., Janssen, Y., Kim, M., Wu, L., Chi, S.X., Lynn, J.W., Aronson, M., "$HfFeGa_2$ and $HfMnGa_2$: Transition-Metal-Based Itinerant Ferromagnets with Low Curie Temperatures," Phys. Rev. B **83**(18), 184435-1 (2011). **[CHRNS]**

Matan, K., Bartlett, B.M., Helton, J.S., Sikolenko, V., Mat'aš, S., Prokeš, K., Chen, Y., Lynn, J.W., Grohol, D., Sato, T.J., Tokunaga, M., Nocera, D.G., Lee, Y.S., "Dzyaloshinskii-Moriya Interaction and Spin Re-Orientation Transition in the Frustrated Kagome Lattice Antiferromagnet," Phys. Rev. B **83**(21), 214406-1 (2011).

Matan, K., Ibuka, S., Morinaga, R., Chi, S.X., Lynn, J.W., Christianson, A.D., Lumsden, M.D., Sato, T.J., "Doping Dependence of Spin Dynamics in Electron-doped $Ba(Fe_{1-x}Co_x)_2As_2$," Phys. Rev. B **82**(5), 05415-1 (2010).

McMullan, J.M., Wagner, N.J., "Directed Self-Assembly of Colloidal Crystals by Dielectrophoretic Ordering Observed with Small Angle Neutron Scattering (SANS)," Soft Matter **6**, 5443 (2010). **[CHRNS]**

Melnichenko, Y.B., He, L., Sakurovs, R., Kholodenko, A.L., Blach, T.P., Mastalerz, M., Radlinski, A.P., Cheng, G., Mildner, D.F.R., "Accessibility of Pores in Coal to Methane and Carbon Dioxide," Fuel, in press. **[CHRNS]**

Melot, B., Goldman, A., Darago, L.E., Furman, J.D., Rodriguez, E., Seshadri, R., "Magnetic Ordering and Magnetodielectric Phenomena in $CoSeO_4$," J. Phys.: Condens. Matter **22**, 506003 (2010).

Micherdzinska, A.M., Bass, C.D., Bass, T.D., Gan, K., Luo, D., Markoff, D.M., Mumm, H.P., Nico, J.S., Opper, A.K., Sharapov, E.I., Snow, W.M., Swanson, H.E., Zhumabekova, V., "Polarized Neutron Beam Properties for Measuring Parity-Violating Spin Rotation in Liquid ^{4}He," Nucl. Instrum. Meth. A **631**, 80 (2011).

Mihailescu, M., Soubias, O., Worcester, D., White, S.H., Gawrisch, K., "Structure and Dynamics of Cholesterol-Containing Polyunsaturated Lipid Membranes Studied by Neutron Diffraction and NMR," Journal of Membrane Biology **239**, 63 (2011).

Mihailescu, M., Vaswani, G.R., Jardon-Valadez, E., Castro-Roman, F., Freites, J.A., Worcester, D.L., Chamberlin, A.R., Tobias, D.J., White, S.H., "Acyl-Chain Methyl Distributions of Liquid-Ordered and -Disordered Membranes," Biophys. J. **100**, 1455 (2011).

Mildner, D.F.R., Gubarev, M.V., "Wolter Optics for Neutron Focusing," Nucl. Instrum. Meth. A **634**, S-7 (2011).

Mishler, J., Wang, Y., Borup, R., Hussey, D.S., Jacobson, D.L., "*In-situ* Investigation of Water Distribution in Polymer Electrolyte Fuel Cell Using Neutron Radiography," ECS Trans. **33**(1), 1443 (2010).

Moyer, Jr., R.O., Gilson, D.F.R., Toby, B.H., "Neutron Powder Diffraction, and Solid-State Deuterium NMR Analyses of Yb_2RuD_6 and Spectroscopic Vibrational Analysis of Yb_2RuD_6 and Yb_2RuH_6," J. Solid State Chem. **184**, 1895 (2011).

Mukundan, R., Davey, J.R., Fairweather, J.D., Spernjak, D., Spendelow, J.S., Hussey, D.S., Jacobson, D.L., Wilde, P., Schweiss, R., Borup, R.L., "Effect of Hydrophilic Treatment of Microporous Layer on Fuel Cell Performance," ECS Trans. **33**(1), 1109 (2010).

Nagao, M., "Temperature and Scattering Contrast Dependences of Thickness Fluctuations in Surfactant Membranes," J. Chem. Phys., in press. **[CHRNS]**

Nagao, M., Chawang, S., Hawa, T., "Interlayer Distance Dependence of Thickness Fluctuations in a Swollen Lamellar Phase," Soft Matter **7**, 6598 (2011).

Nagpure, S.C., Downing, R.G., Bhushan, B., Babu, S.S., Cao, L., "Neutron Depth Profiling Technique for Studying Aging in Li-ion Batteries," Electrochim. Acta **56**, 4735 (2011).

Nambu, Y., Zhao, L.L., Morosan, E., Kim, K., Kotliar, G., Zajdel, P., Green, M. A., Ratcliff, II, W., Rodriguez-Rivera, J., Broholm, C.L., "Incommensurate Magnetism in FeAs Strips: Neutron Scattering from $CaFe_4As_3$," Phys. Rev. Lett. **106**(3), 037201-1 (2011). **[CHRNS]**

Nanda, H., Datta, S., Heinrich, F., Loesche, M., Rein, A., Krueger, S., Curtis, J., "Electrostatic Interactions and Binding Orientation of HIV-1 Matrix Studied by Neutron Reflectivity," Biophys. J. **99**, 2516 (2010).

Nedoma, A.J., Lai, P., Jackson, A., Robertson, M.L., Balsara, N.P., "Phase Behavior of Off-Critical A/B/A-C Blends," Macromol. **43**, 7852 (2010). **[CHRNS]**

Nedoma, A.J., Lai, P., Jackson, A., Robertson, M.L., Wanakule, N.S., Balsara, N.P., "Phase Diagrams of Blends of Polyisobutylene and Deuterated Polybutadiene as a Function of Chain Length," Macromol. **44**, 3077 (2011). **[CHRNS]**

Neeraj, T., Gnäupel-Herold, T.H., Prask, H.J., Ayer, R., "Residual Stresses in Girth Welds of Carbon Steel Pipes: A Comparison between Ferritic and Austenitic Weld Metals," Sci. Tech. Weld. Join. **16**(3), 249 (2011).

Newbloom, G.M., Kim, F.S., Jenekhe, S.A., Pozzo, D., "Mesoscale Morphology and Charge Transport in Colloidal Networks of Poly(3-hexylthiophene)," Macromol. **44**, 3801 (2011). **[CHRNS]**

Ni, N., Jia, S., Huang, Q., Climent-Pascual, E., Cava, R.J., "Structural, Transport, Thermodynamic, and Neutron Diffraction Studies of Layered $R_2O_3Fe_2Se_2$ (R = Ce, Pr, Nd, and Sm)," Phys. Rev. B **83**(22), 24403-1 (2011).

Nieh, M., Kucerka, N., Katsaras, J., "Formation Mechanism of Self-Assembled Unilamellar Vesicles," Canadian J. Phys. **88**, 735 (2010). **[CHRNS]**

Nolte, M.W., Liberatore, M.W., "Viscosity of Biomass Pyrolysis Oils from Various Feedstocks," Energy Fuels **24**, 6601 (2010).

Ofer, O., Keren, A., Gardner, J.S., Ren, Y., MacFarlane, W.A., "Origin of Magnetic Freezing in Pyrochlore $Y_2Mo_2O_7$," Phys. Rev. B **82**(9), 092403-1 (2010).

Ortony, J.H., Chatterjee, T., Garner, L.E., Chworos, A., Mikhailovsky, A., Kramer, E.J., Bazan, G.C., "Self-Assembly of an Optically Active Conjugated Oligoelectrolyte," J. Am. Chem. Soc. **133**, 8380 (2011). **[CHRNS]**

Ospinal-Jimenez, M., Pozzo, D., "Structural Analysis of Protein Complexes with Sodium Alkyl Sulfates by Small-Angle Scattering and Polyacrylamide Gel Electrophoresis," Langmuir **27**(3), 928 (2011). **[CHRNS]**

Pafiti, K.S., Philippou, Z., Loizou, E., Porcar, L., Patrickios, C.S., "End-Linked Poly[2-(dimethylamino)ethyl Methacrylate]-Poly(methacrylic Acid) Polyampholyte Conetworks: Synthesis by Sequential RAFT Polymerization and Swelling and SANS Characterization," Macromol. **44**, 5352 (2011).

Palsson, G.K., Kapaklis, V., Dura, J.A., Jacob, J., Jayanetti, S., Rennie, A.R., Hjorvarsson, B., "Deuterium-Induced Volume Expansion in $Fe_{0.5}V_{0.5}$/V Superlattices," Phys. Rev. B **82**(24), 24524-1 (2010).

Patel, A.J., Rappl, T.J., Balsara, N.P., "Similarity of the Signatures of the Initial Stages of Phase Separation in Metastable and Unstable Polymer Blends," Phys. Rev. Lett. **106**(3), 035702-1 (2011). **[CHRNS]**

Paul, R.L., "Evaluation of Radiochemical Neutron Activation Analysis Methods for Determination of Arsenic in Biological Materials," Anal. Chem. **83**(1), 152 (2010).

Peri, S.R., Habersberger, B., Akgun, B., Jiang, H., Enlow, J., Bunning, T.J., Majkrzak, C.F., Foster, M.D., "Variations in Cross-link Density with Deposition Pressure in Ultrathin Plasma Polymerized Benzene and Octafluorocyclobutane Films," Polymer **51**, 4390 (2010).

Peri, S.R., Kim, H., Akgun, B., Enlow, J., Jiang, H., Bunning, T.J., Li, X., Foster, M.D., "Structure of Copolymer Films Created by Plasma Enhanced Chemical Vapor Deposition," Polymer **51**, 3971 (2010).

Peterson, V.K., Brown, C.M., Liu, Y., Kepert, C.J., "Structural Study of D2 Within the Trimodal Pore System of a Metal Organic Framework," J. Am. Chem. Soc. **115**, 8851 (2011).

Petit, C., Burress, J., Bandosz, T.J., "Cu-Based MOF / Graphene Composites: Synthesis and Surface Characterization," Carbon **49**(2), 563 (2011).

Petorak, C., Ilavsky, J., Wang, H., Porter, W., Trice, R., "Microstructural Evolution of 7 wt.% Y_2O_3-ZrO_2 Thermal Barrier Coatings due to Stress Relaxation at Elevated Temperatures and the Concomitant Changes in Thermal Conductivity," Surf. Coat. Technol. **57**, 205 (2010).

Phelan, D.P., Long, X., Xie, Y., Ye, Z., Glazer, A.M., Yokota, H., Thomas, P.A., Gehring, P.M., "Single Crystal Study of Competing Rhombohedral and Monoclinic Order in Lead Zirconate Titanate," Phys. Rev. Lett. **105**(20), 207601-1 (2010). **[CHRNS]**

Phelan, D.P., Millican, J., Gehring, P.M., "Dissimilarity of Polar Displacements in Barium and Lead Based Relaxors," Appl. Phys. Lett. **97**(7), 072903-1 (2010).

Pochan, D.J., Zhu, J., Zhang, K., Wooley, K.L., Miesch, C., Emrick, T., "Multicompartment and Multigeometry Nanoparticle Assembly," Soft Matter **7**, 2500 (2011).

Porcar, L., Pozzo, D., Langenbucher, G., Moyer, J., Butler, P.D., "Rheo–Small-Angle Neutron Scattering at the National Institute of Standards and Technology Center for Neutron Research," Rev. Sci. Instrum., in press. **[CHRNS]**

Prabhu, V.M., Kang, S., Kline, R.J., DeLongchamp, D.M., Fischer, D.A., Wu, W., Satija, S.K., Bonnesen, P.V., Sha, J., Ober, C.K., "Characterization of the Non-uniform Reaction in Chemically Amplified Calix[4] resorcinarene Molecular Resist Thin Films," Australian J. Chem., in press.

Prabhu, V.M., Kang, S., VanderHart, D.L., Satija, S.K., Lin, E.K., Wu, W., "Photoresist Latent and Developer Images as Probed by Neutron Reflectivity Methods," Adv. Mater. **23**, 388 (2011).

Preston, J.S., Fu, R.S., Pasaogullari, U., Hussey, D.S., Jacobson, D.L., "Consideration of the Role of Micro-Porous Layer on Liquid Water Distribution in Polymer Electrolyte Fuel Cells," J. Electrochem. Soc. **158**(2), B239 (2010).

Prisk, T., Tyagi, M., Sokol, P.E., "Dynamics of Small-Molecule Glass Formers Confined in Nanopores," J. Chem. Phys. **134**(11), 114506-1 (2011). **[CHRNS]**

Quan, P., Lai, M., Hussey, D.S., Jacobson, D.L., Kumar, A., Hirano, S., "Time-Resolved Water Measurement in a PEM Fuel Cell Using High-Resolution Neutron Imaging Technique," J. Fuel Cell Sci. Technol. **7**(5), 051009-1 (2010).

Ramachandran, R., Beaucage, G., McFaddin, D., Merrick-Mack, J., Galiatsatos, V., Mirabella, F., "Branch Length Distribution in TREF Fractionated Polyethylene," Polymer **52**(12), 2661 (2011).

Ramazanoglu, M., Ratcliff, II, W., Choi, Y.J., Lee, S., Cheong, S., Kiryukhin, V., "Temperature-Dependent Properties of the Magnetic Order in Single-Crystal $BiFeO_3$," Phys. Rev. B **83**(17), 174434-1 (2011).

Ramazanoglu, M., Ratcliff, II, W., Yi, H.T., Sirenko, A.A., Cheong, S.W., Kiryukhin, V., "Giant Effect of Uniaxial Pressure on Magnetic Domain Populations in Multiferroic Bismuth Ferrite," Phys. Rev. Lett. **107**(6), 067203-1 (2011).

Ratcliff, II, W., Kan, D., Chen, W., Watson, S., Chi, S., Erwin, R.W., McIntyre, G.J., Capelli, S., Takeuchi, I., "Neutron Diffraction Investigations of Magnetism in $BiFeO_3$ Epitaxial Films," Adv. Func. Mater. **21**(9), 1567 (2011).

Révay, Z., Lindstrom, R.M., Mackey, E.A., Belgya, T., "Neutron-Induced Prompt Gamma Activation Analysis (PGAA)" in "Handbook of Nuclear Chemistry," edited by Vértes, A., Nagy, S., Klencsár, Z., Lovas, R.G., Rösch, F. (Springer Science and Business Media), Vol. 3, Chap. 30, 1619 (2011).

Richter, A.G., Dergunov, S.A., Ganus, B., Thomas, Z., Pingali, S.V., Urban, V., Liu, Y., Porcar, L., Pinkhassik, E., "Scattering Studies of Hydrophobic Monomers in Liposomal Bilayers: An Expanding Shell Model of Monomer Distribution," Langmuir **27**(7), 3792 (2011).

Riley, G.V., Hussey, D.S., Jacobson, D.L., "In Situ Neutron Imaging of Alkaline and Lithium Batteries," ECS Trans. **25**(35), 75 (2009).

Ripley, E.M., Li, C., Moore, C.H., Elswick, E.R., Maynard, J.B., Paul, R.L., Sylvester, P., Seo, J.H., Shimizu, N., "Analytical Methods for Sulfur Determination in Glasses, Rocks, Minerals and Fluid Inclusions," Rev. Mineralogy Geochem. **73**(1), 9 (2011).

Roberts, N.J., Jones, L.N., Wang, Z., Liu, Y., Wang, Q., Chen, X., Luo, H., Rong, C., Kralik, M., Park, H., Choi, K.O., Pereira, W.W., da Fonseca, E.S., Cassette, P., Dewey, M.S., Moiseev, N.N., Kharitonov, I.A., "International Key Comparison of Measurements of Neutron Source Emission Rate (1999-2005)-CCRI(III)-K9.AmBe," Metrologia **48**, 06018 (2011).

Rodriguez, E.E., Poineau, F., Llobet, A., Kennedy, B.J., Avdeev, M., Thorogood, G.J., Carter, M.L., Seshadri, R., Singh, D.J., Cheetham, A.K., "High Temperature Magnetic Ordering in the 4*d* Perovskite $SrTcO_3$," Phys. Rev. Lett. **106**(6), 067201-1 (2011).

Rodriguez, E.E., Poineau, F., Llobet, A., Thompson, J.D., Seshadri, R., Cheetham, A.K., "Preparation, Magnetism and Electronic Structures of Cadmium Technetates," J. Mater. Chem. **21**, 1496 (2011).

Rodriguez, E.E., Stock, C., Hsieh, P., Butch, N.P., Paglione, J., Green, M., "Chemical Control of Interstitial Iron Leading to Superconductivity in $Fe_{1+x}Te_{0.7}Se_{0.3}$," Chem. Sci. **2**, 1782 (2011). **[CHRNS]**

Rodriguez, E.E., Stock, C., Krycka, K., Majkrzak, C.F., Zajdel, P., Kirshenbaum, K., Butch, N.P., Saha, S.R., Paglione, J., Green, M.A., "Noncollinear Spin-density-wave Antiferromagnetism in FeAs," Phys. Rev. B **83**(13), 134438-1 (2011).

Rodriguez, E.E., Stock, C., Zajdel, P., Krycka, K.L., Majkrzak, C.F., Zavalij, P., Green, M.A., "Magnetic-Crystallographic Phase Diagram of the Superconducting Parent Compound $Fe_{1+x}Te$," Phys. Rev. B **84**(6), 064403-1 (2011). **[CHRNS]**

Romanyukha, A., Minniti, R.N., Moscovitch, M., Thompson, A.K., Trompier, F., Colle, R.N., Sucheta, A., Voss, S.P., Benevides, L.A., "Effect of Neutron Irradiation on Dosimetric Properties of TLD-600H (^{6}LiF:Mg,Cu,P)," Radiat. Meas., in press.

Ruff, J.P.C., Gaulin, B.D., Rule, K.C., Gardner, J.S., "Superlattice Correlations in $Tb_2Ti_2O_7$ Under the Application of [110] Magnetic Field," Phys. Rev. B **82**(10), 100401-1 (2010). **[CHRNS]**

Rush, J.J., Cappelletti, R.L., "The NIST Center for Neutron Research: Over 40 Years Serving NIST/NBS and the Nation," NIST SP 1120 (2011).

Russo, D., Teixeira, J., Kneller, L., Copley, J.R.D., Ollivier, J., Perticaroli, S., Pellegrini, E., Gonzalez, M.A., "Vibrational Density of States of Hydration Water at Biomolecular Sites: Hydrophobicity Promotes Low Density Amorphous Ice Behavior," J. Am. Chem. Soc. **133**, 4882 (2011). **[CHRNS]**

Sadakane, K., Iguchi, N., Nagao, M., Endo, H., Melnichenko, Y.B., Seto, H., "2D-Ising-like Critical Behavior in Mixtures of Water and 3-Methylpyridine Including Antagonistic Salt or Ionic Surfactant," Soft Matter **7**, 1334 (2011).

Şahin, Ĭ., "Random Lines: A Novel Population Set-Based Evolutionary Global Optimization Algorithm" in "Lecture Notes in Computer Science – Volume 6621," edited by Silva, S., Foster, J.A., Nicolau, M., Machado, P., Giacobini, M., (Springer-Verlag, April 2011, Torino, Italy), 97 (2011).

Sakuma, Y., Urakami, N., Ogata, Y., Nagao, M., Komura, S., Kawakatsu, T., Imai, M., "Diffusion of Domains on Nanometer Sized Vesicle," J. Phys.: Conf. Series **251**, 012036 (2010). **[CHRNS]**

Schwieters, C.D., Suh, J., Grishaev, A., Ghirlando, R., Takayama, Y., Clore, G.M., "Solution Structure of the 128 kDa Enzyme Dimer from *Escherichia coli* and its 146kDa Complex with HPr Using Residual Dipolar Couplings and Small and Wide-Angle X-ray Scattering," J. Am. Chem. Soc. **132**, 13026 (2010). **[CHRNS]**

Segawa, K., Kofu, M., Lee, S., Tsukada, I., Hiraka, H., Fujita, M., Chang, S., Yamada, K., Ando, Y., "Zero-Doping State and Electron-Hole Asymmetry in an Ambipolar Cuprate," Nat. Phys. **6**, 579 (2010). **[CHRNS]**

Senkov, O.N., Wilks, G.B., Scott, J.M., Miracle, D.B., "Mechanical Properties of $Nb_{25}Mo_{25}W_{25}$ and $V_{20}Nb_{20}Ta_{20}W_{20}$ Refractory High Entropy Alloys," Intermetallics **19**, 698 (2011).

Shekhar, P., Nanda, H., Lösche, M., Heinrich, F., "Continous Distribution Model for the Investigation of Complex Molecular Architectures Near Interfaces with Scattering Techniques," J. Appl. Phys., in press.

Shenoy, S., Moldovan, R., Fitzpatrick, J., Vanderah, D.J., Deserno, M., Loesche, M., "In-Plane Homogeneity and Lipid Dynamics in Tethered Bilayer Lipid Membranes (tBLMs)," Soft Matter **6**, 1263 (2010).

Shi, X., Yang, J., Salvador, J.R., Chi, M., Cho, J.Y., Wang, H., Bai, S., Yang, J., Zhang, W., Chen, L., "Multiple-Filled Skutterudites: High Thermoelectric Figure of Merit Through Separately Optimizing Electrical and Thermal Transports," J. Am. Chem. Soc. **133**, 7837 (2011). **[CHRNS]**

Shiomi, T., Fu, R.S., Pasaogullari, U., Tabuchi, Y., Miyazaki, S., Kubo, N., Shinohara, K., Hussey, D.S., Jacobson, D.L., "Effect of Liquid Water Saturation on Oxygen Transport in Gas Diffusion Layers of Polymer Electrolyte Fuel Cells," in "Proceedings of the ASME 2010 Eighth International Fuel Cell Science, Engineering and Technology Conference: Volume 1," (ASME, June 2010, Brooklyn, NY) Paper no. FuelCell2010-33225, 667 (2010).

Siegel, J.B., Bohac, S.V., Stefanopoulou, A.G., Yesilyurt, S., "Nitrogen Front Evolution in Purged Polymer Electrolyte Membrane Fuel Cell with Dead-Ended Anode," J. Electrochem. Soc. **157**(7), B1081 (2010).

Siegel, J.B., Lin, X., Stefanopoulou, A.G., Gorsich, D., "Neutron Imaging of Lithium Concentration in Battery Pouch Cells," in "2011 American Control Conference," (IEEE Conf. Proc., June 2011, San Francisco, CA) 376 (2011).

Silvera-Batista, C.A., Ziegler, K.J., "Swelling the Hydrophobic Core of Surfactant-Suspended Single-Walled Carbon Nanotubes: A SANS Study," Langmuir **27**, 11372 (2011). **[CHRNS]**

Simmons, J.M., Wu, H., Zhou, W., Yildirim, T., "Carbon Capture in Metal-Organic Frameworks - A Comparative Study," Energy Environ. Sci. **4**, 2177 (2011).

Singh, D.K., Thamizhavel, A., Chang, S., Lynn, J.W., Joshi, D.A., Dhar, S.K., Chi, S.X., "Coupling of Field-Induced Spin Fluctuations and Spin Density Wave in Intermetallic $CeAg_2Ge_2$," Phys. Rev. Lett. **84**(5), 052401-1 (2011).

Singh, D.K., Tuominen, M.T., "The Realization of Artificial Kondo Lattices in Nanostructured Arrays," Phys. Rev. B **83**(1), 014408-1 (2011).

Sinha, K., Maranas, J.K., "Segmental Dynamics and Ion Association in PEO-Based Single Ion Conductors," Macromol. **44**, 5381 (2011). **[CHRNS]**

Siritanon, T., Li, J., Stalick, J.K., Macaluso, R.T., Sleight, A.W., Subramanian, M.A., "$CsTe_2O_6$-x: Novel Mixed-Valence Tellurium Oxides with Framework-Deficient Pyrochlore-Related Structure," Inorg. Chem. **50**(17), 8494 (2011).

Skripov, A.V., Mushnikov, N.V., Terent'ev, P.B., Gaviko, V.S., Udovic, T.J., Rush, J.J., "Hydrogen Dynamics in $Ce_2Fe_{17}H_5$: Inelastic and Quasielastic Neutron Scattering Studies," J. Phys.: Condens. Matter **23**, 405402-1 (2011). [CHRNS]

Skripov, A.V., Udovic, T.J., Rush, J.J., Uimin, M., "A Neutron Scattering Study of Hydrogen Dynamics in Coarse-Grained and Nanostructured $ZrCr_2H_3$," J. Phys.: Condens. Matter **23**, 065402 (2011). [CHRNS]

Snow, W.M., Bass, C.D., Bass, T.D., Crawford, B.E., Gan, K., Snow, W.M., Bass, C.D., Bass, T.D., Crawford, B.E., Gan, K., Heckel, B.R., Luo, D., Markoff, D.M., Micherdzinksa, A.M., Mumm, H.P., Nico, J.S., Opper, A.K., Sarsour, M., Sharapov, E.I., Swanson, H.E., Walbridge, S.C., Zhumabekova, V., "Upper Bound on Parity-Violating Neutron Spin Rotation in ^4He," Phys. Rev. C **83**(2), 022501-1 (2011).

Spernjak, D., Mukherjee, P.P., Mukundan, R., Davey, J.R., Hussey, D.S., Jacobson, D.L., Borup, R.L., "Measurement of Water Content in Polymer Electrolyte Membranes Using High Resolution Neutron Imaging," ECS Trans. **33**(1), 1451 (2010).

Srinivas, G., Burress, J., Ford, J., Yildirim, T., "Porous Graphene Oxide Frameworks: Synthesis and Gas Sorption Properties," J. Mater. Chem. **21**, 11323 (2011).

Srinivas, G., Ford, J., Zhou, W., Wu, H., Udovic, T.J., Yildirim, T., "Nanoconfinement and Catalytic Dehydrogenation of Ammonia Borane by Magnesium-Metal–Organic Framework-74," Chem. Eur. J. **17**, 6043 (2011).

Srinivas, G., Ford, J., Zhou, W., Yildirim, T., "Zn-MOF Assisted Dehydrogenation of Ammonia Borane: Enhanced Kinetics and Clean Hydrogen Generation," Int. J. Hydrogen Energy, in press.

Stock, C., Chapon, L.C., Schneidewind, A., Su, Y., Radaelli, P.G., McMorrow, D.F., Bombardi, A., Lee, N., Cheong, S.W., "Helical Spin-waves, Magnetic Order, and Fluctuations in the Langasite Compound $Ba_3NbFe_3Si_2O_{14}$," Phys. Rev. B **83**(10), 104426-1 (2011).

Stock, C., Cowley, R.A., Buyers, W.J.L., Frost, C.D., Taylor, J.W., Peets, D., Liang, R., Bonn, D., Hardy, W.N., "Effect of the Pseudogap on Suppressing High Energy Inelastic Neutron Scattering in Superconducting $YBa_2Cu_3O_{6.5}$," Phys. Rev. B **82**(17), 174505-1 (2010).

Stock, C., Cowley, R.A., Taylor, J.W., Bennington, S.M., "Reply to "Comment on 'High-Energy Neutron Scattering from Hydrogen using a Direct Geometry Spectrometer'," Phys. Rev. B, in press.

Stock, C., Rodriguez, E., Green, M., Zavalij, P., Rodriguez, J.A., "Interstitial Iron Tuning of the Spin Fluctuations in the Nonsuperconducting Parent Phase $Fe_{1+x}Te$," Phys. Rev. B **84**(4), 045124-1 (2011). [CHRNS]

Sumida, K., Brown, C.M., Herm, Z.R., Chavan, S., Bordiga, S., Long, J.R., "Hydrogen Storage Properties and Neutron Scattering Studies of Mg_2(dobdc) - A Metal-Organic Framework with Open Mg_{2+} Adsorption Sites," Chem. Comm. **47**, 1157 (2010). [CHRNS]

Sumida, K., Her, J., Dinca, M., Murray, L.J., Schloss, J.M., Pierce, C.J., Thompson, B.A., FitzGerald, S.A., Brown, C.M., Long, J.R., "Neutron Scattering and Spectroscopic Studies of Hydrogen Adsorption in $Cr_3(BTC)_2$ - A Metal-Organic Framework with Exposed Cr^{2+} Sites," J. Phys. Chem. C **115**, 8414 (2011).

Sumida, K., Horike, S., Kaye, S.S., Herm, Z.R., Queen, W., Brown, C.M., Grandjean, F., Long, G.J., Dailly, A., Long, J.R., "Hydrogen Storage and Carbon Dioxide Capture in an Iron-Based Sodalite-Type Metal-Organic Framework (Fe-BTT) Discovered *via* High-Throughput Methods," Chem. Sci. **1**, 184 (2010).

Tanimura, S., Dieregsweiler, U.M., Wyslouzil, B.E., "Binary Nucleation Rates for Ethanol/Water Mixtures in Supersonic Laval Nozzles," J. Chem. Phys. **133**, 174305 (2010).

Tassel, C., Kang, J., Lee, C., Hernandez, O., Qiu, Y., Paulus, W., Collet, E., Lake, B., Guidi, T., Whangbo, M., Ritter, C., Kageyama, H., Lee, S.-H., "Ferromagnetically Coupled Shastry-Sutherland Quantum Spin Singlets in (CuCl) $LaNb_2O_7$," Phys. Rev. Lett. **105**(16), 167205-1 (2010). [CHRNS]

Thompson, D.G., Brown, G.W., Olinger, B., Mang, J.T., Patterson, B., DeLuca, R., Hagelberg, S., "The Effects of TATB Ratchet Growth on PBX 9502," Propellants Explos. Pyrotech. **35**(6), 507 (2010). [CHRNS]

Thompson, S.M., Ma, H.B., Wilson, C., "Investigation of a Flat-Plate Oscillating Heat Pipe with Tesla-Type Check Valves," Exp. Therm. Fluid Sci., in press.

Tian, W., Li, J., Li, H., Lynn, J.W., Zarestky, J.L., Vaknin, D., "Neutron Scattering Studies of $LiCoPO_4$ & $LiMnPO_4$," J. Phys.: Conf. Series **251**, 012005 (2010). [CHRNS]

Tian, W., Ratcliff, II, W., Kim, M.G., Yan, J.-Q., Kienzle, P.A., Huang, Q., Jensen, B., Dennis, K.W., McCallum, R.W., Lograsso, T.A., McQueeney, R., Goldman, A.I., Lynn, J.W., Kreyssig, A., "Interplay Between Fe and Nd Magnetism in NdFeAsO Single Crystals," Phys. Rev. B **82**(6), 060514-1 (2010).

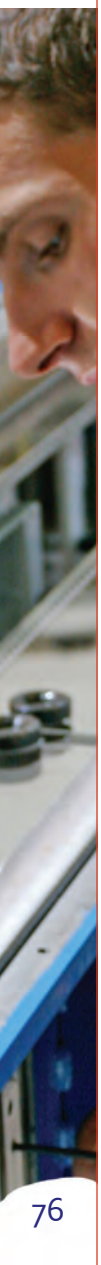

Tigelaar, D.M., Palker, A.E., He, R., Scheiman, D.A., Petek, T., Savinelli, R., Yoonessi, M., "Synthesis and Properties of Sulfonated and Unsulfonated Poly(arylene ether triazine)s with Pendant Diphenylamine Groups for Fuel Cell Applications," J. Membr. Sci. **369**, 455 (2011).

Tomiyasu, K., Crawford, M.K., Adroja, D., Manuel, P., Tominaga, A., Hara, S., Sato, H., Watanabe, T., Ikeda, S.I., Lynn, J.W., Iwasa, K., Yamada, K., "Molecular Spin Excitations in the Orbitally Frustrated Spinel $GeCo_2O_4$," Phys. Rev. B **84**(5), 054405-1 (2011).

Tong, P., Huang, Q., Kofu, M., Lehman, M.C., Yu, J., Louca, D., "A Complex Magnetic Structure in the Magnetoresistive $La_{0.82}Ba_{0.18}CoO_3$," J. Phys.: Conf. Series **251**(1), 012015 (2010).

Tong, P., Yu, J., Huang, Q., Yamada, K., Louca, D., "Possible Link of a Structurally Driven Spin Flip Transition and the Insulator-Metal Transition in the Perovskite $La_{1-x}Ba_xCoO_3$," Phys. Rev. Lett. **106**(15), 156407-1 (2011).

Tong, X., Pierce, J., Lee, W.T., Fleenor, M., Chen, W., Jones, G.L., Robertson, J.L., "Electrical Heating for SEOP-based polarized ^{3}He system," J. Phys.: Conf. Series **251**, 012087 (2010).

Top, A., Zhong, S., Yan, C., Roberts, C.J., Pochan, D.J., Kiick, K.L., "Controlling Assembly of Helical Polypeptides *via* PEGylation Strategies," Soft Matter, in press.

Torija, M.A., Sharma, M., Gazquez, J., Varela, M., He, C., Schmitt, J., Borchers, J.A., El-Khatib, S., "Chemically Driven Nanoscopic Magnetic Phase Separation at the $SrTiO_3(001)/La_{1-x}Sr_xCoO_3$ Interface," Adv. Mater. **23**, 2711 (2011). **[CHRNS]**

Trinkle, D.R., Ju, H., Heuser, B.J., Udovic, T.J., "Nanoscale Hydride Formation at Dislocations in Palladium:*Ab initio* Theory and Inelastic Neutron Scattering Measurements," Phys. Rev. B **83**(17), 174116-1 (2011).

Tsao, C., Li, M., Zhang, Y., Leão, J.B., Chiang, W., Chung, T., Tzeng, Y., Yu, M., Chen, S., "Probing the Room Temperature Spatial Distribution of Hydrogen in Nanoporous Carbon by Use of Small-Angle Neutron Scattering," J. Phys. Chem. C **114**, 19895 (2010).

Tun, Z., Noel, J.J., Bohdanowicz, T., Cao, L.R., Downing, R.G., Goncharova, L.V., "Cold-Neutron Depth Profiling as a Research Tool for the Study of Surface Oxides on Metals," Canadian J. Phys. **88**, 751 (2010).

Vaknin, D., Garlea, V.O., Demmel, F., Mamontov, E., Nojiri, H., Martin, C., Chiorescu, I., Qiu, Y., Kögerler, P., Fielden, J., Engelhardt, L., Rainey, C., Luban, M., "Level Crossings and Zero-field Splitting in the $\{Cr_8\}$-Cubane Spin-cluster by Inelastic Neutron Scattering and Magnetization Studies," J. Phys.: Condens. Matter **22**, 466001-1 (2010). **[CHRNS]**

Verdal, N., Udovic, T.J., Copley, J.R.D., Rush, J.J., "Detection of Dynamical Transitions in Hydrogenous Materials Using Transmission Measurements with Very Cold Neutrons," J. Solid State Chem. **184**, 2635 (2011). **[CHRNS]**

Verdal, N., Udovic, T.J., Rush, J.J., Cappelletti, R.L., Zhou, W., "Hydrogen Dynamics of the Dodecahydro-closo-dodecaborate Crystals," Prepr. Pap. Am. Chem. Soc., Div. Fuel Chem. **56**(2), 181 (2011). **[CHRNS]**

Verdal, N., Udovic, T.J., Rush, J.J., Cappelletti, R.L., Zhou, W., "Reorientational Dynamics of the Dodecahydro-*Closo*-Codecaborate Anion in $Cs_2B_{12}H_{12}$," J. Phys. Chem. A **115**(14), 2933 (2011). **[CHRNS]**

Verdal, N., Udovic, T.J., Rush, J.J., Stavila, V., Wu, H., Zhou, W., Jenkins, T., "Low-Temperature Tunneling and Rotational Dynamics of the Ammonium Cations in $(NH_4)_2B_{12}H_{12}$," J. Chem. Phys. **135**(9), 094501-1 (2011). **[CHRNS]**

Verdal, N., Zhou, W., Stavila, V., Her, J.-H., Yousufuddin, M., Yildirim, T., Udovic, T.J., "Alkali and Alkaline-Earth Metal Dodecahydro-*Closo*-Dodecaborates: Probing Structural Variations via Neutron Vibrational Spectroscopy," J. Alloys Compd., in press.

Vogt, B.D., O'Brien, B.O., Allee, D.R., Loy, D., Akgun, B., Satija, S.K., "Distribution of Hydrogen in Low Temperature Passivated Amorphous Silicon (a-Si:H) Films from Neutron Reflectivity," J. Non-Cryst. Solids **357**, 1114 (2011).

Wacklin, H.P., "Neutron Reflection from Supported Lipid Membranes," Curr. Opin. Colloid Interface Sci. **15**, 445 (2010).

Walker, M.L., Vanderah, D.J., Rubinson, K.A., "*In-situ* Characterization of Self-Assembled Monolayers of Water-Soluble Oligo(ethylene oxide) Compounds," Colloids Surf. B **82**(2), 450 (2011).

Wang, C.H., Christianson, A.D., Lawrence, J.M., Bauer, E.D., Goremychkin, E.A., Kolesnikov, A.I., Trouw, F., Ronning, F., Thompson, J.D., Lumsden, M.D., Ni, N., Mun, E.D., Jia, S., Canfield, P.C., Qiu, Y., Copley, J.R.D., "Neutron Scattering and Scaling Behavior in URu_2Zn_{20} and $YbFe_2Zn_{20}$," Phys. Rev. B **82**, 184407 (2010). **[CHRNS]**

Wang, C.H., Lawrence, J.M., Bauer, E.D., Kothapalli, K., Gardner, J.S., Ronning, F., Gofryk, K., Thompson, J.D., Nakotte, H., Trouw, F., "Unusual Signatures of the Ferromagnetic Transition in the Heavy Fermion Compound UMn_2Al_{20}," Phys. Rev. B **82**(9), 094406-1 (2010).

Wang, C.H., Lawrence, J.M., Christianson, A.D., Chang, S., Gofryk, K., Bauer, E.D., Ronning, F., Thompson, J.D., McClellan, K.J., Rodriguez, J.A., Lynn, J.W., "Quantum Critical Behavior in the Heavy Fermion Single Crystal $Ce(Ni_{0.935}Pd_{0.065})_2Ge_2$," J. Phys.: Conf. Series **273**, 012018 (2011). **[CHRNS]**

Wang, M., Luo, H., Wang, M., Chi, S.X., Rodriguez, J.A., Singh, D., Chang, S., Lynn, J.W., Dai, P., "Magnetic Field Effect on the Static Antiferromagnetic Order and Spin Excitations in Underdoped Iron Arsenide Superconductor $BaFe_{1.92}Ni_{0.08}As_2$," Phys. Rev. B **83**(9), 094516-1 (2011). **[CHRNS]**

Wang, M., Wang, X.C., Abernathy, D.L., Harriger, L.W., Luo, H.Q., Zhou, Y., Lynn, J.W., Liu, Q.Q., Jin, C.Q., Fang, C., Hu, J., Dai, P., "Antiferromagnetic Spin Excitations in Single Crystals of Nonsuperconducting $Li_{1-x}FeAs$," Phys. Rev. Lett. **83**(22), 220515-1 (2011).

Wang, S.-C., Mirarefi, P., Faraone, A., Lee, C.T., "Light-Controlled Protein Dynamics Observed with Neutron Spin Echo Measurements," Biochemistry, in press. **[CHRNS]**

Wang, S.-K., Mamontov, E., Bai, M., Hansen, F.Y., Taub, H., Copley, J.R.D., Garcia, S.V., Gasparovic, G., Jenkins, T., Tyagi, M., Herwig, K.W., Neumann, D.A., Montfrooij, W., Volkmann, U., "Localized Diffusive Motion on Two Different Time Scales in Solid Alkane Nanoparticles," Europhys. Lett. **91**, 66007 (2010). **[CHRNS]**

Wang, X., Hanson, H.A., Ling, X.S., Majkrzak, C.F., Maranville, B.B., "Three-Dimensional Spatially Resolved Neutron Diffraction from a Disordered Vortex Lattice," J. Appl. Crystallogr. **44**, 414 (2011).

Wang, X., Huang, Q., Deng, J., Yu, R., Chen, J., Xing, X., "Phase Transformation and Negative Thermal Expansion in $TaVO_5$," Inorg. Chem. **50**, 2685 (2011).

Wang, X., Van Nguyen, T., Hussey, D.S., Jacobson, D.L., "An Experimental Study of Relative Permeability of Porous Media Used in Proton Exchange Membrane Fuel Cells," J. Electrochem. Soc. **157**(12), B1777 (2010).

Wang, X., Van Nguyen, T., Hussey, D.S., Jacobson, D.L., "Experimental Study of Relative Permeability of Porous Media Used in PEM Fuel Cells," ECS Trans. **33**(1), 1151 (2010).

Waters, D.J., Engberg, K., Parke-Houben, R., Ta, C.N., Jackson, A., Toney, M.F., Frank, C.W., "Structure and Mechanism of Strength Enhancement in Interpenetrating Polymer Networks Hydrogels," Macromol. **44**, 5576 (2011).

Weck, P.F., Kim, E., Poineau, F., Rodriguez, E.E., Sattelberger, A.P., Czerwinski, K.R., "Structural and Electronic Trends in Rare-Earth Technetate Pyrochlores," Dalton Trans. **39**, 7207 (2010). **[CHRNS]**

West, D.V., Davies, P.K., "Triclinic and Monoclinic Structures of $SrLaCuNbO_6$ and $SrLaCuTaO_6$ Double Perovskites," J. Appl. Crystallogr. **45**, 595 (2011).

White, II, G.V., Kitchens, C.L., "Small-Angle Neutron Scattering of Silver Nanoparticles in Gas-Expanded Hexane," J. Phys. Chem. C **114**, 16285 (2010).

White, II, G.V., Mohammed, F.S., Kitchens, C.L., "Small-Angle Neutron Scattering Investigation of Gold Nanoparticle Clustering and Ligand Stucture Under Antisolvent Conditions," J. Phys. Chem. C **115**, 18397 (2011).

Wilking, J.N., Chang, C.B., Fryd, M.M., Porcar, L., Mason, T.G., "Shear-Induced Disruption of Dense Nanoemulsion Gels," Langmuir **27**, 5204 (2011).

Wilson, S.D., Yamani, Z., Rotundu, C.R., Freelon, B., Valdivia, P.N., Bourret-Courchesne, E., Lynn, J.W., Chi, S., Hong, T., Birgeneau, R.J., "Antiferromagnetic Critical Fluctuations in $BaFe_2As_2$," Phys. Rev. B **82**, 144502-1 (2010).

Wolff, M., Gutfreund, P., Rühm, A., Akgun, B., Zabel, H., "Nanoscale Discontinuities at the Boundary of Flowing Liquids: A Look into Structure," J. Phys.: Condens. Matter **23**, 184102 (2011).

Wong-Ng, W., Espinal, L., Allen, A.J., Kaduk, J.A., Suchomel, M.R., Wu, H., "High-Resolution Synchrotron X-ray Powder Diffraction Study of bis(2-methylimidazolyl)-zinc $C_8H_{10}N_4Zn$ (ZIF-9)," Powder Diffr. **26**(3), 234 (2011).

Wong-Ng, W., Lu, T., Xie, W., Tang, W.H., Kaduk, J.A., Huang, Q., Yan, Y.N., Chattopadhyay, S., Tang, X., "Phase Diagram, Crystal Chemistry and Thermoelectric Properties of Compounds in the Ca-Co-Zn-O System," J. Solid State Chem. **184**, 2159 (2011).

Wu, H., Zhou, W., Pinkerton, F.E., Meyer, M.S., Srinivas, G., Yildirim, T., Udovic, T.J., Rush, J.J., "A New Family of Metal Borohydride Ammonia Borane Complexes: Synthesis, Structures, and Hydrogen Storage Properties," J. Mater. Chem. **20**, 6550 (2010).

Wu, H., Zhou, W., Pinkerton, F.E., Meyer, M.S., Yao, Q., Srinivas, G., Udovic, T.J., Yildirim, T., Rush, J.J., "Sodium Magnesium Amidoborane: The First Mixed-Metal Amidoborane," Chem. Comm. **47**, 4102 (2011).

Xie, T., Page, K.A., Eastman, S.A., "Strain-Based Temperature Memory Effect for Nafion and Its Molecular Origins," Adv. Func. Mater. **21**, 2057 (2011).

Xie, W., He, J., Tang, X., Zhu, S., Laver, M., Wang, S., Copley, J.R.D., Brown, C.M., Zhang, Q., Tritt, T.M., "Identifying the Specific Nanostructures Responsible for the High Thermoelectric Performance of $(Bi,Sb)_2Te_3$ Nanocomposites," Nano Lett. **10**, 3283 (2010). **[CHRNS]**

Xu, J., Yang, B., Hammouda, B., "Thermal Conductivity and Viscosity of Self-Assembled Alcohol/Polyalphaolefin Nanoemulsion Fluids," Nanoscale Res. Lett. **6**, 274-1 (2011).

Xu, Z., Wen, J., Xu, G., Chi, S., Ku, W., Gu, G.D., Tranquada, J.M., "Local-Moment Magnetism in Superconducting $FeTe_{0.35}Se_{0.65}$ as Seen via Inelastic Neutron Scattering," Phys. Rev. B **84**(5), 052506-1 (2011).

Xu, Z., Wen, J., Xu, G., Jie, Q., Lin, Z., Li, Q., Chi, S.X., Singh, D.K., Gu, G.D., Tranquada, J.M., "Disappearance of Static Magnetic Order and Evolution of Spin Fluctuations in $Fe_{1+\delta}Se_xTe_{1-x}$," Phys. Rev. B **82**(10), 104525-1 (2010).

Xu, Z., Wen, J., Xu, G., Stock, C., Gardner, J.S., Gehring, P.M., "A Two-Component Model of the Neutron Diffuse Scattering in the Relaxor Ferroelectric PZN-4.5%PT," Phys. Rev. B **82**(13), 134124-1 (2010). **[CHRNS]**

Yamamuro, O., Yamada, T., Kofu, M., Nakakoshi, M., Nagao, M., "Hierarchical Structure and Dynamics of an Ionic Liquid 1-Octyl-3-methylimidazolium Chloride," J. Chem. Phys., in press. **[CHRNS]**

Yan, C., Altunbas, A., Yucel, T., Nagarkar, R.P., Schneider, J.P., Pochan, D.J., "Injectable Solid Hydrogel: Mechanism of Shear-Thinning and Immediate Recovery of Injectable β-Hairpin Peptide Hydrogels," Soft Matter **6**, 5143 (2010).

Yang, K.X., Kitto, M.E., Orsini, J.P., Swami, K., Beach, S.E., "Evaluation of Sample Pretreatment Methods for Multiwalled and Single-walled Carbon Nanotubes for the Determination of Metal Impurities by ICPMS, ICPOES, and Instrument Neutron Activation Analysis," J. Anal. At. Spectrom. **25**, 1290 (2010).

Yang, M., Li, K., Su, J., Huang, Q., Bao, W., You, L., Li, Z., Wang, Y., Jiang, Y., Liao, F., Lin, J., "Study on the Crystal Structure of the Rare Earth Oxyborate $Yb_{26}B_{12}O_{57}$ from Powder X-ray and Neutron Diffraction," J. Alloys Compd. **509**, 4707 (2011).

Yang, Y., Brown, C.M., Zhao, C., Chafee, A.L., Nick, B., Zhao, D., Webley, P.A., Schalch, J., Simmons, J.M., Liu, Y., Her, J., Buckley, C.E., Sheppard, D.A., "Micro-Channel Development and Hydrogen Adsorption Properties in Templated Microporous Carbons Containing Platinum Nanoparticles," Carbon **49**, 1305 (2011). **[CHRNS]**

Yang, Y., Wang, T., Li, G.N., Huang, Q., Gao, Q.Q., Li, J.B., Liu, G.Y., Rao, G.H., "Magnetic Structure and Preferential Occupation of Fe in the Composite Compound Nd_2Co_6Fe," Physica B **406**, 1995 (2011).

Yi, Z., Nagao, M., Bossev, D.P., "How Lidocaine Influences the Bilayer Thickness and Bending Elasticity of Biomembranes," J. Phys.: Conf. Series **251**, 012037 (2010). **[CHRNS]**

Yin, L., Hillmyer, M.A., "Disklike Micelles in Water from Polyethylene-Containing Diblock Copolymers," Macromol. **44**, 3021 (2011).

Yoonessi, M., Gaier, J.R., "Highly Conductive Multifunctional Graphene Polycarbonate Nanocomposites," ACS Nano **4**(12), 7211 (2010). **[CHRNS]**

Yuan, G., Li, C., Satija, S.K., Karim, A., Douglas, J.F., Han, C.C., "Observation of a Characteristic Length Scale in the Healing of Glassy Polymer Interfaces," Soft Matter **6**, 2153 (2010).

Zajdel, P., Hsieh, P., Rodriguez, E.E., Butch, N.P., Magill, J.D., Paglione, J., Zavalij, P., Suchomel, M.R., Green, M.A., "Phase Separation and Suppression of the Structural and Magnetic Transitions in Superconducting Doped Iron Tellurides, $Fe_{1+x}Te_{1-y}S_y$," J. Am. Chem. Soc. **132**, 13000 (2010).

Zavalij, P., Bao, W., Wang, X.F., Ying, J.J., Chen, X.H., Wang, D.M., He, J.B., Wang, X.Q., Chen, G.F., Hsieh, P., Huang, Q., Green, M.A., "Structure of Vacancy-Ordered Single-Crystalline Superconducting Potassium Iron Selenide," Phys. Rev. B **83**(13), 132509-1 (2011).

Zeisler, R., Oflaz, R., Paul, R.L., Fagan, J.A., "Use of Neutron Activation Analysis for the Characterization of Single-Wall Carbon Nanotube Materials," J. Radioanal. Nucl. Chem., in press.

Zeisler, R., Paul, R.L., Oflaz Spatz, R., Yu, L.L., Mann, J.L., Kelly, W.R., Lang, B.E., Leigh, S.D., Fagan, J., "Elemental Analysis of a Single-Wall Carbon Nanotube Candidate Reference Material," Anal. Bioanal. Chem. **399**, 509 (2010).

Zeisler, R.L., Vajda, N., Kennedy, G.J., Lamaze, G.P., Molnár, G., "Activation Analysis," in "Handbook of Nuclear Chemistry," edited by Vértes, A., Nagy, S., Klencsár, Z., Lovas, R.G., Rösch, F. (Springer Science and Business Media), Vol. 3, Chap. 30, 1553 (2011).

Zhang, C., Grass, M.E., McDaniel, A.H., DeCaluwe, S.C., El Gabaly, F., Liu, Z., McCarty, K.F., Farrow, R.L., Linne, M.A., Hussain, Z., Jackson, G.S., Bluhm, H., Eichhor, B.W., "Measuring Fundamental Properties in Operating Solid Oxide Electrochemical Cells by Using *in Situ* X-ray Photoelectron Spectroscopy," Nat. Mater. **9**, 944 (2010).

Zhang, W., Lin, M., Winesett, A., Dhez, O., Kilcoyne, L.A., Ade, H., Rubinstein, M., Shafi, K.V.P.M., Ulman, A., Dersappe, D., Tenne, R., Rafailovich, M., Sokolov, J., Frisch, H.L., "The Use of Functionalized Nanoparticles as Non-Specific Compatibilizers for Polymers Blends," Polym. Adv. Tech. **22**, 65 (2011).

Zhang, Y., Faraone, A., Kamitakahara, W., Liu, K., Mou, C., Leão, J.B., Chang, S., Chen, S., "Density Hysteresis of Heavy Water Confined in a Nanoporous Silica Matrix," Proc. Natl. Acad. Sci. USA **108**(30), 12206 (2011).

Zhang, Y., Tyagi, M., Mamontov, E., Chen, S., "Quasi-Elastic Neutron Scattering Studies of the Slow Dynamics of Supercooled and Glassy Aspirin," J. Phys.: Condens. Matter, in press. **[CHRNS]**

Zhou, H.D., Barlas, Y., Wiebe, C.R., Qiu, Y., Copley, J.R.D., Gardner, J.S., "Inter-and Intratrimer Excitations in the Multiferroic $Ba_3NbFe_3Si_2O_{14}$," Phys. Rev. B **82**(13), 132408-1 (2010). **[CHRNS]**

Zhou, H.D., Choi, E.S., Li, G., Balicas, L., Wiebe, C.R., Qiu, Y., Copley, J.R.D., Gardner, J.S., "Spin Liquid State in the $S = 1/2$ Triangular Lattice $Ba_3CuSb_2O_9$," Phys. Rev. Lett. **106**(14), 147204-1 (2011). **[CHRNS]**

Zhou, S., Zhang, J., Liu, D., Lin, Z., Huang, Q., Bao, L., Ma, R., Wei, Y., "Synthesis and Properties of Nanostructured Dense LaB_6 Cathodes by Arc Plasma and Reactive Spark Plasma Sintering," Acta Mater. **58**, 4978 (2010).

Zhou, W., Wu, H., Yildirim, T., "Structural Stability and Elastic Properties of Prototypical Covalent Organic Frameworks," Chem. Phys. Lett. **499**, 103 (2010).

Ziserman, L., Lee, H., Raghavan, S.R., Mor, A., Danino, D., "Unraveling the Mechanism of Nanotube Formation by Chiral Self-Assembly of Amphiphiles," J. Am. Chem. Soc. **133**, 2511 (2011)

Instruments and Contacts

Instruments and Contacts: (name, tel. 301-975-xxxx, email)

High resolution powder diffractometer (BT-1):

- J.K. Stalick, 6223, judith.stalick@nist.gov
- Q.Z. Huang, 6164, qing.huang@nist.gov
- M. Green, 4297, mark.green@nist.gov
- H. Wu, 2387, hui.wu@nist.gov

Residual stress diffractometer (BT-8):

- T. Gnaeupel-Herold, 5380, thomas.gnaeupel-herold@nist.gov

30-m SANS instrument (NG-7):

- Yun Liu, 6235, yun.liu@nist.gov
- Gil Toombes, 8396, gilman.toombes@nist.gov
- Paul Butler, 2028, paul.butler@nist.gov
- Jeff Krzywon, 6650, jkrzywon@nist.gov

30-m SANS instrument (NG-3) (CHRNS):

- Boualem Hammouda, 3961, hammouda@nist.gov
- Steve Kline, 6243, steven.kline@nist.gov
- Susan Krueger, 6734, susan.krueger@nist.gov
- Cedric Gagnon, 2020, cedric.gagnon@nist.gov

USANS, Perfect Crystal SANS (BT-5) (CHRNS):

- David Mildner, 6366, david.mildner@nist.gov
- Paul Butler, 2028, paul.butler@nist.gov

Polarized Beam Reflectometer (NG-D):

- B.J. Kirby, 8395, brian.kirby@nist.gov
- J.A. Borchers, 6597, julie.borchers@nist.gov
- C.F. Majkrzak, 5251, cmajkrzak@nist.gov

MAGIk, Off-Specular Reflectometer (NG-D):

- B.B. Maranville, 6034, brian.maranville@nist.gov
- J.A. Dura, 6251, joseph.dura@nist.gov

Neutron reflectometer-horizontal sample (NG-7):

- S.K. Satija, 5250, satija@nist.gov
- B. Akgun, 6469, bulent.akgun@nist.gov

Double-focusing triple-axis Spectrometer (BT-7)

- Y. Zhao, 2164, yang.zhao@nist.gov
- J. Helton, 4899, joel.helton@nist.gov
- J.W. Lynn, 6246, jeff.lynn@nist.gov

SPINS, Spin-polarized triple-axis spectrometer (NG-5) (CHRNS):

- P. Gehring, 3946, peter.gehring@nist.gov
- D. Singh, 4863, deepak.singh@nist.gov

Triple-axis spectrometer (BT-4):

- W. Ratcliff, 4316, william.ratcliff@nist.gov

FANS, Filter-analyzer neutron spectrometer (BT-4):

- T.J. Udovic, 6241, udovic@nist.gov
- J. Leao, 8867, juscelino.leao@nist.gov

DCS, Disk-chopper time-of-flight spectrometer (NG-4) (CHRNS):

- J.R.D. Copley, 5133, jcopley@nist.gov
- Y. Qiu., 3274, yiming.qiu@nist.gov
- C. M. Brown, 5134, craig.brown@nist.gov

HFBS, High-flux backscattering spectrometer (NG-2) (CHRNS):

- M. Tyagi, 2046, madhusudan.tyagi@nist.gov
- T. Jenkins, 8396, timothy.jenkins@nist.gov

NSE, Neutron spin echo spectrometer (NG-5) (CHRNS):

- A. Faraone, 5254, antonio.faraone@nist.gov
- J.S. Gardner, 8396, jason.gardner@nist.gov
- M. Nagao, 5505, michihiro.nagao@nist.gov

MACS, Multi-angle crystal spectrometer (BT-9) (CHRNS):

- J. Rodriguez, 6019, jose.rodriguez@nist.gov
- C. Stock, 6422, chris.stock@nist.gov

Cold-neutron prompt-gamma neutron activation analysis (NG-D):

- R.L. Paul, 6287, rpaul@nist.gov

Thermal-neutron prompt-gamma activation analysis (VT-5):

- G. Downing, 3782, gregory.downing@nist.gov

Other activation analysis facilities:

- G. Downing, 3782, gregory.downing@nist.gov

Cold neutron depth profiling (NG-1):

- G. Downing, 3782, gregory.downing@nist.gov

Neutron Imaging Station (BT-2)

- D. Jacobson, 6207, david.jacobson@nist.gov
- D. Hussey, 6465, daniel.hussey@nist.gov
- M.Arif, 6303, muhammad.arif@nist.gov

Neutron interferometer (NG-7):

- M. Arif, 6303, muhammad.arif@nist.gov
- D. Jacobson, 6207, david.jacobson@nist.gov
- D. Hussey, 6465, daniel.hussey@nist.gov

Fundamental neutron physics station (NG-6):

- NG-6M: M.S. Dewey, 4843, mdewey@nist.gov
- NG-6U: H.P. Mumm, 8355, pieter.mumm@nist.gov
- NG-6: J. Nico, 4663, nico@nist.gov

Theory and modeling:

- J.E. Curtis, 3959, joseph.curtis@nist.gov
- T. Yildirim, 6228, taner@nist.gov
- W. Zhou, 8169, wei.zhou@nist.gov

NIST CENTER FOR NEUTRON RESEARCH CONTACTS

Copies of annual reports, facility information, user information, And research proposal guidelines are available electronically.

Please visit our website: http://www.ncnr.nist.gov

For a paper copy of this report:

Ron Cappelletti
301-975-6221
ron.cappelletti@nist.gov

For general information on the facility:

Rob Dimeo
301-975-6210
robert.dimeo@nist.gov

Dan Neumann
301-975-5252
dan.neumann@nist.gov

For information on visiting the facility and/or user access questions:

Julie Keyser
301-975-8200
julie.keyser@nist.gov

Mary Ann FitzGerald
301-975-8200
maryann.fitzgerald@nist.gov

For information on performing research at the facility:

Bill Kamitakahara
301-975-6878
william.kamitakahara@nist.gov

Facility address:

NIST Center for Neutron Research
National Institute of Standards and Technology
100 Bureau Drive, Mail Stop 6100
Gaithersburg, MD 20899-6100
USA

NIST CENTER FOR NEUTRON RESEARCH
National Institute of Standards and Technology
100 Bureau Drive, MS 6100
Gaithersburg, MD 20899-6100

www.ncnr.nist.gov